STRATIFICATION IN THE CORES OF EARTH AND OTHER PLANETS

EDITED BY: Hagay Amit, Renaud Deguen, Peter Driscoll and Takashi Nakagawa
PUBLISHED IN: Frontiers in Earth Science

frontiers Research Topics

ISSN 1664-8714
ISBN 978-2-88963-104-9
DOI 10.3389/978-2-88963-104-9

About Frontiers

Frontiers is more than just an open-access publisher of scholarly articles: it is a pioneering approach to the world of academia, radically improving the way scholarly research is managed. The grand vision of Frontiers is a world where all people have an equal opportunity to seek, share and generate knowledge. Frontiers provides immediate and permanent online open access to all its publications, but this alone is not enough to realize our grand goals.

Frontiers Journal Series

The Frontiers Journal Series is a multi-tier and interdisciplinary set of open-access, online journals, promising a paradigm shift from the current review, selection and dissemination processes in academic publishing. All Frontiers journals are driven by researchers for researchers; therefore, they constitute a service to the scholarly community. At the same time, the Frontiers Journal Series operates on a revolutionary invention, the tiered publishing system, initially addressing specific communities of scholars, and gradually climbing up to broader public understanding, thus serving the interests of the lay society, too.

Dedication to Quality

Each Frontiers article is a landmark of the highest quality, thanks to genuinely collaborative interactions between authors and review editors, who include some of the world's best academicians. Research must be certified by peers before entering a stream of knowledge that may eventually reach the public - and shape society; therefore, Frontiers only applies the most rigorous and unbiased reviews.
Frontiers revolutionizes research publishing by freely delivering the most outstanding research, evaluated with no bias from both the academic and social point of view. By applying the most advanced information technologies, Frontiers is catapulting scholarly publishing into a new generation.

What are Frontiers Research Topics?

Frontiers Research Topics are very popular trademarks of the Frontiers Journals Series: they are collections of at least ten articles, all centered on a particular subject. With their unique mix of varied contributions from Original Research to Review Articles, Frontiers Research Topics unify the most influential researchers, the latest key findings and historical advances in a hot research area! Find out more on how to host your own Frontiers Research Topic or contribute to one as an author by contacting the Frontiers Editorial Office: researchtopics@frontiersin.org

STRATIFICATION IN THE CORES OF EARTH AND OTHER PLANETS

Topic Editors:
Hagay Amit, CNRS UMR 6112, Université de Nantes, France
Renaud Deguen, Université de Lyon, UCBL, ENSL, CNRS, LGL-TPE, France
Peter Driscoll, Carnegie Institution for Science, United States
Takashi Nakagawa, University of Hong Kong, Hong Kong

Citation: Amit, H., Deguen, R., Driscoll, P., Nakagawa, T., eds. (2019). Stratification in the Cores of Earth and Other Planets. Lausanne: Frontiers Media.
doi: 10.3389/978-2-88963-104-9

Table of Contents

frontiers in Earth Science

EDITORIAL
published: 26 June 2019
doi: 10.3389/feart.2019.00165

Editorial: Stratification in the Cores of Earth and Other Planets

Hagay Amit[1]*, *Renaud Deguen*[2], *Peter Driscoll*[3] and *Takashi Nakagawa*[4]

[1] Laboratoire de Planétologie et de Géodynamique, CNRS UMR 6112, Université de Nantes, Nantes, France, [2] Université de Lyon, UCBL, ENSL, CNRS, LGL-TPE, Villeurbanne, France, [3] Department of Terrestrial Magnetism, Carnegie Institution for Science, Washington, DC, United States, [4] Department of Earth Sciences, University of Hong Kong, Hong Kong, Hong Kong

Keywords: core, stratification, convection, magnetic field, planets

Editorial on the Research Topic

Stratification in the Cores of Earth and other Planets

Based on mineral physics and seismic studies, it has been proposed that parts of the liquid outer core of the Earth and other planets are stably stratified, in particular near the boundaries. Such stratification may have profound impacts on the convective state of these cores and the morphology of the generated magnetic fields. Stratification at the top of Earth's core may have consequences for interpretations of the secular variation (SV), including magnetic flux concentration, diffusion, and dipole changes. It has also been suggested that a stratified layer (possibly slurry) prevails above the inner core boundary. Such a layer may be associated with the growth and/or internal dynamics of the inner core and the release of light elements to the outer core which is the primary source of energy for the geodynamo. Chemically stratified layers may be primordial or form slowly through differentiation, such as the solidification of the inner core or bulk precipitation of a minor species. Stratification may prevail in other planets as well. For example, the weak intensity of Mercury's magnetic field and the axisymmetry of Saturn's magnetic field may both be explained by a skin effect due to stratification at these planets. The scope of this Research Topic encompasses evidence for (or against) stratification at the outer cores of Earth and other planets, and their dynamical consequences for core convection and the generated planetary magnetic fields. The Research Topic involves multiple disciplines, including mineral physics, seismology, geomagnetism, dynamo simulations, thermal history models, and more.

Mineral physics inferences of thermal conductivity have consequences for the convective state at the top of the core (e.g., Pozzo et al., 2012). The anisotropy of the thermal conductivity of hcp iron was experimentally examined using synchrotron X-ray diffraction experiments and thermal conductivity measurements by Ohta et al. They found that the thermal conductivity of single crystal hcp iron along c axis is significantly larger than that along a axis, which could have caused the controversial values of thermal conductivity of hcp iron at Earth's core conditions. Gomi and Yoshino carried first-principles calculations on the band structure and the impurity resistivity of substitutionally disordered hcp and fcc Fe based alloys. Their results provide a model for the heat flux across the thermal boundary layer at the bottom of the mantle which favors thermal stratification at the top of Earth's and super-Earth's cores.

Geomagnetic as well as geodetic observations may provide evidence for or against stratification (e.g., Buffett, 2014). Glane and Buffet proposed a new coupling mechanism that relies on the presence of stable stratification at the top of the core to explain length of day (LOD) variations. Steady core flow over boundary topography promotes radial motion, but stratification opposes it.

Edited and reviewed by:
Kenneth Philip Kodama, Lehigh University, United States

***Correspondence:**
Hagay Amit
Hagay.Amit@univ-nantes.fr

Specialty section:
This article was submitted to Geomagnetism and Paleomagnetism, a section of the journal Frontiers in Earth Science

Received: *24 May 2019*
Accepted: *07 June 2019*
Published: *26 June 2019*

Citation:
Amit H, Deguen R, Driscoll P and Nakagawa T (2019) Editorial: Stratification in the Cores of Earth and Other Planets. Front. Earth Sci. 7:165. doi: 10.3389/feart.2019.00165

Steep vertical gradients develop in the resulting flow, causing horizontal electromagnetic forces in the presence of a radial magnetic field. The associated pressure field exerts a net horizontal force on the boundary and stresses that are sufficient to account for the observed changes in LOD. Huguet et al. proved that non-zero SV of the total geomagnetic energy on the core-mantle boundary (CMB) requires presence of radial motions extending to the top of the core. Using geomagnetic field and SV models, they found comparable balance of sources and sinks of the SV of the total geomagnetic energy and the SV of the geomagnetic dipole intensity and tilt, indicating that upwelling/downwelling reach the top of the core, hence providing observational evidence for either no stratified layer or its penetration.

These observations constrain dynamical models, which in turn provide insights to the impact of stratification on convection and the induced magnetic fields (e.g., Christensen, 2006). In addition, such simulations may unravel the mechanisms for the construction, destruction or penetration of stratified layers. Olson et al. compared magnetic fields produced by numerical dynamos with heterogeneous CMB heat flux and stable thermal stratification at the top of the shell vs. observed geomagnetic field models. They found that reversed flux patches and stratification are difficult to reconcile. They concluded that the thermal stratified layer in Earth's core is up to 400 km and permeable. Using numerical dynamos with non-diffusive compositional convection, Bouffard et al. obtained self-consistent formation of a chemically stratified layer at the top of the shell caused by the accumulation of chemical plumes emitted at the bottom boundary. Application to Earth's core conditions suggest weak stratification. Dietrich and Wicht applied their numerical investigation to Saturn's dynamics by setting a sandwiched stable stratified layer surrounded by two convective zones. They found that the mean penetration depth of the layer is controlled by the ratio of stratified and unstratified buoyancy gradients, i.e., independent of rotation. However, the penetration depth depends on latitude, since in the rapidly rotating regime axial convective columns pierce predominantly outside the tangent cylinder.

Simpler models may also shed light on the nature of stratified layers (e.g., Labrosse et al., 1997). For example, Takehiro and Sasaki designed a 1D thermal and compositional balance model of the Earth's core. They showed that a thermally stable layer becomes thinner when the effect of compositional convection is considered compared with the results of previous studies where the existence of a stable layer is evaluated based on the convective flux only.

In summary, the eight papers that comprise this Research Topic tackled the problem of core stratification using various approches—experimental, observational, numerical, and theoretical. Applications included various bodies—primarily Earth but also Saturn and super-Earths. The papers addressed various aspects of stratification—existence, erosion, penetration, and signature on observable quantities. We anticipate that stratification will continue to stimulate deep planetary dynamics research. For example, recovering geomagnetic field morphology with a stratified layer is still elusive. For Jupiter, reconciling new magnetic field models inferred from the Juno mission (Moore et al., 2018) with alternating zonal jets is a major challenge. Erosion of a stratified layer by core convection has not yet been fully addressed. Such open questions guarantee that this topic will likely grow in interest in the future.

AUTHOR CONTRIBUTIONS

All authors listed have made a substantial, direct and intellectual contribution to the work, and approved it for publication.

REFERENCES

Buffett, B. A. (2014). Geomagnetic fluctuations reveal stable stratification at the top of the earth's core. *Nature* 507, 484–487. doi: 10.1038/nature 13122

Christensen, U. R. (2006). A deep dynamo generating Mercury's magnetic field. *Nature* 444, 1056–1058. doi: 10.1038/nature05342

Labrosse, S., Poirier, J. P., and Le Mouël, J.-L. (1997). On cooling of the earth's core. *Phys. Earth Planet. Inter.* 99, 1–17.

Moore, K. M., Yadav, R. K., Kulowski, L., Cao, H., Bloxham, J., Connerney, J. E. P., et al. (2018). A complex dynamo inferred from the hemispheric dichotomy of Jupiter's magnetic field. *Nature* 561, 76–78. doi: 10.1038/s41586-018-0468-5

Pozzo, M., Davies, C., Gubbins, D., and Alfè, D. (2012). Thermal and electrical conductivity of iron at Earth's core conditions. *Nature* 485, 355–358. doi: 10.1038/nature 11031

Conflict of Interest Statement: The authors declare that the research was conducted in the absence of any commercial or financial relationships that could be construed as a potential conflict of interest.

frontiers in Earth Science

ORIGINAL RESEARCH
published: 10 May 2019
doi: 10.3389/feart.2019.00099

Chemical Convection and Stratification in the Earth's Outer Core

Mathieu Bouffard[1]*, *Gaël Choblet*[2], *Stéphane Labrosse*[3] and *Johannes Wicht*[1]

[1] Department Planets and Comets, Max Planck Institute for Solar System Research, Göttingen, Germany, [2] Laboratoire de Planétologie et Géodynamique, Université de Nantes, Nantes, France, [3] Laboratoire de Géologie de Lyon, Université de Lyon, École Normale Supérieure de Lyon, Université Lyon-1, CNRS, UMR 5276, Lyon, France

Convection in the Earth's outer core is driven by buoyancy sources of both thermal and compositional origin. The thermal and compositional molecular diffusivities differ by several orders of magnitude, which can affect the dynamics in various ways. So far, the large majority of numerical simulations have been performed within the codensity framework that consists in combining temperature and composition, assuming artificially enhanced diffusivities for both variables. In this study, we use a particle-in-cell method implemented in a 3D dynamo code to conduct a first qualitative exploration of pure compositional convection in a rotating spherical shell. We focus on the end-member case of infinite Schmidt number by totally neglecting the compositional diffusivity. We show that compositional convection has a very rich physics that deserves several more focused and quantitative studies. We also report, for the first time in numerical simulations, the self-consistent formation of a chemically stratified layer at the top of the shell caused by the accumulation of chemical plumes and blobs emitted at the bottom boundary. When applied to likely numbers for the Earth's core, some (possibly simplistic) physical considerations suggest that a stratified layer formed in such a scenario would be probably weakly stratified and may be compatible with magnetic observations.

Keywords: compositional convection, stratification, core dynamics, particle-in-cell, infinite Schmidt number

OPEN ACCESS

Edited by:
Peter E. Driscoll, Carnegie Institution for Science (CIS), United States

Reviewed by:
Binod Sreenivasan, Indian Institute of Science (IISc), India
Kenneth Philip Kodama, Lehigh University, United States

***Correspondence:**
Mathieu Bouffard
bouffard@mps.mpg.de

Specialty section:
This article was submitted to Geomagnetism and Paleomagnetism, a section of the journal Frontiers in Earth Science

Received: *15 July 2018*
Accepted: *23 April 2019*
Published: *10 May 2019*

Citation:
Bouffard M, Choblet G, Labrosse S and Wicht J (2019) Chemical Convection and Stratification in the Earth's Outer Core. Front. Earth Sci. 7:99. doi: 10.3389/feart.2019.00099

1. INTRODUCTION

Convection in the Earth's outer core is presently driven by buoyancy sources of both thermal and compositional origin. The thermal source results from the combination of the heat extracted by the mantle, the latent heat released at the bottom of the fluid core by the crystallization of the inner core and possibly the decay of radioactive elements. The chemical source is the consequence of the crystallization of the inner core which releases light elements into the fluid core (Braginsky, 1963; Braginsky and Roberts, 1995) and may also originate from chemical interactions with the mantle through magnesium exsolution (Badro et al., 2016; O'Rourke and Stevenson, 2016) or crystallization of SiO_2 (Hirose et al., 2017). A major difference between these buoyancy sources is tied to their molecular diffusivities which differ by several orders of magnitude, the chemical diffusivity being much weaker than its thermal counterpart. Different values have been proposed for the thermal and chemical molecular diffusivities, respectively κ^T and κ^ξ, and for the kinematic

viscosity ν of liquid iron in core conditions, with typical ranges: $\kappa^T \sim 5 \times 10^{-6} - 10^{-5}$ m^{2}s^{-1} (Poirier, 1988; de Wijs et al., 1998; Roberts and King, 2013), $\kappa^\xi \sim 5 \times 10^{-9} - 2 \times 10^{-8}$ m^{2}s^{-1} (Dobson, 2002; Pozzo et al., 2013; Ichikawa and Tsuchiya, 2015; Posner et al., 2017), and $\nu \sim 5 \times 10^{-7} - 5 \times 10^{-6}$ m^{2}s^{-1} (de Wijs et al., 1998; Vočadlo et al., 2000; Perrillat et al., 2010). These estimates lead to the following ranges for the Prandtl, Schmidt, and Lewis numbers (respectively, $Pr = \nu/\kappa^T$, $Sc = \nu/\kappa^\xi$, and $Le = \kappa^T/\kappa^\xi = Sc/Pr$) which are formed from the ratios of these diffusivities:

$$Pr \simeq 0.05-1 \quad ; \quad Sc \simeq 25-1,000 \quad ; \quad Le \simeq 250-5,000, \quad (1)$$

the Schmidt number Sc being the chemical equivalent to the Prandtl number. Convection in the Earth's outer core is therefore a combination of thermal convection, characterized by a Prandtl number close to 1 or smaller, and chemical convection associated with a much larger Schmidt number.

Classically, the diffusivity difference is ignored in numerical simulations. The thermal and compositional fields are combined into one single variable, the so-called "codensity" (Braginsky and Roberts, 1995; Lister and Buffett, 1995), under the assumption that the mixing action of the unresolved sub-grid-scale turbulence would lead to comparable effective diffusivities for temperature and composition,

$$\kappa^T = \kappa^\xi = \kappa^{\text{turb}}, \quad (2)$$

where κ^{turb} is a homogeneous and isotropic "turbulent" or "eddy" diffusivity. Since turbulent mixing would affect all quantities in a similar way, the Prandtl, Schmidt, and Lewis numbers should be of order one:

$$Pr = Sc = Le = 1. \quad (3)$$

This approximation is convenient to implement in numerical codes but relies on debatable approximations. First, the turbulent regime of the core is not known, though under the effect of rotation it is probably anisotropic (Braginsky and Roberts, 1995; Matsushima, 2004) as suggested by the low value of the Rossby number $Ro = U/D\Omega \sim 10^{-6}$, where U, D, and Ω are, respectively the typical velocity of the fluid, the thickness of the liquid core and the Earth's rotation rate. Rotating MHD turbulence is extremely complex and some of the results of the classic theory of turbulence (established for non-rotating and non-magnetic cases) may not apply in this context (Nataf and Gagniere, 2008; Nataf and Schaeffer, 2015). Turbulence can also be studied through different prisms: while some models favor a spectral description, other authors (Loper and Moffatt, 1993; Moffatt and Loper, 1994; Loper, 2007) consider buoyant plumes or blobs as the elementary structures at the origin of turbulent motions in the core. It is unlikely that the "turbulent" diffusivity parameterization accounts for all these complexities, even though it could provide a reasonable first-order description in some specific turbulent regimes. Second, the codensity approximation is particularly problematic where the net contribution of both fields produces a stable density gradient. In such context, turbulence is probably partially or totally suppressed and any notion of "turbulent" diffusivity becomes highly questionable (Braginsky and Roberts, 1995). The existence of stably stratified layers has been evoked for several planetary cores (Christensen, 2006, 2015; Manglik et al., 2010) including that of the Earth (Gomi et al., 2013). These arguments provide motivation for treating the temperature and composition fields separately without invoking any uncertain parametrization of the turbulence. Furthermore, although certainly still a matter of debate (Konôpková et al., 2016), recent high estimates of the thermal conductivity of the core (de Koker et al., 2012; Pozzo et al., 2012; Gomi et al., 2013; Ohta et al., 2016) suggest that, at present, a large fraction of the heat leaving the Earth's core is simply conducted down the adiabat and is not available for driving thermal convection. Compositional convection may thus play a crucial role in powering Earth's dynamo (Lister and Buffett, 1995; Labrosse, 2015) so that, to first-order, the dynamics of the fluid core can be modeled by considering only compositional convection with a large Schmidt number. Very different properties can be expected for the dynamics of rapidly-rotating convection at high Prandtl/Schmidt numbers compared to more moderate values (Busse, 2002; Simitev and Busse, 2003, 2005). However, the large Prandtl/Schmidt number case has not yet been systematically explored in numerical simulations.

In addition to the high value of the Schmidt number, another fundamental specificity of compositional convection arises from the complexity of the chemical processes occurring at the "mushy layer" that may exist at the interface between the fluid outer core and the crystallizing inner core. Experiments conducted on model systems involving the freezing of ammonium chloride in solution (Chen and Chen, 1991; Huguet et al., 2016) showed that the gravitational instability manifests itself through eruptions of buoyant fluid in the form of chemical plumes emerging through localized "chimneys" that are spontaneously created in the mushy layer. Fluid from the bulk core percolates through the mush and becomes gradually lighter as it converges horizontally into the chimneys. Contrary to thermal plumes, which are more rapidly diffused, chemical plumes emanating from the mushy layer can be expected to keep a coherent shape for a longer time due to their lower molecular diffusivity. This led several authors to speculate about the potential role played by such chemical plumes on the turbulence, convective dynamics, and dynamo action (Gubbins et al., 1982; Moffatt, 1989; Loper and Moffatt, 1993; Bergman and Fearn, 1994; Braginsky, 1994; Moffatt and Loper, 1994; Loper, 2007). Moffatt and Loper (1994) conjectured that light fluid erupts from the mushy layer rather in the form of chemical "blobs" which would keep a coherent shape throughout their path across the core controlled by a magnetostrophic force balance, a prediction challenged by St Pierre (1996) who argued, using numerical simulations, that such blobs would rapidly break-up into plate-like structures elongated in the direction of the rotation axis. The existence of chemical blobs was then reported a few years later in laboratory experiments as the result of instabilities causing the chemical plumes to bend horizontally and break-up (Claßen et al., 1999). However, the authors did not observe the blobs elongation anticipated by St Pierre (1996), possibly because these experiments are good analogs of only the polar regions on

Earth. The predictions for the existence and dynamics of such chemical structures have not yet been verified in global-scale numerical simulations.

A second interesting phenomenon envisioned by Moffatt and Loper (1994) is that the blobs may not completely mix with the bulk of the fluid core but accumulate below the core mantle boundary, thereby gradually forming a chemically stratified layer at the top of the core via a mechanism analogous to the "filling-box" models (Baines and Turner, 1969). This prediction is particularly noteworthy since the existence of a stably stratified layer in the outermost region of the core has been suggested by numerous seismic observations for several decades (Lay and Young, 1990; Tanaka, 2007; Helffrich and Kaneshima, 2010; Kaneshima, 2018). Buffett (2014) also invokes the presence of a stratified layer below the CMB to explain the 60-year period in the geomagnetic secular variation as well as fluctuations in the dipole field. A stably stratified layer at the top of the core is expected to have important implications for the geodynamo, the dynamics, and evolution of the core (Christensen and Wicht, 2008; Nakagawa, 2011; Helffrich and Kaneshima, 2013; Labrosse, 2015; Olson et al., 2017). Though several mechanisms have been proposed to explain the formation of such a layer, its origin remains unknown. The layer could be chemically stratified and produced by the accumulation of "chemical blobs" as proposed by Moffatt and Loper (1994), chemical exchanges with the mantle (Buffett and Seagle, 2010) or result from the incomplete mixing between the primitive core of the Earth and that of a giant impactor (Landeau et al., 2016). Alternatively, the layer could be thermally stratified if the CMB heat flow is sub-isentropic (Gubbins et al., 1982; Labrosse et al., 1997; Lister and Buffett, 1998; Gomi et al., 2013; Labrosse, 2015; Olson et al., 2017, 2018; Christensen, 2018). So far, no numerical simulation has been able to self-consistently produce a stable chemically stratified layer at the top of the core that would emerge from the "chemical blobs" scenario advocated by Moffatt and Loper (1994). The reason may be partly inherent to the codensity framework in which the large majority of the simulations have been conducted up to the present day.

Here, we propose to explore pure chemical convection at high Schmidt number by means of numerical simulations and test whether the accumulation of chemically buoyant parcels of fluid can lead to the formation of a stably stratified layer at the top of the core. Focusing on compositional effects only allows us to gain insight into the specific phenomena involved, independently of an additional forcing of thermal buoyancy. However, though moderately large Prandtl numbers can be reached with the classical codes (for instance, Simitev and Busse, 2005 use up to $Pr = 20$), the study of larger Prandtl or Schmidt numbers requires prohibitive resolutions. Here we use a recently developed version of the PARODY code including a particle-in-cell method (Bouffard et al., 2017) to conduct a first exploratory study of rapidly-rotating pure chemical convection in the end-member case of infinite Schmidt number. Note that we consider $Sc = +\infty$ by setting $\kappa^{\xi} = 0$ and that our approach thus differs from that of Zhang and Busse (1990), Zhang (1991, 1992) who achieved infinite Prandtl number by using an infinite viscosity ($\nu = +\infty$). As will be shown, the phenomena involved in rotating pure compositional convection are rich and numerous. In this exploratory study, we aim at giving a first descriptive and qualitative insight into this particular physics. We also assess whether the stably stratified layer at the top of the core can be formed by the accumulation of chemically buoyant parcels of fluids emanating from the inner core boundary.

This paper is organized as follows. In section 2, the mathematical model and the numerical method are described. The results of a series of numerical simulations of pure compositional convection are then presented. The chemical structures and their dynamics are first studied in section 3. In section 4 we show that, when no light elements are allowed to cross the core-mantle boundary, a chemically stratified layer systematically forms at the top of the spherical shell in all simulations. The potential implications for the Earth's outer core are discussed in section 5. The final section 6 gives a general conclusion.

2. MATHEMATICAL AND NUMERICAL MODELING

2.1. Principal Equations

The fluid considered is a mixture of a heavy component, representing iron and nickel, and a light constituent, whose compositional mass fraction is denoted by ξ. As thermal effects are neglected here, the density ρ can be modeled as a function of the compositional mass fraction only,

$$\rho = \rho_0 \left[1 - \beta(\xi - \xi_0)\right], \tag{4}$$

where ξ_0 and ρ_0 are the reference compositional mass fraction and density, respectively, and β denotes the coefficient of chemical expansivity.

In addition to the mass conservation,

$$\vec{\nabla} \cdot \vec{\mathbf{u}} = 0, \tag{5}$$

we solve for the momentum conservation, expressed in the form of the well-known Navier-Stokes equation, for a Newtonian rotating fluid in the Boussinesq approximation,

$$\frac{\partial \vec{\mathbf{u}}}{\partial t} + \vec{\mathbf{u}} \cdot \bar{\bar{\nabla}} \vec{\mathbf{u}} + 2\Omega(\vec{\mathbf{e}}_{\mathbf{z}} \times \vec{\mathbf{u}}) = -\frac{1}{\rho_0} \vec{\nabla} \Pi + \nu \vec{\nabla}^2 \vec{\mathbf{u}} + \beta \xi g_o \frac{\vec{\mathbf{r}}}{r_o}, \tag{6}$$

where $\vec{u}$ is the fluid velocity, t the time, Ω the Earth's rotation rate around an axis oriented by $\vec{e}_z$, Π the dynamic pressure and g_o the gravitational acceleration at the top of the shell at radius $r = r_o$. The Lorentz force is neglected. We adopt the viscous time scale D^2/ν in which the thickness of the shell $D = r_o - r_i$ is taken as the typical length scale, r_i being the radius of the inner boundary. Hence, using $(\rho_0 \nu \Omega)$ as a scaling for pressure, one can write the dimensionless momentum equation,

$$E\left(\frac{\partial \vec{\mathbf{u}}}{\partial t} + \vec{\mathbf{u}} \cdot \bar{\bar{\nabla}} \vec{\mathbf{u}} - \vec{\nabla}^2 \vec{\mathbf{u}}\right) + 2\vec{\mathbf{e}}_{\mathbf{z}} \times \vec{\mathbf{u}} + \vec{\nabla} \Pi = Ra_{\xi} \xi \frac{\vec{\mathbf{r}}}{r_o}, \tag{7}$$

in which E is the Ekman number, defined by

$$E = \frac{\nu}{\Omega D^2}, \tag{8}$$

and Ra_ξ a "modified" compositional Rayleigh (or Roberts-Rayleigh) number,

$$Ra_\xi = \frac{g_0 \beta C^* D}{\nu \Omega}, \tag{9}$$

where C^*/D is a measure for the global compositional variation driving convection. C^* depends on the prescribed boundary conditions which are discussed in section 2.2. Note that, in the infinite Prandtl number case, the classical Rayleigh number constructed using the time scale D^2/κ_ξ based on the chemical diffusivity,

$$Ra_\xi^{\kappa^\xi} = \frac{g_0 \beta C^* D}{\kappa^\xi \Omega}, \tag{10}$$

cannot be used as it is infinite, which means that even a very small value of Ra_ξ would lead to buoyancy-driven fluid motion and the notion of super-criticality is no longer relevant in this case.

In the Earth's fluid core, chemicals can be transported by advection and diffusion. The corresponding equation yields

$$\frac{\partial \xi}{\partial t} + \vec{\mathbf{u}} \cdot \vec{\nabla} \xi = \kappa^\xi \vec{\nabla}^2 \xi + \sigma^\xi, \tag{11}$$

in which σ^ξ is a numerical sink/source term ensuring that the mean composition remains constant throughout the simulation (see section 2.2 for details). The equivalent dimensionless equation reads

$$\frac{\partial \xi}{\partial t} + \vec{\mathbf{u}} \cdot \vec{\nabla} \xi = \frac{1}{Sc} \vec{\nabla}^2 \xi + \sigma^\xi. \tag{12}$$

In the end-member case $Sc = +\infty$ ($\kappa^\xi = 0$) considered here, Equation (12) becomes a first-order hyperbolic equation:

$$\frac{\partial \xi}{\partial t} + \vec{\mathbf{u}} \cdot \vec{\nabla} \xi = \sigma^\xi. \tag{13}$$

2.2. Boundary Conditions

We adopt non-penetration and no-slip conditions at both boundaries which implies

$$\vec{\mathbf{u}}(r = r_o) = \vec{\mathbf{u}}(r = r_i) = \vec{\mathbf{0}}. \tag{14}$$

The first-order nature of Equation (13) combined with the condition (14) on the velocity implies that no chemical "signal" imposed at a boundary can propagate inside the shell, neither by advection nor diffusion. The value of the composition at a boundary has therefore no effect on the compositional field inside the shell and will in turn not be affected by the latter. Consequently, once the initial condition has been specified (for instance $\xi = 0$ everywhere), there is *mathematically* no need to impose any boundary condition for the compositional field. At the top boundary, we do not consider chemical interactions with the mantle so that the compositional flux equals zero. This physical condition is automatically satisfied by the mathematical formulation of the problem as explained above. At the bottom boundary, however, we wish to model a total flux of light elements I_i^ξ resulting from the crystallization of the inner core. Since this cannot be accommodated in the framework of our mathematical formulation, we inject the mass flux I_i^ξ via a source term σ_i^ξ distributed within a thin layer of thickness h above the ICB, so that the integrated added mass fraction matches the ICB chemical flux:

$$4\pi \int_{r=r_i}^{r_i+h} r^2 \sigma_i^\xi(r) \mathrm{d}r = I_i^\xi. \tag{15}$$

The choice of an adequate function for $\sigma_i^\xi(r)$ requires some care. Indeed, since the velocity vanishes in the Ekman layer to accommodate condition (14), any buoyant fluid injected at the bottom of this layer tends to "stick" to the boundary in the absence of chemical diffusion, hardly moves upward and does not participate in the convective dynamics. Adding the light elements slightly above in a region that extends beyond the Ekman layer (see **Figure 1**) allows some destabilization and prevents a detrimental accumulation of light elements in the layer over time. This can be performed smoothly using a Gaussian-like function:

$$\sigma_i^\xi(r) = \frac{\sigma_0}{r^2} \exp\left\{ -\left[r - \left(r_i + \frac{h}{2} \right) \right]^2 / \sigma^2 \right\}. \tag{16}$$

The constants in the exponential function are empirically set to $\sigma = h/5$ and $h = 0.4E^{1/3}$. These values will be justified later in section 3.1. The scaling factor σ_0 is computed to satisfy Equation (15). Mathematically, this formulation is equivalent to solving the transport equation

$$\frac{\partial \xi}{\partial t} + \vec{\mathbf{u}} \cdot \vec{\nabla} \xi = \sigma^\xi + \sigma_i^\xi \mathcal{H}\left[(r_i + h) - r \right] \tag{17}$$

and imposing no boundary conditions for the composition (at least, "mathematically" speaking). The injection of light elements occurring in the ICB region is accounted for by the local source term $\sigma_i^\xi \mathcal{H}\left[(r_i + h) - r \right]$, where $\mathcal{H}$ is a Heaviside function, and

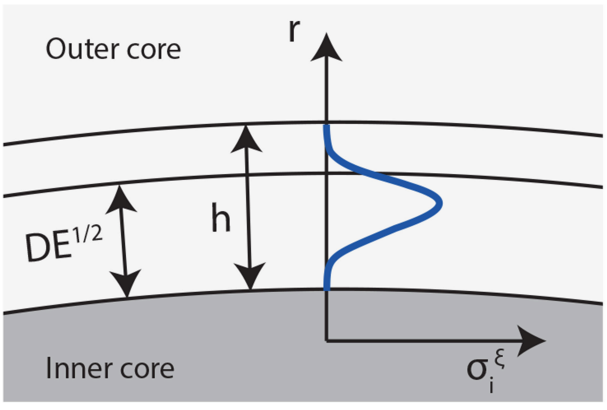

FIGURE 1 | Illustration of the shape of the source term σ_i^ξ applied above the inner core boundary.

is balanced by a uniform sink term σ^ξ in the entire shell so that the mean composition remains constant with time:

$$\int_{r_i}^{r_o} \left(\sigma^\xi + \sigma_i^\xi \mathcal{H}\left[(r_i + h) - r\right]\right) r^2 \mathrm{d}r = 0. \quad (18)$$

Using the corresponding compositional buoyancy flow injected at the inner boundary,

$$f_i^\xi = \beta g I_i^\xi, \quad (19)$$

one can derive the following scale for composition:

$$C^* = \frac{f_i^\xi}{4\pi D \beta \rho_0 g \nu}. \quad (20)$$

The expression of the modified compositional Rayleigh number then becomes

$$Ra_\xi = \frac{f_i^\xi}{4\pi \rho_0 \nu^2 \Omega}. \quad (21)$$

2.3. Numerical Method

Though moderate Schmidt numbers (< 50) may be numerically accessible with most classic dynamo codes, the infinite Schmidt number case requires a specific numerical method. Indeed, the time integration schemes classically used in the spherical dynamo codes (Crank-Nicolson for diffusion and Adams-Bashforth for the non-linear terms) are conditionally stable and produce spurious oscillations when the chemical diffusivity is set to zero. Other numerical methods such as TVD schemes have been specifically designed for hyperbolic equations but still introduce some amount of numerical diffusion and/or "clipping" effects (see Munz, 1988 for comparison of several TVD schemes). An interesting alternative is the "particle-in-cell" (PIC) method which has been extensively used for a wide range of physical problems (see Brackbill et al., 1988; Huang et al., 1992; Tackley and King, 2003; Tskhakaya et al., 2007; Sironi and Spitkovsky, 2009 for a non-exhaustive list of examples).

In this work, we use a recently developed version of the dynamo code PARODY-JA (Aubert et al., 2008) which includes a PIC method to treat the compositional field. Details on the numerical method can be found in Bouffard et al. (2017), together with the results of two benchmarks that validate the implementation of the PIC method. We performed a total of 11 numerical simulations summarized in **Table 1** to conduct a first exploratory study of non-magnetic pure chemical convection in a rapidly-rotating spherical shell in the end-member case of infinite Schmidt number ($\kappa^\xi = 0$). For one simulation (case 9*), the homogeneous sink term σ^ξ in Equation (17) is replaced by a sink term near the top boundary equivalent to σ_i^ξ that equilibrates the light elements injected at the bottom. As will be emphasized later, we limited ourselves to a small number of cases in this first preliminary study due to the high computational cost, particularly at low Ekman numbers. In order to decrease the computation time, we considered flows which are $2\pi/m_c$-periodic along the longitude (see **Table 1**). In all cases, we ensured that the width of the computational domain remained large compared to the size of the individual chemical structures (see section 3), so that no physical property of chemical convection is lost by assuming these symmetries. The addition of two cases in full spherical shell (cases 1 and 2) for which no qualitative difference was observed with the other cases gives further support to this statement. Also, for reasons that will be explained in section 4.2, no simulation was run until a statistically stationary state was reached. As the mean values of diagnostic quantities (for instance, the kinetic energy) fluctuate throughout one simulation, we did not report output values such as Reynolds and Rossby numbers in **Table 1**. The Rossby numbers given in the figures throughout the manuscript correspond to instantaneous values associated with the snapshots displayed.

TABLE 1 | Summary of the parameters used for the different simulations.

Case	(N_r, ℓ_{max})	N_p ($\times 10^6$)	m_c	E	Ra
1	(150,200)	200	1	10^{-3}	5×10^2
2	(150,200)	200	1	10^{-3}	10^4
3	(150,200)	50	4	10^{-3}	10^5
4	(150,200)	50	4	10^{-3}	5×10^5
5	(150,200)	50	4	10^{-3}	10^6
6	(200,270)	110	6	3×10^{-4}	10^5
7	(200,270)	110	6	3×10^{-4}	10^6
8	(250,360)	250	8	10^{-4}	10^5
9*	(250,360)	250	8	10^{-4}	10^3
10	(300,540)	500	12	3×10^{-5}	2×10^6
11	(350,720)	800	16	10^{-5}	10^6

N_r is the number of radial layers. ℓ_{max} is the maximal degree of spherical harmonics, equal to the maximal order m_{max} in all simulations. N_p is the number of particles, m_c the symmetry in longitude (1 for full spherical shell, higher value for $2\pi/m_c$-symmetric solutions). In all simulations, the grid aspect ratio is fixed and equal to $r_i/r_o = 0.35$. For case 9, no volumetric sink term is introduced in the shell. It is replaced by a top flow, imposed in the form of a local sink term that balances the bottom flow.*

3. PROPERTIES AND DYNAMICS OF CHEMICAL PLUMES AND BLOBS

3.1. Destabilization of the Bottom Light Layer

The continuous injection of light elements creates a lighter layer immediately above the bottom boundary. This configuration is prone to the Rayleigh-Taylor instability which, after some time, causes the layer to destabilize, forming thin rising filamentary chemical plumes with a "sheet-like" or "curtain" shape elongated in the direction of the rotation axis owing to the Taylor-Proudman constraint (see **Figure 2A**). Such structures are qualitatively in agreement with previous laboratory experiments by Cardin and Olson (1992) and are also typically observed for thermal plumes in simulations of rotating convection in a spherical shell (see, for instance, **Figure 2** from Gastine et al., 2016). However, there seems to be a transition from "sheet-like"

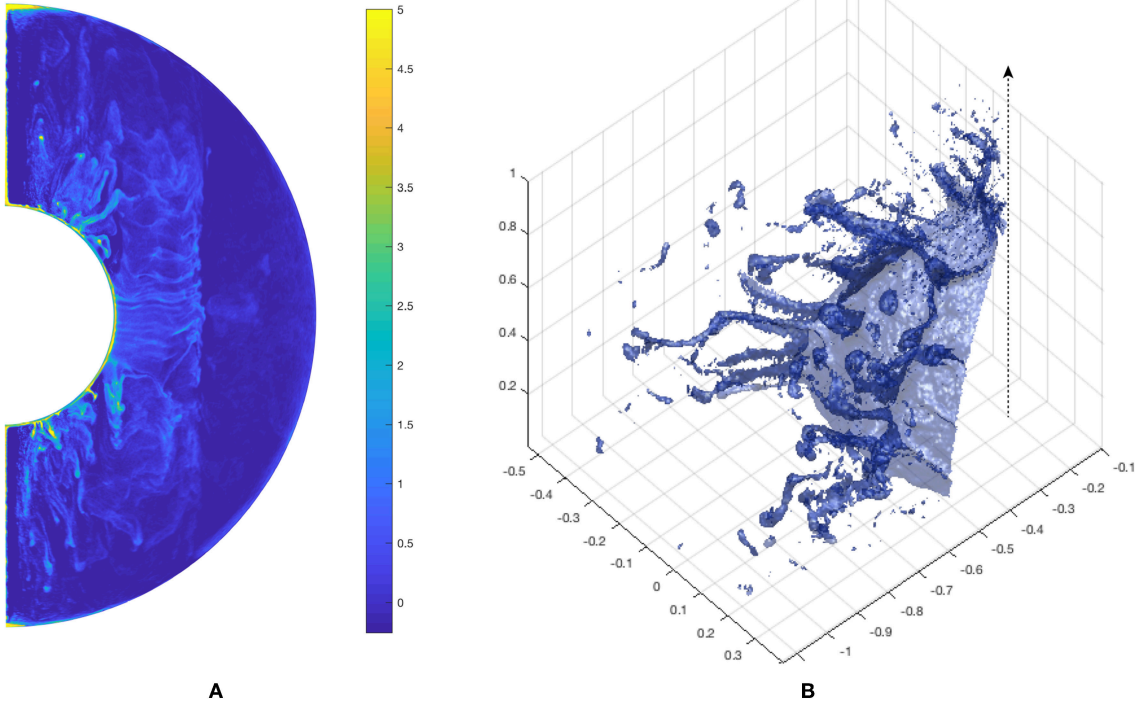

FIGURE 2 | (A) Azimuthal section of the compositional field corresponding to case 8 shortly after the destabilization of the initial bottom light layer. To better visualize the curtain shape, an azimuthal average was performed over a smaller interval $\Delta\phi = 0.01$ around the longitude ϕ_0 centered on a chemical "curtain." **(B)** Isosurface corresponding to a constant composition for case 3. The vertical dotted line shows the position and orientation of the rotation axis.

structures to more isolated plumes when crossing the tangent cylinder (see, for example, **Figures 2A,B**).

When they rise, the first chemical plumes carry away light elements and make the bottom light layer more heterogeneous. As a consequence, the following generations of compositional "sheets" assume a more complex and discontinuous structure since light elements are not always locally available to supply the rising curtains (see **Figure 2B**). Plumes may also merge and their location evolves over time.

We measured the mean thickness δ of these sheet-like or filamentary rising plumes for five different values of the Ekman number in the range $10^{-5} - 10^{-3}$. We estimated δ for the first generation of plumes by plotting zonal profiles of the composition in the equatorial plane, at a short distance above the bottom light layer. For each "peak" corresponding to a plume in the compositional profile, we define the width of the plume as the distance over which the composition is positive. This is facilitated by the fact that, at the beginning of the simulation, the background composition is homogeneous and negative due to the volumetric sink term σ^{ξ}. The results are displayed on **Figure 3** and support a scaling law with a 1/3 exponent,

$$\delta \sim 0.2E^{0.328}, \tag{22}$$

which is the same exponent as the onset of classical thermal convection in a rotating spherical shell (Jones et al., 2000). In order to rule out any extra dependence on the Rayleigh number, we varied this parameter over two orders of magnitude while keeping a fixed Ekman number. No measurable difference was found for the average thickness of the chemical plumes. The thickness of the injection layer was also varied. The size of the chemical plumes was found to be affected as soon as the thickness of the injection layer becomes smaller than the size of the chemical plumes called for by Equation (22). The constant h in Equation (16) was therefore adjusted to be slightly larger than the predicted size of the plumes, but kept as small as possible in order to model local processes occurring close to the bottom boundary.

The exact value of the pre-factor in the scaling law (22) may be slightly sensitive to the parameters σ and h characterizing the injection layer in Equation (16) and depends on the definition of δ but remains small anyway compared to the typical pre-factors for thermal convection. Consequently, the size of chemical plumes is always a very small fraction of the shell's thickness. This has an important numerical implication for the grid (and tracers) resolution which must be very high to correctly resolve chemical plumes. This requirement is visible on the chemical spectrum shown on **Figure 4** left, which is remarkably flat before dropping abruptly. The small size of the chemical structures also produces smaller scales in the velocity field. For comparable Rayleigh numbers, the kinetic energy spectra contain significantly less

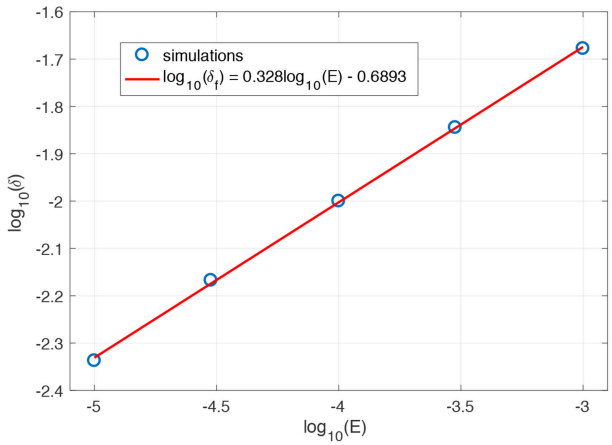

FIGURE 3 | Mean thickness of the chemical plumes measured in the equatorial plane for different values of the Ekman number.

energy at low degrees and drop much more slowly for compositional convection compared to thermal (codensity) convection (**Figure 4B**). However, in the simulations listed in **Table 1**, resolving the chemical structures sets a stronger constraint on the resolution than the kinetic energy spectra. The 1/3 exponent in the scaling law (22) implies that the resolution should be approximately doubled for each decade dropped for the Ekman number, which justifies the high spherical harmonic degrees employed in the simulations (see **Table 1**). At fixed Ekman number, the numerical demand of compositional convection is significantly higher than an equivalent codensity run. We therefore restricted ourselves to a small number of simulations in this exploratory study and considered longitudinal symmetries to decrease the computation time (see **Table 1**). Note that the fraction of the computation time spent in the PIC method is dominant but decreases when lower Ekman numbers are employed.

3.2. Dynamics of Chemical Plumes

3.2.1. Effect of the Taylor-Proudman Constraint on the Ascension of Plumes

When rotational effects remain moderate, chemical plumes rise almost radially (see **Figure 5A**). When the rotational constraint is increased and therefore the Rossby number $Ro = U/D\Omega$ (with U the root-mean-squared velocity) is lowered, the tangent cylinder (TC), an imaginary cylinder parallel to the rotation axis that touches the inner core at the equator, becomes less penetrable (Aurnou et al., 2003; Jones, 2015). The velocity field outside the TC is mostly invariant along the rotation axis by assuming a columnar form (see **Figure 6**). The light elements released at mid to high latitudes tend to stay inside the TC and rise more vertically along the z coordinate (see **Figures 5A–C**, **7B**). The light elements released in the vicinity where the TC touches the inner boundary still have a chance to cross this imaginary boundary. As a result, the mass fraction of light elements is significantly higher inside the TC (which only represents 15% of the volume of the spherical shell) than outside. This is visible on **Figures 5A–C** and we checked that the mass fraction of light elements inside (*resp.* outside) the TC is systematically larger (smaller) than the mean composition in the entire shell.

3.2.2. Secondary "Blobs" Instabilities

Due to the absence of chemical diffusion, rising chemical plumes can be affected by secondary instabilities, some of which are usually not observed for thermal plumes (Kerr and Mériaux, 2004; Kerr et al., 2008). These instabilities may have distinct origins in the polar and equatorial portions of the shell since rotation acts differently in these regions.

Several laboratory experiments have been dedicated to the study of the dynamics of buoyant plumes in a rotating environment. These were conducted in rotating cylinders in which the rotation axis is parallel to the gravity vector, a situation that is analogous to polar regions in the Earth's outer core. When discharging a single point turbulent plume at the top of a water-filled rotating tank, Frank et al. (2017) reported a systematic anticyclonic precession of the plume in the whole range spanned for the Rossby number $Ro = \left(B_0\Omega^{-3}\right)^{1/4} H^{-1} = 0.02 - 1.3$, where H is the height of water tank and B_0 the source buoyancy flux. The vertical extent of the precession region and the time necessary for the development of precession were found to decrease with the Rossby number. Helical motions were also reported for turbulent thermal plumes in laboratory experiments of rotating convection modeling the tangent cylinder region (Aurnou et al., 2003). In another series of experiments, in which laminar chemical plumes are produced by the crystallization of a mush at the bottom of a rotating cylinder cooled from below, Claßen et al. (1999) observed three-dimensional helical undulations of the chemical plumes, both in the rotating and non-rotating cases. In this experiment, increasing rotation exacerbates these undulations and deflects the chemical plumes horizontally. Past a critical angle, the plumes become susceptible to a Rayleigh-Taylor instability which causes chemical "blobs" to detach from the initial plumes and rise vertically. This so-called "blob-instability" was found to occur closer to the mush when the Ekman number decreases. It is not clear whether the phenomena reported by Claßen et al. (1999), Aurnou et al. (2003), and Frank et al. (2017) for the dynamics of chemical plumes have a common physical origin or result from distinct instabilities.

We observed similar behaviors for chemical plumes in our simulations. On **Figure 5B** with $E = 3 \times 10^{-4}$ and $Ro = 1.9 \times 10^{-3}$, the pronounced plume at the north pole shows some helical undulation before a chemical blob detaches and continues to rise, a phenomenon similar to that reported by Claßen et al. (1999). This phenomenon is less easily visible for case 10 at a lower Ekman number $E = 3 \times 10^{-5}$ and $Ro = 4.4 \times 10^{-4}$ (see **Figure 7**). In this case, blobs still detach from the initial plumes but undulations and horizontal bending are often not as manifest. However, the plume denoted by an arrow on **Figure 7** experiences a helical motion within a short distance from the plume's

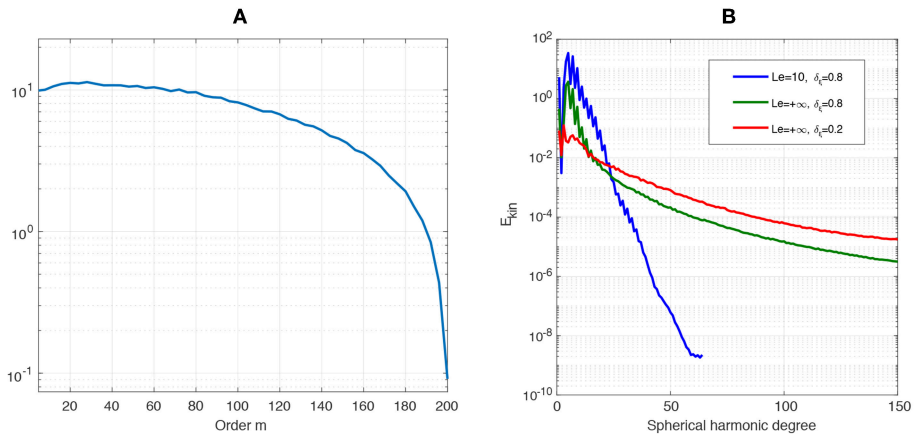

FIGURE 4 | (A) *m* spectrum of the chemical field for case 3. **(B)** kinetic energy spectra corresponding to the benchmark proposed by Breuer et al. (2010) and extended to the infinite Lewis number case (see Bouffard et al., 2017). δ_ξ denotes the fraction of chemical forcing.

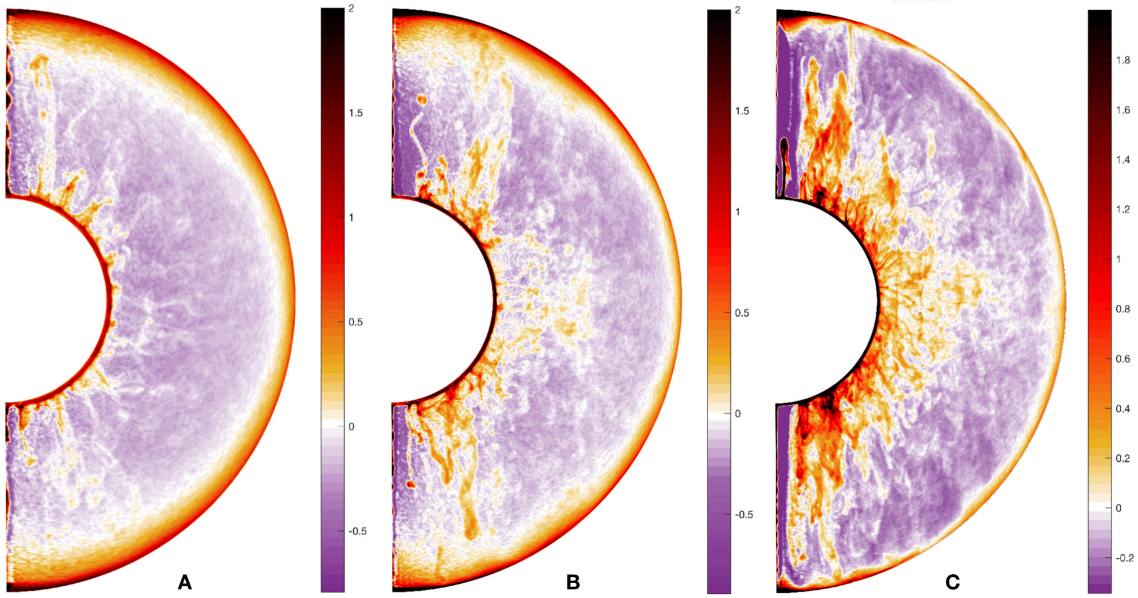

FIGURE 5 | Azimuthal average of the chemical field for cases 3 ($t = 1$; **A**), 6 ($t = 1$; **B**), and 8 ($t = 0.4$; **C**). Rossby numbers are, respectively: $Ro = 9.4 \times 10^{-3}$, $Ro = 1.9 \times 10^{-3}$ and $Ro = 4.5 \times 10^{-4}$. The color scales have been deliberately modified and saturated in order to better visualize the structure of the compositional field in the convecting region.

source which bears some resemblance with the precessions and undulations reported, respectively by Aurnou et al. (2003) and Frank et al. (2017) (for a comparison, see respectively **Figures 2**, **6** in these papers). The local Rossby number $Ro_\delta \sim U/\delta\Omega$ computed at the scale of the plume δ based on Equation (22) is close to 0.07 in the case corresponding to **Figure 7** and falls in the range explored by Frank et al. (2017), though the authors use a slightly different definition of the Rossby number.

We also observed other "blob-instabilities" similar to that reported by Claßen et al. (1999) in the equatorial plane, though the underlying physical mechanisms seem to contrast with the polar region. An illustration of a "blob-instability" in the equatorial plane is displayed on **Figure 8** where the plume indicated by an arrow bends horizontally before a secondary "blob-like" plume detaches and continues to rise. The bending occurs closer to the boundary when the Ekman number is decreased. However, a fraction of the plumes bend in a direction that is not compatible with a deflection by the Coriolis force. Furthermore, it typically takes a few tens of rotation times (for instance about 20 in the case corresponding to **Figure 9B**) before the plumes bend and break-up, which suggests that the

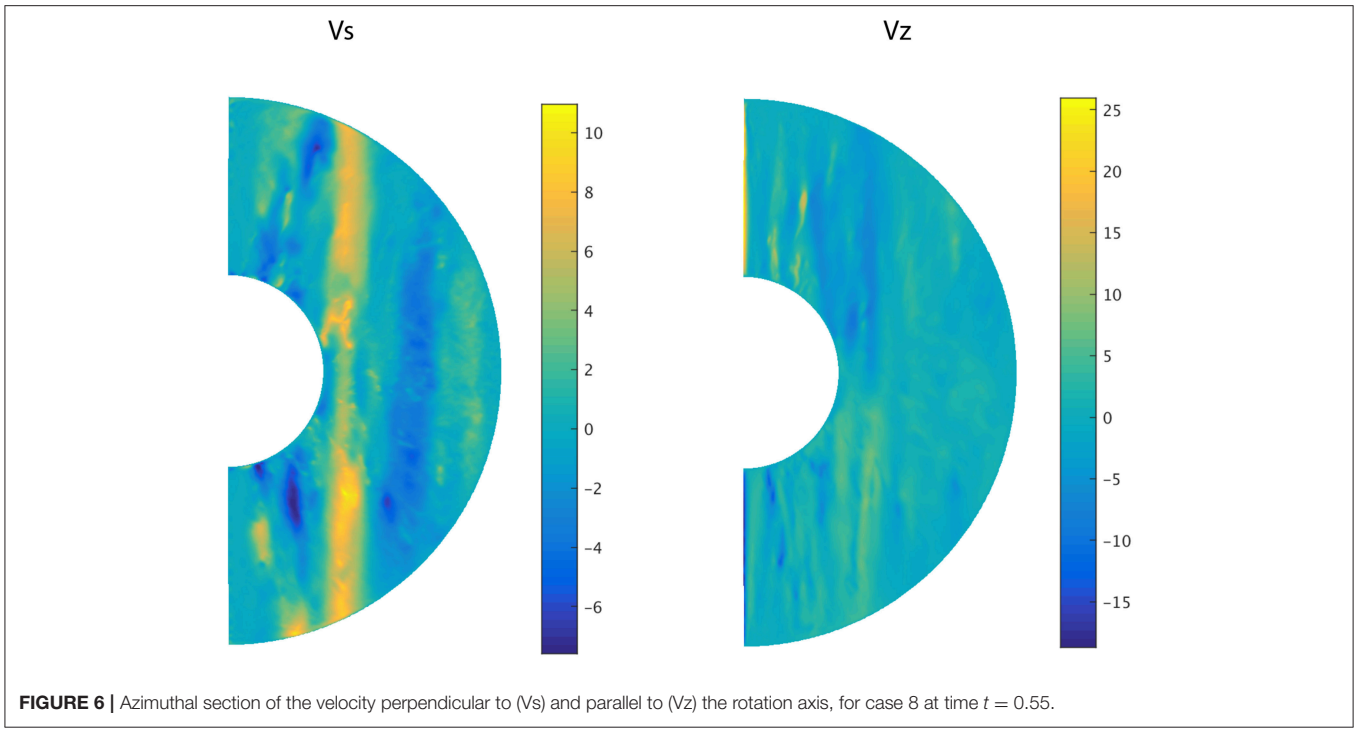

FIGURE 6 | Azimuthal section of the velocity perpendicular to (Vs) and parallel to (Vz) the rotation axis, for case 8 at time $t = 0.55$.

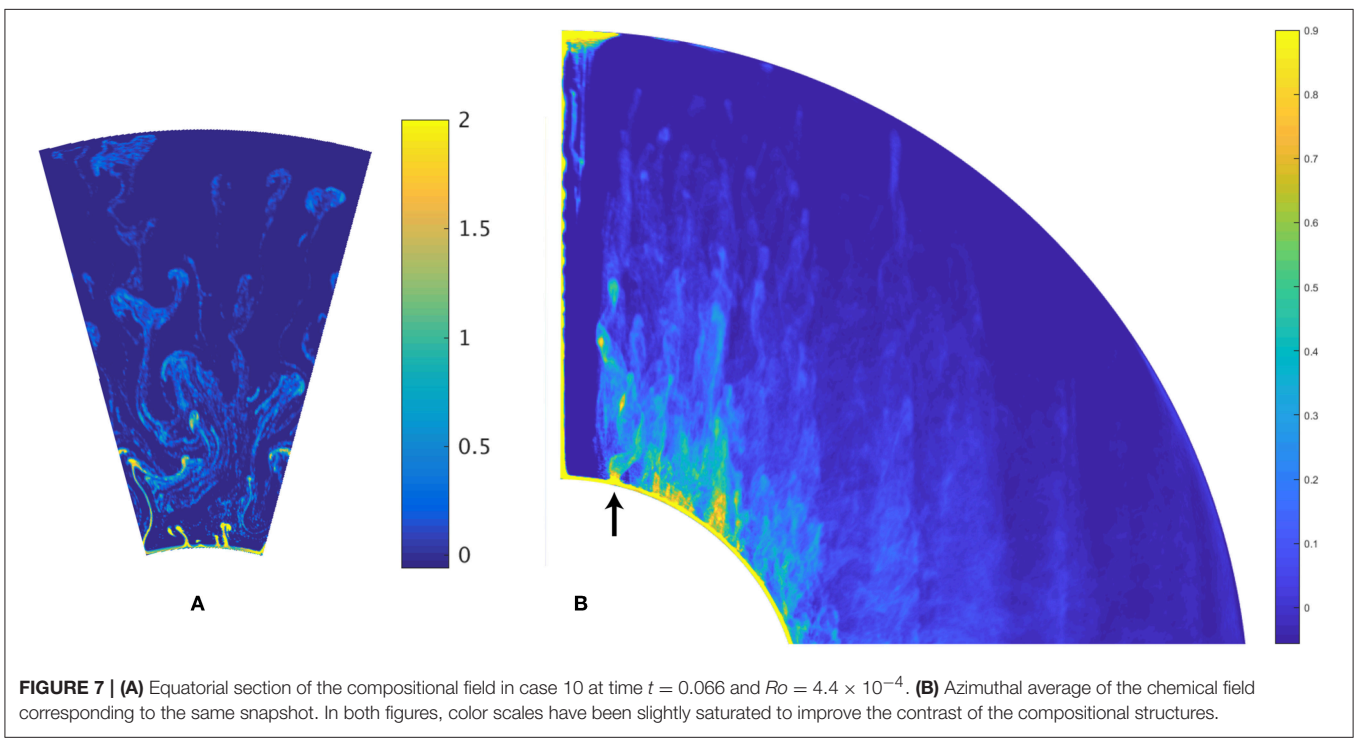

FIGURE 7 | (A) Equatorial section of the compositional field in case 10 at time $t = 0.066$ and $Ro = 4.4 \times 10^{-4}$. **(B)** Azimuthal average of the chemical field corresponding to the same snapshot. In both figures, color scales have been slightly saturated to improve the contrast of the compositional structures.

bending is not primarily caused by the Coriolis force. In addition, blobs may still detach from the plumes even in the absence of bending (see, for instance, **Figure 9A**). Different instabilities may therefore affect the dynamics of chemical plumes and should be clarified in the future. We did not observe any obvious and significant elongation of chemical blobs in the direction of the rotation axis as predicted by St Pierre (1996), but this may be because monitoring the shape of chemical blobs over time is quite arduous. However, in the long term, the fragmentation and stirring of the chemical plumes and blobs combined with

the absence of chemical diffusion produces a granular "flaky" aspect in the compositional field (see, for example, **Figure 9A**), a feature that contrasts with the smoothness of the temperature (codensity) field in low Prandtl number simulations.

3.2.3. Jet-Instability and Mixing of the Chemical Plumes

Though plumes have a rather laminar behavior in our simulations (which operate at low Reynolds numbers), **Figure 8** shows that some laminar chemical plumes evolve to a more "turbulent" state characterized by entrainment of ambient fluid that causes the gradual dilution of the plumes. This is also visible for a lower Ekman number on **Figure 7A**, which shows very thin chemical plumes transforming into large blobs that reach the top boundary. This transition to a more "turbulent" state is qualitatively similar to the so-called "jet" instability, in which a straight laminar flow destabilizes after some time and leads to a more complex jet flow (Michalke, 1984). The initial jet can fragment into smaller drops or break-up into blobs with a size comparable to the width of the initial jet. Eddies may also form at the interface and start entraining ambient fluid, causing the jet to widen. **Figure 10** shows that there is a qualitative agreement between the dynamics of some plumes from our simulations and laboratory experiments of the jet instability. We observe that, at the beginning of the simulations, when the background composition is homogeneous, the first plumes quickly start entraining ambient fluid. In the later generations of plumes however, when the background composition is more heterogeneous, a significant fraction of plumes bend and break-up into blobs before they start entraining surrounding fluid. This suggests that the background composition plays a role in the dynamics of plumes, though its precise influence remains to be investigated.

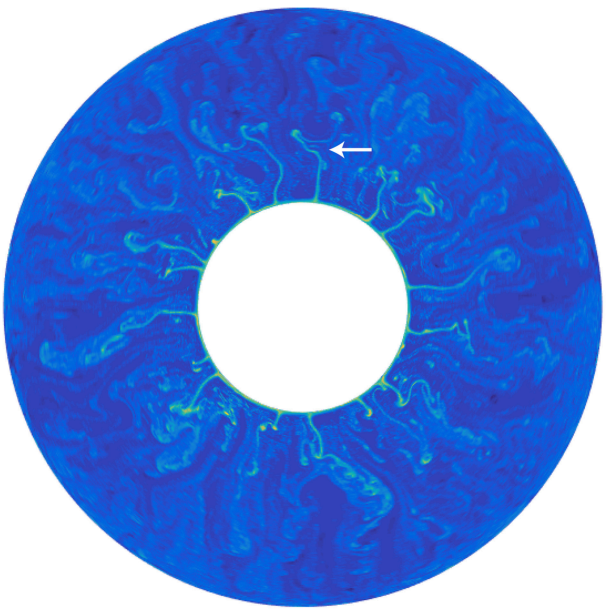

FIGURE 8 | Equatorial snapshot of the compositional field for case 9*.

The efficiency of plumes mixing caused by the entrainment of heavier fluid differs between the rotating and non-rotating cases. Many studies have pointed out that turbulent mixing and lateral entrainment of fluid are inhibited in rotating flows (Helfrich and Battisti, 1991; Fernando et al., 1998; Levy and Fernando, 2002; Goodman et al., 2004; Gastine et al., 2016). Mixing processes may also be different inside and outside the TC. In our simulations, lateral entrainment of ambient fluid seems partially inhibited in polar regions where the plumes and blobs are little diluted

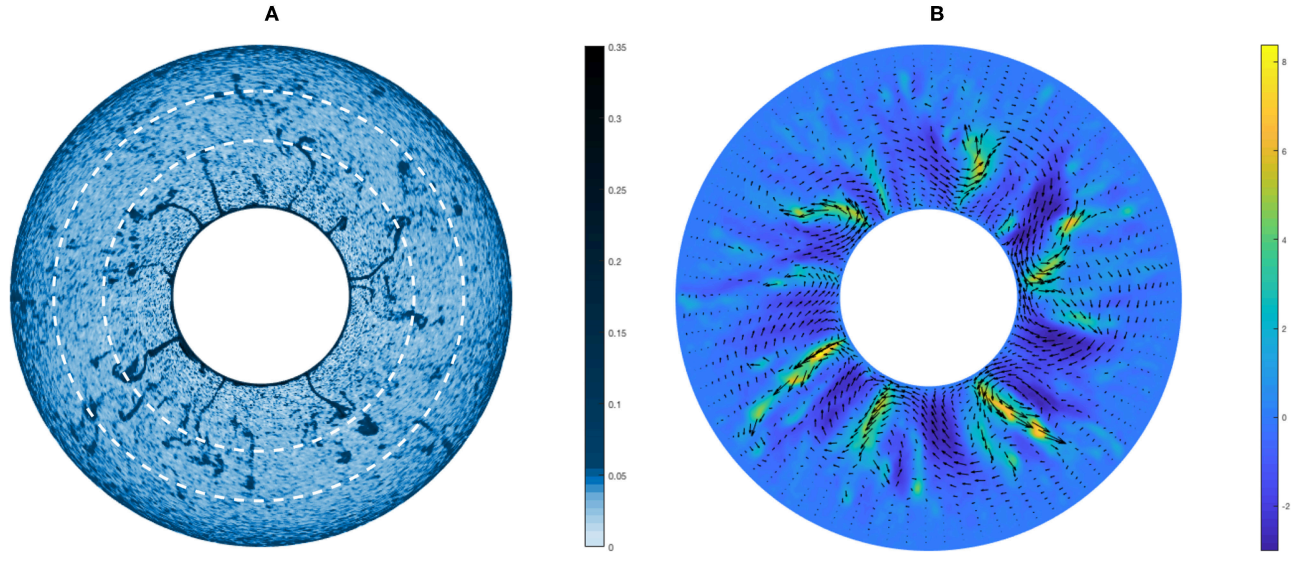

FIGURE 9 | (A) Equatorial section of the compositional field at $t = 6$ for case 1. The color scale has been saturated so that the top stratified layer becomes more apparent. The white dashed lines delimit qualitatively three regions in the spherical shell: a bottom plumes region, an intermediate more or less well mixed blobs region and a stratified layer at the top. **(B)** Equatorial section of the radial velocity field (in color) for the same snapshot. Arrows denote local horizontal velocity vectors.

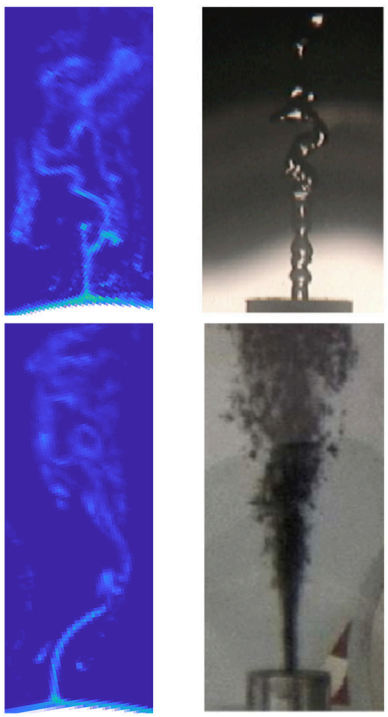

FIGURE 10 | (Left) Examples of chemical plumes for case 9* after the initial bottom light layer starts destabilizing at the beginning of the simulation. **(Right)** Examples of some regimes of jet instability in laboratory experiments. Taken from Tang et al. (2003).

during their vertical ascension. In contrast, in the equatorial plane, plumes experience more significant stirring, though lateral entrainment may still be partially inhibited compared to a non-rotating case. The different mixing efficiency of chemical plumes between polar and equatorial regions is visible on **Figures 5B,C**. A more detailed and quantitative study involving more turbulent flows will be necessary to better understand the mixing dynamics of chemical plumes.

4. FORMATION OF A CHEMICALLY STRATIFIED LAYER AT THE TOP OF THE SHELL

4.1. Accumulation of Chemical Plumes and Blobs at the Top of the Spherical Shell

In all our simulations, a fraction of the rising chemical plumes and blobs reach the top of the spherical shell where they accumulate to form a stably stratified layer. This layer is clearly visible on equatorial sections of the chemical field (**Figure 9A**), azimuthal projections of the ϕ-average compositional field (**Figure 5**), and on radial profiles of the mean composition (**Figure 11A**) which all show that the mass fraction of light elements increases radially in the top portion of the shell. Defining the extent of the stably stratified layer is a delicate task. One possibility is to define the bottom of the stratified region as the radius r_b above which the mean Brunt-Väisälä frequency N is positive:

$$N^2 = -\frac{g}{\rho}\frac{\partial \overline{\rho}}{\partial r} > 0 \quad \text{for} \quad r > r_b, \tag{23}$$

where $\overline{\rho}(r)$ denotes the average density at radius r . For pure compositional convection, Equation (23) is equivalent to

$$\frac{\partial \overline{\xi}}{\partial r} > 0 \quad \text{for} \quad r > r_b, \tag{24}$$

in which $\overline{\xi}(r)$ is the mean composition at radius r. The bottom of the stratified layer r_b, defined by Equation (24), is indicated by dashed lines on **Figures 11A,B**, which show radial profiles of the mean composition and $(N/\Omega)^2$ ratio, respectively. Similar shapes are observed for these profiles in the other simulations. **Figure 11B** illustrates that the Brunt-Väisälä frequency increases very rapidly in the top half portion of the shell where the N/Ω ratio reaches a value close to 0.7 in this case. In contrast, the bottom half of the layer is weakly stratified with $N/\Omega < 0.1$. A first disadvantage of the definition (23) is that the weak slope of N in the lower part of the stable layer causes strong fluctuations in the value of r_b which require time averaging. In addition, the definition of r_b remains somehow arbitrary since there is dynamically no neat boundary delimiting the convective and stratified regions. Indeed, the low values of the N/Ω ratio across the layer do not suppress radial movements caused by penetrating plumes and blobs and allow for the penetration of columnar convection as expected from the linear theory (Takehiro and Lister, 2001) (see, for instance, **Figure 6**). Simpler definitions of the layer based, for example, on the intersection of tangents, are also arbitrary and difficult to implement in practice due to the complexity of the shape of the chemical profiles. In fact, these profiles are self-similar and do not seem to fit any classical mathematical function. Determining a relevant criterion for the definition of the top light layer will be the object of future investigations.

Figure 9 suggests that the spherical shell can be roughly divided into three regions as anticipated by Loper (2007): a bottom part dominated by plumes, a more or less "well-mixed" intermediate blobs region and a stably stratified layer at the top. The height of the plumes region is also imprecise and fluctuates spatially due to different plume dynamics inside and outside the TC. Moreover, as we will explain below, the relative extent of these regions evolves with time and depends on the Ekman number: the stratified layer thickens over time, but shrinks when the Ekman number is decreased.

4.2. Dynamics and Evolution of the Layer

4.2.1. Latitudinal Topography

Figures 5A–C show that the thickness of the stably stratified layer is lower at the equator and increases toward the poles, creating a latitudinal topography. We attribute this to a direct consequence of the tendency of high latitudes plumes to rise almost vertically along the rotation axis and remain inside the TC, which results in a differential growth rate of the layer between the low and high latitudes.

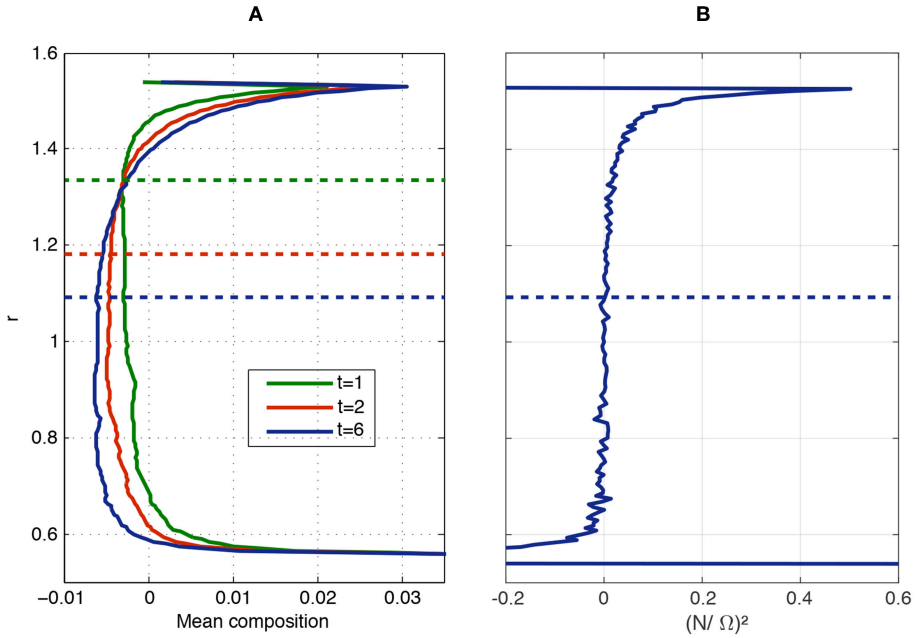

FIGURE 11 | (A) Radial profile of the mean composition at different times (in viscous time units) for case 1. The dashed lines indicate the bottom of the layer as defined by Equation (24). **(B)** $(N/\Omega)^2$ ratio at time $t = 6$ for the same case.

Furthermore, the mass fraction of light elements at the very top of the stratified layer also increases from the equator to the poles. We make the hypothesis that this is due to the different mixing efficiency of the plumes inside and outside the TC. In polar regions, plumes rise almost vertically and experience less mixing and dilution than in the equatorial plane. Consequently, they reach the stratified region with a higher mass anomaly than equatorial plumes which experience more fragmentation and mixing.

4.2.2. Time Evolution

After a first phase of rapid growth of the layer caused by the destabilization of the initial bottom light layer, the thickness of the layer [based on definition (24)] increases very slowly. **Figure 11** shows that the stratified layer extends to about 35% of the spherical shell's thickness after 2 viscous times, whereas it takes 6 viscous times for the layer to fill 45% of the shell. Several tens of viscous times are in fact necessary to reach a statistically steady-state in the simulations. The resulting computational demand is enormous, especially for low Ekman numbers, and we ran none of our simulations until the statistically steady-state was reached in the present study. Even though running the simulations for very long times is probably not necessary (since the Earth is not in a statistically steady state), fitting the time evolution of the layer's thickness with a particular mathematical function may still require costly simulations. Comparison of the different runs suggests that the growth rate is dependent on the Ekman number and, to a lesser extent, the Rayleigh number. For instance, after one viscous time, the stratified layer extends to about 25% of the shell for case 1 with $E = 10^{-3}$ and only 20% for case 6 with $E = 3 \times 10^{-4}$ and comparable Rayleigh numbers (see **Figures 5A,B**). Deriving scaling laws will require a proper definition of the layer and a more systematic (and cumbersome) exploration of the parameter space that we will perform in the future.

4.3. Analogy With the "Filling-Box" Models

This situation bears some interesting resemblance to the "filling-box" models studied experimentally by Baines and Turner (1969). In these experiments, a buoyant turbulent plume is injected at the bottom of a box of finite volume. As it moves upwards, the first plume entrains ambient fluid that is then mixed internally by the efficient turbulence of the plume. When it reaches the top boundary, the plume spreads horizontally and forms a homogenous light layer at the top of the box separated from the rest of the fluid by a density jump. When the second rising plume enters this light region, it entrains lighter fluid and therefore reaches the top of the box even lighter than the first plume. It then spreads horizontally, pushing downwards the first light layer. The process repeats, gradually forming a stably stratified layer at the top of the box that slowly grows until it fills the entire box (see Figure 1 of the paper by Worster and Huppert, 1983 for a schematic illustration).

In the idealized "filling-box" model described above, parametrization of the turbulent plume allows to derive analytically the time evolution of the density profile and the position of the first front (Baines and Turner, 1969). However, a series of differences prevents a direct extrapolation of these results to our simulations of chemical convection. In addition to the spherical geometry and a higher number of plumes, two

major specificities of our simulations are the presence of rotation and a different plumes dynamics (undulations, fragmentation into blobs, jet instability, inhibition of lateral mixing...). This makes the classic parametrization of "turbulent plumes" dubious in this context. The filling-box models also assume the total absence of turbulence and mixing in the stratified region which may not be the case for our simulations in which no clear separation in the dynamics can be drawn between the bottom of the layer and the convecting region.

The compositional profiles shown on **Figure 11** also contrast with the density profiles in the "filling-box" models notably by the absence of a density jump at the bottom, and by the profile of the Brunt-Väisälä frequency which increases with the radial position whereas it decreases with height in the filling-box models. This confirms that different mechanisms occur in our simulations and that the adaptation of the original filling-box model to the case of rotating chemical convection in a spherical shell requires extra investigations.

5. IMPLICATIONS FOR THE EARTH'S CORE

5.1. Limitations of the Present Study

Determining the implication of the results shown above for the Earth is a delicate task that is impeded by several factors. First, assessing the "plausibility" of a given scenario for the formation of a stably stratified layer below the CMB is complicated by the apparent inconsistency between studies based on magnetic and seismic observations (see **Table 2** for a summary). Buffett et al. (2016) show that a rather thin (< 140 km) and weakly stratified ($N \lesssim 5.4 - 6.1 \times 10^{-5}$ s^{-1}) layer can explain both the 60-year period in the geomagnetic secular variations together with fluctuations in the dipole field and, possibly, length of the day. Dynamo simulations suggest that the morphology of the magnetic field becomes too little Earth-like when the stratified layer is thicker than 400 km (Olson et al., 2017; Christensen, 2018). Analysis of the appearance of inverse flux patches in the southern hemisphere suggests an upper bound of only 100 km (Gubbins, 2007). Another study of geomagnetic secular variations remains unconclusive (Lesur et al., 2015). On the side of seismology, some studies based on the analysis of SmKS waves traveling in the outermost core are in favor of a thick layer (up to 450 km) with a strong stratification ($N \sim 10^{-3}$ s^{-1}) (Helffrich and Kaneshima, 2010; Kaneshima and Matsuzawa, 2015; Kaneshima, 2018). However, two seismic studies found no evidence for a stratification (Alexandrakis and Eaton, 2010; Irving et al., 2018), though this may simply indicate that the layer is too weakly stratified to leave a seismic signature. Second, the limited set of simulations presented in this study does not allow for the derivation of scaling laws, which prevents any direct extrapolation to the Earth's core. Third, several physical ingredients are not considered in the present study such as the magnetic field, thermal convection, and turbulence.

The presence of a magnetic field can influence the dynamics of buoyant parcels of fluid in a non-trivial way (Moffatt and Loper, 1994; Sreenivasan and Narasimhan, 2017) and should be incorporated in future studies. One may also argue that adding the destabilizing effect of thermal convection (omitted in this study) could destroy the chemically stratified layer. Although some preliminary simulations of thermochemical convection (not shown in this paper) suggest this is not the case—at least when both fields contribute equally to the buoyancy flux—the dynamics of thermochemical convection remains to be explored. Note that thermal effects may not necessarily be destabilizing. The recently revised value of the thermal conductivity (de Koker et al., 2012; Pozzo et al., 2012; Gomi et al., 2013; Ohta et al., 2016) seems to imply that the top of the core is thermally stratified (Labrosse, 2015). The presence of a thermally stratified layer at the top of the core may ease the formation of chemical stratification as well. The present study also ignores any possible double-diffusive phenomena that may affect the dynamics of a stably stratified layer in various ways.

On the other hand, the method of light elements injection in our simulations may not adequately reflect the complex chemical processes occurring in the inner core boundary region. Indeed, injecting light elements via a homogeneous source term above the bottom boundary tends to generate plumes with a sheet-like structure instead of the cylindrical shape that would be expected if plumes erupt from isolated chimneys. A step forward toward a more realistic modeling of the mushy layer could consist of injecting light elements within randomly distributed "patches" mimicking local chimneys, although this brings extra complexities since the number of mush chimneys in the ICB conditions is not constrained. Furthermore, the scaling law (22) may not be relevant to predict the size of chemical plumes in core conditions if these plumes erupt from localized chimneys formed in the mushy layer. The initial width of the plumes would in that case likely be controlled by the dynamics of the mushy layer rather than by the Rayleigh-Taylor destabilization of a homogeneous light layer. Unfortunately, the size of the chimneys formed in the mush is presently unknown in core conditions. An alternative scenario is the presence of a slurry layer above the inner core boundary (Loper and Roberts, 1981; Gubbins et al., 2008; Wong et al., 2018) which may not be adequately modeled by a simple compositional volumetric source term. Also, note that the term "compositional convection" referred to in this study could be subject to a semantic debate: Rayleigh-Taylor instability and Rayleigh-Bénard convection are both buoyancy-driven instabilities but the former is for two layers of different densities while the latter seems to imply a more continuous density variation associated with diffusion. It is not clear whether the nature of the first instability affects what we observe in the shell away from the boundary.

Another crucial question is whether chemical plumes would experience a complete turbulent mixing in core conditions. Laboratory experiments by Jellinek et al. (1999), in which a buoyant fluid is released at the bottom of a non-rotating box, show that plumes experience efficient turbulent mixing as soon as their associated plumes Reynolds number exceeds 100, which can prevent the formation of a stratified layer at the top of the tank. In our simulations, the local Reynolds number at the scale

TABLE 2 | List of the main studies that proposed some constraints on the stratified layer at the top of the Earth's core based on either magnetic or seismic observations.

Study	Method	Stratification?	Thickness (km)	$N = \sqrt{\frac{g}{\rho}\frac{\partial \rho}{\partial r}}$ (s^{-1})	Main results/comments
Lay and Young, 1990	SKS-SKKS	Yes	50–100	–	1–2% Slower P-waves.
Tanaka, 2007	SmKS	Maybe	140	–	0.8% Slower P-waves, Possible contamination of the lowermost mantle.
Gubbins, 2007	Magnetic	Maybe	$\lesssim 100$	–	Upwelling necessary near the top of the core.
Helffrich and Kaneshima, 2010	SmKS	Yes	300	$\lesssim 10^{-3}$ ($N/\Omega \sim 10$)	$\lesssim$ 0.3% Slower P-waves. Total light-element enrichment is up to 5 wt% at the top of the core.
Alexandrakis and Eaton, 2010	SmKS	No	–	–	Different analysis of SmKS waves.
Kaneshima and Helffrich, 2013	SmKS	Yes	300	–	$\lesssim$ 0.45% Slower P-waves.
Buffett, 2014	Magnetic	Maybe	140	$\lesssim 7.4 \times 10^{-5}$ s^{-1}	Stratification is compatible with the 60-year period in the geomagnetic secular variation and fluctuations in the dipole field.
Kaneshima and Matsuzawa, 2015	SmKS	Yes	300	–	$\lesssim$ 0.45% Slower P-waves.
Lesur et al., 2015	Magnetic	Maybe	–	–	Small poloidal flow required below the CMB.
Buffett et al., 2016	Magnetic	Maybe	130–140	$\lesssim 5.4 - 6.1 \times 10^{-5}$ s^{-1}	Time-dependent zonal flow at the top of the core, fluctuations of the dipole field, and length of day can be explained by a stratified layer.
Kaneshima, 2018	SmKS	Yes	Up to 450	–	$\lesssim$ 0.45% Slower P-waves.
Irving et al., 2018	Normal modes	No	–	Close to neutral	Stratification not required to fit observations.

δ of the chemical plumes yields

$$Re_\delta \sim U\delta/\nu. \tag{25}$$

Assuming the scaling law (22) can be used as a good proxy for the size of chemical plumes in core conditions, we can estimate

$$Re_\delta \sim 0.2\, ReE^{1/3}. \tag{26}$$

Taking $E = 10^{-15}$ and $Re = 10^8$ for the core, one obtains $Re_\delta \sim 200$, which suggests that plumes would be totally mixed during their ascension in the core, a phenomenon that cannot be captured in our simulations that operate at low global-scale Reynolds numbers (< 100) and therefore, even lower plumes' Reynolds numbers. However, as rotation is known to partially inhibit lateral entrainment of fluid and subsequent mixing (Helfrich and Battisti, 1991; Fernando et al., 1998; Levy and Fernando, 2002; Goodman et al., 2004; Gastine et al., 2016), it is not clear whether chemical plumes would experience significant mixing and dilution in core conditions. The local Rossby number based on the plumes length scale called for by Equation (22) writes

$$Ro_\delta \sim \frac{U}{\delta\Omega} \sim 5\, RoE^{-1/3}. \tag{27}$$

Taking $Ro = U/D\Omega \sim 10^{-6}$ in core conditions, we get $Ro_\delta \sim 0.5$ which suggests that rotational effects may still be influencial for chemical plumes. Future investigations will be necessary to quantify the mixing of chemical plumes and the role played by rotation in more turbulent flow regimes.

One may also question the relevance of the infinite Schmidt number approximation used in the simulations. The dynamics of a rising chemical plume is susceptible to be affected by chemical diffusion if the latter acts at a length scale comparable with the size of the plume (or larger) during its typical rising time. Using the scaling law (22) for the average width of the plumes, one can estimate the typical time τ necessary for chemical diffusion to operate at the scale of a chemical plume or blob of size δ,

$$\tau \sim \frac{\delta^2}{\kappa^\xi} \sim 0.04\, ScE^{2/3} \times \tau_{visc}, \tag{28}$$

where τ_{visc} denotes the viscous time D^2/ν. For example, $E = 10^{-4}$ and $Sc \sim 100$ give $\tau \sim 0.01\tau_{visc}$. This time must be compared with the typical time it takes for a chemical plume or blob to reach the top boundary, which likely depends on the convective regime. For instance, in case 8 with $E = 10^{-4}$ and $Sc = +\infty$, chemical plumes typically reach the top stratified region within $0.1\tau_{visc}$. For a finite value of Sc, the typical diffusion length ℓ during this time period would be

$$\ell \sim D\sqrt{0.1/Sc} \sim D/30 \sim 3\delta. \tag{29}$$

For intermediate Schmidt numbers, chemical diffusion would therefore not be negligible for the dynamics of chemical plumes. A higher value $Sc = 1,000$, corresponding to the upper part of the plausible range expected for the Schmidt number

(cf. Equation 1), would give $\ell \sim D\sqrt{0.1/Sc} \sim D/100 \sim \delta$, a more moderate but still non negligible value. Chemical diffusion could also be a significant contributor to the long-term dynamics of the chemically stratified layer, since the latter builds over long time scales in the simulations. Diffusion would probably "smooth" the granular "flaky" aspect of the compositional field (visible for instance on **Figure 9A**) over time and cause the stratified layer to grow downwards, like in the models of Buffett and Seagle (2010) and Gubbins and Davies (2013). In the case of turbulent flows, chemical diffusion may also act at small scales and allow compositional mixing. Only stirring occurs when chemical diffusion is neglected. The infinite Schmidt number approximation may thus be debatable for the modeling of chemical convection, but this end-member case is certainly a better approximation than the codensity approach in the sense that it can capture physical aspects that are specific to the weakly-diffusive compositional field.

5.2. Physical Constraints on the Properties of a Chemically Stratified Layer Formed by Accumulation of Chemical Blobs

Despite the numerous limitations of the present study listed above that prevent any direct extrapolation of our results to the Earth's core, some physical considerations can be invoked to constrain the properties of a chemically stratified layer built by the accumulation of light chemical blobs emitted at the ICB. In such a scenario, the total density anomaly $\Delta\rho_L$ across the stably stratified layer is bounded by that $\Delta\rho$ of the chemical blobs erupting from the mushy layer ($\Delta\rho_L \leq \Delta\rho$). The density anomaly $\Delta\rho$ of such chemical blobs is not known and may have varied throughout the history of the inner core. Here we try to obtain an order of magnitude for this density anomaly using very simple hypotheses and calculations. Following Moffatt (1989) (but see Moffatt and Loper, 1994 for a more elaborate study), we assume that the dynamics of erupting chemical blobs is governed by a force balance between the Coriolis and buoyancy forces. Using the approximate relation $\rho_s \sim 1.05\rho$, where ρ_s is the density of the inner core and ρ that of the bulk fluid core, one can write

$$f^{1/2}\frac{\Delta\rho}{\rho} \sim \left(\frac{\Omega\dot{R}}{20g}\right)^{1/2} \quad ; \quad f^{1/2}w \sim \left(\frac{g\dot{R}}{20\Omega}\right), \tag{30}$$

where f denotes the surface fraction of the mushy layer occupied by chimneys, w the upward velocity of the chemical blobs and $\dot{R}$ the growh rate of the inner core. Taking $\dot{R} \sim 10^{-11}$ m s^{-1} (Labrosse, 2015), $\Omega \sim 7 \times 10^{-5}$ s^{-1} and $g \sim 3$ m s^{-2} leads to

$$f^{1/2}\frac{\Delta\rho}{\rho} \sim 3 \times 10^{-9} \quad ; \quad f^{1/2}w \sim 2 \times 10^{-4}\,\mathrm{m\,s^{-1}}. \tag{31}$$

The parameter f was found to be close to $10^{-3} - 10^{-2}$ in some laboratory experiments (Copley et al., 1970), but is unknown for the mushy layer in core conditions. The range of acceptable values is however constrained by the typical velocity expected for the fluid core. The latter can be inferred from the inversion of magnetic observations and was estimated to be of order 4×10^{-4} m s^{-1} below the CMB (Finlay and Amit, 2011). Estimations from numerical simulations predict a slightly higher root-mean-square (RMS) velocity of order 10^{-3} m s^{-1} (Christensen and Aubert, 2006). Since velocities have a statistical distribution, the velocities of erupting blobs may be significantly larger than the RMS velocity in the convecting region. Assuming a typical velocity 10^{-2} m s^{-1} for the chemical blobs gives

$$f \sim 4 \times 10^{-4} \quad ; \quad \frac{\Delta\rho}{\rho} \sim 1.5 \times 10^{-7}. \tag{32}$$

Figure 12 shows the mean Brunt-Väisälä frequency N obtained when spreading linearly a density anomaly $\Delta\rho \sim 10^{-7}\rho$ over a stratified layer of thickness H,

$$N \sim \sqrt{\frac{g}{H}\frac{\Delta\rho}{\rho}}. \tag{33}$$

For instance, $g \sim 10$ m s^{-2} and $H = 100$ km would give $N \sim 3 \times 10^{-6}$ s^{-1}, which is just slightly smaller than the estimation required by Buffett (2014) and Buffett et al. (2016) to explain some properties of the geomagnetic field, and more than two orders of magnitude smaller than the value suggested by Helffrich and Kaneshima (2010) based on seismic observations. Obtaining a mean buoyancy frequency of order $N \sim 10^{-5}$ s^{-1} compatible with magnetic observations would require either a thinner stratified layer ($H \sim 10$ km) or a higher density anomaly such that $\Delta\rho/\rho \sim 10^{-6}$. This density ratio ratio would then give $f \sim 10^{-5}$ and $w \sim 0.1$ m s^{-1}. It should be noted that the mean Brunt–Väisälä frequency of the layer estimated using Equation (33) constitutes an upper bound corresponding to the ideal case in which there is no dilution of the chemical blobs along their path to the top of the core ($\Delta\rho_L \sim \Delta\rho$). Provided the force balance proposed by Moffatt (1989) is reasonable, it is therefore clear that matching the strong stratification ($N \lesssim 10^{-3}$ s^{-1}) called for by some seismic studies can be achieved only by invoking unrealistically high blobs velocities ($w \gtrsim 10^2$ m s^{-1}). One may however criticize the simplicity of this assumption by arguing that the properties of the blobs erupting from the mush chimneys would rather be controlled by the dynamics of the mushy layer. Though it seems more likely that a stratified layer at the top of the core formed by the accumulation of chemical blobs emitted at the ICB would be weakly stratified (most likely $N < 10^{-5}$ s^{-1}) and, very likely, seismically invisible, we cannot exclude stronger stratifications depending on the precise processes occurring in the ICB region.

Should the accumulation of chemical blobs alone be unable to explain the presence of a thick stably stratified layer at the top of the core, it might still play an important role. Gubbins and Davies (2013) studied the possible formation of a chemically stratified layer by barodiffusion. Though their model produces a layer that may be compatible with observations, the authors mention that a crucial prerequisite in their scenario is the presence of an initial "embryo" of layer that is not mixed by convection. The latter could well be produced by the accumulation of

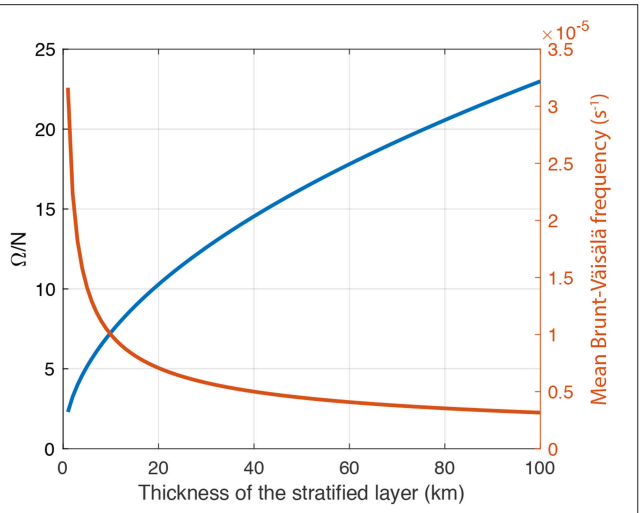

FIGURE 12 | Mean Brunt-Väisälä frequency (orange) and N/Ω ratio (blue) obtained when spreading linearly a density difference $\Delta\rho$ across a stratified layer of given thickness (x-axis), for $\Delta\rho/\rho = 10^{-7}$.

incompletely mixed chemical blobs emitted at the inner core boundary. Though the absence of scaling laws prevents us from making a prediction on the thickness of such a layer, the stratified layer rapidly extends well beyond the Ekman layer in all our simulations. We therefore suggest that the accumulation of incompletely mixed chemical plumes may form a stratified layer of sufficient thickness to allow a thicker layer to grow according to the scenario of Gubbins and Davies (2013).

6. DISCUSSION AND CONCLUSION

Using a new version of the PARODY code including a particle-in-cell method, we ran a first series of exploratory simulations of pure chemical convection at infinite Schmidt number in a rotating spherical shell. In these simulations, light elements are injected within a thin layer above the bottom boundary. This preliminary work remains descriptive and qualitative, but reveals that chemical convection in the Earth's outer core is a rich and vast topic that warrants several more focused and quantitative studies. We showed that, principally as a result of their lower diffusivity, chemical plumes have a complex dynamics that may be influenced by several distinct instabilities in the different regions of the shell. We observed secondary instabilities such as undulations, plumes precession, fragmentation into chemical "blobs" that comply qualitatively well with some previous predictions and laboratory experiments. Plumes may also experience jet-instability and start widening and entraining ambient fluid. A particularly interesting result is the systematic formation of a chemically stratified layer at the top of the shell in all simulations. The layer has a latitudinal topography and slowly grows owing to the accumulation of incompletely mixed chemical plumes and blobs emitted at the bottom boundary.

The existence of a stably stratified layer at the top of the core has been proposed for several decades based on seismic and magnetic observations (Lay and Young, 1990; Tanaka, 2007; Helffrich and Kaneshima, 2010; Buffett, 2014; Kaneshima, 2018) as well as core evolution models (Labrosse, 2015). The debate concerning the existence and properties of this layer (thermal and/or chemical stratification, thickness, and strength of stratification) remains open and our exploratory study does not bring definitive answers to any of these points. However, to our knowledge, this is the first time that the self-consistent formation of a stratified layer is observed in numerical simulations. The layer forms through mechanisms that bear some similarity with the scenario envisioned by Moffatt and Loper (1994) and the "filling-box" models (Baines and Turner, 1969).

As our simulations operate with control parameters that are very remote from core conditions and miss some important ingredients like thermal convection, magnetic field and turbulence, it is not clear whether the results shown in this study would hold when approaching more realistic conditions. Future studies should aim at incorporating these essential ingredients and systematically exploring the parameter space in order to understand more quantitatively the physics of compositional convection and make predictions for the Earth. Our preliminary study suggests that a chemically stratified layer formed by the accumulation of chemically buoyant parcels of fluid released at the bottom of the core would probably be weakly stratified and thus, likely seismically invisible. However, this relies on a force balance assumption that may be irrelevant. Constraints on the stratification that can be produced by such a scenario may rather come from the precise dynamics of the mushy layer which is presently poorly understood and deserves future investigations.

AUTHOR CONTRIBUTIONS

MB ran the simulations, analyzed the data, and wrote the manuscript. GC, SL, and JW significantly contributed to the physical reflection, the interpretation of the results, and to the elaboration of the paper.

FUNDING

This study is partly funded by the French Agence Nationale de la Recherche (grant 446 number ANR-15-CE31-0018-01, MaCoMaOc). The simulations were performed on the ADA machine of the IDRIS center (Orsay, Paris), with grant number i2016047436 and on the Hydra cluster of the Max Planck Society (Garching, Germany).

ACKNOWLEDGMENTS

We thank David Gubbins, Binod Sreenivasan, and Kenneth P. Kodama for their valuable comments which were very helpful to improve the manuscript. We also thank Philippe Cardin and Hagay Amit for fruitful discussions on this topic.

REFERENCES

Alexandrakis, C., and Eaton, D. W. (2010). Precise seismic-wave velocity atop Earth's core: No evidence for outer-core stratification. *Phys. Earth Planet. Inter.* 180, 59–65. doi: 10.1016/j.pepi.2010.02.011

Aubert, J., Aurnou, J., and Wicht, J. (2008). The magnetic structure of convection-driven numerical dynamos. *Geophys. J. Int.* 172, 945–956. doi: 10.1111/j.1365-246X.2007.03693.x

Aurnou, J., Andreadis, S., Zhu, L., and Olson, P. (2003). Experiments on convection in Earth's core tangent cylinder. *Earth Planet. Sci. Lett.* 212, 119–134. doi: 10.1016/S0012-821X(03)00237-1

Badro, J., Siebert, J., and Nimmo, F. (2016). An early geodynamo driven by exsolution of mantle components from Earth's core. *Nature* 536:326. doi: 10.1038/nature18594

Baines, W., and Turner, J. (1969). Turbulent buoyant convection from a source in a confined region. *J. Fluid Mech.* 37, 51–80. doi: 10.1017/S0022112069000413

Bergman, M. I., and Fearn, D. R. (1994). Chimneys on the Earth's inner-outer core boundary? *Geophys. Res. Lett.* 21, 477–480. doi: 10.1029/94GL00028

Bouffard, M., Labrosse, S., Choblet, G., Fournier, A., Aubert, J., and Tackley, P. J. (2017). A particle-in-cell method for studying double-diffusive convection in the liquid layers of planetary interiors. *J. Comput. Phys.* 346, 552–571. doi: 10.1016/j.jcp.2017.06.028

Brackbill, J. U., Kothe, D. B., and Ruppel, H. M. (1988). FLIP: a low-dissipation, particle-in-cell method for fluid flow. *Comput. Phys. Commun.* 48, 25–38. doi: 10.1016/0010-4655(88)90020-3

Braginsky, S. (1963). Structure of the F layer and reasons for convection in the Earth's core. *Soviet Phys. Dokl.* 149, 8–10.

Braginsky, S. (1994). MAC-oscillations of the hidden ocean of the core. *J. Geomagn. Geoelectr.* 45, 1517–1538. doi: 10.5636/jgg.45.1517

Braginsky, S. I., and Roberts, P. H. (1995). Equations governing convection in Earth's core and the geodynamo. *Geophys. Astrophys. Fluid Dyn.* 79, 1–97. doi: 10.1080/03091929508228992

Breuer, M., Manglik, A., Wicht, J., Trümper, T., Harder, H., and Hansen, U. (2010). Thermochemically driven convection in a rotating spherical shell. *Geophys. J. Int.* 183, 150–162. doi: 10.1111/j.1365-246X.2010.04722.x

Buffett, B. (2014). Geomagnetic fluctuations reveal stable stratification at the top of the Earth's core. *Nature* 507:484. doi: 10.1038/nature13122

Buffett, B., Knezek, N., and Holme, R. (2016). Evidence for MAC waves at the top of Earth's core and implications for variations in length of day. *Geophys. J. Int.* 204, 1789–1800. doi: 10.1093/gji/ggv552

Buffett, B. A., and Seagle, C. T. (2010). Stratification of the top of the core due to chemical interactions with the mantle. *J. Geophys. Res.* 115:B04407. doi: 10.1029/2009JB006751

Busse, F. (2002). Is low Rayleigh number convection possible in the Earth's core? *Geophys. Res. Lett.* 29, 9–1. doi: 10.1029/2001GL014597

Cardin, P., and Olson, P. (1992). An experimental approach to thermochemical convection in the Earth's core. *Geophys. Res. Lett.* 19, 1995–1998. doi: 10.1029/92GL01883

Chen, C., and Chen, F. (1991). Experimental study of directional solidification of aqueous ammonium chloride solution. *J. Fluid Mech.* 227, 567–586. doi: 10.1017/S0022112091000253

Christensen, U. R. (2006). A deep dynamo generating Mercury's magnetic field. *Nature* 444, 1056–1058. doi: 10.1038/nature05342

Christensen, U. R. (2015). Iron snow dynamo models for Ganymede. *Icarus* 247, 248–259. doi: 10.1016/j.icarus.2014.10.024259

Christensen, U. R. (2018). Geodynamo models with a stable layer and heterogeneous heat flow at the top of the core. *Geophys. J. Int.* 215, 1338–1351. doi: 10.1093/gji/ggy352

Christensen, U. R., and Aubert, J. (2006). Scaling properties of convection-driven dynamos in rotating spherical shells and application to planetary magnetic fields. *Geophys. J. Int.* 166, 97–114. doi: 10.1111/j.1365-246X.2006.03009.x

Christensen, U. R., and Wicht, J. (2008). Models of magnetic field generation in partly stable planetary cores: applications to Mercury and Saturn. *Icarus* 196, 16–34. doi: 10.1016/j.icarus.2008.02.013

Claßen, S., Heimpel, M., and Christensen, U. (1999). Blob instability in rotating compositional convection. *Geophys. Res. Lett.* 26, 135–138. doi: 10.1029/1998GL900227

Copley, S., Giamei, A. F., Johnson, S., and Hornbecker, M. (1970). The origin of freckles in unidirectionally solidified castings. *Metall. Mater. Trans. B* 1, 3455–3455. doi: 10.1007/BF02643435

de Koker, N., Steinle-Neumann, G., and Vlček, V. (2012). Electrical resistivity and thermal conductivity of liquid Fe alloys at high P and T, and heat flux in Earth's core. *Proc. Nat. Acad. Sci. U.S.A.* 109, 4070–4073. doi: 10.1073/pnas.1111841109

de Wijs, G. A., Kresse, G., Vočadlo, L., Dobson, D., Alfe, D., Gillan, M. J., et al. (1998). The viscosity of liquid iron at the physical conditions of the Earth's core. *Nature* 392, 805–807. doi: 10.1038/33905

Dobson, D. P. (2002). Self-diffusion in liquid Fe at high pressure. *Phys. Earth Planet. Inter.* 130, 271–284. doi: 10.1016/S0031-9201(02)00011-0

Fernando, H., Chen, R., and Ayotte, B. (1998). Development of a point plume in the presence of background rotation. *Phys. Fluids* 10, 2369–2383. doi: 10.1063/1.869754

Finlay, C. C., and Amit, H. (2011). On flow magnitude and field-flow alignment at Earth's core surface. *Geophys. J. Int.* 186, 175–192. doi: 10.1111/j.1365-246X.2011.05032.x

Frank, D., Landel, J., Dalziel, S., and Linden, P. (2017). Anticyclonic precession of a plume in a rotating environment. *Geophys. Res. Lett.* 44, 9400–9407. doi: 10.1002/2017GL074191

Gastine, T., Wicht, J., and Aubert, J. (2016). Scaling regimes in spherical shell rotating convection. *J. Fluid Mech.* 808, 690–732. doi: 10.1017/jfm.2016.659

Gomi, H., Ohta, K., Hirose, K., Labrosse, S., Caracas, R., Verstraete, M., et al. (2013). The high conductivity of iron and thermal evolution of the Earth's core. *Phys. Earth Planet. Inter.* 224, 88–103. doi: 10.1016/j.pepi.2013.07.010

Goodman, J. C., Collins, G. C., Marshall, J., and Pierrehumbert, R. T. (2004). Hydrothermal plume dynamics on Europa: implications for chaos formation. *J. Geophys. Res.* 109:E03008. doi: 10.1029/2003JE002073

Gubbins, D. (2007). Geomagnetic constraints on stratification at the top of Earth's core. *Earth Planets Space* 59, 661–664. doi: 10.1186/BF03352728

Gubbins, D., and Davies, C. (2013). The stratified layer at the core–mantle boundary caused by barodiffusion of oxygen, sulphur and silicon. *Phys. Earth Planet. Inter.* 215, 21–28. doi: 10.1016/j.pepi.2012.11.001

Gubbins, D., Masters, G., and Nimmo, F. (2008). A thermochemical boundary layer at the base of Earth's outer core and independent estimate of core heat flux. *Geophys. J. Int.* 174, 1007–1018. doi: 10.1111/j.1365-246X.2008.03879.x

Gubbins, D., Thomson, C., and Whaler, K. (1982). Stable regions in the Earth's liquid core. *Geophys. J. Int.* 68, 241–251. doi: 10.1111/j.1365-246X.1982.tb06972.x

Helffrich, G., and Kaneshima, S. (2010). Outer core compositional stratification from observed core wave speed profiles. *Nature* 468, 807–810. doi: 10.1038/nature09636

Helffrich, G., and Kaneshima, S. (2013). Causes and consequences of outer core stratification. *Phys. Earth Planet. Inter.* 223, 2–7. doi: 10.1016/j.pepi.2013.07.005

Helfrich, K. R., and Battisti, T. M. (1991). Experiments on baroclinic vortex shedding from hydrothermal plumes. *J. Geophys. Res.* 96, 12511–12518. doi: 10.1029/90JC02643

Hirose, K., Morard, G., Sinmyo, R., Umemoto, K., Hernlund, J., Helffrich, G., et al. (2017). Crystallization of silicon dioxide and compositional evolution of the Earth's core. *Nature* 543, 99–102. doi: 10.1038/nature21367

Huang, K., Zhang, R., van Genuchten, M. T., Ewing, R., Brebbia, C., Gray, W., et al. (1992). A simple particle tracking technique for solving the convection-dispersion equation. *Comput. Methods Water Resour.* 1, 87–96.

Huguet, L., Alboussière, T., Bergman, M., Deguen, R., Labrosse, S., and Lesoeur, G. (2016). Structure of a mushy layer under hypergravity with implications for Earth's inner core. *Geophys. J. Int.* 204, 1729–1755. doi: 10.1093/gji/ggv554

Ichikawa, H., and Tsuchiya, T. (2015). Atomic transport property of Fe–O liquid alloys in the Earth's outer core P, T condition. *Phys. Earth Planet. Inter.* 247, 27–35. doi: 10.1016/j.pepi.2015.03.006

Irving, J. C., Cottaar, S., and Lekić, V. (2018). Seismically determined elastic parameters for Earth's outer core. *Sci. Adv.* 4:eaar2538. doi: 10.1126/sciadv.aar2538

Jellinek, A. M., Kerr, R. C., and Griffiths, R. W. (1999). Mixing and compositional stratification produced by natural convection: 1. experiments and their application to Earth's core and mantle. *J. Geophys. Res.* 104, 7183–7201.

Jones, C. (2015). "Thermal and compositional convection in the outer core," in *Treatise on Geophysics: Core Dynamics, 2nd Edn, Vol. 8,* eds P. Olson and G. Schubert (Amsterdam: Elsevier), 131–185.

Jones, C. A., Soward, A. M., and Mussa, A. I. (2000). The onset of thermal convection in a rapidly rotating sphere. *J. Fluid Mech.* 405, 157–179. doi: 10.1017/S0022112099007235

Kaneshima, S. (2018). Array analyses of SmKS waves and the stratification of Earth's outermost core. *Phys. Earth Planet. Inter.* 276, 234–246. doi: 10.1016/j.pepi.2017.03.006

Kaneshima, S., and Helffrich, G. (2013). Vp structure of the outermost core derived from analysing large-scale array data of SmKS waves. *Geophys. J. Int.* 193, 1537–1555. doi: 10.1093/gji/ggt042

Kaneshima, S., and Matsuzawa, T. (2015). Stratification of Earth's outermost core inferred from SmKS array data. *Prog. Earth Planet. Sc.* 2:15. doi: 10.1186/s40645-015-0046-5

Kerr, R. C., and Mériaux, C. (2004). Structure and dynamics of sheared mantle plumes. *Geochem. Geophys.* 5:Q12009. doi: 10.1029/2004GC000749

Kerr, R. C., Mériaux, C., and Lister, J. R. (2008). Effect of thermal diffusion on the stability of strongly tilted mantle plume tails. *J. Geophys. Res.* 113:B09401. doi: 10.1029/2007JB005510

Konôpková, Z., McWilliams, R. S., Gómez-Pérez, N., and Goncharov, A. F. (2016). Direct measurement of thermal conductivity in solid iron at planetary core conditions. *Nature* 534:99. doi: 10.1038/nature18009

Labrosse, S. (2015). Thermal evolution of the core with a high thermal conductivity. *Phys. Earth Planet. Inter.* 247, 36–55. doi: 10.1016/j.pepi.2015.02.002

Labrosse, S., Poirier, J.-P., and Mouël, J.-L. L. (1997). On cooling of the Earth's core. *Phys. Earth Planet. Inter.* 99, 1–17. doi: 10.1016/S0031-9201(96)03207-4

Landeau, M., Olson, P., Deguen, R., and Hirsh, B. H. (2016). Core merging and stratification following giant impact. *Nat. Geosci.* 9:786. doi: 10.1038/ngeo2808

Lay, T., and Young, C. J. (1990). The stably-stratified outermost core revisited. *Geophys. Res. Lett.* 17, 2001–2004. doi: 10.1029/GL017i011p02001

Lesur, V., Whaler, K., and Wardinski, I. (2015). Are geomagnetic data consistent with stably stratified flow at the core–mantle boundary? *Geophys. J. Int.* 201, 929–946. doi: 10.1093/gji/ggv031

Levy, M., and Fernando, H. (2002). Turbulent thermal convection in a rotating stratified fluid. *J. Fluid Mech.* 467, 19–40. doi: 10.1017/S0022112002001350

Lister, J. R., and Buffett, B. A. (1995). The strength and efficiency of thermal and compositional convection in the geodynamo. *Phys. Earth Planet. Inter.* 91, 17–30. doi: 10.1016/0031-9201(95)03042-U

Lister, J. R., and Buffett, B. A. (1998). Stratification of the outer core at the core-mantle boundary. *Phys. Earth Planet. Inter.* 105, 5–19. doi: 10.1016/S0031-9201(97)00082-4

Loper, D. (2007). Turbulence and small-scale dynamics in the core. *Treat. Geophys.* 8, 187–206. doi: 10.1016/B978-044452748-6/00131-0

Loper, D. E., and Moffatt, H. K. (1993). Small-scale hydromagnetic flow in the Earth's core: rise of a vertical buoyant plume. *Geophys. Astrophys. Fluid Dyn.* 68, 177–202. doi: 10.1080/03091929308203567

Loper, D. E., and Roberts, P. H. (1981). A study of conditions at the inner core boundary of the Earth. *Phys. Earth Planet. Inter.* 24, 302–307. doi: 10.1016/0031-9201(81)90117-5

Manglik, A., Wicht, J., and Christensen, U. R. (2010). A dynamo model with double diffusive convection for Mercury's core. *Earth Planet. Sci. Lett.* 289, 619–628. doi: 10.1016/j.epsl.2009.12.007

Matsushima, M. (2004). Scale similarity of mhd turbulence in the earth's core. *Earth Planets Space* 56, 599–605. doi: 10.1186/BF03352520

Michalke, A. (1984). Survey on jet instability theory. *Prog. Aerosp. Sci.* 21, 159–199. doi: 10.1016/0376-0421(84)90005-8

Moffatt, H. (1989). "Liquid metal MHD and the geodynamo," *Proceedings of IUTAM Symposium on Liquid Metal Magnetohydrodynamics* (Riga), 403–412.

Moffatt, H., and Loper, D. (1994). The magnetostrophic rise of a buoyant parcel in the Earth's core. *Geophys. J. Int.* 117, 394–402. doi: 10.1111/j.1365-246X.1994.tb03939.x

Munz, C.-D. (1988). On the numerical dissipation of high resolution schemes for hyperbolic conservation laws. *J. Comput. Phys.* 77, 18–39. doi: 10.1016/0021-9991(88)90154-4

Nakagawa, T. (2011). Effect of a stably stratified layer near the outer boundary in numerical simulations of a magnetohydrodynamic dynamo in a rotating spherical shell and its implications for Earth's core. *Phys. Earth Planet. Inter.* 187, 342–352. doi: 10.1016/j.pepi.2011.06.001

Nataf, H.-C., and Gagniere, N. (2008). On the peculiar nature of turbulence in planetary dynamos. *C R Phys.* 9, 702–710. doi: 10.1016/j.crhy.2008.07.009

Nataf, H.-C., and Schaeffer, N. (2015). "Turbulence in the core," in *Treatise on Geophysics,16 2nd Edn.* (Amsterdam: Elsevier), 161–181.

Ohta, K., Kuwayama, Y., Hirose, K., Shimizu, K., and Ohishi, Y. (2016). Experimental determination of the electrical resistivity of iron at Earth's core conditions. *Nature* 534, 95–98. doi: 10.1038/nature17957

Olson, P., Landeau, M., and Reynolds, E. (2017). Dynamo tests for stratification below the core-mantle boundary. *Phys. Earth Planet. Inter.* 271, 1–18. doi: 10.1016/j.pepi.2017.07.003

Olson, P., Landeau, M., and Reynolds, E. (2018). Outer core stratification from the high latitude structure of the geomagnetic field. *Front. Earth Sci.* 6:140. doi: 10.3389/feart.2018.00140

O'Rourke, J. G., and Stevenson, D. J. (2016). Powering Earth's dynamo with magnesium precipitation from the core. *Nature* 529, 387–389. doi: 10.1038/nature16495

Perrillat, J.-P., Mezouar, M., Garbarino, G., and Bauchau, S. (2010). *In situ* viscometry of high-pressure melts in the Paris–Edinburgh cell: application to liquid FeS. *High Press. Res.* 30, 415–423. doi: 10.1080/08957959.2010.494844

Poirier, J. (1988). Transport properties of liquid metals and viscosity of the Earth's core. *Geophys. J. Int.* 92, 99–105. doi: 10.1111/j.1365-246X.1988.tb01124.x

Posner, E. S., Rubie, D. C., Frost, D. J., and Steinle-Neumann, G. (2017). Experimental determination of oxygen diffusion in liquid iron at high pressure. *Earth Planet. Sci. Lett.* 464, 116–123. doi: 10.1016/j.epsl.2017.02.020

Pozzo, M., Davies, C., Gubbins, D., and Alfe, D. (2012). Thermal and electrical conductivity of iron at Earth's core conditions. *Nature* 485, 355–358. doi: 10.1038/nature11031

Pozzo, M., Davies, C., Gubbins, D., and Alfè, D. (2013). Transport properties for liquid silicon-oxygen-iron mixtures at Earth's core conditions. *Phys. Rev. B* 87:014110. doi: 10.1103/PhysRevB.87.014110

Roberts, P. H., and King, E. M. (2013). On the genesis of the Earth's magnetism. *Rep. Prog. Phys.* 76:096801. doi: 10.1088/0034-4885/76/9/096801

Simitev, R., and Busse, F. (2003). Patterns of convection in rotating spherical shells. *New J. Phys.* 5:97. doi: 10.1088/1367-2630/5/1/397

Simitev, R., and Busse, F. (2005). Prandtl-number dependence of convection-driven dynamos in rotating spherical fluid shells. *J. Fluid Mech.* 532, 365–388. doi: 10.1017/S0022112005004398

Sironi, L., and Spitkovsky, A. (2009). Synthetic spectra from particle-in-cell simulations of relativistic collisionless shocks. *Astrophys. J. Lett.* 707:L92. doi: 10.1088/0004-637X/707/1/L92

Sreenivasan, B., and Narasimhan, G. (2017). Damping of magnetohydrodynamic waves in a rotating fluid. *J. Fluid Mech.* 828, 867–905. doi: 10.1017/jfm.2017.550

St Pierre, M. G. (1996). On the local nature of turbulence in Earth's outer core. *Geophys. Astrophys. Fluid Dyn.* 83, 293–306. doi: 10.1080/03091929608208969

Tackley, P. J., and King, S. D. (2003). Testing the tracer ratio method for modeling active compositional fields in mantle convection simulations. *Geochem. Geophys.* 4. doi: 10.1029/2001GC000214

Takehiro, S.-I., and Lister, J. R. (2001). Penetration of columnar convection into an outer stably stratified layer in rapidly rotating spherical fluid shells. *Earth Planet. Sci. Lett.* 187, 357–366. doi: 10.1016/S0012-821X(01)00283-7

Tanaka, S. (2007). Possibility of a low P-wave velocity layer in the outermost core from global SmKS waveforms. *Earth Planet. Sci. Lett.* 259, 486–499. doi: 10.1016/j.epsl.2007.05.007

Tang, L., Masutani, S. M., et al. (2003). "Laminar to turbulent flow liquid-liquid jet instability and breakup," in *The Thirteenth International Offshore and Polar Engineering Conference* (Honolulu, HI).

Tskhakaya, D., Matyash, K., Schneider, R., and Taccogna, F. (2007). The Particle-In-Cell Method. *Contrib. Plasm. Phys.* 47, 563–594. doi: 10.1002/ctpp.200710072

Vočadlo, L., Alfè, D., Price, G. D., and Gillan, M. J. (2000). First principles calculations on the diffusivity and viscosity of liquid Fe–S at experimentally accessible conditions. *Phys. Earth Planet. Inter.* 120, 145–152. doi: 10.1016/S0031-9201(00)00151-5

Wong, J., Davies, C. J., and Jones, C. A. (2018). A Boussinesq slurry model of the F–layer at the base of Earth's outer core. *Geophys. J. Int.* 214, 2236–2249. doi: 10.1093/gji/ggy245

Worster, M. G., and Huppert, H. E. (1983). Time-dependent density profiles in a filling box. *J. Fluid Mech.* 132, 457–466. doi: 10.1017/S002211208300172X

Zhang, K.-K. (1991). Convection in a rapidly rotating spherical shell at infinite Prandtl number: steadily drifting rolls. *Phys. Earth Planet. Inter.* 68, 156–169. doi: 10.1016/0031-9201(91)90015-A

Zhang, K.-K. (1992). Convection in a rapidly rotating spherical shell at infinite Prandtl number: transition to vacillating flows. *Phys. Earth Planet. Inter.* 72, 236–248. doi: 10.1016/0031-9201(92)90204-9

Zhang, K.-K., and Busse, F. (1990). Generation of magnetic fields by convection in a rotating spherical fluid shell of infinite Prandtl number. *Phys. Earth Planet. Inter.* 59, 208–222. doi: 10.1016/0031-9201(90)90226-N

Conflict of Interest Statement: The authors declare that the research was conducted in the absence of any commercial or financial relationships that could be construed as a potential conflict of interest.

frontiers in Earth Science

ORIGINAL RESEARCH
published: 29 November 2018
doi: 10.3389/feart.2018.00217

Impurity Resistivity of fcc and hcp Fe-Based Alloys: Thermal Stratification at the Top of the Core of Super-Earths

Hitoshi Gomi and Takashi Yoshino*

Institute for Planetary Materials, Okayama University, Tottori, Japan

It is widely known that the Earth's Fe dominant core contains a certain amount of light elements such as H, C, N, O, Si, and S. We report the results of first-principles calculations on the band structure and the impurity resistivity of substitutionally disordered hcp and fcc Fe based alloys. The calculation was conducted by using the AkaiKKR (machikaneyama) package, which employed the Korringa-Kohn-Rostoker (KKR) method with the atomic sphere approximation (ASA). The local density approximation (LDA) was adopted for the exchange-correlation potential. The coherent potential approximation (CPA) was used to treat substitutional disorder effect. The impurity resistivity is calculated from the Kubo-Greenwood formula with the vertex correction. In dilute alloys with 1 at. % impurity concentration, calculated impurity resistivities of C, N, O, S are comparable to that of Si. On the other hand, in concentrated alloys up to 30 at. %, Si impurity resistivity is the highest followed by C impurity resistivity. Ni impurity resistivity is the smallest. N, O, and S impurity resistivities lie between Si and Ni. Impurity resistivities of hcp-based alloys show systematically higher values than fcc alloys. We also calculated the electronic specific heat from the density of states (DOS). For pure Fe, the results show the deviation from the Sommerfeld value at high temperature, which is consistent with previous calculation. However, the degree of deviation becomes smaller with increasing impurity concentration. The violation of the Sommerfeld expansion is one of the possible sources of the violation of the Wiedemann-Franz law, but the present results could not resolve the inconsistency between recent electrical resistivity and thermal conductivity measurements. Based on the present thermal conductivity model, we calculated the conductive heat flux at the top of terrestrial cores, which is comparable to the heat flux across the thermal boundary layer at the bottom of the mantle. This indicates that the thermal stratification may develop at the top of the liquid core of super-Earths, and hence, chemical buoyancies associated with the inner core growth and/or precipitations are required to generate the global magnetic field through the geodynamo.

Keywords: band structure, density of states, electrical resistivity, thermal conductivity, Linde's rule, KKR-CPA

OPEN ACCESS

Edited by:
Takashi Nakagawa,
University of Hong Kong, Hong Kong

Reviewed by:
Monica Pozzo,
University College London,
United Kingdom
Shin-ichi Takehiro,
Kyoto University, Japan

****Correspondence:***
Hitoshi Gomi
hitoshi.gomi@okayama-u.ac.jp

Specialty section:
This article was submitted to Geomagnetism and Paleomagnetism, a section of the journal Frontiers in Earth Science

Received: *31 May 2018*
Accepted: *07 November 2018*
Published: *29 November 2018*

Citation:
Gomi H and Yoshino T (2018) Impurity Resistivity of fcc and hcp Fe-Based Alloys: Thermal Stratification at the Top of the Core of Super-Earths. Front. Earth Sci. 6:217. doi: 10.3389/feart.2018.00217

INTRODUCTION

Because the electrical current and the heat are mainly transported by mobile electrons in the metallic core, it is important to understand the electron scattering mechanisms in Fe-based alloys at high pressure and temperature to estimate the thermal conductivity and the electrical resistivity. Gomi et al. (2013) proposed the core resistivity model that the resistivity saturation was firstly taken into account. Later, many studies (Kiarasi and Secco, 2015; Gomi et al., 2016; Ohta et al., 2016, 2018; Pozzo and Alfè, 2016a,b; Wagle et al., 2018; Xu et al., 2018) investigated the resistivity saturation. Because of its universality, we expect that the resistivity saturation model is applicable to metallic cores of terrestrial planets with various pressure, temperature and compositions. In order to improve our previous model, we address the following two topics in this study.

The first topic of this study is the compositional effect on the electrical resistivity of cores, namely impurity resistivity. On the one hand, first-principles molecular dynamics (FPMD) studies computed the effects of alloying Si, O, and S (de Koker et al., 2012; Pozzo et al., 2013, 2014; Wagle et al., 2018). On the other hand, high pressure experimental works investigated the impurity resistivities of Si, Ni, S and C (Matassov, 1977; Gomi et al., 2013, 2016; Seagle et al., 2013; Gomi and Hirose, 2015; Kiarasi and Secco, 2015; Suehiro et al., 2017; Ohta et al., 2018; Zhang et al., 2018). In order to understand the relative importance of light elements, Gomi et al. (2013) calculated the impurity resistivities of C, S, and O from the impurity resistivity of silicon by using the Linde's rule (Norbury, 1921; Linde, 1932). However, Suehiro et al. (2017) demonstrated the violation of the Linde's rule from measurements on Fe-Si-S ternary alloys. The Linde's rule is known as a model for impurity resistivity in noble metal hosts, which predicts a parabolic dependence as a function of valence difference Z between impurity element and the host metal. The Linde's rule is valid for impurity elements located at the right hand side of the host noble metal in the periodic table, however, it is strongly violated for magnetic transition metal impurity. Therefore, application to transition metal hosts is indeed questionable. Instead of the Linde's rule, we will show the relative importance of the impurity resistivity of light alloying elements in fcc and hcp Fe by means of the Korringa-Kohn-Rostoker method combined with the coherent potential approximation (KKR-CPA) (Oshita et al., 2009; Kou and Akai, 2018), which successfully reproduces the impurity resistivities of Si and Ni in hcp Fe (Gomi et al., 2016).

The second topic of this study is the validity of the Widemann-Franz law. The Widemann-Franz law predicts the thermal conductivity from the electrical resistivity as:

$$k = \frac{LT}{\rho} \tag{1}$$

where k is the thermal conductivity, L is the Lorenz number, T is the absolute temperature and ρ is the electrical resistivity. The Lorenz number is almost independent of temperature and common for almost all metals. The Sommerfeld value $L_{Somm} = \frac{1}{3}\frac{\pi^2 k_B^2}{e^2} = 2.445 \times 10^{-8}$ WΩ/K^2 is widely used as the Lorenz number, where k_B is the Boltzmann's constant and e is electronic charge (e.g., Anderson, 1998; Poirier, 2000; see also Appendix of Gomi and Hirose, 2015). However, FPMD studies predict the deviation of the Lorenz number from the Sommerfeld value (de Koker et al., 2012; Pozzo et al., 2012, 2013, 2014; Pozzo and Alfè, 2016b). More importantly, the experimentally determined Lorenz number of hcp Fe, which is calculated from recent laser heated diamond-anvil cell (LHDAC) measurements on the electrical resistivity (Ohta et al., 2016) and the thermal conductivity (Konôpková et al., 2016), exhibit substantially smaller than the Sommerfeld value. Even though these LHDAC results may have large uncertainty (Dobson, 2016), this fact suggests potential violation of the Widemann-Franz law. Gomi and Hirose (2015) pointed out three important approximations, which potentially violate the Wiedemann-Franz law: omitting the additional contribution from lattice or ionic conductivity, neglecting the anelastic scattering, and the application of the Sommerfeld expansion. Additionally, electron-electron scattering may affect the Lorenz number (Pourovskii et al., 2017). Among them, the violation of the Sommerfeld expansion may cause 2–43% deviation from the Sommerfeld value of the Lorenz number, if we adopt the calculated electron density of states (DOS) of fcc and hcp Fe reported by Boness et al. (1986). However, this argument is limited to pure Fe. As well as the impurity resistivity calculation, the KKR-CPA method can easily simulate the DOS of disordered alloys (Gomi et al., 2016, 2018).

This paper is organized as follows. In the section Methods, the first-principles methods were described. The impurity resistivities of various impurities in fcc Au were first calculated to examine the validity and the physical origin of the violation of the Linde's rule (section Dilute Alloys). Then, impurity resistivities in fcc and hcp Fe-based alloys were simulated at high pressure (sections Dilute Alloys and Concentrated Alloys). Simultaneously, electron DOS were computed. The electronic specific heat was then estimated by numerical integration based on the DOS. The numerically-calculated specific heat values were compared with that was obtained by the Sommerfeld expansion to discuss the possible deviation of the Lorenz number from its Sommerfeld value (section Electronic Specific Heat and Wiedemann-Franz Law). Combined with the present impurity resistivity and the Lorenz number, we revised our thermal conductivity model (Gomi et al., 2016) (section Electrical Resistivity and Thermal Conductivity of the Earth's Core). Finally, the model was applied to the planetary cores with various planetary mass from 0.1 to 10 times Earth mass (section Heat Flux at the CMB of Super-Earths).

METHODS

We carried out the first-principles electronic band structure calculation of fcc Au-, hcp and fcc Fe-based alloys. For fcc Au alloys, the lattice parameters are set to $a = 7.71$ Bohr, which correspond the ambient pressure value. For hcp Fe alloys, the

lattice volumes are set to 19.10, 16.27, and 9.80 Å^3. These values correspond to 40, 120, and 1,000 GPa pressure at ambient temperature (Dewaele et al., 2006). The axial ratio was set to the ideal value ($c/a = 1.633$). For fcc Fe alloys, we used the same atomic volumes as for hcp Fe alloys. The Kohn-Sham equation was solved by means of Korringa-Kohn-Rostoker (KKR) Green function method, which implemented in AkaiKKR package (Akai, 1989). The local density approximation (LDA) was adapted to exchange-correlation potential (Moruzzi et al., 1978); the specific choice of the exchange-correlation functional may not significantly affect the resistivity value (see Supplementary Figure S1 of Gomi et al., 2016). The crystal potential was approximated by using the atomic spherical approximation (ASA). The maximum angular momentum quantum number was set to $l = 3$. Relativistic effects are considered in the scalar relativistic approximation. The substitutional chemical disorder is described in the coherent potential approximation (CPA). The electrical resistivity is calculated from the Kubo-Greenwood formula with the vertex correction (Butler, 1985; Oshita et al., 2009; Gomi et al., 2016; Kou and Akai, 2018). The hcp Fe-alloys have two independent resistivity components with respect to crystallographic orientation; $\rho_{||}$ and $\rho_{\perp}$ are the resistivities calculated parallel and perpendicular to the c-axis, respectively. The resistivities of polycrystalline hcp Fe-alloys are calculated as $\rho_{\mathrm{poly}} = (2\rho_{\perp} + \rho_{||})/3$ (Alstad et al., 1961).

DILUTE ALLOYS

Norbury (1921) conducted systematic measurements of impurity resistivity of dilute alloys, and found that the impurity resistivity is enhanced with increasing horizontal distance between the positions of impurity element and host metal in the periodic table. Linde (1932) reported that impurity resistivity of noble metal-based alloys is proportional to Z^2, where Z is the difference in valence between impurity element and host metal. This relationship is observed in the noble metal alloyed with the impurity element located at the right hand side of the noble metal in the periodic table, and is so-called the Linde's rule. Mott (1936) provided an interpretation for Linde's rule, assuming the impurity atom to be a point charge $Z \times e$, where e is the elementary electrical charge. This approximation successfully explained the Z^2 dependence of the impurity resistivity. However, impurity elements on the left hand side of the noble metal exhibit complicated behavior. This is reasonably explained by Friedel model with the idea of the virtual bond state (VBS) (Friedel, 1956).

Figure 1A shows the impurity resistivities of impurity elements with the atomic numbers from 1 (H) to 18 (Kr) in fcc Au host. We tried to simulate both of non-magnetic and local magnetic disorder (LMD) state for all these impurity elements, and the LMD solution was obtained only for V, Cr, Mn, Fe, Co, and Ni impurity. For these six impurity elements, the impurity resistivity value is largely different between the non-magnetic state and the LMD state, and the LMD results are consistent with previous experimental results. The impurity resistivities of the other 12 elements without local magnetic moments show good agreement with previous experimental results (Friedel, 1956).

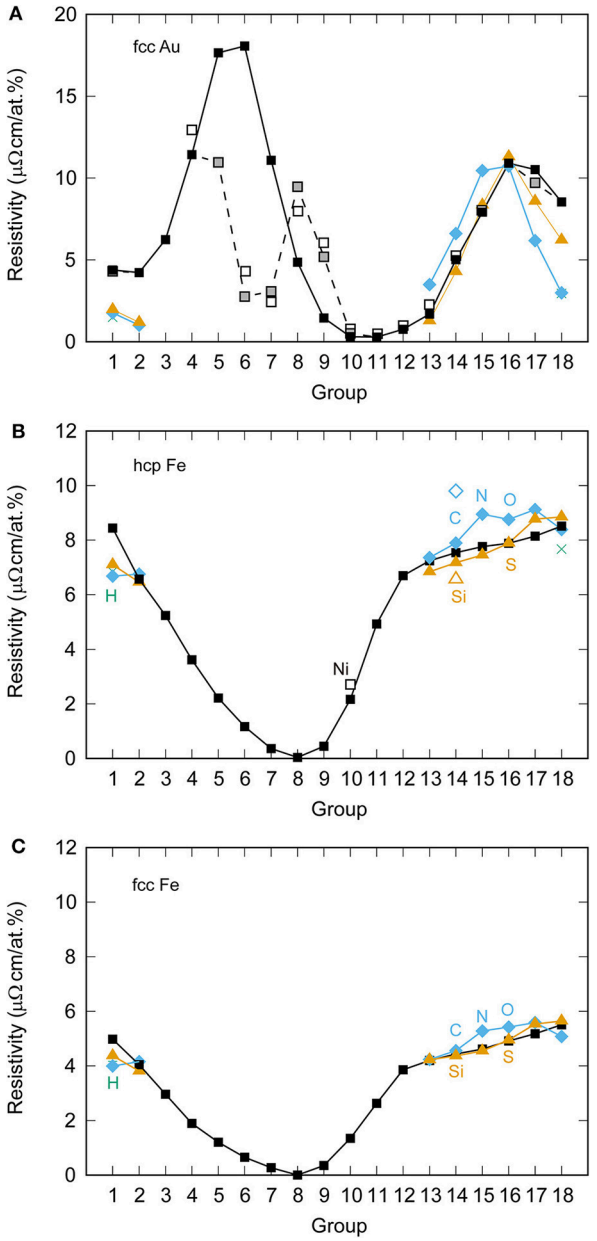

FIGURE 1 | Impurity resistivities of 1st (green cross; H and He), 2nd (blue diamond; Li, Be, B, C, N, O, F and Ne), 3rd (orange triangle; Na, Mg, Al, Si, P, S, Cl, and Ar) and 4th (black square; K, Ca, Sc, Ti, V, Cr, Mn, Fe, Co, Ni, Cu, Zn, Ga, Ge, As, Se, Br and Kr) period elements. **(A)** fcc Au-alloys at 1 bar compared with literature values (Friedel, 1956). **(B)** hcp Fe-alloys at 40 GPa compared with previous DAC experiments (Ni: Gomi and Hirose, 2015; Si: Gomi et al., 2016; C: Zhang et al., 2018). **(C)** fcc Fe-alloys at 40 GPa. In common, solid symbols with solid lines are present nonmagnetic calculations, gray square symbols with broken line are obtained from present LMD calculations and open symbols represent previous experiments.

For 3rd period impurity elements located at the right hand side of Cu in the periodic table, namely Zn, Ga, Ge and As, are known to follow the Linde's rule (Norbury, 1921; Linde, 1932), and our first-principles calculations without local magnetic moment well reproduce previous experimental results (Friedel, 1956). Our calculations on 13 to 15 group of 2nd and 3rd period elements, which include the possible candidates of the light elements alloying with planetary cores (C, N, O, Si, S), also show the similar trend predicted by the Linde's rule.

In the **Figure 1A**, filled squares are present first-principles calculation without spin-polarization, which show parabola dependence. Open squares indicate present first-principles with local magnetic disorder (LMD), which reproduce previous experimental results (Friedel, 1956). To discuss the Friedel mode, we computed the partial density of states (PDOS) of impurity elements in fcc Au (**Figure 2**). **Figure 2A** shows the non-magnetic PDOS of Ti, V, Cr, Mn, Fe, Co, and Ni. In fcc Au, PDOS of these transition impurities have a sharp peak at the vicinity of the Fermi level, which is so-called virtual bond state (VBS) (Friedel, 1956; Mertig, 1999). The peak position shifts from high energy to low energy with increasing the atomic number. The impurity resistivities of non-magnetic fcc Au-based alloys exhibit the maximum coincidence with the VBS peak across the Fermi energy. Experimental and LMD impurity resistivity can also be explained by the peak position relevant to the Fermi energy. **Figure 2B** represents the PDOS of Cr with non-magnetic (solid line) and LMD (broken lines). The impurity resistivity of non-magnetic Cr is predicted to be 1.0×10^{-7} Ωm, which is larger than the experimental value of 4.0×10^{-8} Ωm. In an opposite manner, non-magnetic Co impurity resistivity is larger than experimental and LMD impurity resistivity. The VBS of non-magnetic Co is a little bit shifted to lower energy compared with the Fermi energy, but, in LMD state, the VBS split and the up spin peak move to the Fermi level. This causes the strong scattering.

Figure 1B shows the impurity resistivities of hcp Fe-based alloys at the volume of 19.1 $Å^3$, which corresponds to the pressure of 40 GPa for pure hcp Fe at 300 K (Dewaele et al., 2006). Experimentally determined impurity resistivities of Ni, Si, and C are also plotted, which is interpolated between binary alloys (Gomi and Hirose, 2015; Gomi et al., 2016; Zhang et al., 2018) and pure Fe (Gomi et al., 2013) at ambient temperature. The present calculations of impurity resistivities of light element candidates (C, N, O, Si, and S) are almost identical and larger than Ni impurity resistivity. It is well-known that the impurity resistivity of 3d transition metal impurity in 3d transition metal host is small, in general (Tsiovkin et al., 2005, 2006). Among the light element candidates, the impurity resistivity increases with increasing atomic number in the same period. Also, in the same group, the second period atoms show higher impurity resistivity than third period atoms, which is consistent with the experimental fact that the impurity resistivity of C (Zhang et al., 2018) is higher than that of Si (Gomi et al., 2016). This trend is also observed for fcc Fe-based alloys (**Figure 1C**). Impurity resistivity of H seems comparable to the other light elements, however, it may be overestimate. In this study, we assumed that the all impurity elements substitute the Fe sites. But H is known to enter the interstitial sites (Antonov et al., 2002; Fukai, 2006). The partial density of states (PDOS) of interstitial H in hcp and double hexagonal close-packed (dhcp) Fe is located at far below the Fermi energy (e.g., Tsumuraya et al., 2012; Gomi et al., 2018). Therefore, Gomi et al. (2018) argued that the impurity resistivity of interstitial hydrogen is negligibly small. This is consistent with recent DAC experiments on fcc FeH_x alloys (Ohta et al., 2018).

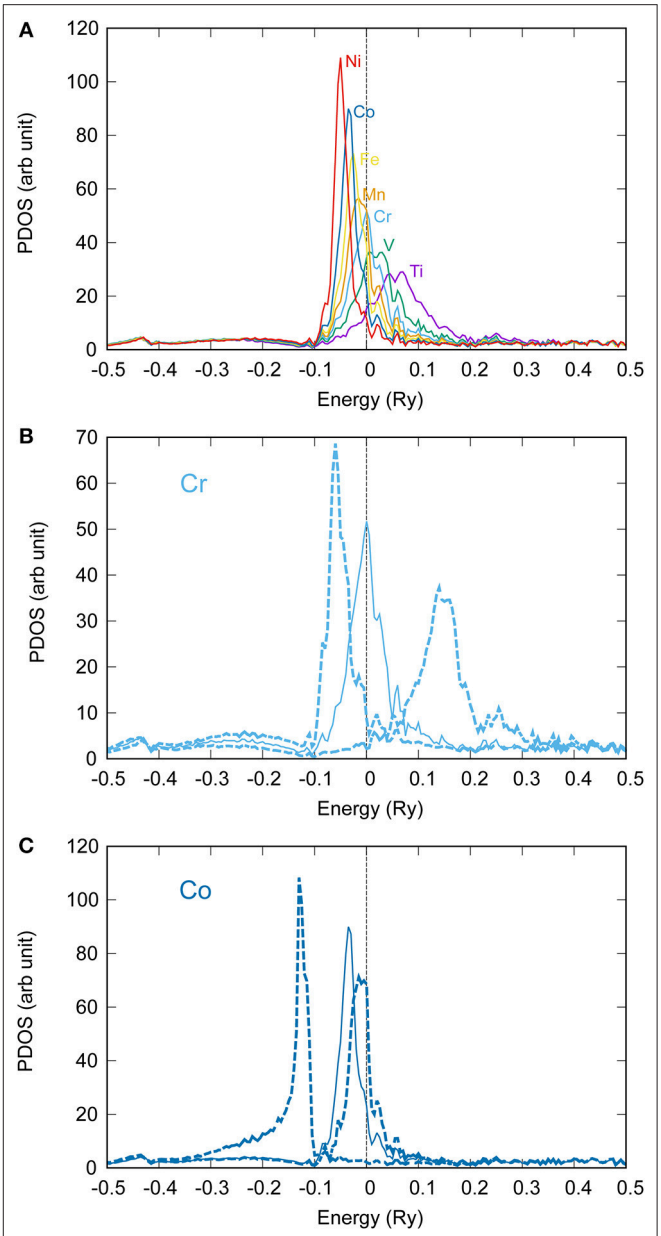

FIGURE 2 | Partial density of states (PDOS) of impurity elements in fcc Au. **(A)** PDOS of Ti (purple), V (green), Cr (cyan), Mn (orange), Fe (yellow), Co (blue), and Ni (red) without local magnetic moment. **(B)** PDOS of Cr with (broken lines) and without (solid line) local magnetic moment. **(C)** PDOS of Co with (broken line) and without (solid line) local magnetic moment.

CONCENTRATED ALLOYS

In the previous section, we discussed dilute alloys, however, the Earth's core should have a large amount of impurity elements (e.g., Hirose et al., 2013). Gomi et al. (2016) reported the resistivity calculation of Fe-Si and Fe-Ni alloys by using the KKR-CPA method, as well as DAC experiments of Fe-Si alloys. Here, we show the systematic survey of impurity resistivity of light element candidates (C, N, O, Si, and S) and Ni in Fe-based high concentration alloys at zero Kelvin (**Figure 3** and **Table 1**). Basically, impurity resistivity of light element candidates is larger than Ni, which agree with dilute alloy results. This can qualitatively be understood in terms of the broadening of energy dispersion via the uncertainty relationship between energy and time; $\Delta E \Delta t \geq \hbar/2$, where ΔE is the uncertainty in energy, Δt is electron life time, and $\hbar$ is the reduced Planck's constant (the Dirac's constant) (Gomi et al., 2016). **Figure 4** shows the Bloch spectral function along with the path, which connects the high symmetry points in the Brillouin zone of the hexagonal lattice. If there is no scattering, the Bloch spectral function is equivalent to the band structure of perfectly ordered crystal. Indeed, the broadening features of Fe-Ni alloys are weaker than that of other Fe-light elements alloys. At 19.10 Å^3 (∼40 GPa), Si shows the largest impurity resistivity, followed by C, S, and N. The smallest impurity resistivity is obtained from O impurity among the light element candidates. Note that this sequential order is completely different from that of dilute alloys (**Figure 1**).

This is potentially explained by the variation of the saturation resistivity due to the chemical composition. The electrical resistivity of transition metals and alloys tends to saturate at high resistivity (Mooij, 1973; Bohnenkamp et al., 2002). This resistivity saturation is observed when the mean free path of conduction electrons becomes comparable to the inter-atomic distance; this condition is so-called the Mott-Ioffe-Regel criteria (Mott, 1972; Gurvitch, 1981). This condition may be graphically identified from the cross sections of the Bloch spectral function at the Fermi energy (**Figure 5**), because the inverse of the mean free path is proportional to the width of the Fermi surface broadening, and the boundary of the first Brillouin zone is proportional to the inverse of the lattice parameter (Butler and Stocks, 1984; Butler, 1985; Banhart et al., 1989; Glasbrenner et al., 2014; Gomi et al., 2016). Gomi et al. (2016) compared the cross section of Fe-Si and Fe-Ni alloys, and argued that the non-linear concentration-resistivity relationship observed in Fe-Ni alloys is explained by the Nordheim's rule, whereas that of Fe-Si alloys is due to the resistivity saturation. Interestingly, the broadening feature of S, C, N and O impurity alloys are similar to the Si alloy. Especially, the O alloy's width seems even larger than that of Si alloy. This suggests that the high-concentration Fe-O alloys satisfies the Mott-Ioffe-Regel criteria, even though the impurity resistivity is smaller than Fe-Si alloy.

We also calculated the impurity resistivity of Fe-Si-S ternary alloys (**Figure 6**). The results are consistent with the DAC measurements by Suehiro et al. (2017). **Figure 6** also implies the violation of the Matthiessen's rule, which is a simple sum rule of resistivity of all the scattering terms. The violation of the Matthiessen's rule is already reported by previous calculations (Glasbrenner et al., 2014; Gomi et al., 2016; Drchal et al., 2017).

ELECTRONIC SPECIFIC HEAT AND WIEDEMANN-FRANZ LAW

Only a few direct thermal conductivity measurements at high pressure and temperature have been reported (Konôpková et al., 2011, 2016; McWilliams et al., 2015). Even though the thermal conductivity can directly be calculated from first-principles calculations (Sha and Cohen, 2011; de Koker et al., 2012; Pozzo et al., 2012, 2013, 2014; Pozzo and Alfè, 2016b; Pourovskii et al., 2017; Wagle et al., 2018; Xu et al., 2018; Yue and Hu, 2018), the Wiedemann-Franz law has been widely used to estimate the thermal conductivity of the Earth's core from the electrical resistivity measurements (Anderson, 1998; Stacey and Anderson, 2001; Stacey and Loper, 2007; Deng et al., 2013; Gomi et al., 2013, 2016; Seagle et al., 2013; Gomi and Hirose, 2015; Ohta et al., 2016, 2018; Hieu et al., 2017; Suehiro et al., 2017; Pommier, 2018; Silber et al., 2018; Zhang et al., 2018) (see Williams, 2018 for a recent review). The Lorenz number is related to the electronic band structure (Vafayi et al., 2006; Gomi and Hirose, 2015; Secco, 2017). Gomi and Hirose (2015) mentioned that the Lorenz number may have up to ∼40 % uncertainty, based on the first-principles calculations on the electronic specific heat reported by Boness et al. (1986). However, this value was calculated only for pure Fe. Therefore, in this section, we investigated how the specific heat deviates from its Sommerfeld value for Fe-based alloys.

At around the ambient temperature, the electronic specific heat can be estimated based on the Sommerfeld expansion,

$$c_{ve}(T) = \frac{\pi^2}{3} k_B^2 D(\varepsilon_F) T \tag{2}$$

where c_{ve} is the electronic specific heat, k_B is the Boltzmann constant, ε_F is the Fermi energy, $D(\varepsilon)$ is the DOS, and T is temperature. However, this relation is violated at high temperatures, as in terrestrial planetary cores (Boness et al., 1986; Boness and Brown, 1990; Tsuchiya and Kawamura, 2002; Lin et al., 2008). The exact values can be calculated from numerical integration with the electronic density of state. Following Boness et al. (1986), we calculated the electronic specific heat from its definition:

$$c_{ve}(T) = \left(\frac{\partial u_e}{\partial T}\right)_v, \tag{3}$$

where u_e is the internal energy of electrons, which can be obtained from electron density of state $D(\varepsilon)$,

$$u_e(T) = \int \varepsilon f(\varepsilon, T) D(\varepsilon) \, \mathrm{d}\varepsilon \tag{4}$$

and $f(\varepsilon, T)$ is the Fermi-Dirac distribution function,

$$f(\varepsilon, T) = \frac{1}{\exp\left\{\frac{\epsilon - \mu(T)}{k_B T}\right\} + 1}. \tag{5}$$

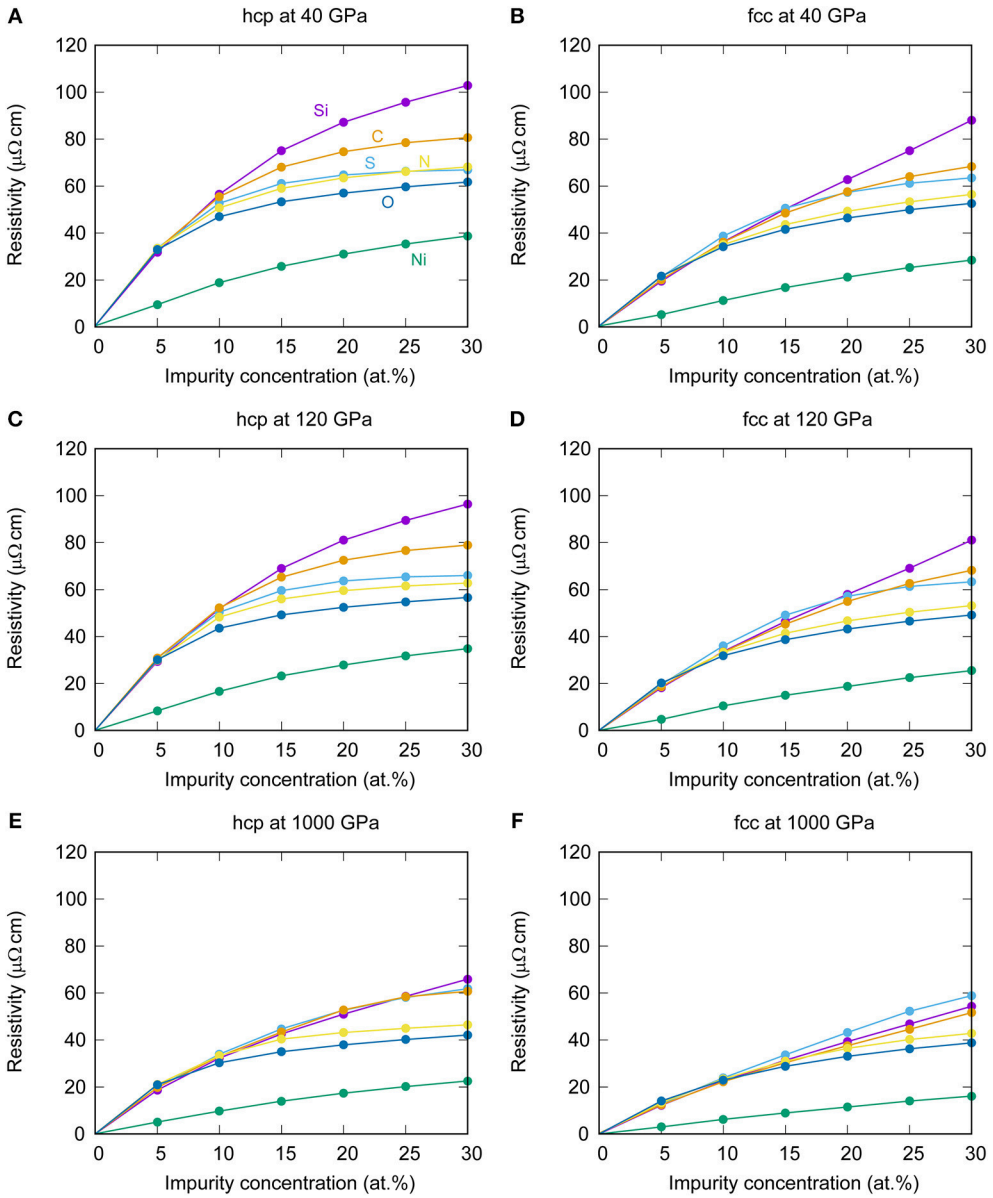

FIGURE 3 | Impurity resistivities of concentrated Fe based alloys **(A)** hcp at 40 GPa, **(B)** fcc at 40 GPa, **(C)** hcp at 120 GPa, **(D)** fcc at 120 GPa, **(E)** hcp at 1000 GPa, **(F)** fcc at 1000 GPa. The alloying elements are Si (purple), Ni (green), S (cyan), C (orange), N (yellow) and O (blue).

The chemical potential $\mu(T)$ is obtained from conservation of number of electrons (n_e),

$$n_e = \int f(\varepsilon, T)\, D(\varepsilon)\, \mathrm{d}\varepsilon. \tag{6}$$

Figure 7 shows the electron DOS of Fe-Si alloys and the corresponding electronic specific heat. In the DOSs of pure Fe, sharp peaks are observed around the Fermi level. However, these sharp peaks are broaden by the effect of alloying of impurity elements (Gomi et al., 2016). In the temperature dependence of the electronic specific heat of Fe and Fe-Si alloys (**Figures 7B,D,F,H**), the solid lines are obtained from numerical calculation (Equations 3–6), whereas the broken lines are calculated based on the Sommerfeld expansion (Equation 2). Boness et al. (1986) and Boness and Brown (1990) argued that both numerical and Sommerfeld values of the electronic specific heat show linear temperature dependences for hcp Fe for temperatures below ∼2,000 K. However, at higher than ∼2,000 K, the numerical value increases more rapidly than the Sommerfeld value, which indicates the violation of the Sommerfeld expansion. Our calculations for pure Fe broadly reproduce this temperature dependence (**Figure 7B**). Such a violation is widely observed in many metals at extremely high temperature (e.g., Tsuchiya and Kawamura, 2002; Lin et al., 2008). On the other hand, as Si content increases, the deviation from the Sommerfeld

expansion becomes small (**Figure 7**). This trend is also found in other Fe-light element alloys. Boness et al. (1986) argued that the relation between the deviation and the location of the Fermi level is within the sharp peaks of the DOS. In this sense, in highly concentrated alloys, these sharp peaks are smeared out because of impurity scattering. This is the reason why the deviation from the Sommerfeld expansion is relatively small in highly concentrated alloys. The Wiedemann-Franz law is based on the fact that the carrier of both of electric current and heat is conduction electrons. The pre-factor of linear temperature dependence attributed to the result of the Sommerfeld expansion, thus, Gomi and Hirose (2015) pointed out the deviation of the Lorenz number from its Sommerfeld value.

Figure 8 represents the deviation of the Lorenz number of Fe alloyed with Ni or light element candidates as function of temperature. The representative values at $V = 16.27$ Å^3 and $T = 4{,}000$ K or 5,500 K are summarized in the **Table 2**. Broadly speaking, Fe-Si alloys show relatively large Lorenz number, whereas the alloying O tend to decrease the Lorenz number. Also, the Lorenz number decreases with increasing impurity concentration and/or temperature. These trends are consistent with previous first-principles molecular dynamics calculation (de Koker et al., 2012).

It is worth mentioning about the relationship between energy-dependent conductivity $\sigma(\varepsilon)$ and the Lorenz number. The thermal conductivity of metals is represented by using the Onsager's kinetic coefficient,

$$K_n = \int \sigma(\varepsilon)(\varepsilon - \mu)^n \left(-\frac{\partial f}{\partial \varepsilon}\right) \mathrm{d}\varepsilon, \tag{7}$$

the electrical resistivity can be described as

$$\sigma = K_0, \tag{8}$$

and the thermal conductivity is

$$k = \frac{1}{e^2 T}\left(K_2 - \frac{K_1^2}{K_0}\right) \tag{9}$$

Applying the relaxation time approximation, the energy-dependent conductivity function can be expressed as

$$\sigma(\varepsilon) = \frac{e^2}{3} D(\varepsilon)\{v(\varepsilon)\}^2 \tau(\varepsilon) \tag{10}$$

where $D(\varepsilon)$ is the density of states, $v(\varepsilon)$ is the group velocity and $\tau(\varepsilon)$ is the relaxation-time. Pourovskii et al. (2017) focused on the energy dependence of the relaxation-time of electron-electron scattering. They conducted the dynamical mean-field theory (DMFT) calculations to incorporate the electron correlation effects and found that the hcp Fe exhibits a nearly perfect Fermi liquid (FL) behavior, which strongly decrease the Lorenz number and hence the thermal conductivity. Xu et al. (2018) also carried out DMFT calculations. Although they did not observe FL behavior at high temperature, the

TABLE 1 | Impurity resistivity of Fe-alloys at zero Kelvin.

χ (at.%)	$\rho_{hcp,\perp}$ (μΩcm)	$\rho_{hcp,\parallel}$ (μΩcm)	$\rho_{hcp,poly}$ (μΩcm)	ρ_{fcc} (μΩcm)
Fe-Si ALLOYS AT V = 9.55 Å^3/ATOM (P∼40 GPa).				
5	29.11	37.40	31.87	19.47
10	50.85	67.75	56.49	36.25
15	67.70	89.84	75.08	50.24
20	79.95	101.67	87.19	62.76
25	89.73	107.71	95.73	75.06
30	98.45	111.69	102.86	88.03
Fe-Ni ALLOYS				
5	8.38	11.61	9.46	5.26
10	18.04	20.50	18.86	11.27
15	24.84	27.84	25.84	16.75
20	29.55	34.00	31.03	21.25
25	33.34	39.21	35.30	25.32
30	36.36	43.43	38.72	28.45
Fe-S ALLOYS				
5	31.49	37.61	33.53	21.31
10	48.34	61.42	52.70	38.72
15	56.38	70.47	61.08	50.62
20	60.74	72.76	64.75	57.37
25	63.28	72.41	66.32	61.25
30	64.78	71.19	66.92	63.47
Fe-C ALLOYS				
5	30.86	37.45	33.05	20.13
10	50.75	64.91	55.47	36.18
15	62.30	79.62	68.07	48.49
20	69.36	85.28	74.66	57.64
25	74.22	86.90	78.45	64.05
30	77.70	86.65	80.68	68.38
Fe-N ALLOYS				
5	31.19	38.11	33.50	21.49
10	46.24	59.67	50.72	35.11
15	54.00	69.07	59.02	43.64
20	58.82	72.79	63.48	49.27
25	62.23	74.12	66.20	53.29
30	64.92	74.52	68.12	56.45
Fe-O ALLOYS				
5	30.32	38.16	32.94	21.61
10	42.43	56.01	46.96	34.20
15	48.33	63.30	53.32	41.58
20	52.20	66.62	57.00	46.41
25	55.22	68.53	59.65	49.97
30	57.61	69.85	61.69	52.65
Fe-Si ALLOYS AT V = 8.14 Å^3/ATOM (P ∼ 120 GPA).				
5	26.82	34.58	29.41	18.22
10	46.62	62.39	51.88	33.59
15	62.08	82.74	68.97	46.44
20	74.07	94.98	81.04	57.92
25	83.55	101.32	89.47	69.12
30	91.98	105.30	96.42	81.03

(Continued)

TABLE 1 | Continued

χ (at.%)	$\rho_{hcp,\perp}$ ($\mu\Omega$cm)	$\rho_{hcp,\parallel}$ ($\mu\Omega$cm)	$\rho_{hcp,poly}$ ($\mu\Omega$cm)	ρ_{fcc} ($\mu\Omega$cm)
Fe-Ni ALLOYS				
5	7.79	9.39	8.33	4.70
10	16.87	16.27	16.67	10.49
15	22.00	25.76	23.25	14.98
20	26.49	30.66	27.88	18.75
25	30.01	35.26	31.76	22.48
30	32.70	39.17	34.86	25.47
Fe-S ALLOYS				
5	28.88	34.75	30.83	19.52
10	46.10	58.91	50.37	36.04
15	54.75	69.09	59.53	49.10
20	59.49	72.01	63.66	57.15
25	62.24	71.80	65.43	61.32
30	63.87	70.34	66.03	63.30
Fe-C ALLOYS				
5	28.60	35.28	30.82	18.63
10	47.58	61.48	52.22	33.43
15	59.42	76.96	65.27	45.27
20	66.91	83.75	72.52	54.99
25	71.97	85.86	76.60	62.62
30	75.54	85.79	78.95	68.20
Fe-N ALLOYS				
5	29.59	30.56	29.92	19.99
10	44.10	56.67	48.29	33.21
15	51.22	65.48	55.97	41.39
20	55.21	68.22	59.54	46.65
25	57.88	68.77	61.51	50.34
30	59.92	68.56	62.80	53.16
Fe-O ALLOYS				
5	28.61	33.23	30.15	20.20
10	39.67	51.43	43.59	31.85
15	44.77	58.07	49.20	38.69
20	48.15	61.04	52.44	43.23
25	50.79	62.67	54.75	46.57
30	53.02	63.83	56.62	49.19
Fe-Si ALLOYS AT $V = 4.90$ Å^3/ATOM (P∼1,000 GPA).				
5	17.83	20.32	18.66	12.24
10	30.13	36.60	32.29	22.49
15	39.60	48.54	42.58	31.36
20	47.84	57.28	50.98	39.29
25	55.60	64.51	58.57	46.80
30	63.12	71.51	65.92	54.36
Fe-Ni ALLOYS				
5	4.87	5.38	5.04	2.98
10	9.48	10.18	9.71	6.21
15	13.60	14.67	13.95	8.92
20	16.66	18.79	17.37	11.46
25	19.14	22.27	20.19	14.00
30	21.29	25.03	22.53	16.10

(Continued)

TABLE 1 | Continued

χ (at.%)	$\rho_{hcp,\perp}$ ($\mu\Omega$cm)	$\rho_{hcp,\parallel}$ ($\mu\Omega$cm)	$\rho_{hcp,poly}$ ($\mu\Omega$cm)	ρ_{fcc} ($\mu\Omega$cm)
Fe-S ALLOYS				
5	19.03	21.11	19.72	12.88
10	31.78	38.30	33.95	23.85
15	41.40	51.35	44.72	33.72
20	48.72	60.63	52.69	43.18
25	53.94	66.41	58.09	52.23
30	58.19	69.22	61.87	58.84
Fe-C ALLOYS				
5	19.11	21.10	19.77	12.43
10	31.05	37.05	33.05	22.27
15	40.35	49.32	43.34	30.34
20	48.49	61.30	52.76	37.55
25	51.74	71.76	58.42	44.55
30	54.73	72.70	60.72	51.64
Fe-N ALLOYS				
5	20.48	22.30	21.08	13.31
10	31.37	37.34	33.36	23.45
15	37.51	46.04	40.35	31.00
20	39.96	49.63	43.18	36.42
25	41.96	50.92	44.95	40.18
30	44.01	51.44	46.48	42.79
Fe-O ALLOYS				
5	20.15	22.56	20.95	14.03
10	28.10	34.64	30.28	22.95
15	32.20	40.61	35.00	28.80
20	35.03	43.81	37.96	33.03
25	37.44	45.78	40.22	36.26
30	39.58	47.14	42.10	38.77

energy dependence of the relaxation-time reduced the Lorenz number by 20–45% of the Sommerfeld value. Yue and Hu (2018) calculated the thermal conductivity of hcp Fe based on the non-equilibrium ab initio molecular dynamics (NEAIMD) simulation, which simultaneously incorporates the electron-phonon and electron-electron scattering. On the other hand, the present study focused on the energy dependence of the DOS, via the electronic specific heat, which also relates to the energy dependent conductivity as Equation (10). These recent theoretical assessments on the Lorenz number have been partly motivated by the inconsistency of experimental results between the electrical resistivity measurement by Ohta et al. (2016) and the thermal conductivity measurements by Konôpková et al. (2016) (see also Dobson, 2016). The theoretical works are broadly consistent with the experimental result of low resistivity (Ohta et al., 2016), however, failed to reproduce the low thermal conductivity (Konôpková et al., 2016). Pourovskii et al. (2017) reported $k = 190$ W/m/K for hcp Fe at the inner core boundary (ICB) condition. Xu et al. (2018) suggested $k = 97$ W/m/K for hcp Fe at the CMB. Yue and Hu (2018) obtained $k \sim 190$ W/m/K for hcp Fe at both of the CMB and ICB. These values are significantly higher than $k = 33$ and 46 W/m/K at the CMB

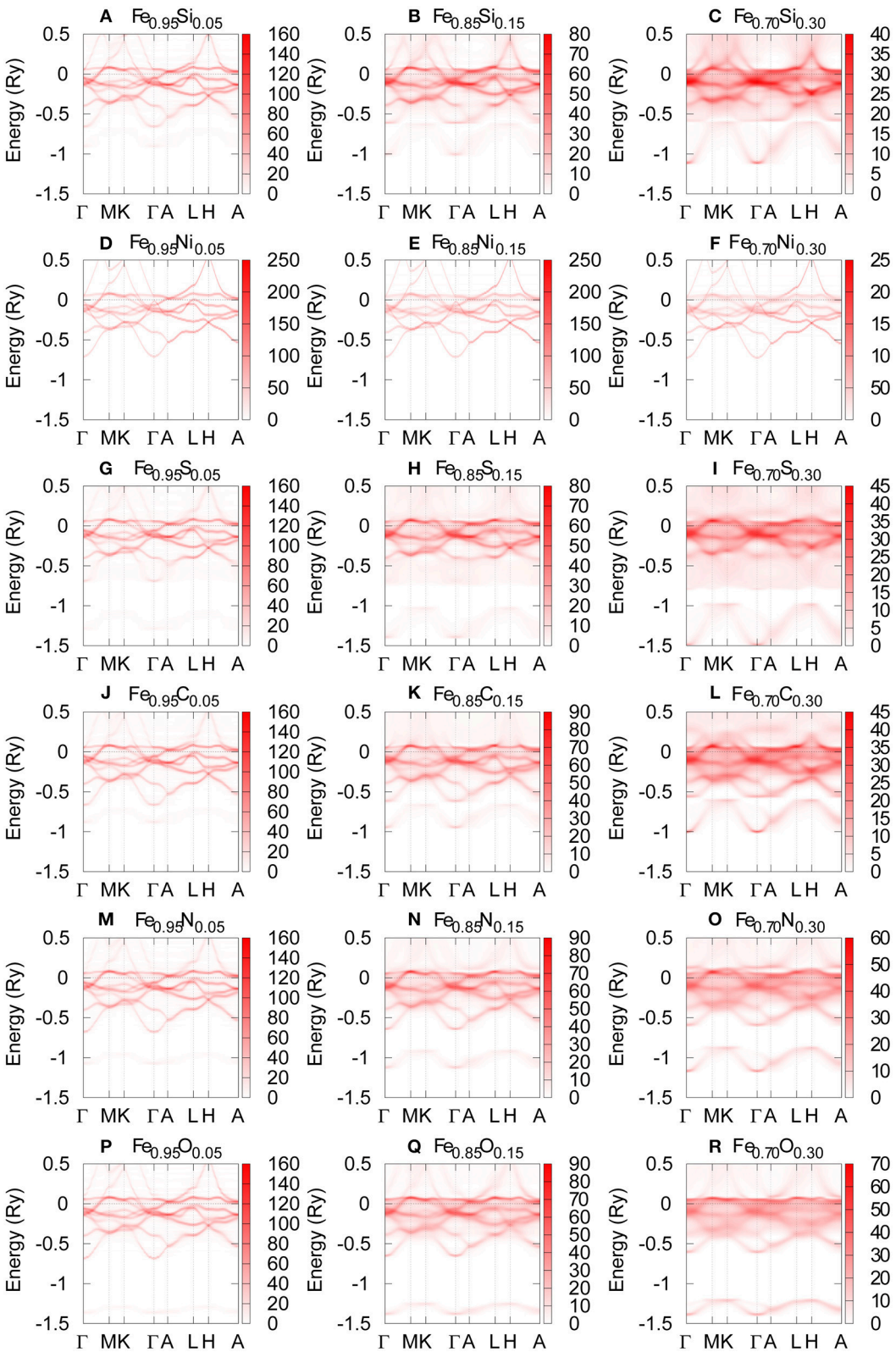

FIGURE 4 | The band structure of hcp Fe-based alloys with the volume of 19.10 Å^3 (~40 GPa). The Fermi energy is set to be 0 Ry. The compositions are **(A)** $Fe_{0.95}Si_{0.05}$, **(B)** $Fe_{0.85}Si_{0.15}$, **(C)** $Fe_{0.70}Si0.30$, **(D)** $Fe_{0.95}Ni_{0.05}$, **(E)** $Fe_{0.85}Ni_{0.15}$, **(F)** $Fe_{0.70}Ni_{0.30}$, **(G)** $Fe_{0.95}S_{0.05}$, **(H)** $Fe_{0.85}S_{0.15}$, **(I)** $Fe_{0.70}Si_{0.30}$, **(J)** $Fe_{0.95}C_{0.05}$, **(K)** $Fe_{0.85}C_{0.15}$, **(L)** $Fe_{0.70}C_{0.30}$, **(M)** $Fe_{0.95}N_{0.05}$, **(N)** $Fe_{0.85}N_{0.15}$, **(O)** $Fe_{0.70}N_{0.30}$, **(P)** $Fe_{0.95}O_{0.05}$, **(Q)** $Fe_{0.85}O_{0.15}$ and **(R)** $Fe_{0.70}O_{0.30}$.

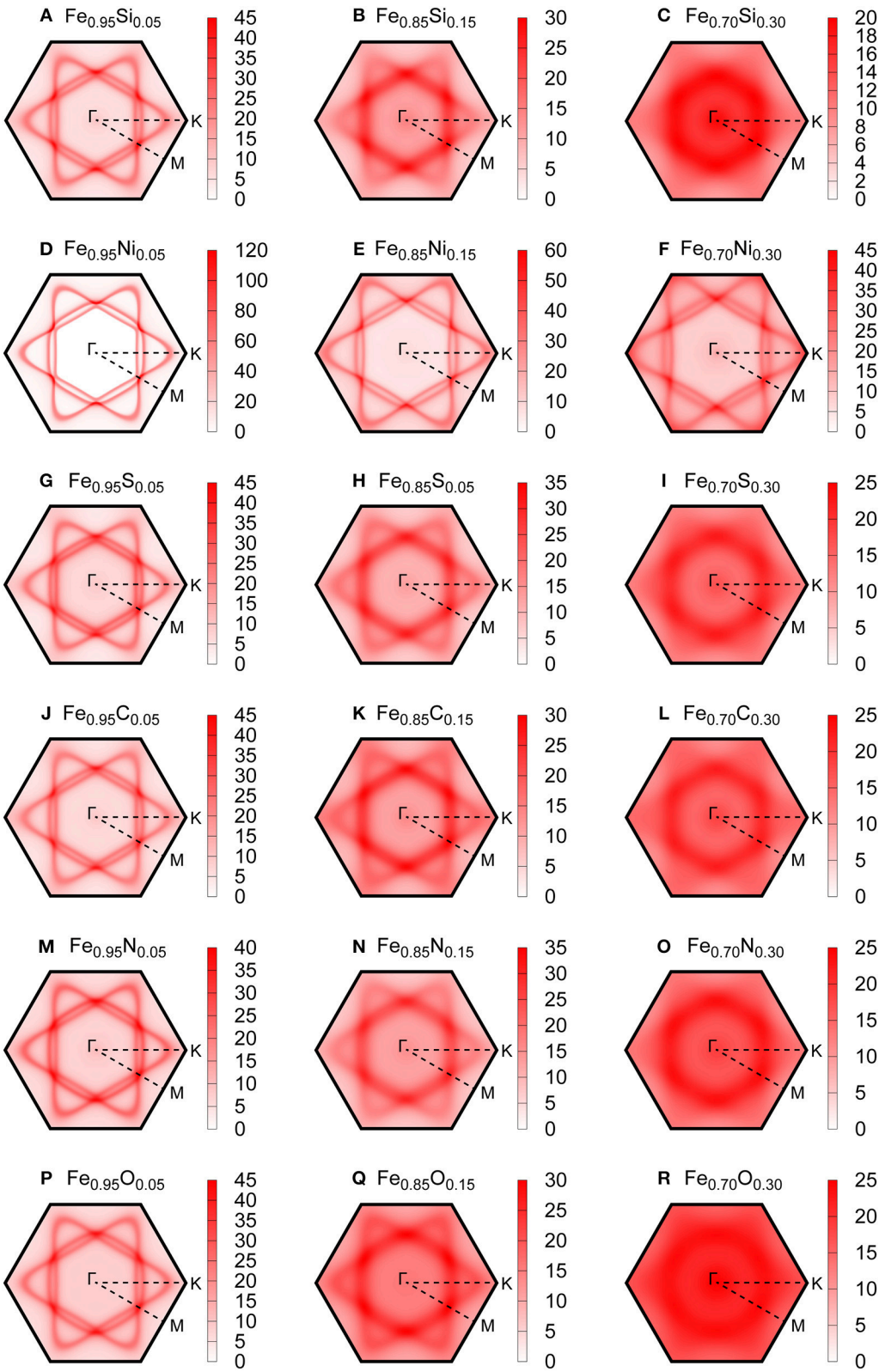

FIGURE 5 | The cross section of the Bloch spectral function at the Fermi energy (Fermi surface) of hcp Fe-based alloys with the volume of 19.10 Å^3 (~40 GPa). The compositions are **(A)** $Fe_{0.95}Si_{0.05}$, **(B)** $Fe_{0.85}Si_{0.15}$, **(C)** $Fe_{0.70}Si_{0.30}$, **(D)** $Fe_{0.95}Ni_{0.05}$, **(E)** $Fe_{0.85}Ni_{0.15}$, **(F)** $Fe_{0.70}Ni_{0.30}$, **(G)** $Fe_{0.95}S_{0.05}$, **(H)** $Fe_{0.85}S_{0.15}$, **(I)** $Fe_{0.70}Si_{0.30}$, **(J)** $Fe_{0.95}C_{0.05}$, **(K)** $Fe_{0.85}C_{0.15}$, **(L)** $Fe_{0.70}C_{0.30}$, **(M)** $Fe_{0.95}N_{0.05}$, **(N)** $Fe_{0.85}N_{0.15}$, **(O)** $Fe_{0.70}N_{0.30}$, **(P)** $Fe_{0.95}O_{0.05}$, **(Q)** $Fe_{0.85}O_{0.15}$ and **(R)** $Fe_{0.70}O_{0.30}$.

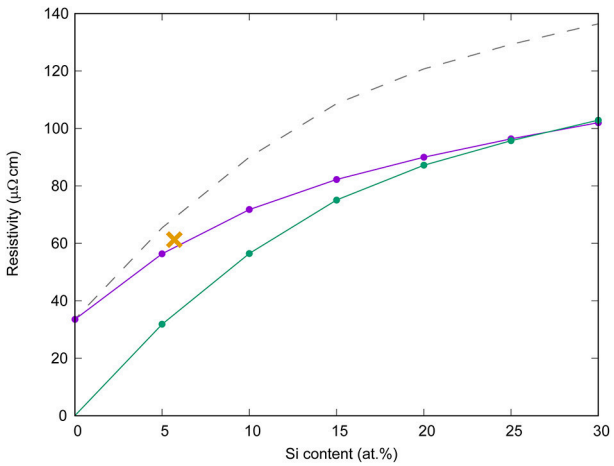

FIGURE 6 | Impurity resistivity of hcp $Fe_{100-x}Si_x$ binary (green) and $Fe_{95-x}Si_xS_5$ ternary (purple) alloys as a function of silicon content at the volume of 19.10 Å (~40 GPa) and zero Kelvin. Gray broken line shows the sum of the resistivity of $Fe_{95}S_5$ and $Fe_{100-x}Si_x$ (the Matthiessen's rule). The orange cross represents the resistivity of hcp $Fe_{89.3}Si_{5.7}S_{5.0}$ alloy measured at ~40 GPa and ambient temperature (Suehiro et al., 2017).

and ICB, respectively (Konôpková et al., 2016). This situation is not altered by considering the effect of alloying on the energy dependence of DOS obtained by this study, and the uncertainties due to the deviation from the Sommerfeld value may be smaller

$$\rho_{\mathrm{ph,ideal}}(V,T) = B(V)\left(\frac{T}{\Theta_D(V)}\right)^5 \int_0^{\frac{\Theta_D(V)}{T}} \frac{x^5 \mathrm{d}x}{(\exp(x)-1)(1-\exp(-x))} \quad (14)$$

than 30% for the Earth's core (see **Table 2**). Therefore, we conclude that, even though it is a not good approximation for pure Fe, the Sommerfeld value is a good proxy of the Lorenz number of the planetary cores.

ELECTRICAL RESISTIVITY AND THERMAL CONDUCTIVITY OF THE EARTH'S CORE

In the section Concentrated Alloys, we computed the impurity resistivity of Ni and light element candidates (C, N, O, Si, and S). In the section Electronic Specific Heat and Wiedemann-Franz Law, we computed the electron DOS of Fe-based alloys to estimate the Lorenz number, which varies with pressure, temperature, impurity species and concentration. In this section, we first calculated the total resistivity of the Earth's core by combining the impurity resistivity and phonon-contributed resistivity following Gomi et al. (2016). Then, we estimated the thermal conductivity via the Wiedemann-Franz law (Equation 1) using the present resistivity and the Lorenz number.

The total electrical resistivity was calculated from the Cote and Meisel (1978) model combined with the present impurity resistivity and the phonon-contributed resistivity modeled by Gomi et al. (2013, 2016, 2018).

$$\rho_{\mathrm{tot}}(V,T) = \left(1 - \frac{\rho_{\mathrm{tot}}(V,T)}{\rho_{\mathrm{sat}}(V)}\right)\rho_{\mathrm{ph,ideal}}(V,T) + \rho_{\mathrm{imp}}(V)\exp(-2W(V,T)) \quad (11)$$

where $\rho_{\mathrm{tot}}(V, T)$ is the total electrical resistivity, $\rho_{\mathrm{sat}}(V)$ is the saturation resistivity, $\rho_{\mathrm{ph,ideal}}(V, T)$ is the "ideal" phonon-contributed resistivity, which neglects the effect of the resistivity saturation, $\rho_{\mathrm{imp}}(V)$ is the impurity resistivity, and $\exp(-2W(V, T))$ is the Debye Waller factor, which gives the temperature dependence of the impurity resistivity. Because the resistivity saturation phenomena occurs when the mean free path becomes comparable to the inter atomic distance, the saturation resistivity may scale by $V^{1/3}$ (Gomi et al., 2013)

$$\rho_{\mathrm{sat}}(V) = \rho_{\mathrm{sat}}(V_0)\left(\frac{V}{V_0}\right)^{\frac{1}{3}} \quad (12)$$

where $\rho_{\mathrm{sat}}(V_0) = 1.68 \times 10^{-6}$ Ωm is the saturation resistivity of bcc and fcc Fe-based alloys (Bohnenkamp et al., 2002). The phonon-contributed resistivity of hcp Fe at ambient temperature was obtained from previous measurement (Gomi et al., 2013) as

$$\rho(V, 300\ \mathrm{K}) = 5.26 \times 10^{-9} \times \left(1.24 - \frac{V}{V_0}\right)^{-3.21} \ \Omega\mathrm{m} \quad (13)$$

The "ideal" phonon-contributed resistivity can be extrapolated from the ambient temperature resistivity by using the Bloch-Grüneisen formula,

where $B(V)$ is the material constant, which can be obtained from Equation (13), and $\Theta_D(V)$ is the Debye temperature (Dewaele et al., 2006). Assuming the Debye model, $W(V, T)$ can be calculated as Markowitz (1977)

$$W(V,T) = \frac{3\hbar^2K^2T^2}{2mk_B\Theta_D^3}\int_0^{\frac{\Theta_D}{T}}\left(\frac{1}{\exp(x)-1}+\frac{1}{2}\right)x\mathrm{d}x \quad (15)$$

where h is the reduced Planck's constant (the Dirac's constant), m is the atomic mass, $K(V) \sim \pi/a$ is the electronic wave vector transfer, where a is the lattice parameter. The impurity resistivity $\rho_{\mathrm{imp}}(V)$ is obtained from the present DFT calculations of hcp Fe-based alloys. The resistivity of the solid Fe alloy depends on the crystal structure (**Figures 1**, **3**). The crystal structure of Fe at the Earth's core pressure is known to be hcp (Tateno et al., 2010; Smith et al., 2018). However, its stability field may be influenced by further compression (Stixrude, 2012). Alloying elements also affect the crystal structure: Ni extends the stability field of fcc phase (Kuwayama et al., 2008), H stabilizes dhcp structure (Gomi et al., 2018) and Si favors B2 or body-centered cubic (bcc) structure (Tateno et al., 2015; Ozawa et al., 2016). Recent shock compression experiments on Fe with 15 wt.% Si suggest that bcc structure is stable at the center of super-Earth with three times Earth mass (Wicks et al., 2018). Although the solid phase crystal structure is important, we simply assumed that the hcp Fe

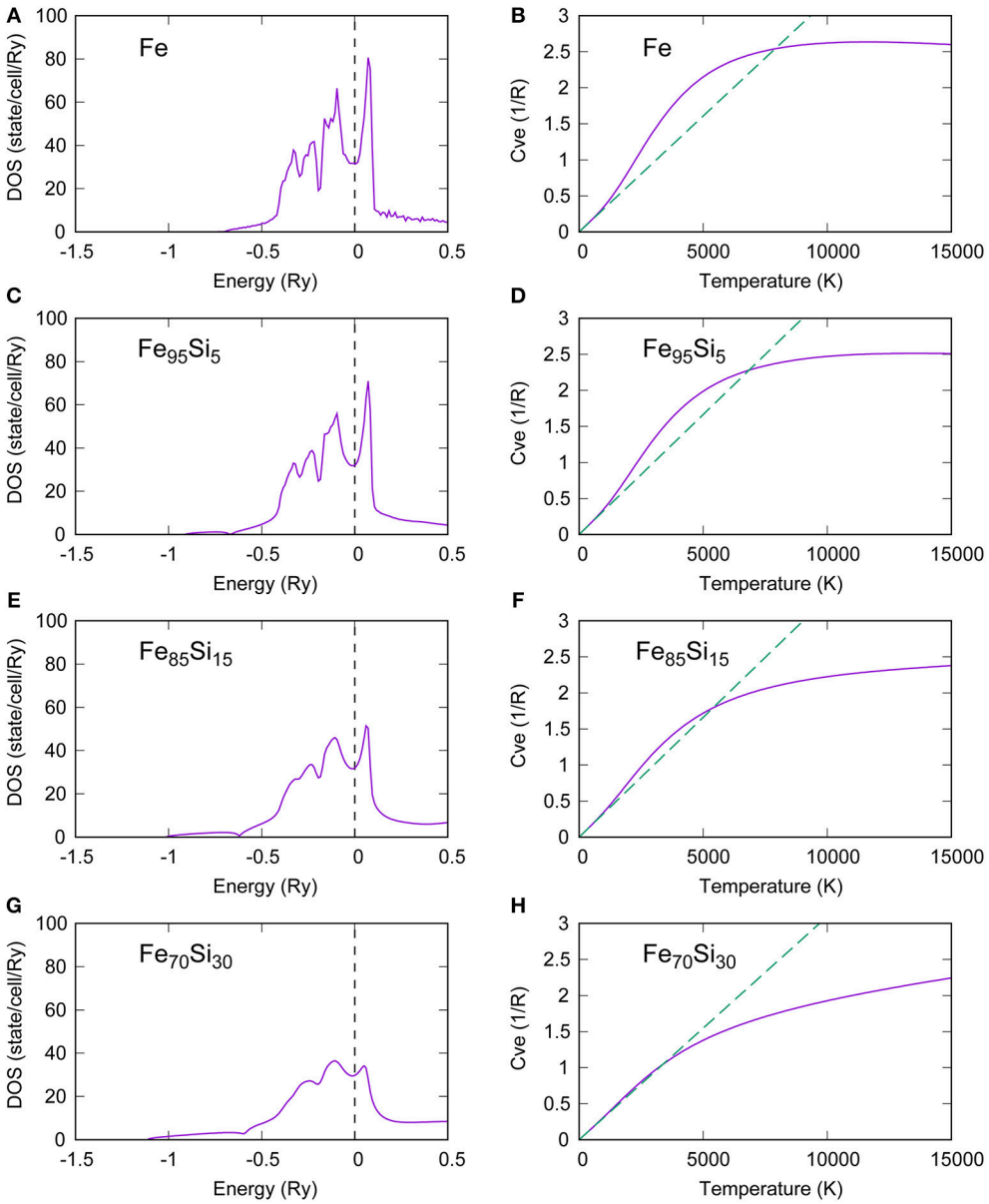

FIGURE 7 | Density of states (DOS) **(A,C,E,G)** and corresponding electronic specific heat **(B,D,F,H)**. Green broken lines represent the electronic specific heat obtained from the Sommerfeld expansion.

alloys are good proxy. The spin disorder scattering is potentially important (Drchal et al., 2017), especially for small planets with hydrogen containing core (Gomi et al., 2018). But in this study, we neglect this effect. It is known that the resistivity change upon melting is very small for transition metals at 1 bar (e.g., Van Zytveld, 1980). Van Zytveld (1980) reported that the resistivity increase upon melting is ∼8% for Fe. The ratio of resistivity between liquid and solid phase at the melting temperature, ρ_L/ρ_S, is generally very close to unity for transition metals, but it is also known to be ∼1.5 for alkali metals and ∼2 for noble metals (Mott, 1934; Cusack and Enderby, 1960; Faber, 1972). This systematic trend was also confirmed by Secco and co-workers at high pressure (Ezenwa and Secco, 2017a,b,c; Ezenwa et al., 2017; Silber et al., 2017, 2018). Mott (1934) considered that the resistivity change upon melting is related to the entropy of fusion, and semi-empirically formulated as follows:

$$\frac{\rho_L}{\rho_S} = \exp\left(\frac{2S_m}{3R}\right) \tag{16}$$

where S_m is the entropy of fusion and R is the gas constant. This model shows good agreement with large resistivity ratio observed in alkali and noble metals, however, it cannot account the small degree of the resistivity jump of transition metals. One possible

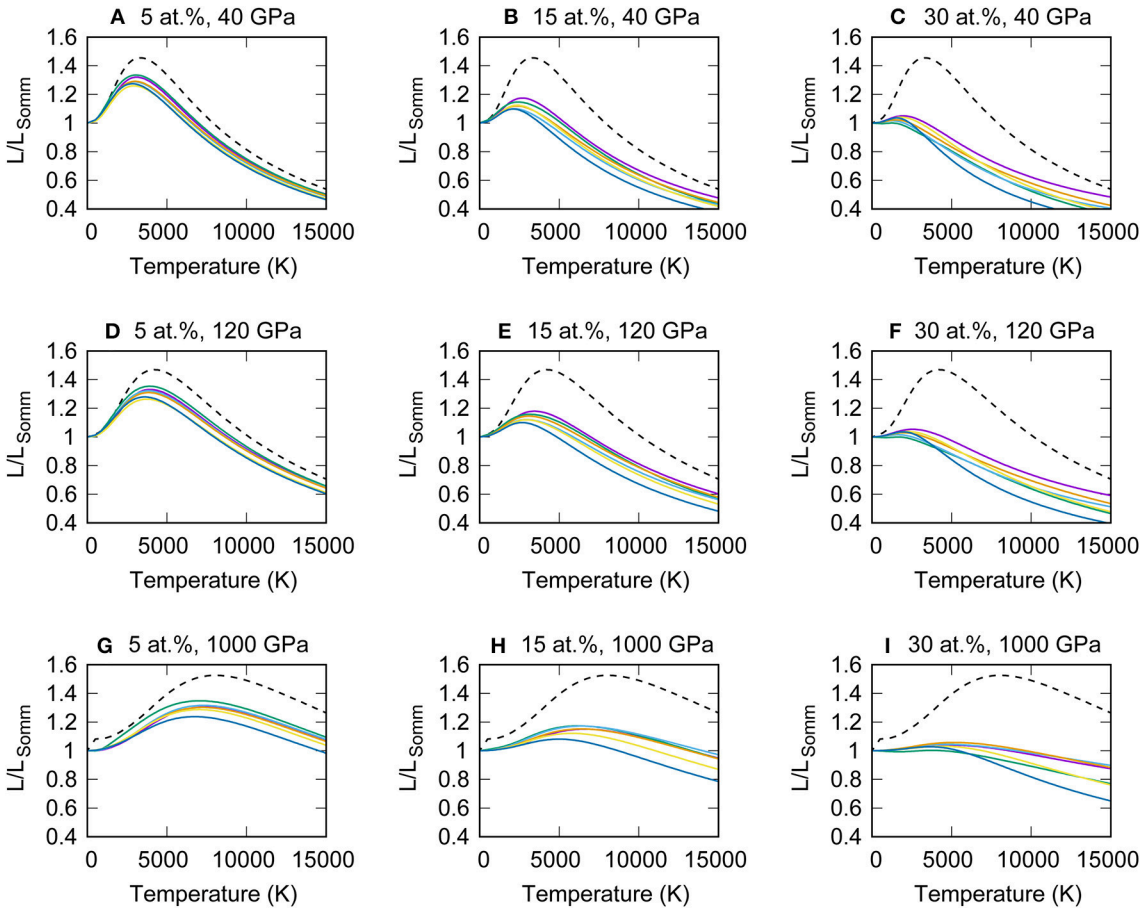

FIGURE 8 | The deviation of the Lorenz number from the Sommerfeld value predicted by the electronic specific heat of hcp $Fe_{0.95}X_{0.05}$, $Fe_{0.85}X_{0.15}$ and $Fe_{0.70}X_{0.30}$, where X is Si (purple), Ni (green), S (cyan), C (orange), N (yellow) and O (blue) at the volume of $V = 19.10$ Å^3 ($P \sim 40$ GPa at 300 K) **(A–C)**, 16.27 Å^3 ($P \sim 120$ GPa at 300 K) **(D–F)** and 9.80 Å^3 ($P \sim 1{,}000$ GPa at 300 K) **(G–I)**. Black broken lines are pure Fe for comparison.

modification of this model is the incorporation of the effect of the resistivity saturation (Mott, 1972); the solid transition metals exhibit already large electrical resistivity at the melting temperature, which is comparable to the saturation resistivity. As a result the saturation suppresses the resistivity jump upon melting. The other model was proposed by Wagle and Steinle-Neumann (2018) based on the Ziman approximation (Ziman, 1961), which yields the following equation

$$\frac{\rho_L}{\rho_S} = \left(\frac{K_{T,L}}{K_{T,S}}\right)^{-1} \left(\frac{\rho_L^{\mathrm{den}}}{\rho_S^{\mathrm{den}}}\right)^{-2} \tag{17}$$

where $K_{T,L}$ and $K_{T,S}$ are the isothermal bulk modulus, ρ_L^{den} and ρ_S^{den} are the density of liquid and solid metal, respectively. This model can reasonably reproduce the small jump of transition metals, as well as the large contrast of simple metals (e.g., Na and Al). However, it systematically underestimates the resistivity ratio of closed d-shell metals (Zn and noble metals). These two models may be verified by investigating the pressure dependence of the resistivity ratio. If the former model is correct, the resistivity ratio may increase with increasing pressure, because the resistivity of hcp Fe decreases faster than the $V^{1/3}$ dependence of the saturation resistivity (Gomi et al., 2013). On the other hands, if the latter model is correct, the resistivity ratio may not significantly change (Wagle and Steinle-Neumann, 2018). The results of high-pressure melting experiments are still controversial. Secco and Schloessin (1989), Silber et al. (2018), and Ezenwa and Secco (2017c) measured the resistivity of Fe and Co, respectively. These measurements on transition metals verified the small degree of the resistivity jump upon melting even at high pressure 12 GPa. Deng et al. (2013) also measured the resistivity of Fe, but their results seem to have large resistivity enhancement upon melting at the identical pressure. Pommier (2018) reproduced the Deng et al. (2013)'s results at 4.5 GPa. Ohta et al. (2016) carried out the melting experiments in a laser-heated diamond-anvil cell showing ~20% increase upon melting at 51 GPa. Bi et al. (2002) measured the electrical resistivity of shock induced melting of Fe with melt fraction of 0.7 at 208 GPa. The resultant resistivity values follow the general trend obtained in the solid phase region along the Hugoniot, which suggests the absence of large resistivity change upon melting. In this

TABLE 2 | Transport properties of Fe-alloys at the Earth's outer core ($V = 16.27$ Å^3).

χ (at.%)	$T = 4{,}000$ K			$T = 5{,}500$ K		
	ρ (μΩcm)	L/L_{somm}	k (W/m/K)	ρ (μΩcm)	L/L_{somm}	k (W/m/K)
Fe-Si ALLOYS						
5	70.92	1.331	183.41	79.93	1.268	213.21
10	85.00	1.241	142.62	92.20	1.172	170.74
15	95.71	1.172	119.67	101.53	1.099	145.48
20	103.27	1.116	105.59	108.12	1.042	129.46
25	108.56	1.065	95.85	112.72	0.991	118.13
30	112.91	1.021	88.36	116.51	0.949	109.41
Fe-Ni ALLOYS						
5	57.71	1.354	229.24	68.43	1.292	253.68
10	62.94	1.238	192.17	72.98	1.171	215.55
15	67.06	1.145	166.83	76.57	1.077	188.95
20	69.96	1.058	147.76	79.10	0.990	168.14
25	72.39	0.985	132.92	81.22	0.916	151.62
30	74.34	0.923	121.29	82.91	0.854	138.37
Fe-S ALLOYS						
5	71.81	1.321	179.80	80.71	1.255	208.93
10	84.05	1.203	139.80	91.38	1.129	166.04
15	89.79	1.099	119.60	96.38	1.023	142.64
20	92.38	1.025	108.41	98.63	0.947	129.01
25	93.49	0.973	101.69	99.60	0.894	120.59
30	93.87	0.935	97.31	99.93	0.856	115.07
Fe-C ALLOYS						
5	71.80	1.309	178.16	80.70	1.245	207.24
10	85.21	1.205	138.22	92.39	1.135	165.01
15	93.39	1.128	118.08	99.51	1.055	142.39
20	97.93	1.063	106.07	103.47	0.988	128.32
25	100.49	1.011	98.28	105.70	0.936	118.94
30	101.96	0.970	93.00	106.98	0.896	112.53
Fe-N ALLOYS						
5	71.24	1.262	173.05	80.21	1.194	199.99
10	82.75	1.162	137.23	90.24	1.084	161.44
15	87.56	1.095	122.17	94.43	1.011	143.87
20	89.80	1.046	113.85	96.38	0.960	133.77
25	91.04	1.011	108.54	97.46	0.924	127.35
30	91.84	0.985	104.84	98.16	0.899	123.05
Fe-O ALLOYS						
5	71.38	1.274	174.43	80.34	1.196	199.98
10	79.81	1.142	139.85	87.68	1.050	160.93
15	83.32	1.055	123.71	90.74	0.953	141.14
20	85.35	0.997	114.11	92.51	0.887	128.87
25	86.80	0.955	107.55	93.77	0.839	120.25
30	87.97	0.924	102.69	94.79	0.803	113.76

study, we assume that the resistivity difference between liquid and solid Fe-alloys is very small. This may be good approximation, because, even if the former model is correct, the total core resistivity may be close to the saturation resistivity because of large impurity resistivity. Finally, the thermal conductivity is calculated via the Wiedemann-Franz law (Equation 1) with the predicted Lorenz number from the electronic specific heat (see section Electronic Specific Heat and Wiedemann-Franz Law).

Figure 9 illustrates the electrical resistivity of Fe alloyed with 5, 15, or 30 atomic % impurity elements at the volume of 19.10, 16.27, and 9.80 Å^3. The electrical resistivity increases with increasing impurity concentration. The impurity resistivity of Si is the largest and that of Ni is the smallest, as already discussed in the section Concentrated Alloys. The electrical resistivity is also enhanced at high temperatures following the Bloch-Grüneisen formula (Equation 14). At high resistivity ∼100 μΩcm, the total resistivity saturates. The saturation resistivity decreases with

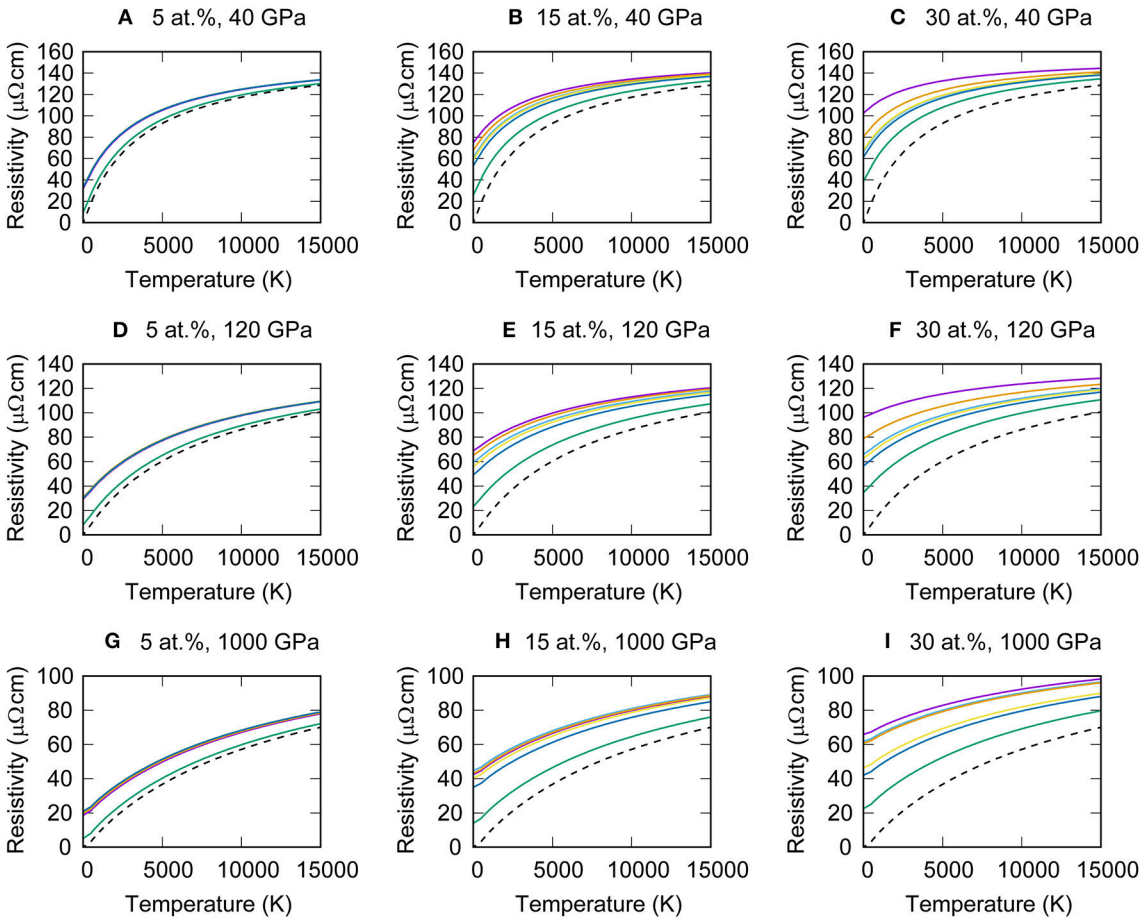

FIGURE 9 | Electrical resistivity of hcp $Fe_{0.95}X_{0.05}$, $Fe_{0.85}X_{0.15}$, and $Fe_{0.70}X_{0.30}$, where X is Si (purple), Ni (green), S (cyan), C (orange), N (yellow), and O (blue) at the volume of $V = 19.10$ Å^3 (P∼40 GPa at 300 K) **(A–C)**, 16.27 Å^3 ($P \sim 120$ GPa at 300 K) **(D–F)**, and 9.80 Å^3 ($P \sim 1{,}000$ GPa at 300 K) **(G–I)**. Black broken lines are pure Fe for comparison.

increasing pressure via the Equation (12). **Figure 10** represents the thermal conductivity of Fe alloyed with 5, 15, or 30 atomic % impurity elements at the volume of 19.10, 16.27, and 9.80 Å^3. The temperature and impurity concentration dependences of the thermal conductivity are more complicated compared with the electrical resistivity. At low temperatures smaller than ∼5,000 K, the thermal conductivities of Fe based alloys have positive temperature coefficient because of the following reason. First, it should be noted that the Wiedemann-Franz law (Equation 1) predicts the linear temperature dependence, if the electrical resistivity and the Lorenz number are independent of temperature. This condition is nearly satisfied for the electrical resistivity of Fe-light element alloys because, at low temperatures, the impurity resistivity is predominant. Also, as shown in **Figure 8**, the Lorenz number exhibits positive temperature coefficient. Combining these two temperature effects, the thermal conductivity initially increases with increasing temperature. Above 5,000 K, the thermal conductivity becomes insensitive to temperature. The temperature coefficient of the resistivity becomes small due to the resistivity saturation (**Figure 9**), whereas the Lorenz number tends to decrease with increasing temperature (**Figure 8**). Therefore, the effects of temperature on the Lorenz number and the linear temperature factor in the Wiedemann-Franz law are canceled out, which result in the nearly constant thermal conductivity at high temperature. **Table 2** summarized the electrical resistivity, the Lorenz number and the thermal conductivity of Fe alloys at $V = 16.27$ Å^3 and $T = 4{,}000$ or 5,500 K, which correspond to the Earth's outer core conditions. Considering the compositional effects, our preferred thermal conductivity is higher than ∼90 W/m/K.

HEAT FLUX AT THE CMB OF SUPER-EARTHS

The recent developments of astronomical observation can allow to find many terrestrial exoplanets. The exoplanets with the masses of <10 times the Earth's mass (M_E) are so-called super-Earths (e.g., Valencia et al., 2007; Charbonneau et al., 2009). Some of these planets locate within the habitable zone, suggesting the presence of liquid water at the surface of the planet (e.g., Anglada-Escudé et al., 2012; Gillon et al., 2017). In term of the

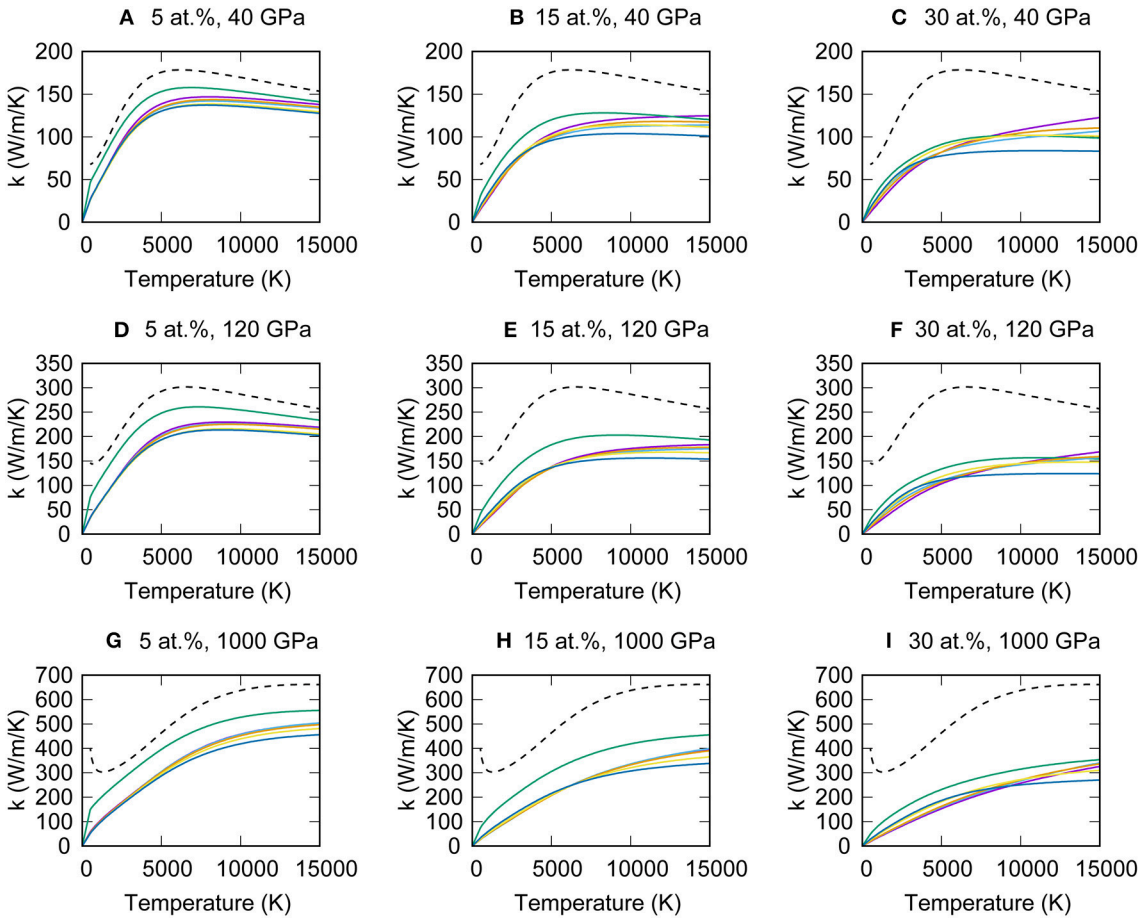

FIGURE 10 | Thermal conductivity of hcp $Fe_{0.95}X_{0.05}$, $Fe_{0.85}X_{0.15}$, and $Fe_{0.70}X_{0.30}$, where X is Si (purple), Ni (green), S (cyan), C (orange), N (yellow), and O (blue) at the volume of $V = 19.10$ Å^3 (P∼40 GPa at 300 K) **(A–C)**, 16.27 Å^3 (P∼120 GPa at 300 K) **(D–F)**, and 9.80 Å^3 (P∼1,000 GPa at 300 K) **(G–I)**. Black broken lines are pure Fe for comparison.

surface habitability, the existence of the global magnetic fields is a necessary condition. The planetary magnetic field is generated via the geodynamo driven by thermal and/or chemical convective motion in the liquid outer core. If super-Earths have thermally driven geodynamo, the heat flux through the bottom of mantle, q_{CMB}, must be higher than the conductive heat flux along the adiabatic temperature gradient at the top of their core

$$q_s = k\left(\frac{\partial T}{\partial r}\right)_S = k\frac{\rho^{\mathrm{den}} g\gamma}{K_S}T \tag{18}$$

where k is the thermal conductivity, ρ^{den} is the density, g is the gravity, γ is the Grüneisen parameter and K_S is the adiabatic bulk modulus. Morard et al. (2011) suggested the absence of liquid core in the super Earth from the first-principles calculation of melting temperature of Fe. Many studies investigated the mantle convection in the super-Earths with varying physical quantities. The effects of depth increasing mantle viscosity (Tackley et al., 2013), thermal conductivity (Kameyama and Yamamoto, 2018) and compressibility (CíŽková et al., 2017) suppress the mantle convection in the deep portion of the super-Earths. The phase transitions of mantle materials with negative Clapeyron slope also contribute as a stratification of the mantle (Umemoto et al., 2006; Tsuchiya and Tsuchiya, 2011; McWilliams et al., 2012). On the other hand, Stixrude (2014) argued the energetics of accretion, giant impact and core formation events of the super-Earths, and concluded that the mantle convection is sufficiently vigorous to sustain the geodynamo. Miyagoshi et al. (2017) demonstrated the occurrence of thermal convection in the mantle of super-Earth from numerical mantle convection simulations with initially hot shallow mantle conditions, which is expected due to giant impacts. Tachinami et al. (2011) calculated the thermal evolution of the cores of super-Earths coupled with the mixing-length theory for the mantle convective heat transfer, in order to discuss the possibility of the thermally driven geodynamo. However, they adopted the core thermal conductivity of $k = 40$ W/m/K, which is one order smaller than the present estimate for the 10 Earth mass planet. The purpose of this section is to calculate the conductive heat flux at the top of the liquid core of super-Earths with high thermal conductivity inferred from the previous sections.

To calculate the energy balance in the super-Earths, one-dimensional density and temperature model is required (e.g., Valencia et al., 2006; Papuc and Davies, 2008; Tachinami et al., 2011). In this study, we read the density profile of super-Earths from Figure 1 of Tachinami et al. (2011). Hence, the planetary masses of our model are 0.1, 0.2, 0.5, 1, 2, 5, and 10 times to the Earth's mass (M_E). The gravity profile can be calculated from

$$g(r) = G\frac{M(r)}{r^2} \tag{19}$$

where $G = 6.67408 \times 10^{-11}$ m^3/kg/s^2 is the gravitational constant, $M(r)$ is the inner mass of the radial position r. The mass of the inner core M_c is assumed to be 30% of the planetary mass M_p. The pressure-density relation at the reference temperature $T_0 = 300$ K is given by the Vinet equation of state (EOS):

$$P(\rho^{\mathrm{den}}, T_0) = 3K_0\left(\frac{\rho_0^{\mathrm{den}}}{\rho^{\mathrm{den}}}\right)^{-\frac{2}{3}}\left\{1-\left(\frac{\rho_0^{\mathrm{den}}}{\rho^{\mathrm{den}}}\right)^{\frac{1}{3}}\right\} \exp\left[\frac{3}{2}\left(K_0{}' - 1\right)\left\{1-\left(\frac{\rho_0^{\mathrm{den}}}{\rho^{\mathrm{den}}}\right)^{\frac{1}{3}}\right\}\right] \tag{20}$$

where ρ_0^{den}, K_0 and K'_0 are density, bulk modulus and its pressure differentiation at zero pressure, respectively. These parameters are given as $\rho_{0,Fe}^{\mathrm{den}} = 8{,}300$ kg/m^3, $K_{0,\mathrm{Fe}} = 164.8$ GPa and $K'_{0,\mathrm{Fe}} = 5.33$ for Fe liquid, whereas $\rho_{0,\mathrm{FeS}}^{\mathrm{den}} = 5{,}330$ kg/m^3, $K_{0,\mathrm{FeS}} = 126$ GPa and $K'_{0,\mathrm{FeS}} = 4.8$ for FeS liquid (see Tachinami et al., 2011 and references therein). The EOS parameters for the outer core of Fe-FeS liquid mixture are given as function of mass fraction of S as

$$x_{\mathrm{FeS}} = x_S\frac{Z_{\mathrm{Fe}} + Z_S}{Z_S} \tag{21}$$

$$\rho_{0,\mathrm{OC}}^{\mathrm{den}} = \left(\frac{1-x_{\mathrm{FeS}}}{\rho_{0,\mathrm{Fe}}^{\mathrm{den}}} + \frac{x_{\mathrm{FeS}}}{\rho_{0,\mathrm{FeS}}^{\mathrm{den}}}\right)^{-1} \tag{22}$$

$$K_{0,\mathrm{OC}} = \frac{1}{\rho_{0,\mathrm{OC}}^{\mathrm{den}}}\frac{1}{\frac{1-x_{\mathrm{FeS}}}{\rho_{0,\mathrm{Fe}}^{\mathrm{den}}}\frac{1}{K_{0,\mathrm{Fe}}} + \frac{x_{\mathrm{FeS}}}{\rho_{0,\mathrm{FeS}}^{\mathrm{den}}}\frac{1}{K_{\mathrm{FeS}}}} \tag{23}$$

$$K'_{0,\mathrm{OC}} = -1 + \rho_{0,\mathrm{Fe}}^{\mathrm{den}}K_{0,\mathrm{OC}}^2\left(\frac{1-x_{\mathrm{FeS}}}{\rho_{0,\mathrm{Fe}}^{\mathrm{den}}}\frac{1+K'_{0,\mathrm{Fe}}}{K_{0,\mathrm{Fe}}^2} + \frac{x_{\mathrm{FeS}}}{\rho_{0,\mathrm{FeS}}^{\mathrm{den}}}\frac{1+K'_{0,\mathrm{FeS}}}{K_{0,\mathrm{FeS}}^2}\right) \tag{24}$$

where x_{Fe}, x_{FeS} are mass fractions of Fe and FeS, $Z_{\mathrm{Fe}} = 55.845$ and $Z_S = 32.065$ are mass of Fe and S. Following Tachinami et al. (2011), we assumed the bulk S content is set to be $x_{0S} = 0.1$ and also assumed that S completely partition into the outer core, the mass fraction of S can be calculated as

$$x_S = x_{0S}\frac{M_c}{M_c - M_{ic}} \tag{25}$$

where M_c and M_{ic} are the mass of bulk and inner core, respectively. In this study, we only considered the situation that $M_{ic} = 0.06\ M_c$, which is close to the present Earth's value. This leads $x_S = 0.10638$. Our assumption of pure Fe inner core may look unrealistic, however, note that the present heat flux calculation does not refer the chemical composition of the inner core. The isothermal bulk modulus at the reference temperature is obtained by differentiation of the Vinet density-pressure equation of states:

$$\begin{aligned} K_T\left(\rho^{\mathrm{den}}, T_0\right) = &\left\{2K_0\left[1-\left(\frac{\rho_0^{\mathrm{den}}}{\rho^{\mathrm{den}}}\right)^{\frac{1}{3}}\right]\left(\frac{\rho^{\mathrm{den}}}{\rho_0^{\mathrm{den}}}\right)^{\frac{2}{3}}\right. \\ &+ \frac{3}{2}\left(K'-1\right)K_0\left[1-\left(\frac{\rho_0^{\mathrm{den}}}{\rho^{\mathrm{den}}}\right)^{\frac{1}{3}}\right]\left(\frac{\rho^{\mathrm{den}}}{\rho_0^{\mathrm{den}}}\right)^{\frac{1}{3}} \\ &\left.+ K_0\left(\frac{\rho^{\mathrm{den}}}{\rho_0^{\mathrm{den}}}\right)^{\frac{1}{3}}\right\}\exp\left\{\frac{3}{2}\left(K'-1\right)\left[1-\left(\frac{\rho_0^{\mathrm{den}}}{\rho^{\mathrm{den}}}\right)^{\frac{1}{3}}\right]\right\} \end{aligned} \tag{26}$$

The thermal effect on the equation of states is incorporated as the thermal corrections by the Mie-Grüneisen equation with the Debye model as:

$$P\left(\rho^{\mathrm{den}}, T\right) = P\left(\rho^{\mathrm{den}}, T_0\right) + \Delta P_{\mathrm{th}}(\rho^{\mathrm{den}}, T) \tag{27}$$

$$\Delta P_{\mathrm{th}}\left(\rho^{\mathrm{den}}, T\right) = \left(\frac{\gamma}{V}\right)\left(E_{th}\left(\rho^{\mathrm{den}},\ T\right) - E_{th}(\rho^{\mathrm{den}}, T_0)\right) \tag{28}$$

Similarly, the thermal effect on the isothermal bulk modulus is represented as follows (Stixrude and Lithgow-Bertelloni, 2005):

$$K_T\left(\rho^{\mathrm{den}}, T\right) = K_T\left(\rho^{\mathrm{den}}, T_0\right) + \Delta K_T(\rho^{\mathrm{den}}, T) \tag{29}$$

$$\begin{aligned} \Delta K_T\left(\rho^{\mathrm{den}}, T\right) = &\left(\gamma + 1 - q\right)\frac{\gamma}{V}\left(E_{th}\left(\rho^{\mathrm{den}}, T\right)\right. \\ &- E_{th}\left(\rho^{\mathrm{den}}, T_0\right)\Big) - \frac{\gamma^2}{V}\left(TC_v\left(\rho^{\mathrm{den}}, T\right)\right. \\ &\left.- T_0C_v\left(\rho^{\mathrm{den}}, T_0\right)\right) \end{aligned} \tag{30}$$

$$E_{th}\left(\rho^{\mathrm{den}}, T\right) = 9nk_BT\left(\frac{T}{\Theta_D}\right)^3\int_0^{\frac{\Theta_D}{T}}\frac{x^3}{\exp\left(x\right)-1}\mathrm{d}x \tag{31}$$

$$C_v\left(\rho^{\mathrm{den}}, T\right) = 9nk_B\left(\frac{T}{\Theta_D}\right)^3\int_0^{\frac{\Theta_D}{T}}\frac{x^4\exp(x)}{\left(\exp\left(x\right)-1\right)^2}\mathrm{d}x \tag{32}$$

where V is the molar volume ($1/V = \rho^{\mathrm{den}}/V_0\rho_0^{\mathrm{den}}$).

$$K_S = K_T(1 + 1\alpha\gamma T) \tag{33}$$

$$\alpha = \frac{\gamma C_v}{VK_T} \tag{34}$$

The Grüneisen parameter can be calculated as follows:

$$\gamma = \gamma_0\left(\frac{\rho_0^{\mathrm{den}}}{\rho^{\mathrm{den}}}\right)^q \tag{35}$$

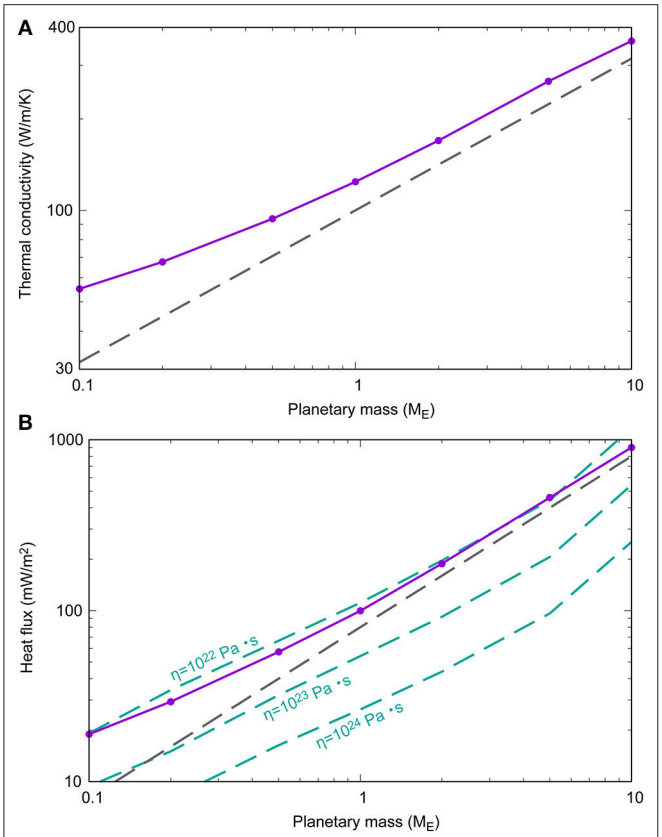

FIGURE 11 | (A) Thermal conductivity of terrestrial planets at the top of the core as functions of planetary mass normalized to the Earth's mass (M_E). Purple line with circles indicates present estimate. Gray broken line represents previous scaling (Stixrude, 2014). **(B)** The heat flux at the CMB as a function of planetary mass. Purple solid line with circles indicates conductive heat flux along the isentropic temperature gradient at the top of the core. Green broken lines indicate the calculated heat flux across the thermal boundary layer (TBL) at the bottom of the mantle with assumed viscosity (see text). Gray broken line shows the previous estimate of the heat flux across the TBL (Stixrude, 2014).

with the parameter values of $\gamma_0 = 1.36$ and $q = 0.91$ for the outer core liquid (see Tachinami et al., 2011 and references therein). The melting temperature of Fe at the ICB is estimated based on Anzellini et al. (2013) as

$$T_{\mathrm{m,Fe}} = T_{\mathrm{TP}} \left(\frac{P - P_{\mathrm{TP}}}{161.2} + 1 \right)^{\frac{1}{1.72}} \tag{36}$$

where $P_{\mathrm{TP}} = 98.5$ GPa and $T_{\mathrm{TP}} = 3{,}712$ K. This extrapolation is same as the first-principles calculation (Morard et al., 2011). The ICB temperature should be equal to the melting temperature of Fe-S alloy at the ICB pressure, which may be lower than the melting temperature of pure Fe. Such melting temperature depression is expressed as $T_{\mathrm{ICB}} = (1 - \chi_S) T_{\mathrm{m,Fe}}$ (Usselman, 1975; Stevenson et al., 1983). Assuming the adiabatic temperature gradient, the temperature profile can be calculated by solving the following ordinary differential equation:

$$\frac{\mathrm{d}T}{\mathrm{d}r} = -\frac{\rho^{\mathrm{den}} g \gamma}{K_S} T \tag{37}$$

We estimated the thermal conductivity of the top of the core of super-Earths from KKR-CPA calculation of $Fe_{82.83}S_{37.13}$ alloys combined with phonon scattering (see section Electrical Resistivity and Thermal Conductivity of the Earth's Core) (**Figure 11A**). The thermal conductivity of 1 M_E planet is calculated to be $k = 124$ W/m/K. The thermal conductivity increases with increasing planetary mass, and is $k = 361$ W/m/K for the 10 M_E planet. Stixrude (2014) extrapolate the thermal conductivity from Pozzo et al. (2012), which yields $k \propto M_p^{\frac{1}{2}}$. Our thermal conductivity values are basically consistent with Stixrude (2014). The actual heat flux across the CMB is regulated by the thermal conduction at the thermal boundary layer (TBL) located at the bottom of the mantle.

$$q_{\mathrm{TBL}} = k_{\mathrm{TBL}} \frac{\Delta T_{\mathrm{TBL}}}{\delta} \tag{38}$$

where $k_{\mathrm{TBL}} = 10$ W/m/K is the thermal conductivity of the TBL, ΔT_{TBL} is the temperature difference between top and bottom of the TBL, and δ is the thickness of the TBL. To discuss the thermal convection in the mantle, a dimensionless number, Ra, which is so-called the Rayleigh number, is usually used.

$$\mathrm{Ra} = \frac{\rho^{\mathrm{den}} g \alpha \Delta T d^3}{\kappa \eta} \tag{39}$$

where ΔT and d are the temperature difference and thickness between top and bottom of the layer, respectively, κ is the thermal diffusivity, and η is the viscosity. Note that

$$\kappa = \frac{k}{\rho^{\mathrm{den}} C_p} \tag{40}$$

where C_P is the isobaric specific heat. According to the thermal boundary layer theory, the thickness of the TBL can be estimated from the condition that the local Rayleigh number of the TBL, Ra_l is nearly equal to the critical Rayleigh number Ra_c, which is ~650 for thermal convection.

$$\mathrm{Ra}_l = \left(\frac{\rho g \alpha}{\kappa \eta} \right)_l \delta^3 \Delta T_{\mathrm{TBL}} \sim \mathrm{Ra_c} \sim 650 \tag{41}$$

The temperature profile of the mantle is calculated from the adiabatic temperature gradient with assumed potential temperature to be 1,600 K. **Figure 11B** plots the conductive heat flux at the top of the liquid core as function of the planetary mass normalized by the Earth's mass (Equation 18). The conductive flux increases rapidly with increasing the planetary mass, mainly because of the internal temperature. The green broken lines indicate the total core cooling across the CMB (Equation 38), which strongly depends on the mantle viscosity. The calculated TBL heat flux values are $q_{\mathrm{TBL}} = 111$, 54 and 26 mW/m^2 for $M_p = 1$ M_E planet with the viscosity values of $\eta = 10^{22}$, 10^{23}, and 10^{24}

Pa·s, respectively. These values correspond to the Earth's CMB heat flux, which is ranging from 33 to 99 mW/m^2 (5–15 TW) (e.g., Lay et al., 2008). At 1 M_E, the core conductive heat flux is comparable or larger than the thermal boundary layer heat flux. In this case, the liquid core may partly stratify (Labrosse et al., 1997; Lister and Buffett, 1998; Pozzo et al., 2012; Gomi et al., 2013; Labrosse, 2015; Nakagawa, 2017), which is consistent with seismic observation (Tanaka, 2007; Helffrich and Kaneshima, 2010). Considering increase of core thermal conductivity with depth, before the onset of the inner core growth, the fluid core tends to be stratified from the bottom (Gomi et al., 2013). This in turn means that purely thermal buoyancy cannot drive the convection, if the top of the core is subisentropic. Hence, additional chemical buoyancies are necessary to maintain the geodynamo. In our Earth, the chemical buoyancy arising from the growing inner core contributes large portion of geodynamo efficiency (e.g., Lister and Buffett, 1995; Labrosse, 2015). Recently, MgO or SiO_2 precipitation is proposed for another source of chemical buoyancy (O'rourke and Stevenson, 2016; Hirose et al., 2017). Assuming that the mantle viscosity is independent of the planetary mass, the magnitude relation between the core adiabatic heat flux and the TBL heat flux of $M_p > 1\ M_E$ is similar to that of $M_p = 1\ M_E$, which suggests that the similar situation is predicted in the super-Earths: thermally stratified layer at the top of the liquid core and a requirement of chemical buoyancies for geodynamo.

In this study, we considered only one specific scenario with many assumptions, however, many scenarios should be considered because of large uncertainties of material properties other than the thermal conductivity of the core. One of the most important uncertainty may be caused by viscosity of the mantle (Tachinami et al., 2011; Tackley et al., 2013). Experimental and theoretical studies suggested that the lattice thermal conductivity of the mantle strongly depends on pressure, temperature and phase transitions (Manthilake et al., 2011; Ohta et al., 2012; Dekura et al., 2013). In addition to the lattice thermal conductivity, the radiative conductivity may become important because it is expected to enhance with temperature, although the value is controversial (Goncharov et al., 2008; Keppler et al., 2008). Since we are interested in the super-Earth located within the habitable zone that have the surface liquid water, we assumed that the mantle potential temperature may be comparable to that of the Earth $T = 1{,}600$ K. On the other hand, Stixrude (2014) suggests a higher mantle potential temperature due to accretion. Miyagoshi et al. (2017) concluded that if shallow part of the mantle was hotter than the adiabatic temperature extrapolated from the deeper mantle at the initial stage of mantle convection, such layered structure continues more than several billion years. Furthermore, if the temperature is sufficiently high to melt the mantle material, dynamo process in the magma ocean can also be possible due to high electrical conductivity of melt (McWilliams et al., 2012; Soubiran and Militzer, 2018). Similarly, the core temperature is also uncertain. We just assumed the inner core radius to determine the core adiabat, however, Morard et al. (2011) suggested that the core temperature is too low to melt the metallic core. The internal temperature should vary with time. Therefore, simulations of coevolution of thermally coupled mantle and core are needed for the future work.

SUMMARY

We conducted KKR-CPA-DFT calculations of impurity resistivity of Fe-based light elements (C, N, O, Si, S) or Ni alloys, which is consistent with recent diamond-anvil cell experiments (Gomi and Hirose, 2015; Gomi et al., 2016; Suehiro et al., 2017; Zhang et al., 2018). The results suggest that impurity resistivity of Si is the largest among the light elements candidates, followed by C, S, N, and O (**Figure 3**). This may be due to the variation of the saturation resistivity on composition (**Figure 5**). The impurity resistivity of Ni is smaller than that of five light elements candidates. The resistivity calculation on Fe-Si-S ternary alloys suggests the violation of the Matthiessen's rule (**Figure 6**). We also computed the electronic specific heat of Fe alloys, which show the violation of the Sommerfeld expansion (Boness et al., 1986) with low impurity concentration. However, the degree of deviation becomes smaller with increasing impurity concentration (**Figures 7**, **8**), which suggests that the Sommerfeld value of the Lorenz number may be good approximation at the terrestrial cores. The implausibility of geodynamo motion in the super-Earths has been discussed in terms of the absence of mantle convection (Tachinami et al., 2011; CíŽková et al., 2017; Kameyama and Yamamoto, 2018). The present study, on the other hand, focused on the thermal conductivity of the core. We modeled the thermal conductivity to be higher than ∼90 W/m/K for the Earth's outer core (**Table 2**). For the super-Earth with 10 M_E, the thermal conductivity of the top of the core is estimated to be 361 W/m/K (**Figure 11A**), which is one order higher than the value of $k = 40$ W/m/K, which adopted previous thermal evolution calculation (Tachinami et al., 2011) and is consistent with result from recent scaling calculation (Stixrude, 2014). The resultant conductive heat flux at the top of the liquid core of terrestrial planets as function of planetary mass is compared with the heat flux across the thermal boundary layer (TBL) at the bottom of mantle (**Figure 11B**). The present result suggests the absence of the thermal convection in the core, which predicts the presence of the thermally stratified layer at the top of the core of super-Earths, similar to the Earth. In order to sustain the geodynamo motion in the liquid core, chemical convection is required, which associates with the inner core growth or precipitation of MgO and/or SiO_2 (O'rourke and Stevenson, 2016; Hirose et al., 2017).

AUTHOR CONTRIBUTIONS

HG conducted the calculations. HG and TY wrote the manuscript.

FUNDING

This work was supported by JSPS MEXT/KAKENHI Grant Number JP15H05827.

ACKNOWLEDGMENTS

We would like to thank Hisazumi Akai for providing the conductivity calculation code implemented in the AkaiKKR package. The authors also thank to Sonju Kou for fruitful discussion. This work was supported by JSPS MEXT/KAKENHI Grant Number JP15H05827. We are grateful to the two reviewers for their comments.

REFERENCES

Akai, H. (1989). Fast Korringa-Kohn-Rostoker coherent potential approximation and its application to FCC Ni-Fe systems. *J Phys.* 1, 8045. doi: 10.1088/0953-8984/1/43/006

Alstad, J., Colvin, R., and Legvold, S. (1961). Single-crystal and polycrystal resistivity relationships for yttrium. *Phys. Rev.* 123, 418–419. doi: 10.1103/PhysRev.123.418

Anderson, O. L. (1998). The Grüneisen parameter for iron at outer core conditions and the resulting conductive heat and power in the core. *Phys. Earth Planet. Inter.* 109, 179–197. doi: 10.1016/S0031-9201(98)00123-X

Anglada-Escudé, G., Arriagada, P., Vogt, S. S., Rivera, E. J., Butler, R. P., Crane, J. D., et al. (2012). A planetary system around the nearby M dwarf GJ 667C with at least one super-Earth in its habitable zone. *Astrophys. J. Lett.* 751, L16. doi: 10.1088/2041-8205/751/1/L16

Antonov, V. E., Baier, M., Dorner, B., Fedotov, V. K., Grosse, G., Kolesnikov, A. I., et al. (2002). High-pressure hydrides of iron and its alloys. *J. Phys.* 14, 6427. doi: 10.1088/0953-8984/14/25/311

Anzellini, S., Dewaele, A., Mezouar, M., Loubeyre, P., and Morard, G. (2013). Melting of iron at Earth's inner core boundary based on fast X-ray diffraction. *Science* 340, 464–466. doi: 10.1126/science.1233514

Banhart, J., Weinberger, P., and Voitlander, J. (1989). Fermi surface and electrical resistivity of Cu-Pt alloys: a relativistic calculation. *J. Phys.* 1, 7013. doi: 10.1088/0953-8984/1/39/012

Bi, Y., Tan, H., and Jing, F. (2002). Electrical conductivity of iron under shock compression up to 200 GPa. *J. Phys.* 14, 10849. doi: 10.1088/0953-8984/14/44/389

Bohnenkamp, U., Sandström, R., and Grimvall, G. (2002). Electrical resistivity of steels and face-centered-cubic iron. *J. Appl. Phys.* 92, 4402–4407. doi: 10.1063/1.1502182

Boness, D. A., and Brown, J. M. (1990). The electronic band structures of iron, sulfur, and oxygen at high pressures and the Earth's core. *J. Geophys. Res.* 95, 21721–21730. doi: 10.1029/JB095iB13p21721

Boness, D. A., Brown, J. M., and McMahan, A. K. (1986). The electronic thermodynamics of iron under Earth core conditions. *Phys. Earth Planet. Inter.* 42, 227–240. doi: 10.1016/0031-9201(86)90025-7

Butler, W. H. (1985). Theory of electronic transport in random alloys: Korringa-Kohn-Rostoker coherent-potential approximation. *Phys. Rev. B* 31:3260. doi: 10.1103/PhysRevB.31.3260

Butler, W. H., and Stocks, G. M. (1984). Calculated electrical conductivity and thermopower of silver-palladium alloys. *Phys. Rev. B* 29, 4217. doi: 10.1103/PhysRevB.29.4217

Charbonneau, D., Berta, Z. K., Irwin, J., Burke, C. J., Nutzman, P., Buchhave, L. A., et al. (2009). A super-Earth transiting a nearby low-mass star. *Nature* 462, 891. doi: 10.1038/nature08679

CíŽková, H., van den Berg, A., and Jacobs, M. (2017). Impact of compressibility on heat transport characteristics of large terrestrial planets. *Phys. Earth Planet. Inter.* 268, 65–77. doi: 10.1016/j.pepi.2017.04.007

Cote, P. J., and Meisel, L. V. (1978). Origin of saturation effects in electron transport. *Phys. Rev. Lett.* 40, 1586–1589. doi: 10.1103/PhysRevLett.40.1586

Cusack, N., and Enderby, J. E. (1960). A note on the resistivity of liquid alkali and noble metals. *Proc. Phys. Soc.* 75, 395. doi: 10.1088/0370-1328/75/3/310

de Koker, N., Steinle-Neumann, G., and Vlček, V. (2012). Electrical resistivity and thermal conductivity of liquid Fe alloys at high P and T, and heat flux in Earth's core. *Proc. Natl. Acad. Sci. U.S.A.* 109, 4070–4073. doi: 10.1073/pnas.1111841109

Dekura, H., Tsuchiya, T., and Tsuchiya, J. (2013). Ab initio lattice thermal conductivity of $MgSiO_3$ perovskite as found in Earth's lower mantle. *Phys. Rev. Lett.* 110:025904. doi: 10.1103/PhysRevLett.110.025904

Deng, L., Seagle, C., Fei, Y., and Shahar, A. (2013). High pressure and temperature electrical resistivity of iron and implications for planetary cores. *Geophys. Res. Lett.* 40, 33–37. doi: 10.1029/2012GL054347

Dewaele, A., Loubeyre, P., Occelli, F., Mezouar, M., Dorogokupets, P. I., and Torrent, M. (2006). Quasihydrostatic equation of state of iron above 2 Mbar. *Phys. Rev. Lett.* 97:215504. doi: 10.1103/PhysRevLett.97.215504

Dobson, D. (2016). Geophysics: earth's core problem. *Nature* 534, 45. doi: 10.1038/534045a

Drchal, V., Kudrnovský, J., Wagenknecht, D., Turek, I., and Khmelevskyi, S. (2017). Transport properties of iron at Earth's core conditions: the effect of spin disorder. *Phys. Rev. B* 96:024432. doi: 10.1103/PhysRevB.96.024432

Ezenwa, I. C., and Secco, R. A. (2017a). Constant electrical resistivity of Zn along the melting boundary up to 5 GPa. *High Press. Res.* 37, 319–333. doi: 10.1080/08957959.2017.1340473

Ezenwa, I. C., and Secco, R. A. (2017b). Electronic transition in solid Nb at high pressure and temperature. *J. Appl. Phys.* 121, 225903. doi: 10.1063/1.4985548

Ezenwa, I. C., and Secco, R. A. (2017c). Invariant electrical resistivity of Co along the melting boundary. *Earth Planet. Sci. Lett.* 474, 120–127. doi: 10.1016/j.epsl.2017.06.032

Ezenwa, I. C., Secco, R. A., Yong, W., Pozzo, M., and Alfè, D. (2017). Electrical resistivity of solid and liquid Cu up to 5 GPa: decrease along the melting boundary. *J. Phys. Chem. Solids* 110, 386–393. doi: 10.1016/j.jpcs.2017.06.030

Faber, T. E. (1972). *An Introduction to the Theory of Liquid Metals*. Cambridge: Cambridge University Press.

Friedel, J. (1956). On some electrical and magnetic properties of metallic solid solutions. *Can. J. Phys.* 34, 1190–1211. doi: 10.1139/p56-134

Fukai, Y. (2006). *The Metal-Hydrogen System: Basic Bulk Properties*, Vol. 21. Berlin; Heidelberg; New York, NY: Springer Science & Business Media.

Gillon, M., Triaud, A. H., Demory, B. O., Jehin, E., Agol, E., Deck, K. M., et al. (2017). Seven temperate terrestrial planets around the nearby ultracool dwarf star TRAPPIST-1. *Nature* 542, 456. doi: 10.1038/nature21360

Glasbrenner, J. K., Pujari, B. S., and Belashchenko, K. D. (2014). Deviations from Matthiessen's rule and resistivity saturation effects in Gd and Fe from first principles. *Phys. Rev. B* 89:174408. doi: 10.1103/PhysRevB.89.174408

Gomi, H., Fei, Y., and Yoshino, T. (2018). The effects of ferromagnetism and interstitial hydrogen on the equation of states of hcp and dhcp FeH_x: implications for the Earth's inner core age. *Am. Mineral.* 103, 1271–1281. doi: 10.2138/am-2018-6295

Gomi, H., and Hirose, K. (2015). Electrical resistivity and thermal conductivity of hcp Fe–Ni alloys under high pressure: implications for thermal convection in the Earth's core. *Phys. Earth Planet. Inter.* 247, 2–10. doi: 10.1016/j.pepi.2015.04.003

Gomi, H., Hirose, K., Akai, H., and Fei, Y. (2016). Electrical resistivity of substitutionally disordered hcp Fe–Si and Fe–Ni alloys: chemically-induced resistivity saturation in the Earth's core. *Eart Planet. Sci. Lett.* 451, 51–61. doi: 10.1016/j.epsl.2016.07.011

Gomi, H., Ohta, K., Hirose, K., Labrosse, S., Caracas, R., Verstraete, M. J., et al. (2013). The high conductivity of iron and thermal evolution of the Earth's core. *Phys. Earth Planet. Inter.* 224, 88–103. doi: 10.1016/j.pepi.2013.07.010

Goncharov, A. F., Haugen, B. D., Struzhkin, V. V., Beck, P., and Jacobsen, S. D. (2008). Radiative conductivity in the Earth's lower mantle. *Nature* 456, 231. doi: 10.1038/nature07412

Gurvitch, M. (1981). Ioffe-Regel criterion and resistivity of metals. *Phys. Rev. B* 24:7404. doi: 10.1103/PhysRevB.24.7404

Helffrich, G., and Kaneshima, S. (2010). Outer-core compositional stratification from observed core wave speed profiles. *Nature* 468, 807. doi: 10.1038/nature09636

Hieu, H. K., Hai, T. T., Hong, N. T., Sang, N. D., and Tuyen, N. V. (2017). Electrical resistivity and thermodynamic properties of iron under high pressure. *J. Electr. Mater.* 46, 3702–3706. doi: 10.1007/s11664-017-5411-2

Hirose, K., Labrosse, S., and Hernlund, J. (2013). Composition and state of the core. *Annu. Rev. Earth Planet. Sci.* 41, 657–691. doi: 10.1146/annurev-earth-050212-124007

Hirose, K., Morard, G., Sinmyo, R., Umemoto, K., Hernlund, J., Helffrich, G., et al. (2017). Crystallization of silicon dioxide and compositional evolution of the Earth's core. *Nature* 543, 99. doi: 10.1038/nature21367

Kameyama, M., and Yamamoto, M. (2018). Numerical experiments on thermal convection of highly compressible fluids with variable viscosity and thermal conductivity: implications for mantle convection of super-Earths. *Phys. Earth Planet. Inter.* 274, 23–36. doi: 10.1016/j.pepi.2017.11.001

Keppler, H., Dubrovinsky, L. S., Narygina, O., and Kantor, I. (2008). Optical absorption and radiative thermal conductivity of silicate perovskite to 125 gigapascals. *Science* 322, 1529–1532. doi: 10.1126/science.1164609

Kiarasi, S., and Secco, R. A. (2015). Pressure-induced electrical resistivity saturation of Fe17Si. *Phys. Status Solidi* (b) 252, 2034–2042. doi: 10.1002/pssb.201552029

Konôpková, Z., Lazor, P., Goncharov, A. F., and Struzhkin, V. V. (2011). Thermal conductivity of hcp iron at high pressure and temperature. *High Press. Res.* 31, 228–236. doi: 10.1080/08957959.2010.545059

Konôpková, Z., McWilliams, R. S., Gómez-Pérez, N., and Goncharov, A. F. (2016). Direct measurement of thermal conductivity in solid iron at planetary core conditions. *Nature* 534, 99. doi: 10.1038/nature18009

Kou, S., and Akai, H. (2018). First-principles calculation of transition-metal Seebeck coefficients. *Solid State Commun.* 276, 1–4. doi: 10.1016/j.ssc.2018.02.018

Kuwayama, Y., Hirose, K., Sata, N., and Ohishi, Y. (2008). Phase relations of iron and iron-nickel alloys up to 300 GPa: implications for composition and structure of the Earth's inner core. *Earth Planet. Sci. Lett.* 273, 379–385. doi: 10.1016/j.epsl.2008.07.001

Labrosse, S. (2015). Thermal evolution of the core with a high thermal conductivity. *Phys. Earth Planet. Inter.* 247, 36–55. doi: 10.1016/j.pepi.2015.02.002

Labrosse, S., Poirier, J. P., and Le Mouël, J. L. (1997). On cooling of the Earth's core. *Phys. Earth Planet. Inter.* 99, 1–17. doi: 10.1016/S0031-9201(96)03207-4

Lay, T., Hernlund, J., and Buffett, B. A. (2008). Core–mantle boundary heat flow. *Nat. Geosci.* 1, 25. doi: 10.1038/ngeo.2007.44

Lin, Z., Zhigilei, L. V., and Celli, V. (2008). Electron-phonon coupling and electron heat capacity of metals under conditions of strong electron-phonon nonequilibrium. *Phys. Rev. B* 77:075133. doi: 10.1103/PhysRevB.77.075133

Linde, J. O. (1932). Elektrische Eigenschaften verdünnter Mischkristallegierungen III. Widerstand von Kupfer-und Goldlegierungen. Gesetzmäßigkeiten der Widerstandserhöhungen. *Ann. Phys.* 407, 219–248. doi: 10.1002/andp.19324070206

Lister, J. R., and Buffett, B. A. (1995). The strength and efficiency of thermal and compositional convection in the geodynamo. *Phys. Earth Planet. Inter.* 91, 17–30. doi: 10.1016/0031-9201(95)03042-U

Lister, J. R., and Buffett, B. A. (1998). Stratification of the outer core at the core-mantle boundary. *Phys. Earth Planet. Inter.* 105, 5–19. doi: 10.1016/S0031-9201(97)00082-4

Manthilake, G. M., de Koker, N., Frost, D. J., and McCammon, C. A. (2011). Lattice thermal conductivity of lower mantle minerals and heat flux from Earth's core. *Proc. Natl. Acad. Sci. U.S.A.* 108, 17901–17904. doi: 10.1073/pnas.1110594108

Markowitz, D. (1977). Calculation of electrical resistivity of highly resistive metallic alloys. *Phys. Rev. B* 15:3617. doi: 10.1103/PhysRevB.15.3617

Matassov, G. (1977). *The Electrical Conductivity of Iron-Silicon Alloys at High Pressures and the Earth's Core*. Ph.D. thesis, Lawrence Livermore Laboratory, University of California.

McWilliams, R. S., Konôpková, Z., and Goncharov, A. F. (2015). A flash heating method for measuring thermal conductivity at high pressure and temperature: application to Pt. *Phys. Earth Planet. Inter.* 247, 17–26. doi: 10.1016/j.pepi.2015.06.002

McWilliams, R. S., Spaulding, D. K., Eggert, J. H., Celliers, P. M., Hicks, D. G., Smith, R. F., et al. (2012). Phase transformations and metallization of magnesium oxide at high pressure and temperature. *Science* 338, 1330–1333. doi: 10.1126/science.1229450

Mertig, I. (1999). Transport properties of dilute alloys. *Rep. Prog. Phys.* 62, 237. doi: 10.1088/0034-4885/62/2/004

Miyagoshi, T., Kameyama, M., and Ogawa, M. (2017). Extremely long transition phase of thermal convection in the mantle of massive super-Earths. *Earth Planets Space* 69, 46. doi: 10.1186/s40623-017-0630-6

Mooij, J. H. (1973). Electrical conduction in concentrated disordered transition metal alloys. *Phys. Status Solidi* 17, 521–530. doi: 10.1002/pssa.2210170217

Morard, G., Bouchet, J., Valencia, D., Mazevet, S., and Guyot, F. (2011). The melting curve of iron at extreme pressures: implications for planetary cores. *High Energy Density Phys.* 7, 141–144. doi: 10.1016/j.hedp.2011.02.001

Moruzzi, V. L., Janak, J. F., and Williams, A. R. (1978). *Calculated Electronic Properties of Metals*. New York, NY: Pergamon Press Inc.

Mott, N. F. (1934). The resistance of liquid metals. *Proc. R. Soc. Lond. A* 146, 465–472. doi: 10.1098/rspa.1934.0166

Mott, N. F. (1936). "The electrical resistance of dilute solid solutions," in *Mathematical Proceedings of the Cambridge Philosophical Society*, Vol. 32 (Cambridge: Cambridge University Press), 281–290.

Mott, N. F. (1972). The electrical resistivity of liquid transition metals. *Philos. Mag.* 26, 1249–1261. doi: 10.1080/14786437208220339

Nakagawa, T. (2017). On the thermo-chemical origin of the stratified region at the top of the Earth's core. *Phys. Earth Planet. Inter.* 276, 172–181. doi: 10.1016/j.pepi.2017.05.011

Norbury, A. L. (1921). The electrical resistivity of dilute metallic solid solutions. *Trans. Faraday Soc.* 16, 570–596. doi: 10.1039/tf9211600570

Ohta, K., Kuwayama, Y., Hirose, K., Shimizu, K., and Ohishi, Y. (2016). Experimental determination of the electrical resistivity of iron at Earth's core conditions. *Nature* 534, 95. doi: 10.1038/nature17957

Ohta, K., Suehiro, S., Hirose, K., and Ohishi, Y. (2018). Electrical resistivity of fcc phase iron hydrides at high pressure and temperatures. *Comptes Rendus Geosci.* doi: 10.1016/j.crte.2018.05.004. [Epub ahead of print].

Ohta, K., Yagi, T., Taketoshi, N., Hirose, K., Komabayashi, T., Baba, T., et al. (2012). Lattice thermal conductivity of $MgSiO_3$ perovskite and post-perovskite at the core–mantle boundary. *Earth Planet. Sci. Lett.* 349, 109–115. doi: 10.1016/j.epsl.2012.06.043

O'rourke, J. G., and Stevenson, D. J. (2016). Powering Earth's dynamo with magnesium precipitation from the core. *Nature* 529, 387. doi: 10.1038/nature16495

Oshita, M., Yotsuhashi, S., Adachi, H., and Akai, H. (2009). Seebeck coefficient calculated by kubo–greenwood formula on the basis of density functional theory. *J. Phys. Soc. Jpn.* 78:024708. doi: 10.1143/JPSJ.78.024708

Ozawa, H., Hirose, K., Yonemitsu, K., and Ohishi, Y. (2016). High-pressure melting experiments on Fe-Si alloys and implications for silicon as a light element in the core. *Earth Planet. Sci. Lett.* 456, 47–54. doi: 10.1016/j.epsl.2016.08.042

Papuc, A. M., and Davies, G. F. (2008). The internal activity and thermal evolution of Earth-like planets. *Icarus* 195, 447–458. doi: 10.1016/j.icarus.2007.12.016

Poirier, J. P. (2000). *Introduction to the Physics of the Earth's Interior*. Cambridge: Cambridge University Press.

Pommier, A. (2018). Influence of sulfur on the electrical resistivity of a crystallizing core in small terrestrial bodies. *Earth Planet. Sci. Lett.* 496, 37–46. doi: 10.1016/j.epsl.2018.05.032

Pourovskii, L. V., Mravlje, J., Georges, A., Simak, S. I., and Abrikosov, I. A. (2017). Electron–electron scattering and thermal conductivity of ϵfnduc at Earth's core conditions. *New J. Phys.* 19, 073022. doi: 10.1088/1367-2630/aa76c9

Pozzo, M., and Alfè, D. (2016a). Saturation of electrical resistivity of solid iron at Earth's core conditions. *Springerplus* 5, 256. doi: 10.1186/s40064-016-1829-x

Pozzo, M., and Alfè, D. (2016b). "Electrical resistivity saturation of solid iron at Earth's core conditions from density functional theory," in *AGU Abstract DI13A-2356, AGU Fall Meeting* (San Fransisco, CA).

Pozzo, M., Davies, C., Gubbins, D., and Alfè, D. (2012). Thermal and electrical conductivity of iron at Earth's core conditions. *Nature* 485, 355. doi: 10.1038/nature11031

Pozzo, M., Davies, C., Gubbins, D., and Alfè, D. (2013). Transport properties for liquid silicon-oxygen-iron mixtures at Earth's core conditions. *Phys. Rev. B* 87:014110. doi: 10.1103/PhysRevB.87.014110

Pozzo, M., Davies, C., Gubbins, D., and Alfè, D. (2014). Thermal and electrical conductivity of solid iron and iron–silicon mixtures at Earth's core conditions. *Earth Planet. Sci. Lett.* 393, 159–164. doi: 10.1016/j.epsl.2014.02.047

Seagle, C. T., Cottrell, E., Fei, Y., Hummer, D. R., and Prakapenka, V. B. (2013). Electrical and thermal transport properties of iron and iron-silicon alloy

at high pressure. *Geophys. Res. Lett.* 40, 5377–5381. doi: 10.1002/2013GL057930

Secco, R. A. (2017). Thermal conductivity and Seebeck coefficient of Fe and Fe-Si alloys: implications for variable Lorenz number. *Phys. Earth Planet. Inter.* 265, 23–34. doi: 10.1016/j.pepi.2017.01.005

Secco, R. A., and Schloessin, H. H. (1989). The electrical resistivity of solid and liquid Fe at pressures up to 7 GPa. *J. Geophys. Res.* 94, 5887–5894. doi: 10.1029/JB094iB05p05887

Sha, X., and Cohen, R. E. (2011). First-principles studies of electrical resistivity of iron under pressure. *J. Phys.* 23:075401. doi: 10.1088/0953-8984/23/7/075401

Silber, R. E., Secco, R. A., and Yong, W. (2017). Constant electrical resistivity of Ni along the melting boundary up to 9 GPa. *J. Geophys. Res.*122, 5064–5081. doi: 10.1002/2017JB014259

Silber, R. E., Secco, R. A., Yong, W., and Littleton, J. A. (2018). Electrical resistivity of liquid Fe to 12 GPa: implications for heat flow in cores of terrestrial bodies. *Sci. Rep.* 8, 10758. doi: 10.1038/s41598-018-28921-w

Smith, R. F., Fratanduono, D. E., Braun, D. G., Duffy, T. S., Wicks, J. K., Celliers, P. M., et al. (2018). Equation of state of iron under core conditions of large rocky exoplanets. *Nat. Astron.* 2, 452–458. doi: 10.1038/s41550-018-0437-9

Soubiran, F., and Militzer, B. (2018). Electrical conductivity and magnetic dynamos in magma oceans of Super-Earths. *Nat. Commun.* 9, 3883. doi: 10.1038/s41467-018-06432-6

Stacey, F. D., and Anderson, O. L. (2001). Electrical and thermal conductivities of Fe–Ni–Si alloy under core conditions. *Phys. Earth Planet. Inter.* 124, 153–162. doi: 10.1016/S0031-9201(01)00186-8

Stacey, F. D., and Loper, D. E. (2007). A revised estimate of the conductivity of iron alloy at high pressure and implications for the core energy balance. *Phys. Earth Planet. Inter.* 161, 13–18. doi: 10.1016/j.pepi.2006.12.001

Stevenson, D. J., Spohn, T., and Schubert, G. (1983). Magnetism and thermal evolution of the terrestrial planets. *Icarus* 54, 466–489. doi: 10.1016/0019-1035(83)90241-5

Stixrude, L. (2012). Structure of Iron to 1 Gbar and 40 000 K. *Phys. Rev. Lett.* 108:055505. doi: 10.1103/PhysRevLett.108.055505

Stixrude, L. (2014). Melting in super-earths. *Philos. Trans. R. Soc. Lond. A Math. Phys. Eng. Sci.* 372, 20130076. doi: 10.1098/rsta.2013.0076

Stixrude, L., and Lithgow-Bertelloni, C. (2005). Thermodynamics of mantle minerals—I. Physical properties. *Geophys. J. Int.* 162, 610–632. doi: 10.1111/j.1365-246X.2005.02642.x

Suehiro, S., Ohta, K., Hirose, K., Morard, G., and Ohishi, Y. (2017). The influence of sulfur on the electrical resistivity of hcp iron: implications for the core conductivity of Mars and Earth. *Geophys. Res. Lett.* 44, 8254–8259. doi: 10.1002/2017GL074021

Tachinami, C., Senshu, H., and Ida, S. (2011). Thermal evolution and lifetime of intrinsic magnetic fields of super-Earths in habitable zones. *Astrophys. J.* 726:70. doi: 10.1088/0004-637X/726/2/70

Tackley, P. J., Ammann, M., Brodholt, J. P., Dobson, D. P., and Valencia, D. (2013). Mantle dynamics in super-Earths: post-perovskite rheology and self-regulation of viscosity. *Icarus* 225, 50–61. doi: 10.1016/j.icarus.2013.03.013

Tanaka, S. (2007). Possibility of a low P-wave velocity layer in the outermost core from global SmKS waveforms. *Earth Planet. Sci. Lett.* 259, 486–499. doi: 10.1016/j.epsl.2007.05.007

Tateno, S., Hirose, K., Ohishi, Y., and Tatsumi, Y. (2010). The structure of iron in Earth's inner core. *Science* 330, 359–361. doi: 10.1126/science.1194662

Tateno, S., Kuwayama, Y., Hirose, K., and Ohishi, Y. (2015). The structure of Fe-Si alloy in Earth's inner core. *Earth Planet. Sci. Lett.* 418, 11–19. doi: 10.1016/j.epsl.2015.02.008

Tsiovkin, Y. Y., Voloshinskii, A. N., Gapontsev, V. V., and Ustinov, V. V. (2005). Residual electrical resistivity in dilute nonmagnetic alloys of transition metals. *Phys. Rev. B* 71:184206. doi: 10.1103/PhysRevB.71.184206

Tsiovkin, Y. Y., Voloshinskii, A. N., Gapontsev, V. V., and Ustinov, V. V. (2006). Theory of the residual resistivity of dilute alloys of nonmagnetic 3 d−5 d transition metals. *Low Temp. Phys.* 32, 863–867. doi: 10.1063/1.2356843

Tsuchiya, T., and Kawamura, K. (2002). First-principles electronic thermal pressure of metal Au and Pt. *Phys. Rev. B* 66:094115. doi: 10.1103/PhysRevB.66.094115

Tsuchiya, T., and Tsuchiya, J. (2011). Prediction of a hexagonal SiO2 phase affecting stabilities of $MgSiO_3$ and $CaSiO_3$ at multimegabar pressures. *Proc. Natl. Acad. Sci. U.S.A.* 108, 1252–1255. doi: 10.1073/pnas.1013594108

Tsumuraya, T., Matsuura, Y., Shishidou, T., and Oguchi, T. (2012). First-principles study on the structural and magnetic properties of iron hydride. *J. Phys. Soc. Jpn.* 81:064707. doi: 10.1143/JPSJ.81.064707

Umemoto, K., Wentzcovitch, R. M., and Allen, P. B. (2006). Dissociation of $MgSiO_3$ in the cores of gas giants and terrestrial exoplanets. *Science* 311, 983–986. doi: 10.1126/science.1120865

Usselman, T. M. (1975). Experimental approach to the state of the core; Part I, The liquidus relations of the Fe-rich portion of the Fe-Ni-S system from 30 to 100 kb. *Am. J. Sci.* 275, 278–290. doi: 10.2475/ajs.275.3.278

Vafayi, K., Calandra, M., and Gunnarsson, O. (2006). Electronic thermal conductivity at high temperatures: violation of the Wiedemann-Franz law in narrow-band metals. *Phys. Rev. B* 74:235116. doi: 10.1103/PhysRevB.74.235116

Valencia, D., O'Connell, R. J., and Saselov, D. (2006). Internal structure of massive terrestrial planets. *Icarus* 181, 545–554. doi: 10.1016/j.icarus.2005.11.021

Valencia, D., Sasselov, D. D., and O'Connell, R. J. (2007). Radius and structure models of the first super-Earth planet. *Astrophys. J.* 656, 545. doi: 10.1086/509800

Van Zytveld, J. B. (1980). Electrical resistivities of liquid transition metals. *Le J. Phys. Colloques* 41, C8–C503. doi: 10.1051/jphyscol:19808126

Wagle, F., and Steinle-Neumann, G. (2018). Electrical resistivity discontinuity of iron along the melting curve. *Geophys. J. Int.* 213, 237–243. doi: 10.1093/gji/ggx526

Wagle, F., Steinle-Neumann, G., and de Koker, N. (2018). Saturation and negative temperature coefficient of electrical resistivity in liquid iron-sulfur alloys at high densities from first principles calculations. *Phys. Rev. B* 97:094307. doi: 10.1103/PhysRevB.97.094307

Wicks, J. K., Smith, R. F., Fratanduono, D. E., Coppari, F., Kraus, R. G., Newman, M. G., et al. (2018). Crystal structure and equation of state of Fe-Si alloys at super-Earth core conditions. *Sci. Adv.* 4:eaao5864. doi: 10.1126/sciadv.aao5864

Williams, Q. (2018). The thermal conductivity of Earth's core: a key geophysical parameter's constraints and uncertainties. *Annu. Rev. Earth Planet. Sci.* 46, 47–66. doi: 10.1146/annurev-earth-082517-010154

Xu, J., Zhang, P., Haule, K., Minar, J., Wimmer, S., Ebert, H., et al. (2018). Thermal conductivity and electrical resistivity of solid iron at Earth's core conditions from first principles. *Phys. Rev. Lett.* 121:096601. doi: 10.1103/PhysRevLett.121.096601

Yue, S. Y., and Hu, M. (2018). Insight of the thermal conductivity of ε iron at Earth's core conditions from the newly developed direct *ab initio* methodology. *arXiv*:1808.10860 [*Preprint*].

Zhang, C., Lin, J. F., Liu, Y., Feng, S., Jin, C., Hou, M., et al. (2018). Electrical resistivity of Fe-C alloy at high pressure: effects of carbon as a light element on the thermal conductivity of the Earth's core. *J. Geophys. Res.* 123, 3564–3577. doi: 10.1029/2017JB015260

Ziman, J. M. (1961). A theory of the electrical properties of liquid metals. I: the monovalent metals. *Philos. Mag.* 6, 1013–1034. doi: 10.1080/14786436108243361

Conflict of Interest Statement: The authors declare that the research was conducted in the absence of any commercial or financial relationships that could be construed as a potential conflict of interest.

frontiers in Earth Science

ORIGINAL RESEARCH
published: 08 November 2018
doi: 10.3389/feart.2018.00189

Penetrative Convection in Partly Stratified Rapidly Rotating Spherical Shells

Wieland Dietrich and Johannes Wicht*

Department of Planets and Comets, Max Planck Institute for Solar System Research, Göttingen, Germany

Many celestial objects are thought to host interfaces between convective and stable stratified interior regions. The interaction between both, e.g., the transfer of heat, mass, or angular momentum depends on whether and how flows penetrate into the stable layer. Powered from the unstable, convective regions, radial flows can pierce into the stable region depending on their inertia (overshooting). In rapidly rotating systems, the dynamics are strongly influenced by the Coriolis force and radial flows penetrate in stratified regions due to the geostrophic invariance of columnar convection even in the limit of vanishing inertia. Within this study, we numerically investigate both mechanisms and hence explore the nature of penetrative convection in rapidly rotating spherical shells. The study covers a broad range of system parameters, such as the strength of the stratification relative to the Coriolis force or the inertia. Guided by the application to Saturn, we model a sandwiched stable stratified layer (SSL) surrounded by two convective zones. A comprehensive analysis of the damping behavior of convective flows at the edges of the SSL showed that the mean penetration depth is controlled by the ratio of stratified and unstratified buoyancy gradients and is hence independent of rotation. A scaling law is derived and suggests that the penetration depth decreases with the square root of the ratio of unstabilizing and stabilizing entropy gradients. The influence of the Coriolis force, however, is evident by a modulation of the penetration depth along latitude, since convective columns are elongated vertically and hence pierce predominantly into the SSL around mid-latitudes and outside the tangent cylinder. Our result also show that the penetration depth decreases linearly with the flow length scale (low pass filter), confirming predictions from the linear theory of rotating partially stratified convection.

Keywords: stable stratification, rapidly rotating spherical shells, penetrative convection, numerical simulation, scaling laws

OPEN ACCESS

Edited by:
Renaud Deguen,
Claude Bernard University Lyon 1, France

Reviewed by:
Moritz Heimpel,
University of Alberta, Canada
Daniel Lecoanet,
Princeton University, United States

****Correspondence:***
Wieland Dietrich
dietrichw@mps.mpg.de

Specialty section:
This article was submitted to Geomagnetism and Paleomagnetism, a section of the journal Frontiers in Earth Science

Received: *18 July 2018*
Accepted: *16 October 2018*
Published: *08 November 2018*

Citation:
Dietrich W and Wicht J (2018) Penetrative Convection in Partly Stratified Rapidly Rotating Spherical Shells. Front. Earth Sci. 6:189. doi: 10.3389/feart.2018.00189

1. INTRODUCTION

When the local temperature gradient is steeper than the one associated with an adiabat, small perturbations from the hydrostatic equilibrium amplify to the well-known Rayleigh-Taylor convective instability. This leads to vigorous convection that very rapidly re-establishes bulk adiabatic gradients of density and temperature due to the inherent mixing and heat transport efficiency.

However, stable stratified regions, in which the heat flux is conductive or radiative, are widespread phenomena in stars and planets. Those regions are caused by either subadiabatic temperature or positive heavy element gradient. In stars, the large efficiency of radiative heat transport induces stratified regions, e.g., in the radiative part of the solar interior (e.g., Zahn, 1991; Brun et al., 2011). Stable stratification due to temperature inversion or subadiabatic temperature lapse rates are known for the Gas Giants (Jupiter Galileo probe, Atkinson et al., 1996) and outermost atmosphere of terrestrial planets, where radiation is most efficient. In the Earth's liquid outer core, the outermost layer seems stratified caused by either a subadiabatic temperature gradient or a local enrichment of light elements (Fearn and Loper, 1981; Lister and Buffett, 1998). Such a layer would have profound consequences for core convection and dynamo action in the core and be traceable in the geomagnetic field (Nakagawa, 2011; Buffett, 2014). A potential effect of electrically conducting, stable stratified layers surrounding a dynamo region are weak amplitude, strongly axisymmetric surface magnetic fields and are often proposed for Mercury's or Saturn's dynamo regions (Stevenson, 1982; Schubert et al., 1988; Christensen, 2006).

For Saturn a particular interesting scenario, consisting of a stratified layer between two convective ones is favored by the H/He demixing behavior (Stevenson and Salpeter, 1977; Püstow et al., 2016; Schöttler and Redmer, 2018) and in agreement with several observational constraints, such as the peculiarly axisymmetric magnetic field (e.g., Cao et al., 2012), the apparently impeded thermal evolution (Leconte and Chabrier, 2013; Nettelmann et al., 2013) and the detection of gravity wave induced pulsations in Saturn's rings (Hedman and Nicholson, 2013; Fuller, 2014). Saturn's interior might have been homogeneously mixed in the early, hot stages of the thermal evolution. Once the adiabatic temperature gradient crosses the demixing curve, He droplets form, sink downwards and are remixed at greater depth. This process builds up a compositional gradient roughly around mid-depth bridging from He-depleted outer to He-enriched inner convective zone (Stevenson and Salpeter, 1977; Schöttler and Redmer, 2018).

Radial, convective flows originating from the unstable regions might penetrate into the stratified region due to inertia or the geostrophy of the columnar convective structures. It is useful to distinguish qualitatively the different end-members scenarios in terms of the dominant forces. In rotating, partially stratified convection, the three main forces, each associated with a timescale, are the Coriolis force (τ_{rot}), the buoyancy of the rising fluid parcel (τ_{buo}) and the inverse buoyancy due to the stratification (τ_{strat}). The time scales are given by the rotation rate Ω, $\tau_{rot} = (2\Omega)^{-1}$, the Brunt-Väisälä frequency N, $\tau_{strat} = \sqrt{N^{-2}} = (-g/\rho\, d\rho/dr)^{-1/2}$ and the time scale of buoyancy to accelerate fluid parcels $\tau_{buo} = (g/\rho\, \rho'/D)^{-1/2}$, respectively. Here ρ' is the density fluctuation of a buoyant fluid parcel, ρ the ambient density, D a typical length scale and g the local gravity. For our setup, τ_{buo} characterizes the convective and τ_{strat} the stratified regions. The ratio of the time scales can be expressed as the convective Rossby number Ro_c and the stratification parameter I_s:

$$Ro_c = \frac{\tau_{rot}}{\tau_{buo}}, \qquad I_s = \frac{2\Omega}{N} = \frac{\tau_{strat}}{\tau_{rot}}\,. \tag{1}$$

In slowly rotating systems, rotational forces are less important ($I_s < 1$, $Ro_c > 1$) and a hot fluid parcel is accelerated by the buoyancy in the convective region, rises radially upwards and eventually pierces into the SSL, where the depth of penetration depends on the previously gained inertia. This represents the classical case of non-rotating penetrative convection, typically called *overshooting* or *inertia* penetration. For this end-member, the penetration depth should be independent of colatitude, and may be the dominant form of penetration close to the rotation axis for $Ro_c < 1$ and in the equatorial regions in our models.

In rapidly rotating systems, convective flows are strongly modified by the rotation ($Ro_c < 1$). The dominant Coriolis force constrains the flow to be invariant along the rotation axis leading to the well-known convective columns and strongly geostrophic zonal flows. This implies that the flows extend into the stratified layer independent of inertia, but with a characteristic colatitudinal modulation. When the Coriolis force is stronger than the gravity force associated with the stratification (i.e., $I_s > 1$, $Ro_c < 1$), *rotational* penetration is strong and acts predominantly at mid-latitudes and outside the tangent cylinder (TC), where convective columns can vertically extend through the whole spherical shell. Since in the equatorial regions and close to the rotation axis no convective columns can be extended into the SSL, rotational penetration yields a characteristic colatitude dependence. If, on the other hand, $I_s < 1$ and $Ro_c < 1$ the SSL should be devoid of radial flows since the stratification is strong enough to efficiently break the vertical stiffness of geostrophic flows.

A fundamental understanding of penetrative convection in rapidly rotating spherical shells is of ample importance in geo- and astrophysics. The efficiency or vigor of penetrative convection controls the transport of heat, mass, angular momentum, and magnetic fields across the interface between unstable and stable stratified regions. If the penetration is strong and the associated heat transport efficient, adiabatic regions are extended into the stratified layers (e.g., Browning et al., 2004). This means that stratified layers can be eroded by the permanent entrainment of convective flows and subsequent efficient mixing (e.g., Ellison and Turner, 1959; Levy and Fernando, 2002). Another complication arises from the combination of spherical geometry and rapid rotation. If rotational forces dominate over the inverse buoyancy associated with the stratification, piercing radial flows are non-uniform along colatitude leading to latitudinal entropy (density) gradients and hence drive baroclinic instabilities. Those in turn will act as a boundary condition for the differential rotation in the convective regions and potentially alter the magnetic field (Stevenson, 1982).

Classic studies of penetrative convection dealt with non-rotating cartesian setups of Rayleigh-Bénard convection (Veronis, 1963). The effect of rotation was firstly considered in the framework of oceanic dynamics (e.g., Julien et al., 1996). The investigation of rotating convection in spherical shells below or

above a stable stratified layer was mainly driven by studies on the interaction and efficiency of radiative and/or convective heat transport in solar or stellar interiors (e.g., Zahn, 1991; Brummell et al., 2002; Rogers et al., 2006). For rapidly rotating A-type stars, where a convective core is surrounded by a radiative outer envelope, Browning et al. (2004) reported that rotational and overshooting penetrative convection generates adiabatic regions in the radiative zone preferentially at higher latitudes (prolate adiabatic core).

Several numerical investigations tuned to the solar setup with a convective envelope enclosing a deeper radiation dominated zone, investigate the parameter dependence of penetrative convection (Zahn, 1991; Hurlburt et al., 1994; Rogers et al., 2006). Since the stratification originates from enhanced radiative heat transport, it is typically assumed that penetration depth is largely characterized by two parameters, one being the Péclet number given by $Pe = UD/\kappa$, where U is a typical flow speed, D a length scale and κ the thermal diffusivity measuring the radiative heat transport (Zahn, 1991; Brummell et al., 2002). The other parameter, S is the ratio of sub- and superadiabaticity in the stable and unstable region (Hurlburt et al., 1994). However, different scaling relations between the penetration depth and S have been reported (Hurlburt et al., 1994; Brummell et al., 2002; Rogers et al., 2006). Interestingly, in models that take spherical geometry and rotation into account, the associated Coriolis forces appear unimportant for the magnitude of the penetration depth.

In the planetary context, the Galileo Probe revealed subadiabatic temperature gradients and non-ceasing zonal flows in Jupiter's outermost atmosphere down to roughly 20 bar of atmospheric pressure. This suggests that zonal flows are not damped, but rather maintained in stratified regions yet disconnected from their potential sources, such as convection or irradiation gradients. Assuming that the axisymmetric winds are driven from correlations of the deep convection (i.e., Reynolds stresses, Zhang and Schubert, 1996, 1997) showed that zonal mean flows are vertically extended by the Coriolis forces in accordance with the Taylor-Proudman theorem, but non-axisymmetric convective flows are damped by the inverse buoyancy gradients due to the stratification. From a more theoretical point of view, the linearized model of inviscid, inertia-less, rapidly rotating penetrative convection as studied by Takehiro and Lister (2001) shows a *linear* length scale dependence of penetration depth such that larger scale flows (like differential rotation) are less damped than short length scale flows typically associated with convective motions. The overall damping amplitude depends on the gravity force associated with the stable stratification relative to the Coriolis force (I_s). Subsequent studies including nonlinear inertia showed a more complex damping behavior (Takehiro and Lister, 2002), but the results offered an attractive explanation how zonal flows are extended through stratified regions.

The major aim of the present study is to understand how overshoot and rotational penetration act across the interface between stratified and unstratified regions in rapidly rotating, spherical shell models, which are most suitable for interiors of planets. Even though the effects of stratification on differential rotation and magnetic fields as far as the emerging waves inside the SSL are left aside in this study, the investigation of fundamental properties of rapidly rotating, penetrative convection serves as a basis of upcoming research. Our models cover a comprehensive part of the parameter space, such that the different regimes appropriate for planets are reached in terms of I_s and Ro_c. The general setup featuring a thin, sandwiched stratified layer centered at mid-depth and surrounded by two thick convective zones is motivated from the application to Saturn.

2. MODEL

The non-dimensional governing equations for conservation of mass, momentum and thermal energy for an ideal gas in the anelastic approximation are given by (Jones, 2011; Gastine and Wicht, 2012; Verhoeven et al., 2015; Wicht et al., 2018):

$$\nabla \cdot \tilde{\rho}\boldsymbol{u} = 0 \tag{2}$$

$$\frac{\partial \boldsymbol{u}}{\partial t} + \boldsymbol{u}\cdot\nabla\boldsymbol{u} + \frac{2}{E}\boldsymbol{e}_z \times \boldsymbol{u} = -\nabla p^\star + \frac{Ra}{Pr} g s' \boldsymbol{e}_r + \boldsymbol{F}_\nu \tag{3}$$

$$\frac{\partial s'}{\partial t} + \boldsymbol{u}\cdot\nabla s' + u_r \frac{d\tilde{s}}{dr} = \frac{1}{Pr\tilde{\rho}\tilde{T}}\nabla\cdot\left(\tilde{\kappa}\tilde{\rho}\tilde{T}\nabla s'\right) + \frac{Pr\,Di}{Ra}\frac{1}{\tilde{\rho}\tilde{T}}Q_\nu\,, \tag{4}$$

where $p^\star$ is the reduced pressure, $\mathbf{F}_\nu$ is the viscous force,

$$\mathbf{F}_\nu = \frac{1}{\bar{\rho}}\left[\frac{\partial}{\partial x_j}\bar{\rho}\left(\frac{\partial u_i}{\partial x_j} + \frac{\partial u_j}{\partial x_i}\right) - \frac{2}{3}\frac{\partial}{\partial x_i}\bar{\rho}\frac{\partial u_j}{\partial x_j}\right] \tag{5}$$

and Q_ν represents viscous heating given by

$$Q_\nu = \sigma_{ij}\frac{\partial u_i}{\partial x_j}\,, \quad \sigma_{ij} = \bar{\rho}\left(\frac{\partial u_i}{\partial x_j} + \frac{\partial u_j}{\partial x_i} - \frac{2}{3}\delta_{ij}\nabla\cdot\mathbf{u}\right)\,, \tag{6}$$

where σ_{ij} is the stress tensor. The non-dimensional parameters are given by

$$Ra = \frac{\alpha_o T_o g_o d^4}{c_p \nu \kappa_0}\left|\frac{d\tilde{s}}{dr}\right|_{r_i}\,, \quad Pr = \frac{\nu}{\kappa_o}\,, \quad E = \frac{\nu}{\Omega d^2}\,. \tag{7}$$

These equations were formulated for an adiabatic background state. In our model, a prescribed non-adiabaticity of the background state powers or suppresses convection. The amplitude of these destabilizing and stabilizing entropy gradients must remain small relative to the adiabat to make sure the equations still hold. The non-adiabaticity of the new background state is thus scaled with $\epsilon_s \ll 1$,

$$\frac{d\tilde{T}}{dr} = \epsilon_s \tilde{T}\frac{d\tilde{s}}{dr} - Di\,\tilde{g}(r)\,, \qquad \frac{1}{\tilde{\rho}}\frac{d\tilde{\rho}}{dr} = \epsilon_s\frac{d\tilde{s}}{dr} - \frac{Di}{\Gamma\tilde{T}}\tilde{g}(r)\,, \tag{8}$$

where $d\tilde{s}/dr$ is the dimensionless analytically prescribed stratification profile and Γ the Grüneisenparameter which is in an ideal gas related to the polytropic index n and specific heats by

$$\Gamma = \frac{c_p}{c_v} - 1 = \frac{1}{n}\,. \tag{9}$$

The background state is characterized by the relative deviation from an adiabat ϵ_s and the dissipation number Di, which sets the background density variation

$$\epsilon_s = \frac{d}{c_p}\left|\frac{d\tilde{s}}{dr}\right|_{r_i}, \quad Di = \frac{\alpha_o g_o d}{c_p}, \tag{10}$$

where $|d\tilde{s}/dr|_{r_i}$ is the dimensional reference entropy gradient at the inner boundary. The background entropy gradient is prescribed analytically and sets convective (unstable stratified, $d\tilde{s}/dr < 0$) and stable ($d\tilde{s}/dr > 0$) regions. The $d\tilde{s}/dr$-profile is given by

$$\frac{d\tilde{s}}{dr} = \left(\frac{A_{SSL}+1}{4}\right)\left(1+\tanh\left[(r-r_{lb})\,d_s\right]\right)\left(1-\tanh\left[(r-r_{ub})\,d_s\right]\right) - 1, \tag{11}$$

where A_{SSL} is the amplitude of stable stratification (basically setting the BV frequency, see Equation 16), r_{lb} and r_{ub} are lower and upper boundary of the SSL. The parameter d_s defines the slope of the profile. When choosing the stratification amplitude, $\epsilon_s A_{SSL} \ll 1$ is required to be compliant with the treatment in the framework of the anelastic approximation, which is based on an adiabatic and steady background state. The gravity profile and Γ are fitted to an interior model of Saturn by Nettelmann et al. (2013) (see also **Figure 1**), where a polynomial of second order is used for the former:

$$\tilde{g}(r) = g_0 + g_1\frac{r}{r_o} + g_2\frac{r_o^2}{r^2}, \tag{12}$$

with

$$g_0 = 1.854 \quad \& \quad g_1 = -0.781 \quad \& \quad g_2 = 0.0558\,. \tag{13}$$

Γ characterizes the nature of the ideal gas and is found by fitting p-T-curves from Nettelmann et al. (2013) with polytropic laws such that

$$p \propto T^{\frac{1+\Gamma}{\Gamma}}, \tag{14}$$

yielding a best fitting $\Gamma = 0.513$ for the deep interior. The mean density contrast is set by $Di = 3$, corresponding to a top-to-bottom ratio of $\rho_i/\rho_o \approx 38$. Then the temperature and density gradient are set by a chosen entropy gradient profile and Equation 8. **Figure 1B**) shows the so derived background state, indicating sub- and superadiabatic temperature gradients (middle panel, upper row). The black, dashed line corresponds to an isentropic ($d\tilde{s}/dr = 0$) model for reference. Note, that the

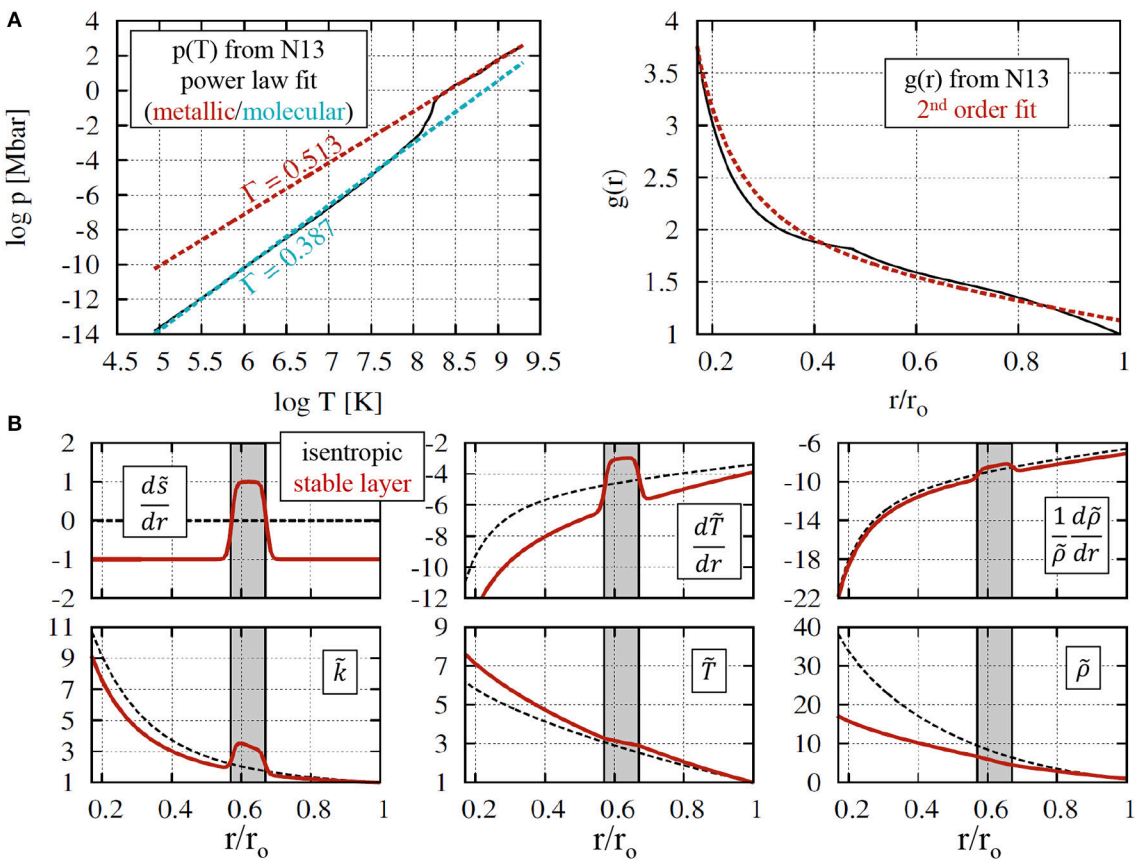

FIGURE 1 | (A) power law (Γ) and 2nd order polynomial (gravity) fits to the interior state model from Nettelmann et al. (2013) **(B)** the non-adiabatic background state is characterized by a prescribed entropy gradient profile ($d\tilde{s}/dr$) setting the temperature, density and thermal conductivity. For visualization purposes the relative non-adiabaticity is strongly exaggerated (parameters $\epsilon_S = 0.5$, $A_{SSL} = 1.0$, $Di = 3.0$, $\Gamma = 0.513$).

non-adiabaticity in the figure is strongly exaggerated using $\epsilon_s = 0.5$ and $A_{SSL} = 1.0$. For production runs, the relative deviation from an adiabatic background must remain small ($\epsilon_s A_{SSL} \ll 1$). To ensure that the newly defined background state is steady, the heat flux must be constant on every radius. Hence a thermal conductivity profile ($\tilde{k} = \tilde{\rho}\tilde{c}_p\tilde{\kappa}$) is set such that

$$\tilde{k} = \frac{Q_0}{4\pi}\left(r^2\frac{d\tilde{T}}{dr}\right)^{-1}, \tag{15}$$

where Q_o is the heat flux at the outer boundary. The profile of $\tilde{k}$ is shown in **Figure 1B**) bottom left plot.

The equations are non-dimensionalized by scaling length with the shell thickness $d = r_o - r_i$, time by the viscous diffusion time $\tau_\nu = d^2/\nu$ and entropy by $d|d\tilde{s}/dr|_{r_i}$. To avoid radius dependent control parameters, reference values for $\tilde{\rho}, \tilde{T}, \tilde{\kappa}, \tilde{g}$ are taken at the outer boundary. The convective Rossby number Ro_c, the non-dimensional Brunt-Väisälä frequency and the non-dimensional stratification parameter are

$$Ro_c = \sqrt{\frac{Ra}{Pr}}E, \quad N = \max\left[\sqrt{\frac{Ra}{Pr}\tilde{g}(r)\frac{d\tilde{s}}{dr}}\right],$$
$$I_s = \max\left[\frac{2}{Ro_c}\left(\tilde{g}(r)\frac{d\tilde{s}}{dr}\right)^{-1/2}\right]. \tag{16}$$

3. NUMERICAL RESULTS

Equations 3, 4 are solved numerically using MagIC 5.6 (Wicht, 2002; Gastine and Wicht, 2012; Schaeffer, 2013) which is modified such that the non-adiabatic background state relations (Equation 8) are integrated. The mechanical confinement yields impenetrable and free-slip conditions at both walls. The entropy boundary conditions are fixed-flux in accordance with the stratification profile (Equation 11), which sets unstable and stable regions. The stratified layer is located between $r_{lb}/r_o = 0.57$ and $r_{ub}/r_o = 0.67$. The numerical grid resolution is $N_r \times N_\vartheta \times N_\phi = 145 \times 256 \times 512$ for $E = 10^{-4}$, $193 \times 320 \times 640$ at $E = 3 \cdot 10^{-5}$ and $241 \times 320 \times 640$ at $E = 10^{-5}$. The spectral resolution is limited to $N_\ell = 2/3\, N_\vartheta$. Fixed parameter values are the aspect ratio $\beta = r_i/r_o = 0.17, \epsilon_s = 10^{-4}, d_s = 75$, gravity according to Equation 12, $Di = 3$ and $\Gamma = 0.513$.

The other parameters, Ra, E, Pr, A_{SSL} are varied to explore the parameter dependencies. **Figure 2** provides an overview of Ro_c and I_s for the four sets of models. In models from group 1 the stratification amplitude (hence I_s) is varied and Ro_c kept fixed. Group 2 investigates the influence of more vigorous convection, where increasing Ra yields a decrease of I_s, but an increase of Ro_c. For group 3, I_s is kept constant, but with different combinations of Pr, Ra, and A_{SSL}. Finally, group 4 investigates the Ekman number (E) dependence.

The immediate effect of adding a stratified layer can be seen in the radial profiles of non-axisymmetric poloidal kinetic energy for models from group 1 displayed in **Figure 3**. For instance, the dark-red profile indicates that the non-axisymmetric poloidal kinetic energy is suppressed by up to four orders of magnitude

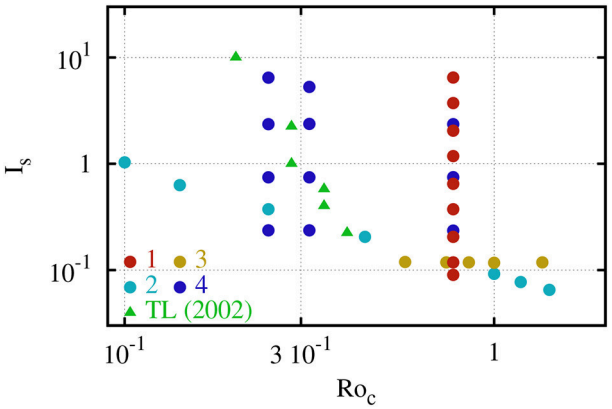

FIGURE 2 | Regime diagram of the numerical models from **Table 1** sorted by their respective convective Rossby (Ro_c) and the stratification relative to rotation rate (I_s). The colors indicate simulations from different groups. The green triangles mark the cases used in Takehiro and Lister (2002).

relative to a model without stratification (gray). Along both edges of the SSL region (highlighted in gray), the kinetic energy drops sharply. The inverse buoyancy in the SSL also reduces the flow amplitude outside of the stable zone. This might be linked to the columnar structures of the convective flows since their vertical extension along the rotation axis is limited by an increasing stratification in the SSL. In addition an asymmetry between the lower and upper interface is clearly visible when the stratification is stronger, where for the upper one the radial flows seem to require more buoyancy to replenish after being reflected at the SSL underneath. This might be due to the fact, that the SSL itself acts as solid bottom wall hence providing a virtual tangent cylinder at $r_{ub}/r_o = 0.67$.

The inverse buoyancy force in stratified regions directly acts to damp radial flows, which are consequently diverged into horizontal directions. Hence, the effect of the SSL should be clearly visible in each of the non-axisymmetric flow components. For example is the time-averaged intensity of radial flows v_r given by:

$$v_r(r,\vartheta) = \frac{1}{2\pi r^2}\sqrt{\langle u_r'^2\rangle_{t,\phi}}, \tag{17}$$

where the prime indicates non-axisymmetric flow. v_ϑ and v_ϕ are defined accordingly. **Figure 3**, right shows the radial profiles of v_r, v_ϕ and v_ϑ for model 1.2 (red profile in panel a). It is obvious, that the poloidal energy is a rather good proxy of the radial flow intensity. Since the radial flows are mainly deflected into horizontal directions, v_ϕ and v_ϑ appear muss less damped inside the SSL. Those represent wave-like, horizontal flows with frequencies smaller than the rotation or Brunt-Väisälä frequency. The strong decay of v_r allows to investigate the damping behavior. For guidance, the dashed lines in the figure represent exponential functions suggestive of exponential damping at the edges of the stratified regions. Their decay exponents are the penetration depths from **Table 1**. The actual determination of the

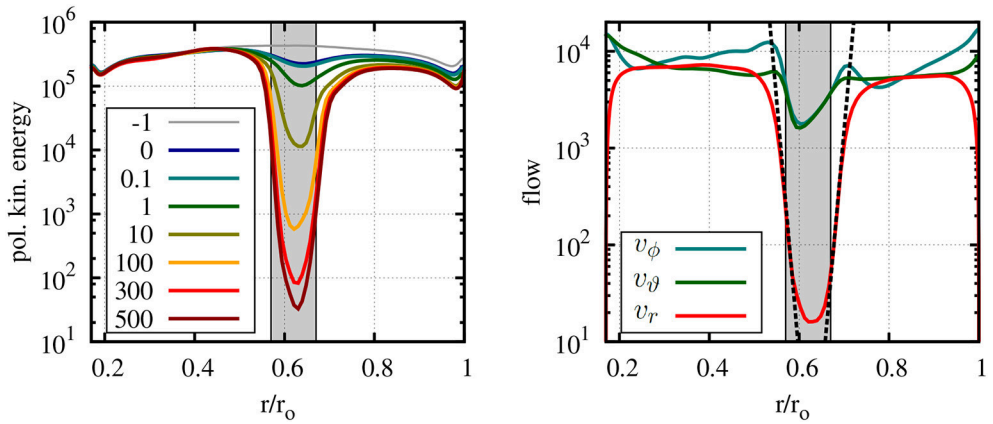

FIGURE 3 | Time averaged radial profiles of the non-axisymmetric poloidal energy for various stratification strength A_{SSL} **(Left)** and horizontally averaged intensity of non-axisymmetric flow components v_r, v_ϕ, v_ϑ for model 1.2 with $A_{SSL} = 300$ **(Right)**. The dashed lines denote the assumed exponential decay laws.

penetration depth is more involved and discussed in section 3.2 and **Figure 9**.

Those models might be biased by the choice of a somewhat large Ekman number (too viscous). For a more detailed inspection, a model with smaller Ro_c hence stronger rotational constraints is favored (model 4.10). **Figure 4** shows the instantaneous radial flow along a meridional cut (a) and in the equatorial plane (b). For this particular model, $I_s = 0.746$ and $Ro_c = 0.245$. It is obvious that the stratification breaks the geostrophy of the convective columns and efficiently wipes out radial flows in the SSL. This shows that in the SSL the inverse buoyancy exceeds the Coriolis force ($I_s < 1$). For both convective regions, the vertical length scale is clearly larger than the horizontal ones showing the effect of $Ro_c < 1$. Further, the convective structures outside the tangent cylinders given by r_i/r_o and r_{ub}/r_o, respectively, are vertically more extended than the corresponding convective flows inside the TCs. Furthermore, **Figure 4C**) indicates that the zonal flow is connected through the SSL between the convective shells. At the outer boundary of the model domain representing the planetary surface, the equatorial region features a wide prograde jet reminiscent of Saturn's equatorial super-rotating jet.

3.1. Radial Flows in the Vicinity of Stratified Layers

The spherical surface projections (**Figures 5A–I**) reveal more details of the damping mechanisms. The nine maps represent several radial levels ranging from below the SSL (a), to the center $r/r_o = 0.62$ (e), and on top of the SSL at $r/r_o = 0.695$ (i). The typical columnar structures in the lower convective layer are apparent outside TC (a, b). As those are more rotationally constrained by the Coriolis force they can penetrate deeper into the stable layer than the spiraling structures at higher latitudes and though cause the radial flow peaks around $\pm 60^\circ$ colatitude (b, c). Deeper inside the SSL, in the equatorial regions, large length scale flows appear more dominant (c), even exceeding the remaining columnar patterns found in higher latitudes (d, e). The rms radial flow amplitude decreases drastically toward the center of the SSL, but at unequal rates for different colatitudes and different length scales. In the center of the SSL (**Figure 5E**) the flow is of weak amplitude and apparently dominated by the larger length scale. The amplitude has been decreased by a factor of 35, where the strongest remaining flows are concentrated in a broad belt around the equator. This is unlikely linked to rotational penetration as no columns can be vertically extended. For inertia penetration to be efficient, the flow must be energetic, what does not seem to be the case for those large scale and weak amplitude flows. Toward the outer edge of the SSL (f-g), the flow amplitudes keep increasing featuring columnar elongated structures outside and small-scale, spiraling convection patterns inside the effective tangent cylinder (h-i). The effective TC is now attached to the upper edge of the SSL at r_{ub}, hence the columnar flows are confined to a much smaller colatitude range.

This indicates that when columns touch on the stratified layer, they penetrate deeper, likely due to the rotational penetration or the Taylor-Proudman theorem. However, in the inner equatorial region and inside the inner TC, this effect is secondary. Even more so for the penetration at the outer boundary, where columns may only directly touch the stratified layer at a low-latitude band. As a result, the inertia penetration dominates, but is somewhat modified by latitudinal effects.

For a more detailed analysis of the apparent colatitudinal variation and the length scales dependencies, a FFT transforms from $v_r(r, \vartheta)$ to $v_r^\star(r, \ell)$, where ℓ is the spherical harmonic degree. For a few radii, this is shown as a function of either colatitude or spectral degree in **Figure 6**. The radial flow intensity drops slightly before reaching the lower SSL edge at $r_{lb}/r_o = 0.57$ (top left), though with weak modulation along colatitude ϑ. At the edge (blue line), the damping is strongest close to the rotation axis and around the equatorial region. In between rotational penetration somewhat reduces the damping of radial flows (profiles are closer to each other). This is the expected behavior, as the Coriolis forces act to extend convective columns into the stratified region predominantly at mid-latitudes outside TC. For the upper edge (top left), the region inside TC is larger and spans roughly the upper half of the colatitude domain. There

TABLE 1 | Numerical models performed.

No.	Ra	Pr	E	A_{SSL}	l_s	Ro_c	δ_r^+	δ_r^-
1.1	$3 \cdot 10^7$	0.5	10^{-4}	500	0.09	0.775	$7.59 \cdot 10^{-3}$	$7.68 \cdot 10^{-3}$
1.2	$3 \cdot 10^7$	0.5	10^{-4}	300	0.118	0.775	$8.24 \cdot 10^{-3}$	$8.35 \cdot 10^{-3}$
1.3	$3 \cdot 10^7$	0.5	10^{-4}	100	0.205	0.775	0.0130	0.0111
1.4	$3 \cdot 10^7$	0.5	10^{-4}	30	0.373	0.775	0.0167	0.0162
1.5	$3 \cdot 10^7$	0.5	10^{-4}	10	0.647	0.775	0.0314	0.0247
1.6	$3 \cdot 10^7$	0.5	10^{-4}	3	1.18	0.775	0.0612	0.0533
1.7	$3 \cdot 10^7$	0.5	10^{-4}	1	2.05	0.775	0.144	0.107
1.8	$3 \cdot 10^7$	0.5	10^{-4}	0.3	3.73	0.775	0.377	0.221
1.9	$3 \cdot 10^7$	0.5	10^{-4}	0.1	6.47	0.775	0.688	0.238
1.10	$3 \cdot 10^7$	0.5	10^{-4}	0	∞	0.775	0.805	0.2446
2.1	$7 \cdot 10^5$	0.5	10^{-4}	300	1.03	0.1	0.0173	0.0721
2.2	$1 \cdot 10^6$	0.5	10^{-4}	300	0.63	0.141	0.0136	0.0561
2.3	$3 \cdot 10^6$	0.5	10^{-4}	300	0.373	0.245	0.0166	0.0266
2.4	$1 \cdot 10^7$	0.5	10^{-4}	300	0.205	0.447	$8.095 \cdot 10^{-3}$	$7.01 \cdot 10^{-3}$
2.5	$5 \cdot 10^7$	0.5	10^{-4}	300	0.092	1.0	$8.875 \cdot 10^{-3}$	$8.40 \cdot 10^{-3}$
2.6	$7 \cdot 10^7$	0.5	10^{-4}	300	0.077	1.18	$8.18 \cdot 10^{-3}$	$8.055 \cdot 10^{-3}$
2.7	$1 \cdot 10^8$	0.5	10^{-4}	300	0.065	1.41	$7.83 \cdot 10^{-3}$	$6.77 \cdot 10^{-3}$
3.1	$1 \cdot 10^7$	0.3	10^{-4}	500	0.119	0.574	$8.02 \cdot 10^{-3}$	$7.585 \cdot 10^{-3}$
3.2	$5.5 \cdot 10^7$	1.0	10^{-4}	330	0.118	0.742	$6.68 \cdot 10^{-3}$	$7.51 \cdot 10^{-3}$
3.3	$5.5 \cdot 10^7$	0.75	10^{-4}	250	0.118	0.854	$7.59 \cdot 10^{-3}$	$6.79 \cdot 10^{-3}$
3.4	$3 \cdot 10^7$	0.3	10^{-4}	200	0.117	1	0.0107	$8.84 \cdot 10^{-3}$
3.5	$5.5 \cdot 10^7$	0.3	10^{-4}	100	0.118	1.352	0.0106	$8.48 \cdot 10^{-3}$
4.1	$3 \cdot 10^7$	0.5	10^{-4}	75	0.236	0.775	0.0132	0.0120
4.2	$3 \cdot 10^7$	0.5	10^{-4}	7.5	0.746	0.775	0.035	0.0292
4.4	$3 \cdot 10^7$	0.5	10^{-4}	0.75	2.36	0.775	0.1748	0.1339
4.5	$1.1 \cdot 10^8$	1.0	$3 \cdot 10^{-5}$	500	0.236	0.316	$6.44 \cdot 10^{-3}$	$7.32 \cdot 10^{-3}$
4.6	$1.1 \cdot 10^8$	1.0	$3 \cdot 10^{-5}$	50	0.746	0.316	0.0145	0.0145
4.7	$1.1 \cdot 10^8$	1.0	$3 \cdot 10^{-5}$	5	2.36	0.316	0.0421	0.0310
4.8	$1.1 \cdot 10^8$	1.0	$3 \cdot 10^{-5}$	1	5.277	0.316	0.143	0.1062
4.9	$6.3 \cdot 10^8$	1.0	10^{-5}	750	0.236	0.245	$6.22 \cdot 10^{-3}$	$9.18 \cdot 10^{-3}$
4.10	$6.3 \cdot 10^8$	1.0	10^{-5}	75	0.746	0.245	0.0117	0.0161
4.11	$6.3 \cdot 10^8$	1.0	10^{-5}	7.5	2.36	0.245	0.0319	0.0309
4.12	$6.3 \cdot 10^8$	1.0	10^{-5}	1.0	6.463	0.245	0.1593	0.1117

***Figure 2**, left plot scatters the models over their associated time scale ratios, i.e., Ro_c and l_s.*

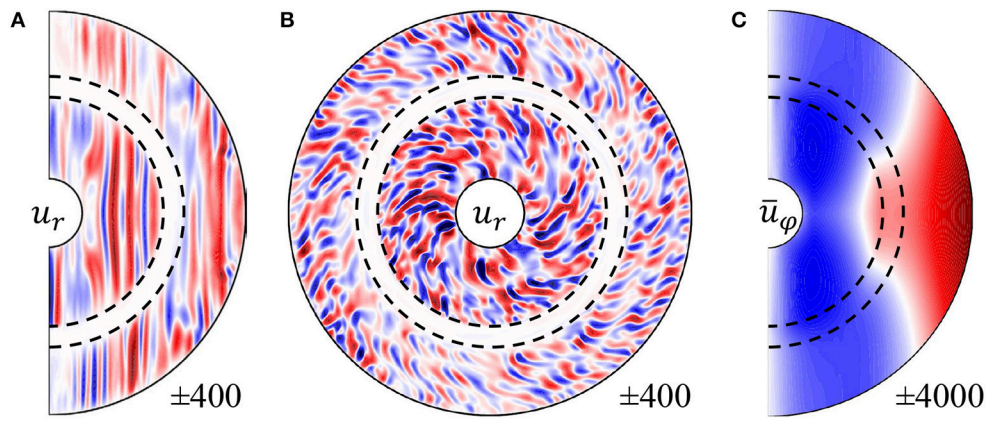

FIGURE 4 | Instantaneous radial flow in a meridional slice **(A)** and in the equatorial plane **(B)** as far as the axisymmetric zonal flow averaged over time **(C)** for model 4.10 from **Table 1**.

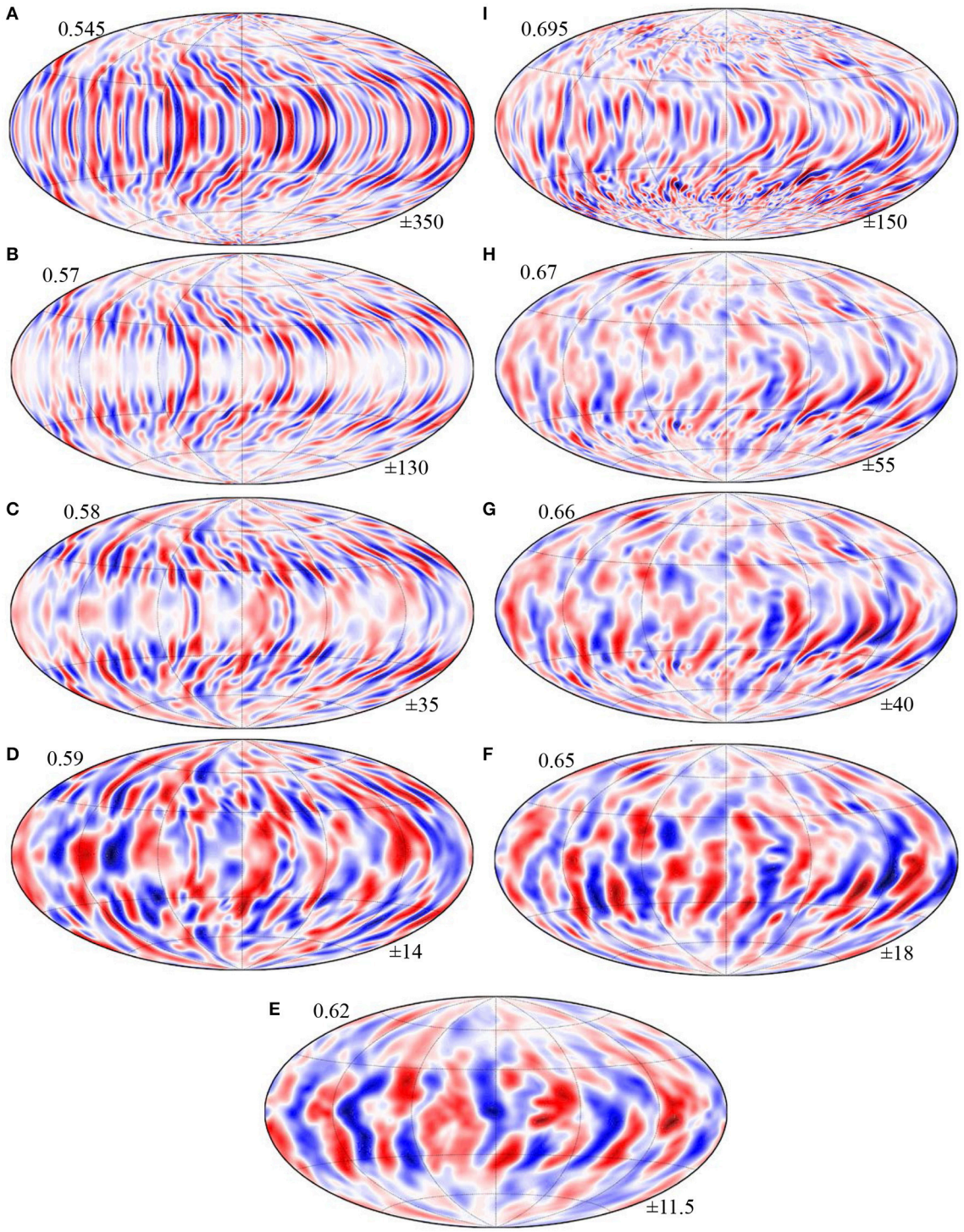

FIGURE 5 | Instantaneous radial flow on spherical surfaces taken at various radii indicated at the top left of each panel, ranging from r = 0.545 **(A)** over the center of the SSL at r = 0.62 **(E)** to r = 0.695 **(I)**. The min/max velocity contour is indicated at the lower right. The velocity scale is the Reynolds-number. Parameters: model 4.10 from **Table 1**, $l_S = 0.746$, $Ro_C = 0.245$.

the radial flows decrease strongly with colatitude toward the poles, but are rather constant outside TC. In general, the radial flows close the equator remain strongest in the center of the SSL.

In the bottom plot of **Figure 6**, the radial flow per spectral degree ℓ is shown at the same depth levels used before. The broad peaks around $\ell = 10 - 50$, indicate the mean convective

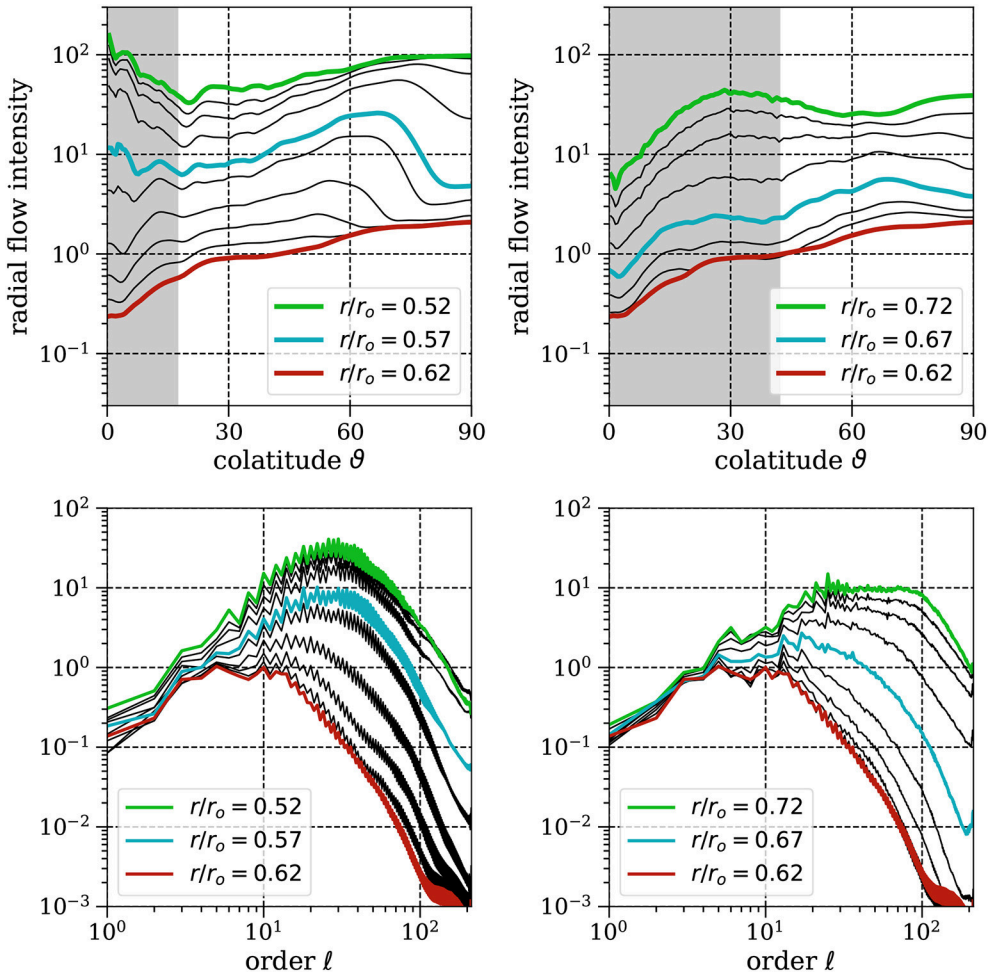

FIGURE 6 | Time and azimuthally averaged intensity of radial flows at various depth around the edge of the SSL $r_{lb} = 0.57$ **(Left)** and $r_{ub} = 0.67$ **(Right)**. The upper plot show profiles along colatitude, the lower for spectral degree (length scale). The gray shaded areas mark colatitude bands inside the tangent cylinder set in the inner convective shell by $\sin\vartheta_{TC} = r_i/r_{lb}$ (top left) and in the outer convective shell by $\sin\vartheta_{TC} = r_{ub}/r_o$.

horizontal length scales outside the SSL (green profiles). In this representation, it is obvious that small length scale flows are stronger suppressed by the inverse buoyancy gradients. Whereas, at the short length scale end of the spectrum at $\ell \approx 100$ the total drop exceeds two orders of magnitude, the large length scales are damped less than one order of magnitude. Especially for the intermediate length scales around $\ell \approx 5 - 50$ the suppression seems most efficient. Comparing the spectra outside the SSL (green profile, **Figure 6**) with those at the bottom of SSL (red) clarifies why the flows seen before in **Figure 5E** are so large scale. This behavior appears rather similar for both edges of the SSL (bottom left). The effects of viscosity are only visible at the largest length scales, where the spectra follow different slopes. At the largest length scales, the flow amplitudes are not damped at all, but rather maintained across the stable layer. This points toward an additional source of radial flows powered by the convergence and dissipation of horizontal flows, which manifest as gravito-inertial waves.

3.2. Penetration Depth

For a qualitative assessment we assume that the penetration depth of radial flows is a linear function of the radial flow intensity itself (Takehiro and Lister, 2001) and potentially varying along colatitude. This implies, that

$$v_r(r,\vartheta) \propto \exp^{-r/\delta}, \tag{18}$$

where the penetration depth δ is defined by the e-fold decay scale height

$$\delta(r,\vartheta) = -v_r(r,\vartheta)\left[\frac{\partial v_r(r,\vartheta)}{\partial r}\right]^{-1} = -\left[\partial_r \log v_r(r,\vartheta)\right]^{-1}. \tag{19}$$

Figure 3, right show that the radial profiles v_r drops exponentially in the vicinity of the neutral buoyancy radii located at $r_{lb}/r_o = 0.57$ and $r_{ub}/r_o = 0.67$, respectively. The penetration depth is calculated as a function of radius using

Equation 19 while averaging over the colatitude ϑ

$$\delta_r(r) = -\left[\partial_r \log \tilde{v}_r(r)\right]^{-1} \quad \text{with} \quad \tilde{v}_r = \frac{1}{2}\int_0^\pi v_r(r,\vartheta)\sin\theta\, d\theta \tag{20}$$

or as function of colatitude taken at the lower edge of the stratified region

$$\delta_\vartheta(\vartheta) = -\left[\partial_r \log v_r(r_{lb},\vartheta)\right]^{-1} . \tag{21}$$

Finally, we also investigate the length scale dependence in terms of the spherical harmonic degree ℓ as used in the linear theory study by Takehiro and Lister (2001):

$$\delta_\ell(\ell) = -\left[\partial_r \log v_r^\star(r_{lb},\ell)\right]^{-1} , \tag{22}$$

where $v_r^\star(r,\ell) = \mathrm{FFT}\left\{v_r(r,\vartheta)\right\}$ is the Fourier-transformed.

Figure 7 shows the colatitude dependence of δ_ϑ for the nine cases (group 4 in **Table 1**). The reference model (no. 4.10) previously being subject of a detailed investigation, is placed left in the middle row. The other cases are set up such that Ro_c is constant for each column and I_s for each row (both indicated at the top right). Inertia increases from left to right, the stratification strength relative to the rotation rate from top to bottom.

The overall penetration depth decreases with decreasing inertia (Ro_c) and increasing stratification (I_s). For the top right model, the inertia is strong and the stratification weak ($Ro_c = 0.78$, $I_s = 2.36$), such that the penetration depth exceeds significantly the thickness of the SSL ($0.1\, r_o$). If I_s is ten-fold decreased (bottom right) the penetration depth is reduced to a fraction of the SSL width and the radial flows are hence tiny deep inside the SSL. For the other columns, smaller Ekman numbers provide smaller Ro_c and consequently smaller penetration depth as the efficiency of overshooting convection is reduced. All models seem to share significant higher penetration depths at mid-latitudes. Inside the TC and in equatorial regions the penetration depth is typically smaller. However, the penetration depth is bounded by the viscosity (horizontal green lines, $\delta_\nu = \sqrt{E}$) and apparently cannot be reduced far below this value. We conclude that the penetration

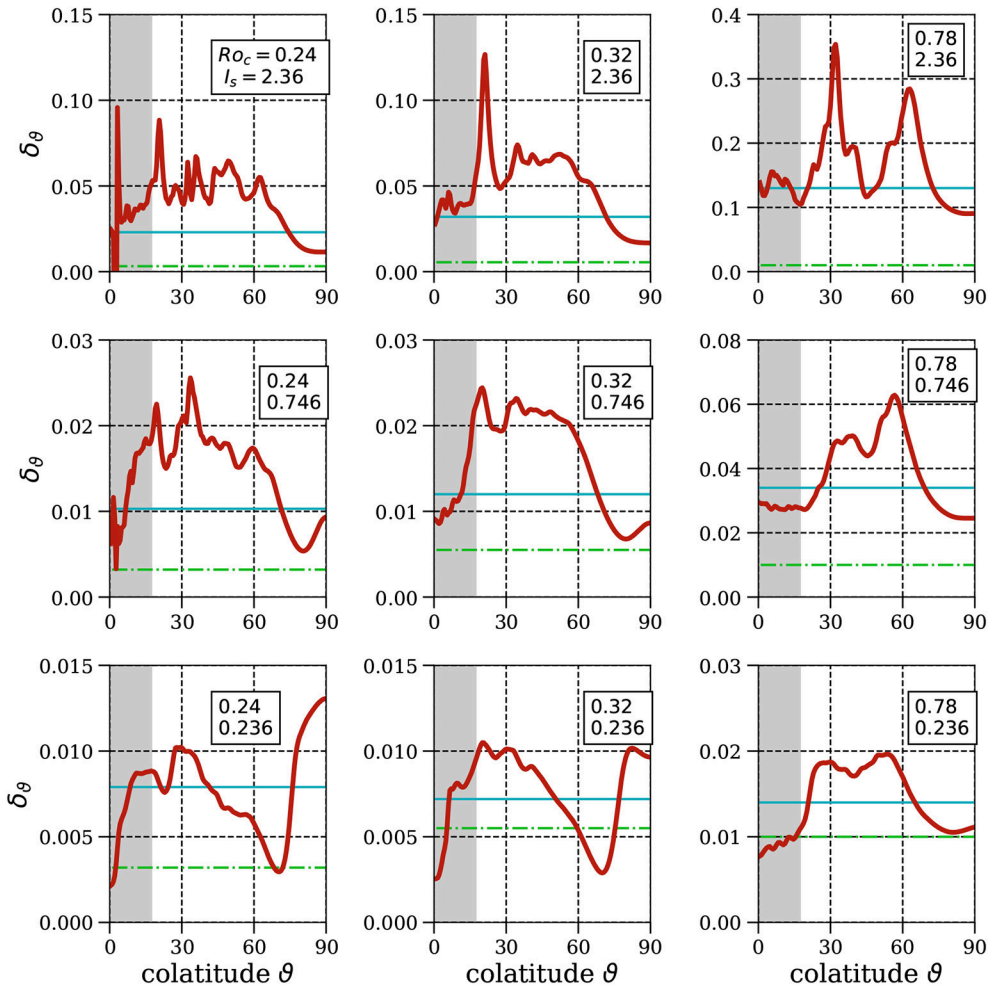

FIGURE 7 | Penetration depth of radial flows as a function of colatitude for nine cases from **Table 1**, group 4 taken at the lower edge of the SSL $r = r_{lb}$. The green line shows the thickness of an Ekman layer $\delta_\nu = \sqrt{E}$. The gray shaded areas mark colatitude bands inside the tangent cylinder set by $\sin\vartheta_{TC} = r_i/r_{lb}$.

depth at intermediate colatitudes of $30 - 60^\circ$ can easily reach twice its mean value, indicated by the blue lines, what is most clearly seen in the bottom right panel. It was shown before that large scale flows remain most dominant in the equatorial regions. Those are obviously only weakly damped (**Figure 6**), bottom, yield larger penetration depth in the equatorial regions (**Figure 7**, left bottom) and might originate from collision of horizontal flows.

Takehiro and Lister (2001) concluded that the stable layer acted as a spectral filter with low pass nature, more precisely they predict that δ_ℓ should decay like $1/|\ell|$. **Figure 8** shows δ_ℓ for the nine cases from group 4 (see **Table 1**, **Figure 7**). The blue horizontal lines denote the mean value listed in **Table 1**, the green one marks the thickness of the Ekman layer.

It can be seen, that penetration depth clearly decays for smaller length scales even for cases with rather large inertia and weak stratification (top right). As shown for the case 4.10 in **Figure 6**, the largest (small ℓ) and smallest length scales (large ℓ) contain little kinetic energy and are excluded from the analysis. Therefore, power laws of the form

$$\delta_\ell \propto \ell^\gamma \tag{23}$$

are fitted over an intermediate ℓ-range that is highlighted in gray. The resulting spectral decay exponent is added on the bottom of each panel. The slopes are all negative and spread amongst $\gamma = [-0.55, -1.03]$, where models with weak inertia and strong stratification approach the $(\gamma = -1)$-scaling predicted by the linear theory of Takehiro and Lister (2001). Those models are most effectively controlled by rotational penetration and not overly biased by inertia. This indicates that the results of Takehiro and Lister (2001) can only be applied to an intermediate length scale range, for which the agreement is striking. The large ℓ part, which has been excluded from the fit, might be controlled by the viscosity and hence the penetration depth is not decreasing below the thickness of the Ekman layer. For the small ℓ part of the spectrum, the associated flows are controlled by other means, where the large scale patterns found in the equatorial

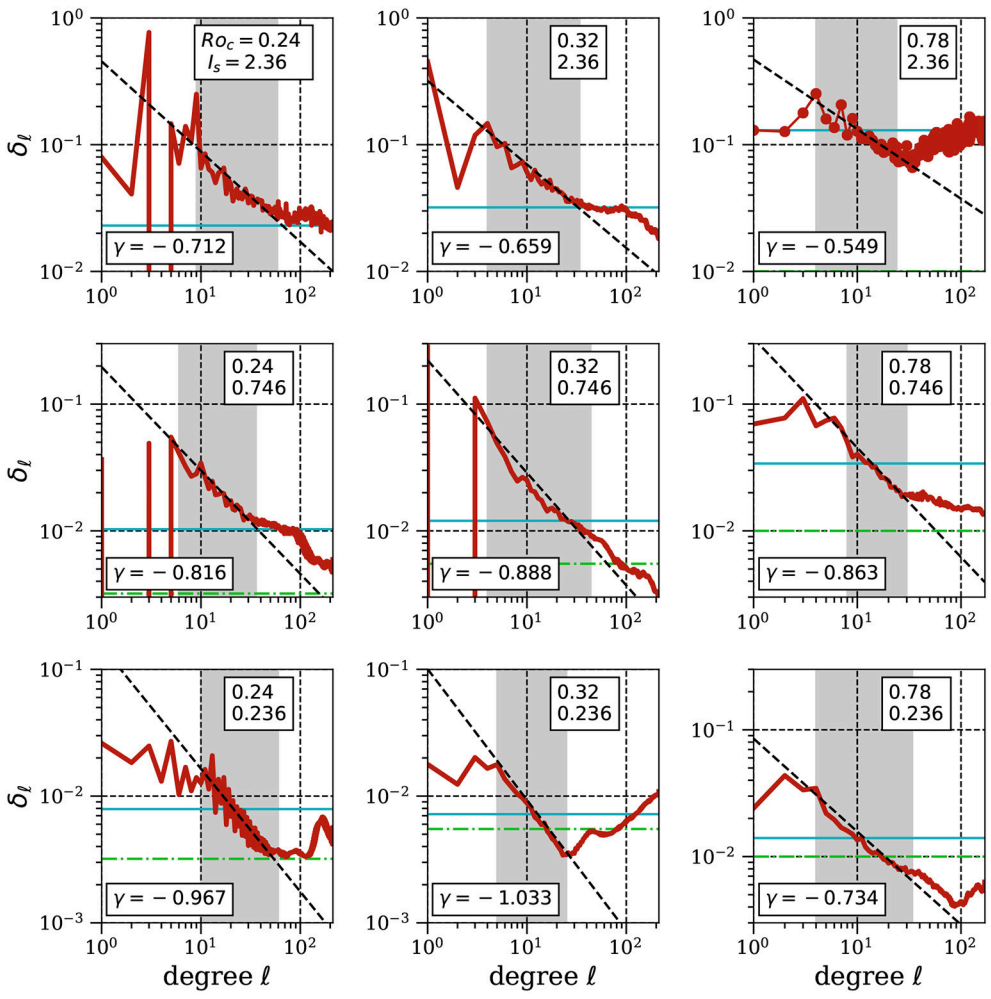

FIGURE 8 | Penetration depth as a function of spectral degree ℓ for the nine case of group 4 in **Table 1**. The horizontal blue lines indicate the mean values. The green line shows the thickness of an Ekman layer $\delta_\nu = \sqrt{E}$. The black lines show power laws fitted over the gray-shaded length scale ranges resulting into a decay exponent γ added at the bottom of each figure.

regions (compare **Figure 5E**) or meridional circulation induced by the latitude-dependent penetration might play a role. Also other typical flows found in stratified regions, such as gravito-inertial waves could be taken into account. Those might then be the same features seen before in the equatorial regions (**Figure 5E**) deep inside the SSL around the equator. If applicable, the radial waves are then excited by dissipating or diverging the horizontal counterparts preferentially in the equatorial belt.

Finally, the dependence of the mean penetration depth on the model parameters (Ra, E, Pr and A_{SSL}) is studied. The penetration depth at the lower and upper boundary of the SSL are indicated by δ_r^+ and δ_r^-. Those are derived by taking the minimal value of δ_r in the vicinity ($\pm 0.01 r_o$) of r_{lb} and the maximal value of $-\delta_r$ near r_{ub} (see also **Figure 9**).

Figure 10 shows δ_r^+ and δ_r^- for all models from **Table 1**. It can be clearly seen, that δ_r decreases with increasing stratification and settles somewhat below $\delta_r = 0.01$. This lower boundary is due to viscosity and hence depending on the Ekman number. For all studied Ekman numbers δ_r can be decreased to values approximatively the Ekman layer thickness ($\delta_E = E^{1/2}$) suggesting that our numerical setup is only limited by the viscosity. Models with δ_r larger than the width of SSL ($0.1\, r_o$) are robustly constrained, as the mean radial flow intensity drops noticeable across the SSL, yet less than e-fold. As shown by the dark-blue profile in the left panel of **Figure 3**, even models with neutral buoyancy gradient ($A_{SSL} = 0$) in the SSL create a strong dimple in the poloidal energy. Apparently δ_r^+ and δ_r^- are nearly identical, suggesting that there is no major dynamic difference between a scenario where the stable region is on top of the convective one and the opposite situation. As the Coriolis force clearly dominates the flows in convective regions ($Ro_c < 1$), it appears reasonable to expect that $I_s = \tau_{strat}/\tau_{rot}$ is the appropriate force ratio to estimate the penetration depth (**Figure 10**, left). However, this does not seem to hold for all Ekman numbers. The right hand plot of **Figure 10** shows an alternative scaling attempt relative to $I_s\, Ro_c = \tau_{strat}/\tau_{buo}$, i.e., the rotational time scale is replaced with the inertia time scale. This indicates that the penetration depth δ_r is independent of rotation and depends, as in a non-rotating system, only on the ratio of inertia and stratification. Further, a power law fit of the form

$$\delta_r = a \cdot (I_s\, Ro_c)^b \tag{24}$$

results in $a = 0.121 \pm 0.008$ and $b = 0.989 \pm 0.1162$ and hence suggesting a linear dependence. For the least-squares fitting procedure only data points were considered for which $I_s\, Ro_c > 0.1$, since they are not biased by viscosity (thick black, dot-dashed line in **Figure 10**, right).

Previous studies targeted to the radiative-convective boundary in the Sun, such as (Hurlburt et al., 1994; Brummell et al., 2002; Rogers et al., 2006) controlled the degree of stratification by reducing or increasing the local polytropic index n_i below or above the adiabatic one n_a. Using the polytropic relations (e.g., $\rho = \rho_o \xi^n$, where ξ is a function of r), the deviation from the adiabat can be expressed by logarithmic density gradients and

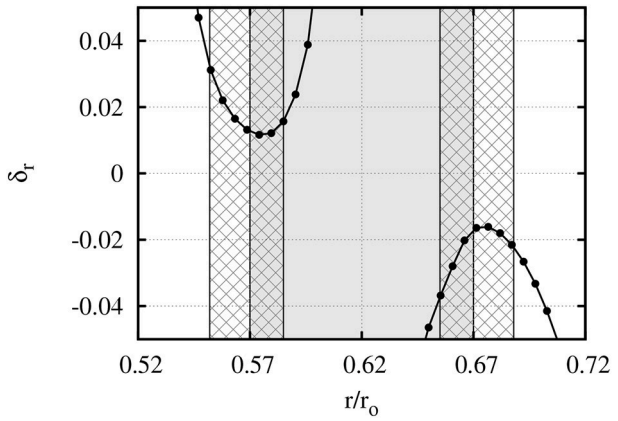

FIGURE 9 | Mean penetration depth along radius for model 4.10. The gray shaded area marks the SSL; the hatched areas indicate the radius range in which the extrema of δ_r are taken.

polytropic indices

$$\frac{1}{\rho}\frac{d\rho}{dr} - \frac{1}{\rho}\frac{d\rho}{dr}\Big|_a \propto (n_i - n_a)\,\frac{\xi'}{\xi} \propto \frac{1}{c_p}\frac{ds}{dr}\,, \tag{25}$$

where index a refers to the adiabat. Consequently, the stratification measure S defines the ratio of subadiabatic (positive) to superadiabatic (negative) entropy gradients and is compatible with our stratification amplitude $S \approx A_{SSL}$. Whereas, the numerical models in the previous study cover stratifications between $S = 1$ and $S = 30$, our parameter space with respect to A_{SSL} spans from 0 to 750 (see **Table 1**). Further the scaling above suggested that

$$\delta_r \propto I_s Ro_c = 2\left(g(r)\frac{d\tilde{s}}{dr}\right)^{-1/2} \approx A_{SSL}^{-1/2}\,. \tag{26}$$

Hence, our results show that the penetration depth increases with the square root of the ratio of positive and negative entropy gradients. Firstly reported by (Hurlburt et al., 1994), comparable models found different scaling exponents, which changed as a function of S. Typically for small S the penetration depth scales with $\delta_r \propto S^{-1}$, but for larger S with a significantly shallower $S^{-1/4}$ (Hurlburt et al., 1994). Other studies only found the weak scaling throughout the studied S-range (Brummell et al., 2002; Rogers et al., 2006). For guidance, both scaling laws are drawn into **Figure 10**, right, thin gray dashed lines. Indeed those predictions seem to approximate the data in local sub-regions of the parameter space. However, the general trend appears much better reproduced by a single scaling law with an exponent of roughly $S^{-1/2}$.

4. SUMMARY AND DISCUSSION

We have performed an extensive numerical modeling campaign of rapidly rotating convection in a spherical shell that exhibits a sandwiched stable stratified layer between two convective

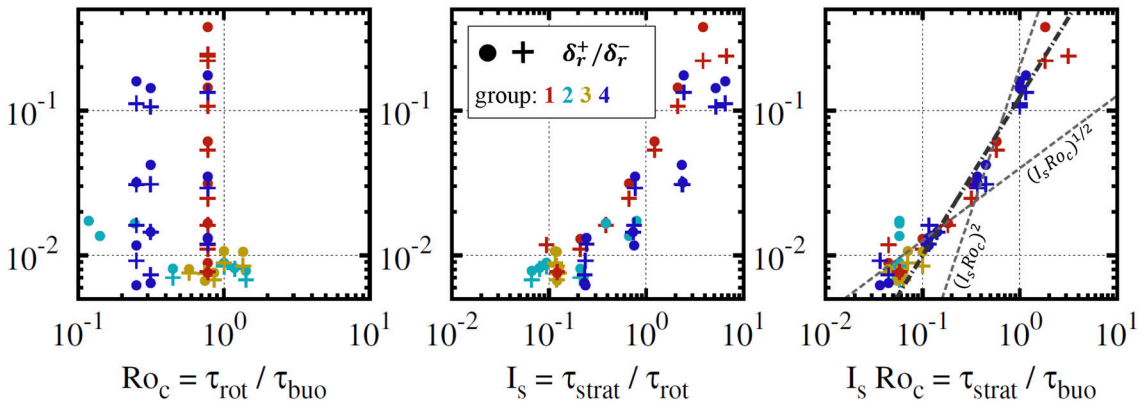

FIGURE 10 | Mean penetration depth at the lower edge (δ_r^+, filled circles) and upper edge (δ_r^-, plus markers) as a function of time scale ratios. Plotted are models from **Table 1**, colors indicate various groups. For the right hand plot a power law is fitted to the data for $I_S\, Ro_C > 0.1$ (thick black, dot-dashed line), showing the almost linear dependence of $\delta_r \propto I_S\, Ro_C$. The thin gray power laws indicate previously published scaling suggestions. For details, see text.

zones. Such a system is most suitable for Saturn, where the H/He demixing generates a compositional gradient around mid-depth and though suppresses thermal convection locally. Our numerical models cover a large fraction of the appropriate parameter space, e.g., in the terms of the stratification relative to rotational forces $2\Omega/N$, where N is the Brunt-Väisälä frequency or relative to the inertia characterized by Ro_c (see also **Table 1**).

Stratification acts directly to suppress radial flows, but radial flows can pierce across the interface by different mechanisms. The classic overshooting penetration depends on the inertia a fluid parcel has gained from buoyancy instabilities. Furthermore, rapid rotation and the spherical geometry allows convective columns to be vertically extended into the stratified regions in accordance with the Taylor-Proudman theorem. We investigate and distinguish the potential effects of both penetration mechanisms by altering the leading order force balances. Our results indicate that the mean penetration depth depends linearly on the square root of the ratio of destabilizing and stabilizing entropy gradients ($\delta_r \approx A_{SSL}^{-1/2}$). This builds on the rather diverse results derived in the solar context (Zahn, 1991; Hurlburt et al., 1994; Brummell et al., 2002; Rogers et al., 2006), where different scaling exponents with stronger scaling for weaker stratification were reported. The exponents in those studies range from $-1/4$ to -1, but the robust $-1/2$-scaling suggested in the present study reproduces the results convincingly. In addition, and in contrast to the expectations from Takehiro and Lister (2001), the magnitude of the penetration depth appears largely unaffected by the rotation.

The Coriolis force, however, adds a characteristic latitudinal modulation of the penetration depth amplifying to $\pm(40-50)\%$ of the mean value, where the strongest penetration resides at mid-latitudes (outside TC). This clearly reflects the action of columnar structures vertically extended by the Coriolis force and hence represents rotational penetration. Therefore, latitudinal density gradients are expected to build up at the edges of stratified regions. Such gradients are known to drive baroclinic instabilities, e.g., thermal winds.

Alongside original studies using linear waves, such as Takehiro and Lister (2001), a spectral (length scale) dependence of the penetration depth is expected and this is indeed found in our strongly non-linear simulations. The decay exponent γ approaches unity, what confirms the expected value from linear theory (Takehiro and Lister, 2001). The SSL though clearly shows the quality of a low pass filter. Consequently, radial flow in the SSL, even though weak in amplitude, must be expected to be of larger length scale than the convective flows pummeling into the SSL. However, the striking agreement with the theoretical predictions is limited to an intermediate length scale range.

As a peculiar result, we have identified wave-like radial flows that seem to somewhat resist the inverse buoyancy forces in the stratified layer. Those are non-geostrophic, of large length scale, weak in amplitude, and predominantly driven in the equatorial regions of the stratified layer. We showed that the required additional source of radial flow is likely not due to the length scale filtering effect of the rotational penetration or due to inertia penetration, but is potentially powered from the convergence of horizontal flows in the shape of gravito-inertial waves.

Finally, we have shown that viscous effects only play a role for very shallow penetration depth and at the smallest length scales. The overall results should not depend on the fact that we have only explored an Ekman number rage limited by the numerical constraints. More important is the spherical geometry. We speculate that a thin stable stratified layer will be significantly penetrated by Coriolis force induced columnar flows vertically extending into the SSL and hence more closely obey the linear theory by Takehiro and Lister (2001).

As an outlook for future work, a thorough investigation of the gravito-inertial waves generated in the SSL, the emergence of thermal winds due to latitude-dependent penetrative convection and consequently how differential rotation is paused through stratified zones. In addition, the effect on a dynamo process originating from underneath will help to understand the dynamics and magnetic fields of partly stratified rapidly rotating

convection, which is most suitable for the planetary atmospheres and interiors.

AUTHOR CONTRIBUTIONS

WD designed and carried out the numerical experiments, analyzed the data, and wrote the paper manuscript. JW provided physical insights, fluid dynamics expertise, and significantly contributed to the manuscript.

ACKNOWLEDGMENTS

The authors would like to thank the reviewers for their valuable comments and suggestions to improve the manuscript. This work was supported by the Deutsche Forschungsgemeinschaft (DFG) in the framework of the priority programs SPP 1488 "Planetary Magnetism" and SPP 1992 "Diversity of Exoplanets". MagIC is available at an online repository (https://github.com/magic-sph/magic).

REFERENCES

Atkinson, D. H., Pollack, J. B., and Seiff, A. (1996). Galileo doppler measurements of the deep zonal winds at jupiter. *Science* 272, 842–843. doi: 10.1126/science.272.5263.842

Browning, M. K., Brun, A. S., and Toomre, J. (2004). Simulations of core convection in rotating A-Type stars: differential rotation and overshooting. *Astrophys. J.* 601, 512–529. doi: 10.1086/380198

Brummell, N. H., Clune, T. L., and Toomre, J. (2002). Penetration and Overshooting in Turbulent Compressible Convection. *Astrophys. J.* 570, 825–854. doi: 10.1086/339626

Brun, A. S., Miesch, M. S., and Toomre, J. (2011). Modeling the dynamical coupling of solar convection with the radiative interior. *Astrophys. J.* 742:79. doi: 10.1088/0004-637X/742/2/79

Buffett, B. (2014). Geomagnetic fluctuations reveal stable stratification at the top of the Earth's core. *Nature* 507, 484–487. doi: 10.1038/nature13122

Cao, H., Russell, C. T., Wicht, J., Christensen, U. R., and Dougherty, M. K. (2012). Saturn's high degree magnetic moments: evidence for a unique planetary dynamo. *Icarus* 221, 388–394. doi: 10.1016/j.icarus.2012.08.007

Christensen, U. R. (2006). A deep dynamo generating Mercury's magnetic field. *Nature* 444, 1056–1058. doi: 10.1038/nature05342

Ellison, T. H., and Turner, J. S. (1959). Turbulent entrainment in stratified flows. *J. Fluid Mech.* 6, 423–448. doi: 10.1017/S0022112059000738

Fearn, D. R., and Loper, D. E. (1981). Compositional convection and stratification of earth's core. *Nature* 289:393. doi: 10.1038/289393a0

Fuller, J. (2014). Saturn ring seismology: evidence for stable stratification in the deep interior of Saturn. *Icarus* 242, 283–296. doi: 10.1016/j.icarus.2014.08.006

Gastine, T., and Wicht, J. (2012). Effects of compressibility on driving zonal flow in gas giants. *Icarus* 219, 428–442. doi: 10.1016/j.icarus.2012.03.018

Hedman, M. M., and Nicholson, P. D. (2013). Kronoseismology: using density waves in Saturn's C ring to probe the planet's interior. *Astron. J.* 146:12. doi: 10.1088/0004-6256/146/1/12

Hurlburt, N. E., Toomre, J., Massaguer, J. M., and Zahn, J.-P. (1994). Penetration below a convective zone. *Astrophys. J.* 421, 245–260. doi: 10.1086/173642

Jones, C. A. (2011). Planetary magnetic fields and fluid dynamos. *Ann. Rev. Fluid Mech.* 43, 583–614. doi: 10.1146/annurev-fluid-122109-160727

Julien, K., Legg, S., McWilliams, J., and Werne, J. (1996). Penetrative convection in rapidly rotating flows: preliminary results from numerical simulation. *Dynam. Atmos. Oceans* 24, 237–249. doi: 10.1016/0377-0265(95)00449-1

Leconte, J., and Chabrier, G. (2013). Layered convection as the origin of Saturn's luminosity anomaly. *Nat. Geosci.* 6, 347–350. doi: 10.1038/ngeo1791

Levy, M. A., and Fernando, H. J. S. (2002). Turbulent thermal convection in a rotating stratified fluid. *J. Fluid Mech.* 467, 19–40. doi: 10.1017/S0022112002001350

Lister, J. R., and Buffett, B. A. (1998). Stratification of the outer core at the core-mantle boundary. *Phys. Earth Planet. Inter.* 105, 5–19. doi: 10.1016/S0031-9201(97)00082-4

Nakagawa, T. (2011). Effect of a stably stratified layer near the outer boundary in numerical simulations of a magnetohydrodynamic dynamo in a rotating spherical shell and its implications for Earth's core. *Phys. Earth Planet. Inter.* 187, 342–352. doi: 10.1016/j.pepi.2011.06.001

Nettelmann, N., Püstow, R., and Redmer, R. (2013). Saturn layered structure and homogeneous evolution models with different EOSs. *Icarus* 225, 548–557. doi: 10.1016/j.icarus.2013.04.018

Püstow, R., Nettelmann, N., Lorenzen, W., and Redmer, R. (2016). H/He demixing and the cooling behavior of Saturn. *Icarus* 267, 323–333. doi: 10.1016/j.icarus.2015.12.009

Rogers, T. M., Glatzmaier, G. A., and Jones, C. A. (2006). Numerical simulations of penetration and overshoot in the sun. *Astrophys. J.* 653, 765–773. doi: 10.1086/508482

Schaeffer, N. (2013). Efficient spherical harmonic transforms aimed at pseudospectral numerical simulations. *Geochem. Geophys. Geosys.* 14, 751–758. doi: 10.1002/ggge.20071

Schöttler, M., and Redmer, R. (2018). Ab initio calculation of the miscibility diagram for hydrogen-helium mixtures. *Phys. Rev. Lett.* 120:115703. doi: 10.1103/PhysRevLett.120.115703

Schubert, G., Ross, M. N., Stevenson, D. J., and Spohn, T. (1988). *Mercury's Thermal History and the Generation of its Magnetic Field*. Tucson, AZ: University of Arizona Press .

Stevenson, D. J. (1982). Reducing the non-axisymmetry of a planetary dynamo and an application to Saturn. *Geophys. Astrophys. Fluid Dyn.* 21, 113–127. doi: 10.1080/03091928208209008

Stevenson, D. J., and Salpeter, E. E. (1977). The dynamics and helium distribution in hydrogen-helium fluid planets. *Astrophys. J.* 35, 239–261. doi: 10.1086/190479

Takehiro, S., and Lister, J. R. (2002). Surface zonal flows induced by thermal convection trapped below a stably stratified layer in a rapidly rotating spherical shell. *Geophys. Res. Lett.* 29:1803. doi: 10.1029/2002GL015450

Takehiro, S.-I., and Lister, J. R. (2001). Penetration of columnar convection into an outer stably stratified layer in rapidly rotating spherical fluid shells. *Earth Planet. Sci. Lett.* 187, 357–366. doi: 10.1016/S0012-821X(01)00283-7

Verhoeven, J., Wiesehöfer, T., and Stellmach, S. (2015). Anelastic versus fully compressible turbulent Rayleigh-Bénard convection. *Astrophys. J.* 805:62. doi: 10.1088/0004-637X/805/1/62

Veronis, G. (1963). Penetrative convection. *Astrophys. J.* 137:641. doi: 10.1086/147538

Wicht, J. (2002). Inner-core conductivity in numerical dynamo simulations. *Pepi* 132, 281–302. doi: 10.1016/S0031-9201(02)00078-X

Wicht, J., French, M., Stellmach, S., Nettelmann, N., Gastine, T., Duarte, L., et al. (2018). "Modeling the interior dynamics of gas planets," in *Magnetic Fields in the Solar System Vol 448, Astrophysics and Space Science Library*, eds H. Lühr, J. Wicht, S. A. Gilder, and M. Holschneider (Cham: Springer), 7–81.

Zahn, J.-P. (1991). Convective penetration in stellar interiors. *Aap* 252, 179–188.

Zhang, K., and Schubert, G. (1996). Penetrative convection and zonal flow on jupiter. *Science* 273, 941–943. doi: 10.1126/science.273.5277.941

Zhang, K., and Schubert, G. (1997). Linear penetrative spherical rotating convection. *J. Atmos. Sci.* 54, 2509–2518. doi: 10.1175/1520-0469(1997)054<2509:LPSRC>2.0.CO;2

Conflict of Interest Statement: The authors declare that the research was conducted in the absence of any commercial or financial relationships that could be construed as a potential conflict of interest.

frontiers in Earth Science

ORIGINAL RESEARCH
published: 06 November 2018
doi: 10.3389/feart.2018.00176

An Experimental Examination of Thermal Conductivity Anisotropy in *hcp* Iron

Kenji Ohta[1]*, *Yu Nishihara*[2], *Yuki Sato*[1], *Kei Hirose*[3,4], *Takashi Yagi*[5], *Saori I. Kawaguchi*[6], *Naohisa Hirao*[6] and *Yasuo Ohishi*[6]

[1] Department of Earth and Planetary Sciences, Tokyo Institute of Technology, Tokyo, Japan, [2] Geodynamics Research Center, Ehime University, Ehime, Japan, [3] Earth-Life Science Institute, Tokyo Institute of Technology, Tokyo, Japan, [4] Department of Earth and Planetary Science, The University of Tokyo, Tokyo, Japan, [5] National Metrology Institute of Japan, National Institute of Advanced Industrial Science and Technology, Ibaraki, Japan, [6] Japan Synchrotron Radiation Research Institute, Hyogo, Japan

The Earth's core mainly consists of iron, and its thermal transport properties are of vital importance for our understanding of the thermal evolution and the dynamics of the core and the mantle. However, the reported values of thermal conductivity of iron at the core conditions are so far inconclusive. Although hexagonal closed-packed (*hcp*) iron is often studied as a proxy metal to investigate the physical properties not only of the inner core, but also the outer core, the anisotropy of the thermal conductivity of *hcp* iron has never been experimentally examined. Here we report the results of texture analyses by means of synchrotron X-ray diffraction experiments and thermal conductivity measurements on polycrystalline *hcp* iron up to 44.5 GPa and 300 K. These results indicate that the thermal conductivity of single crystal *hcp* iron along *c* axis is about 3–4 times higher than that along *a* axis, which could have partially caused the controversial values of the thermal conductivity of *hcp* iron at the Earth's core conditions.

Keywords: *hcp* iron, Earth's core, thermal conductivity, XRD, thermoreflectance (TR), diamond anvil cell (DAC)

OPEN ACCESS

Edited by:
Takashi Nakagawa,
University of Hong Kong, Hong Kong

Reviewed by:
Ikuro Sumita,
Kanazawa University, Japan
Bin Chen,
University of Hawaii at Manoa, United States

***Correspondence:**
Kenji Ohta
k-ohta@geo.titech.ac.jp

Specialty section:
This article was submitted to Solid Earth Geophysics, a section of the journal Frontiers in Earth Science

Received: *19 June 2018*
Accepted: *10 October 2018*
Published: *06 November 2018*

Citation:
Ohta K, Nishihara Y, Sato Y, Hirose K, Yagi T, Kawaguchi SI, Hirao N and Ohishi Y (2018) An Experimental Examination of Thermal Conductivity Anisotropy in hcp Iron. Front. Earth Sci. 6:176. doi: 10.3389/feart.2018.00176

INTRODUCTION

At some point in the past, the Earth's liquid iron alloy core began to crystallize at Earth's center, resulting in the birth and growth of the solid inner core. Energy considerations indicate that the power delivered to the present-day geodynamo comes mainly from the growth of the solid inner core that induces light element and latent heat releases at the inner core boundary (ICB) (Verhoogen, 1961; Braginsky, 1963; Lister, 2003). On the other hand, before the birth of an inner core, the geodynamo was powered by secular cooling alone, or was possibly helped by an exsolution of MgO and SiO_2 (Badro et al., 2016; O'Rourke and Stevenson, 2016; Du et al., 2017; Hirose et al., 2017). On this note, the birth of the inner core must have been a major event for the geodynamo and could be observed in the paleointensity records (Biggin et al., 2015; Smirnov et al., 2016; Landeau et al., 2017). However, the age of the inner core is still under hot debate, mainly due to controversial estimates of the thermal conductivity of iron that critically affect thermal evolution of the core (e.g., Williams, 2018).

The conductivity of hexagonal closed-packed (*hcp*) iron has been experimentally determined in a laser-heated diamond anvil cell (DAC) at the pressure (P) and temperature (T) conditions corresponding to the upper part of Earth's outer core (Konôpková et al., 2016; Ohta et al., 2016). It was surprising to see that the reported thermal conductivity of *hcp* iron showed about septuple difference at 135 GPa and 4,000 K corresponding to the Earth's core-mantle boundary (CMB) condition. Due to the experimental difficulty in measuring thermal conductivity at such extremely high P-T conditions, conventional studies have measured electrical conductivity (σ, the inverse of electrical resistivity) of iron and iron alloys, and then converted it to the electronic thermal conductivity (κ_{el}) via the Wiedemann-Franz relation,

$$\kappa_{el} = \sigma TL, \tag{1}$$

where T is absolute temperature and L is the Lorenz number. The ideal (i.e., Sommerfeld) Lorenz number L_0 is 2.45×10^{-8} $W\Omega/K^2$. Ohta et al. (2016) likewise measured the electrical resistivity of solid iron to the core pressure and temperature conditions. Their resistivity data demonstrated the κ_{el} of *hcp* iron to be 226(+71/−31) W/m/K at the CMB when the Wiedemann-Franz relation with L_0 was applied. On the other hand, Konôpková et al. (2016) carried out fast thermal radiation detection experiments and estimated high-P/high-T thermal conductivity of iron on the basis of finite element modeling to reproduce the detected temperature decay in a laser-heated DAC. Their study advocated the thermal conductivity value of iron at the CMB to be 33 ± 7 W/m/K. What causes the discrepancy between these two studies? One possibility is that the Wiedemann-Franz relation cannot be directly applied at very high P-T conditions corresponding to the core conditions (Dobson, 2016). The Lorenz number might be strongly temperature and pressure dependent. Inelastic electron-electron scattering might be enhanced at the extreme pressures and temperatures, which is not considered in the Wiedemann-Franz law (Pourovskii et al., 2017; Secco, 2017). Indeed, liquid lead (Pb) and tin (Sn) show breakdown of the Wiedemann-Franz law at high temperature conditions (Yamasue et al., 2003).

Anisotropic conductivity in a *hcp* iron sample with strong crystallographic preferred orientation (CPO) is another likely culprit of the discrepancy in the estimated iron conductivities by Konôpková et al. (2016) and Ohta et al. (2016). Both studies used iron foil as a sample and compressed it to its thickness direction in a DAC. The direction of thermal conductivity measurement performed by Konôpková et al. (2016) was parallel to the compression axis of the DAC, while the direction of electrical resistivity measurement by Ohta et al. (2016) was perpendicular to the DAC compression. If the *hcp* iron sample used in their studies had strong CPO and the conductivity of *hcp* iron is crystallographically anisotropic, the measured conductivities would differ from each other. However, to our knowledge, the conductivity anisotropy in *hcp* iron has never been examined. The *hcp* phase of iron is stable above 13 GPa and unquenchable to ambient conditions, so that *in-situ* high-P determination of anisotropic conductivity is imperative. As analog materials of *hcp* iron, one can review reports of the conductivity anisotropy in other *hcp* metals that are stable at ambient conditions, which shows that the magnitudes of conductivity anisotropy differ from each other (Hall et al., 1959; Nellis and Legvold, 1969; Spedding et al., 1971; Alderson and Hurd, 1975; Stierman et al., 1983; Sanborn et al., 1989; Balog and Secco, 1999; Secco and Balog, 2001). For instance, the electrical conductivity of *hcp* scandium (Sc) along the c axis is 2.3 times as high as that along the a axis (Spedding et al., 1971), while the conductivity of *hcp* cobalt (Co) along the a axis is 80% larger than that along the c axis (Sanborn et al., 1989).

As an experimental examination of the thermal conductivity anisotropy in *hcp* iron, we performed synchrotron X-ray diffraction (XRD) and thermal conductivity measurements on polycrystalline *hcp* iron with CPO *in-situ* at high P up to 44.5 GPa and 300 K in a DAC. We analyzed the results and found anisotropic thermal conductivity of *hcp* iron single crystal; thermal conductivity along the c axis (κ_c) is about 3∼4 times higher than that along the a axis (κ_a). The anisotropy in the *hcp* iron thermal conductivity could partially be the cause of the discrepancy between the reported iron conductivity values (Konôpková et al., 2016; Ohta et al., 2016). If the observed conductivity anisotropy in *hcp* iron is preserved to the Earth's inner core conditions, it may have a strong influence on the heat transfer in the Earth's inner core.

TABLE 1 | Experimental conditions and the results.

Run #	Starting material	Pressure, P (GPa)	Thermal diffusivity, D (mm^2/s)	Density, ρ (kg/m^3)	Isobaric heat capacity, C_P (J/kg/K)	Thermal conductivity, κ (W/m/K)
1	Wire	16.0 (20)	4.7 (4)	8966.4	510.2	21.7 (17)
2	Foil	18.5 (2)	3.6 (2)	9046.4	502.2	16.5 (7)
3	Foil	23.1 (11)	4.9 (6)	9191.1	488.1	21.9 (28)
4	Foil	24.5 (11)	4.4 (2)	9235.4	483.9	19.6 (9)
5	Powder	39.9 (14)	7.1 (9)	9669.2	444.6	30.4 (40)
6	Wire	41.2 (23)	9.3 (14)	9704.2	441.6	39.9 (61)
7	Foil	41.6 (7)	6.8 (5)	9712.3	441.2	29.3 (23)
8	Wire	44.5 (17)	9.6 (4)	9787.9	434.5	41.0 (17)

MATERIALS AND METHODS

We performed eight separate sets of experiments to examine the anisotropy in the thermal conductivity of single crystal *hcp* iron up to 44.5 GPa at 300 K (**Table 1**). Our procedure follows these four steps:

1. We used three types of iron starting materials with different CPO and transformed them to *hcp* iron in a DAC.
2. We collected XRD data of the *hcp* iron samples in two directions: parallel and orthogonal to the DAC compression axis. The obtained XRD data were analyzed to determine CPO in the *hcp* iron samples as reported in the previous studies (Merkel et al., 2004; Miyagi et al., 2008; Nishihara et al., 2018).

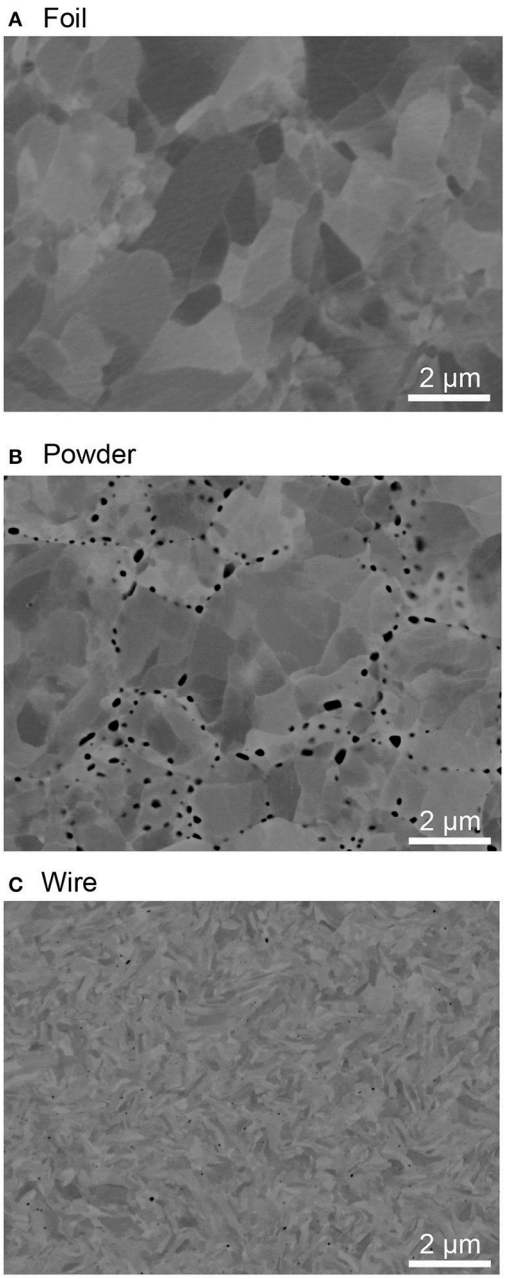

FIGURE 1 | Back-scattered electron (BSE) image of the *bcc* iron starting materials; **(A)** foil, **(B)** sintered and deformed powder, and **(C)** wire. These images were obtained using a scanning electron microscope equipped with a field emission gun (FE-SEM, JEO JSM-7000F) with accelerating voltage of 10 kV and probe current of 8 nA. Observed cross sections are normal to compression axis in the subsequent DAC experiments. Contrast in gray area is orientation contrast in iron whereas black dots in **(B)** are iron oxide.

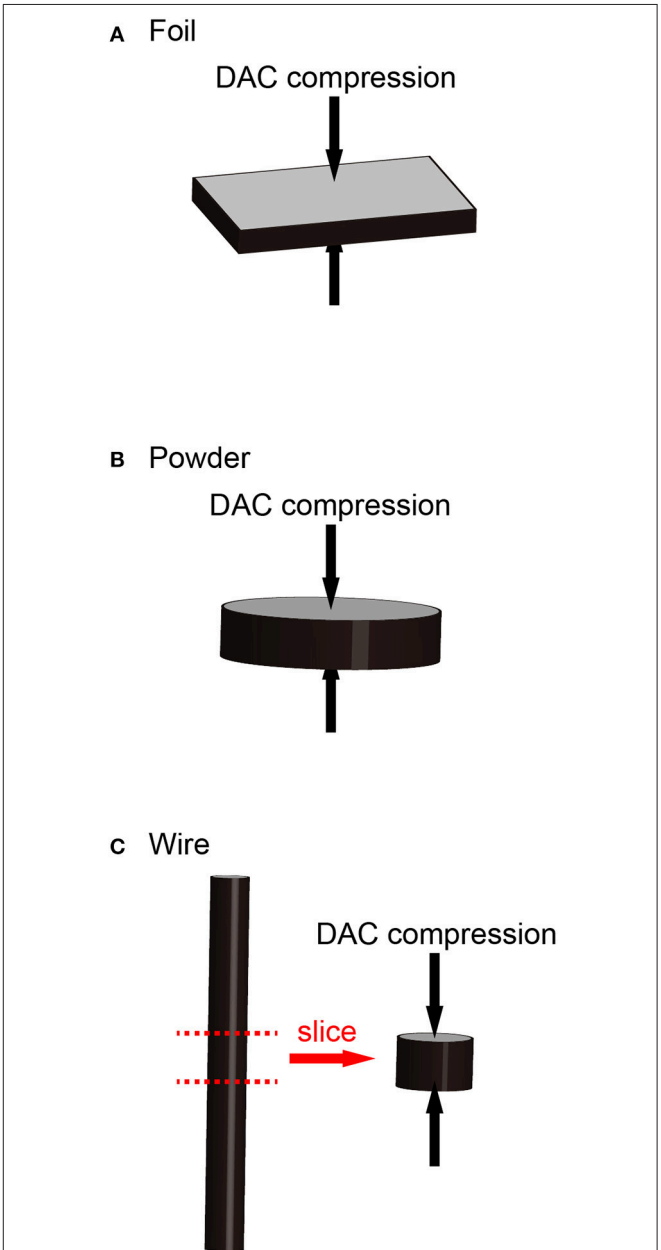

FIGURE 2 | Schematics of iron starting materials. Black arrows indicate the compressional direction of a DAC. **(A)** Iron foil with initial thickness of 10 μm. **(B)** Iron powder that was sintered in a D-DIA apparatus at 2 GPa and 600°C for 1 h, then deformed uniaxially with approximate strain rate of 2×10^{-5} s^{-1} at room temperature. **(C)** Iron wire (100 μm in diameter) was sliced to about 10 μm thick.

3. After the CPO analyses, thermal conductivity measurements were performed on the textured *hcp* iron *in-situ* at high *P*.
4. We calculated κ_a and κ_c of single crystal *hcp* iron from the obtained CPO information and measured thermal conductivity of the polycrystalline *hcp* iron sample assuming an aggregate texture.

High Pressure Apparatus and Iron Starting Materials

High-*P* conditions were generated in a symmetric-type DAC with 300 μm flat culet diamond anvils. Body centered cubic (*bcc*) to *hcp* phase transformation of iron occurring around 13 GPa and 300 K is considered to be a prototypical martensitic transition. A number of studies reported that the texture of *hcp* iron is basically inherited from *bcc* iron across the transition (Merkel et al., 2004; Miyagi et al., 2008; Ishimatsu et al., 2014; Dewaele et al., 2015; Nishihara et al., 2018). Therefore, we anticipated synthesizing *hcp* iron samples with different textures in a DAC by using various types of textured *bcc* iron starting material. Here we used three types of *bcc* iron sample: foil, sintered powder, and wire. A high-purity iron foil (99.99%) with 10 μm initial thickness was cut into a disk shape and compressed to its thickness direction in a DAC (**Figures 1A**, **2A**). The iron foil has a relatively heterogeneous grain-size distribution, with the largest grains being a few micro-meters in size (**Figure 1A**). This foil sample was also used in the previous studies (Gomi et al., 2013; Ohta et al., 2016). Iron powder (99.9% purity) with a few micro-meters grain size was sintered in a deformation-DIA apparatus (D-DIA), MADONNA-I, at the Geodynamics Research Center, Ehime University. It was sintered at 2 GPa and 600°C for 1 h, then deformed by advancing each differential-ram by 0.4 mm (**Figure 1B**). We cut a disk (90 μm in diameter and 10 μm initial thickness) out of the sintered and deformed iron batch and loaded it into a DAC (**Figure 2B**). Compression direction by a DAC is parallel to the deformation direction by a D-DIA. In the sintered iron powder, an array of iron oxide (black dots in **Figure 1B**) that originally formed on the surface of grains in the powder was observed. The volume fraction of the iron oxide was estimated to be <2% based on the image analysis. The grain size of iron in this starting material is judged to be significantly smaller than that of the original powder (a few hundred nanometers). The *bcc* iron wire (99.99% purity) with 100 μm in diameter was sliced to about 10 μm thick, and then loaded into the sample chamber of a DAC. The iron wire has a homogeneous microstructure, which consists of very small, wavy grains with about 0.1 μm width (**Figure 1C**). The compression direction in a DAC is parallel to the length direction of the *bcc* iron wire (**Figure 2C**). We employed the two-stage amorphous boron plus Kapton gasket that enabled us to perform radial XRD measurement for sample texture analysis (Merkel and Yagi, 2005) (**Figures 3**, **4**). SiO_2 glass was used as a pressure transmitting medium.

Synchrotron XRD Measurements and Texture Analysis

For phase identification and texture analyses, angle-dispersive two-dimensional XRD measurements were conducted on the iron samples in a DAC at BL10XU, SPring-8. The wavelengths of the monochromatic incident X-ray beam were 0.247∼0.413 Å (30∼50 keV) and the incident X-ray was collimated to about 10 μm in diameter. The XRD images were recorded on an imaging plate (IP) detector (RIGAKU R-AXIS V^{++}) with a typical exposure time of 30 s. The XRD data for the iron sample in a DAC were collected in both axial and radial diffraction geometries where the sample is irradiated with X-rays both parallel and perpendicular to the DAC compression axis, respectively, in order to increase pole figure coverage (**Figure 3A**). In runs 1 and 4, only the axial XRD spectrum was collected. Pressures were determined by using an equation of state (EOS) of *hcp* iron (Yamazaki et al., 2012).

Axial and radial XRD images were quantitatively analyzed for determination of CPO using the Rietveld method as implemented in the software package MAUD (Lutterotti et al., 2014). First, the XRD images were integrated from 0° to 360°

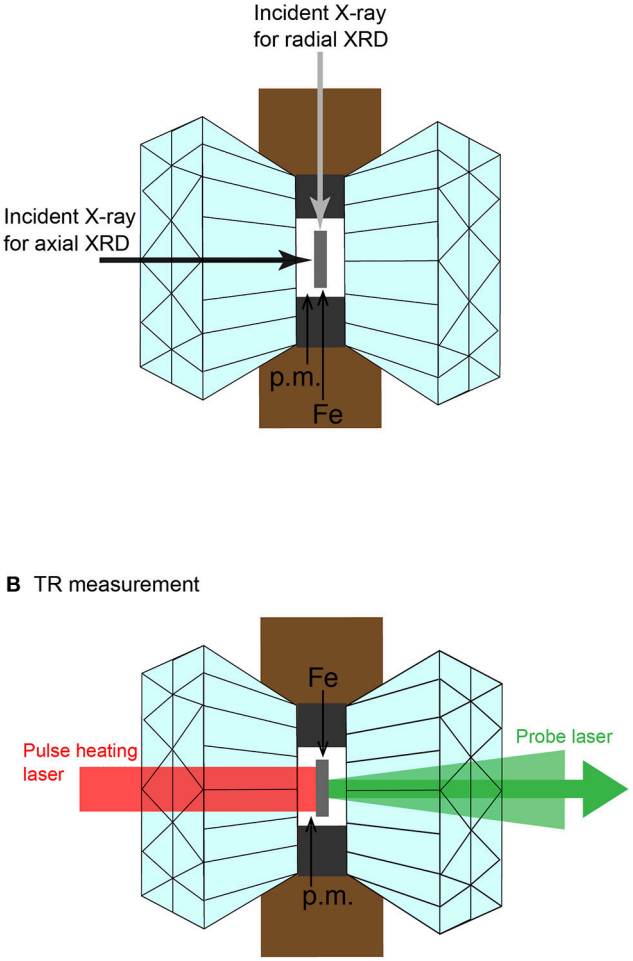

FIGURE 3 | Schematics of the experiment. **(A)** Directions of incident X-ray for axial and radial XRD measurements. **(B)** Ray paths of laser beams for thermoreflectance measurements in a DAC. p.m. indicates pressure transmitting medium.

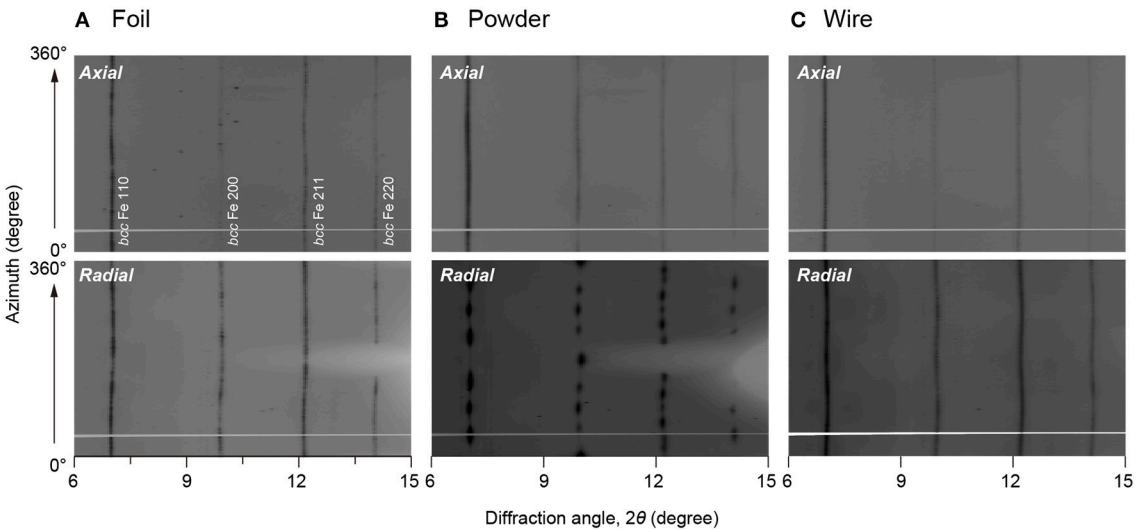

FIGURE 4 | Unrolled XRD images of iron starting materials, **(A)** foil, **(B)** sintered powder, and **(C)** wire obtained at 1 bar. Upper panels show XRD images obtained from the axial geometry, and lower panels are the radial XRD images. Miller indices of *bcc* iron are shown in the upper left panel. Horizontal gray line in each image is a shadow of beam stopper holder. Wavelength of incident X-ray was 0.247 Å.

azimuth angles over 5° sectors to produce 72 patterns (**Figure 4**). Sample to the IP distance, wavelength of incident X-ray, and the IP geometry were calibrated with CeO_2 standard. The sample CPO is calculated by the E-WIMV algorithm to produce an orientation distribution function (ODF) with a resolution of 15°. No symmetry constraint was applied in the analysis.

High-Pressure Thermal Conductivity Measurement

Thermal conductivity (κ) is a function of thermal diffusivity (D), density (ρ), and isobaric heat capacity (C_P): $\kappa = D\rho C_P$. The D of *hcp* iron at high P was measured by means of the pulsed light heating thermoreflectance technique in a DAC at Tokyo Institute of Technology (**Figure 3B**). Details of the measurement system and the analytical methods of this technique have been described in the literature (Yagi et al., 2011; Ohta et al., 2017). The density (ρ) of *hcp* iron was determined from the present XRD data. The isobaric specific heat capacity (C_P) was calculated from the thermodynamic relations and the reported thermoelastic parameters of *hcp* iron (Yamazaki et al., 2012).

RESULTS

Crystallographic-Preferred Orientation of Iron Samples

Prior to the high-P experiments, we investigated the CPO of *bcc* iron starting materials loaded into a DAC at ambient conditions. **Figure 4** presents the variations in the diffraction intensity for (110), (200), (211), and (220) diffractions of the three-types of *bcc* iron starting material. We used these four XRD peaks for texture analyses with the MAUD program, and acquired pole figures of the *bcc* samples (**Figure 5**). Pole densities are expressed in multiples of random distribution (m.r.d.). The *bcc* iron foil showed a single crystal-like CPO with an alignment of <111> along its compression axis and an alignment of <110> on the radial plane (**Figure 5A**). Since the foil included large grains, as shown in **Figure 1A**, the number of grains in a diffraction volume might be limited. This would be the reason for the single crystal-like CPO of this sample. Although the CPO of *bcc* iron foil was only determined in Run 3, the CPO could be entirely different in each run due to the limited number of grains in a sample volume of a DAC experiment. The sintered and deformed *bcc* iron powder showed an almost axi-symmetric CPO pattern with concentrations of <100> and <111> along its compression axis (**Figure 5B**). This is consistent with reports by Merkel et al. (2004) and Nishihara et al. (2018), where similar CPO was formed by uniaxial compression of randomly textured *bcc* iron. The *bcc* iron wire had an almost random texture as shown in **Figure 5C**.

The polycrystalline *bcc* iron starting materials loaded into a DAC were squeezed to transform them into *hcp* iron. In all eight runs, we collected XRD data for *hcp* iron and obtained their CPO patterns. **Figure 6** shows the representative XRD data for *hcp* iron obtained at 41.6 GPa in both axial and radial geometries. Five XRD peaks from the $(10\bar{1}0)$, (0002), $(10\bar{1}1)$, $(10\bar{1}2)$, and $(11\bar{2}0)$ diffractions were used for texture analyses. The obtained pole figures of *hcp* iron clearly show that the CPO of *hcp* iron differs depending on the texture of the starting materials (**Figure 7**). The CPO of *hcp* phase derived from powder *bcc* iron is characterized by an alignment of $<11\bar{2}0>$ parallel to the compression axis and <0001> on the radial plane (**Figure 6B**). This is largely consistent with the Burgers orientation relationship, $\{110\}_{bcc}//\{0001\}_{hcp}$ and $<111>_{bcc}//<11\bar{2}0>_{hcp}$, for a martensitic transformation between *bcc* and *hcp* phases. The orientation of <0001> is not axi-symmetric, but lies along a particular direction (**Figure 7B**);

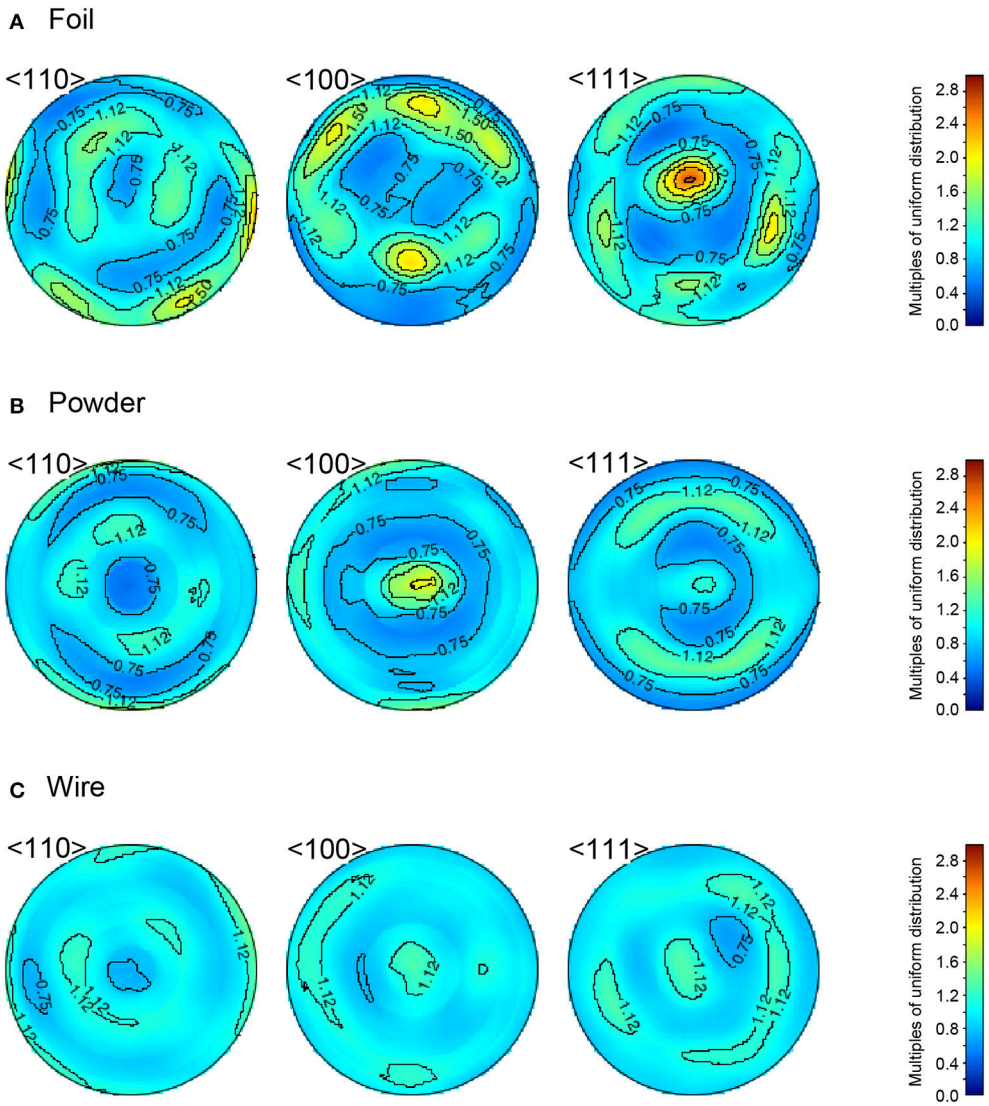

FIGURE 5 | Pole figures of **(A)** foil, **(B)** powder, and **(C)** wire of *bcc* iron starting materials at ambient conditions showing the variation in the crystallographic orientation of the <110>, <100>, and <111> directions. The direction of a DAC compression is in the center of the pole figure.

although the orientation of <110> in the *bcc* starting material is nearly axi-symmetric (**Figure 5B**). This is presumably due to strong variant selection in the *bcc* to *hcp* phase transformation under high deviatoric stress in a DAC. The CPO pattern of *hcp* iron from *bcc* wire is characterized by a strong concentration of <0001> parallel to its compression axis (**Figure 7C**), and this pattern is accompanied by a weaker concentration of <0001> along the radial direction at lower *P* (Run 1). This observation is reasonably interpreted as follows. The <111> (and <100>) is aligned parallel to the compression axis from initial random texture by compression of *bcc* phase at low pressure. The *bcc* to *hcp* phase transformation yields an alignment of <0001> along the radial direction following the Burgers relationship, and subsequent uniaxial compression to higher pressure gradually aligns <0001> along the compression axis through the basal slip dominant viscous creep (e.g., Merkel et al., 2004; Nishihara et al., 2018). In *hcp* iron that was transformed from *bcc* foil, completely different CPO patterns were observed depending on the run: $<10\bar{1}0>$ was aligned along the compression axis in Runs 2 and 7 (**Figure 7A**), whereas <0001> was aligned along the compression axis in Runs 3 and 4. This is probably because the CPO of *bcc* iron foil was different in each run due to its large grain size (**Figure 1A**). However, the CPO of the *bcc* phase is not perfectly inherited by the *hcp* phase along with the Burgers orientation relationship. In reality, the situation is complicated by the existence of internal stresses between grains that develop during the phase transformation. They also influence the orientation relations and variant selection and their effects cannot be deduced from simple crystallographic considerations.

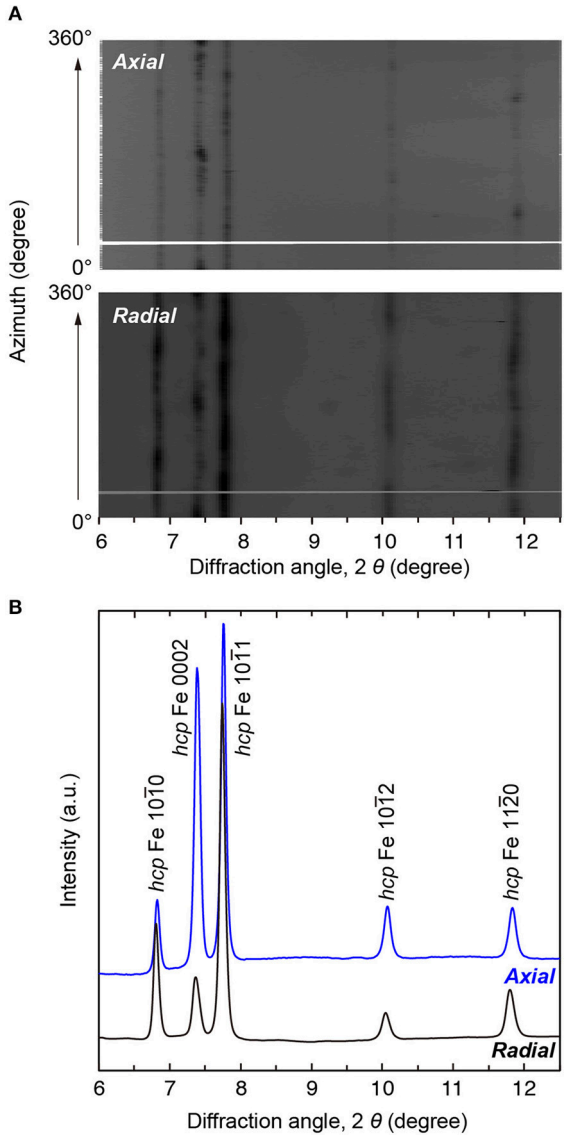

FIGURE 6 | XRD patterns of *hcp* iron obtained at 41.6 GPa and 300 K in Run #7. **(A)** Unrolled XRD images of *hcp* iron measured in axial (upper panel) and radial (lower panel) geometries. **(B)** Integrated XRD patterns of *hcp* iron measured in axial (blue) and radial (black) geometries. Wavelength of incident X-ray was 0.247 Å.

Figure 8 indicates the emergence distributions of crystals with angle θ between the DAC compression axis and <0001> of *hcp* iron, which means the frequency of *hcp* iron grains with angles between the *c* axis and compressional axis. This was calculated from <0001> pole figure (hence from ODF), and a distribution is normalized such that its integration in the hole interval to be unity.

Thermal Conductivity of the Polycrystalline *hcp* Iron

After the XRD experiments and the subsequent CPO analyses, we measured high-*P* thermal conductivity of the polycrystalline *hcp* iron by means of the pulsed light heating thermoreflectance technique (**Table 1**). The transient temperature change in a *hcp* iron sample by pulse laser heating was recorded at high *P* as shown in **Figure 9A**. The obtained temperature history curve was analyzed considering the one-dimensional heat diffusion in iron and pressure medium (SiO_2 glass):

$$T(t) = \overline{T}\sqrt{\frac{\tau}{\pi t}}\sum_{n=0}^{\infty}\gamma^{2n}exp\left[-\frac{(2n+1)^2}{4}\frac{\tau}{t}\right], \qquad (2)$$

where $T(t)$ is temperature, $\bar{T}$ is a constant, t is time, and γ expresses heat effusion to pressure medium (Yagi et al., 2011). τ is the heat diffusion time across the iron sample. We obtained $\bar{T}$, γ, and τ by fitting the measured curves to Equation (2). The sample thickness (d) was measured in a sample recovered from the DAC. Its cross section was prepared by using the focused ion beam (FIB) apparatus, and the thickness of the iron sample was measured under a scanning microscope (SEM) (**Figure 9B**). The effect of lattice volume expansion due to decompression and transformation from *hcp* to *bcc* phase was corrected to determine d by using the EOSs of *hcp* iron (Yamazaki et al., 2012). The τ and d gives high-*P* thermal diffusivity;

$$D = d^2/\tau. \qquad (3)$$

Multiplication of the D, ρ, and C_P yields the high-*P* thermal conductivity of *hcp* iron.

The obtained thermal conductivity of *hcp* iron at high *P* and 300 K is shown in **Figure 10**. The *hcp* iron samples from the wire starting material show higher conductivity than those from the foil and powder samples at similar pressures. The aforementioned CPO analyses showed that *hcp* iron from *bcc* wire shows a strong orientation of <0001> parallel to the compression axis, while *hcp* iron from powder and foil tends to show an alignment of <0001> on the radial plane. This CPO information and polycrystalline *hcp* iron conductivity imply that the thermal conductivity of *hcp* iron along the *c* axis (κ_c) is higher than that along the *a* axis (κ_a). For comparison, we calculated high-*P*/room-*T* κ_{el} of polycrystalline *hcp* iron from the reported electrical resistivity (Gomi et al., 2013) and the Wiedemann-Franz law with the L_0 (Equation 1) (**Figure 10**). The present values of thermal conductivity of *hcp* iron are about half of the calculated κ_{el}. Such a difference could be due to anisotropy in the thermal conductivity of *hcp* iron because (Gomi et al., 2013) measured the high-*P* resistivity during decompression after squeezing the iron foil up to 100 GPa at 300 K. The measurement direction of the high-*P* resistivity was perpendicular to that of the present thermal conductivity. Since all the compared data are at 300 K, the influence of electron-electron scattering on thermal conductivity should be negligible (Pourovskii et al., 2017).

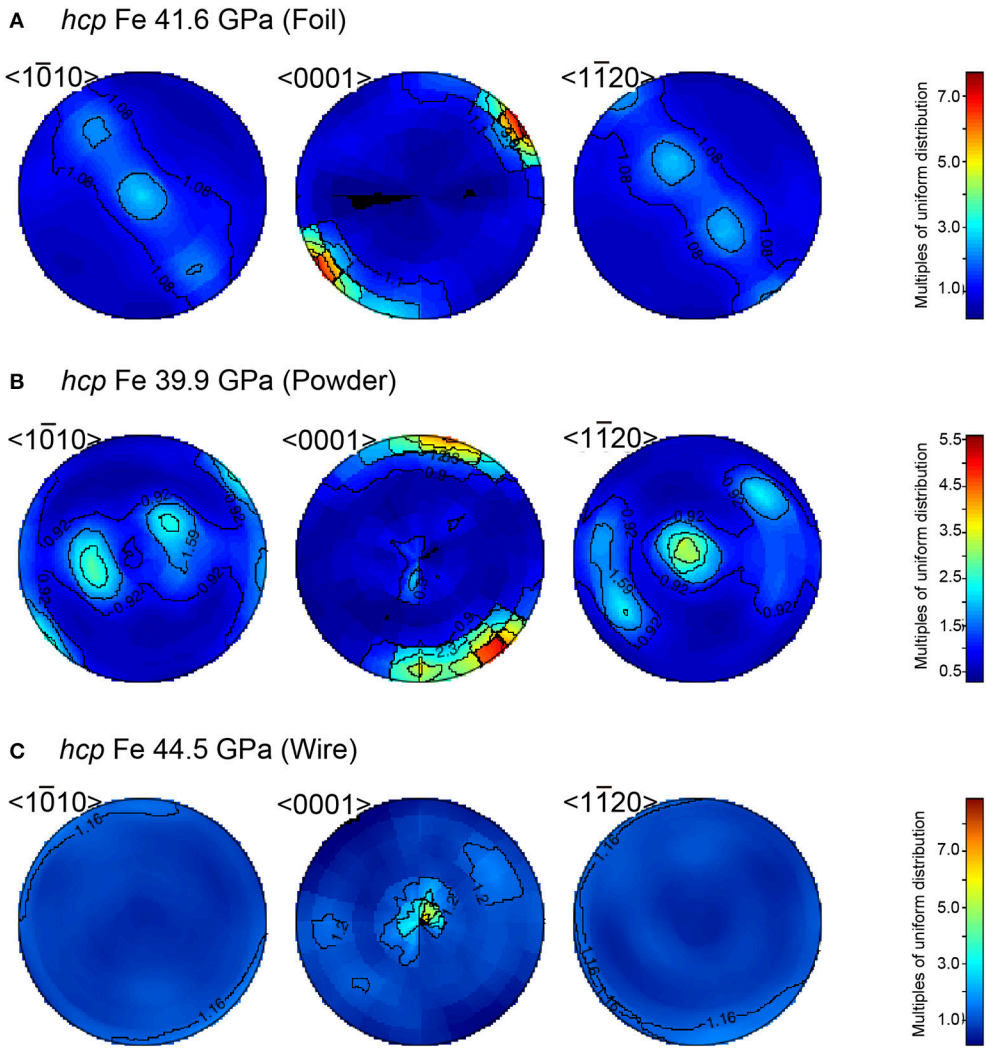

FIGURE 7 | Pole figures of *hcp* iron showing the variation in the crystallographic orientation of the <10$\bar{1}$0>, <0001>, and <11$\bar{2}$0> directions. **(A)** *hcp* iron at 41.6 GPa transformed from *bcc* iron foil. **(B)** *hcp* iron at 39.9 GPa synthesized from sintered powder sample. **(C)** *hcp* iron at 44.5 GPa that was made from *bcc* iron wire. The direction of a DAC compression is in the center of the pole figure.

DISCUSSION

Estimation of Single Crystal Thermal Conductivity Anisotropy in *hcp* Iron

Here we quantitatively evaluate the anisotropy in the crystallographic thermal conductivity of *hcp* iron single crystal based on the present results of CPO analyses and thermal conductivity measurements (**Figures 7**, **8**, **10**). The thermal conductivity of polycrystalline *hcp* iron we measured can be regarded as the effective thermal conductivity of a *hcp* iron single crystal aggregate along the obtained CPO (**Figure 10**). First, we define the effective thermal conductivity of a *hcp* crystal along a direction θ ($\kappa(\theta)$) as follows:

$$\kappa(\theta) = \kappa_a sin^2\theta + \kappa_c cos^2\theta \quad (4)$$

where θ is an angle between the heat flow direction and the *c* axis (**Figure 8** inset) (see **Appendix**). In this study, the heat flow direction is parallel to the DAC compression direction (**Figure 3B**). Then, we calculated the anisotropy in thermal conductivity of a *hcp* iron crystal assuming two-types of $\kappa(\theta)$ mixing model as described below.

Approach I: Layered Texture Solved by Parallel and Series Models

We consider a layered structure in which each layer consists of *hcp* iron crystals having the same θ value. When the heat flow and DAC compression directions are perpendicular to the stacking direction, the effective thermal conductivity of the layered *hcp* iron aggregate along the heat flux can be expressed by an equivalent equation of the parallel resistor model (**Figure 11A** inset):

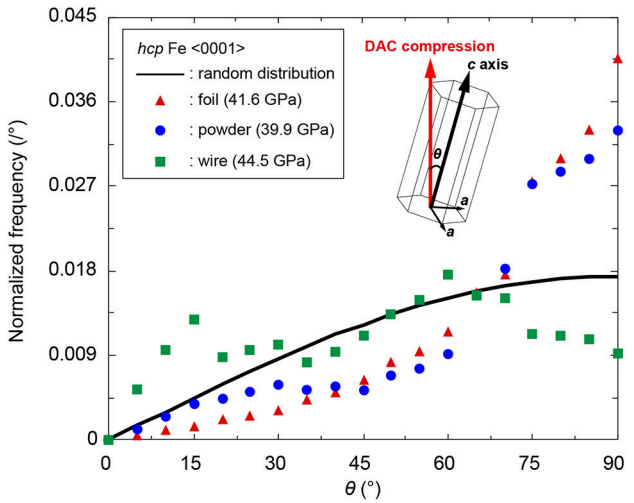

FIGURE 8 | Distribution of angle between <0001> and DAC compression axis in three *hcp* iron samples. Red triangles; *hcp* iron from foil starting material, blue circles; *hcp* iron from sintered powder, green squares; *hcp* iron from wire sample. Black line shows randomly oriented *hcp* iron. θ is defined as an angle between DAC compression direction and *c* axis of *hcp* iron (inset).

$$\kappa_{parallel} = \int_0^{90} p\,(\theta)\,\kappa\,(\theta)\,d\theta, \tag{5}$$

where $\kappa_{parallel}$ is an effective thermal conductivity assuming the parallel model and $p(\theta)$ is the emergence distribution of angles between the <0001> axis and heat flow (DAC compression) direction (e.g., **Figure 8**). When the heat flow (DAC compression) direction is parallel to the stacking direction, the effective thermal conductivity can be regarded as the series resistor model (**Figure 11B** inset):

$$\frac{1}{\kappa_{series}} = \int_0^{90} p(\theta)\frac{1}{\kappa(\theta)}d\theta, \tag{6}$$

where κ_{series} denotes an effective thermal conductivity considering the series model. Using these models (Equations 4–6) and pairs of the present thermal conductivity of polycrystalline *hcp* iron at similar *P*, we found the κ_a and κ_c of *hcp* iron at high *P* (**Table 2** and **Figures 11A,B**). Based on the mixing theory (Guéguen and Palciauskas, 1994), the solution of the parallel model gives the lower limit, while the series model provides the upper bound limit. The results clearly indicate anisotropy in the single crystal thermal conductivity of *hcp* iron.

The solutions of the parallel model indicate that κ_c is about four-fold higher than κ_a. And, the values of κ_c are comparable to the κ_{el} of *hcp* iron from the electrical resistivity data reported by Gomi et al. (2013) (**Figure 11A**). The series model also shows a similar trend, although the absolute values of the κ_a and κ_c are different from the solutions of the parallel model (**Figure 11B**).

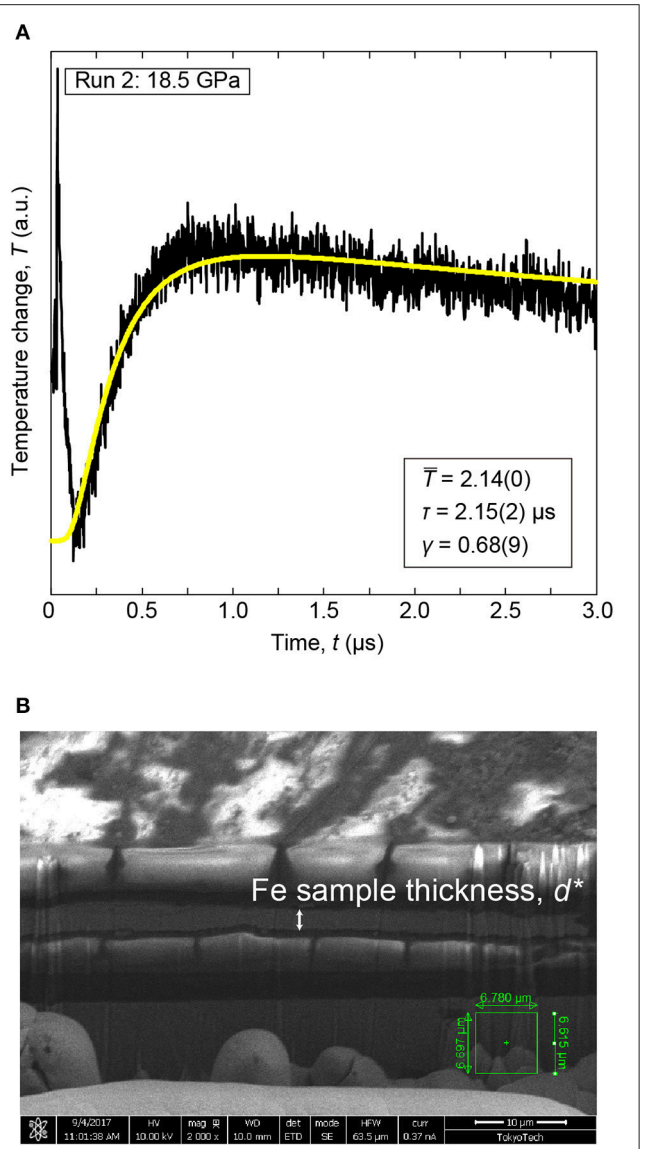

FIGURE 9 | Representatives of **(A)** Transient temperature curve of *hcp* iron obtained at 18.5 GPa and 300 K (Run #2) and **(B)** SEM image of a cross section of the recovered sample prepared by the FIB apparatus. The transient temperature curve was fitted by Equation (2) (yellow curve). In this case, we set $n = 5$. The obtained fitting parameters are shown in **(A)**. Note that this SEM image has been acquired from an oblique direction to sample stage, and thus the apparent thickness shown in this figure is different from the actual sample thickness.

Approach II: Random Distribution Texture Solved by Effective Medium Approximation

This is a realistic case in which each *hcp* iron crystal with the same orientation (i.e., the same θ) is randomly distributed in the polycrystalline aggregate sample, rather than forming the laminated structure considered above (**Figure 11C** inset). We thus employ effective medium approximation to calculate the thermal conductivity anisotropy in a *hcp* iron crystal that is

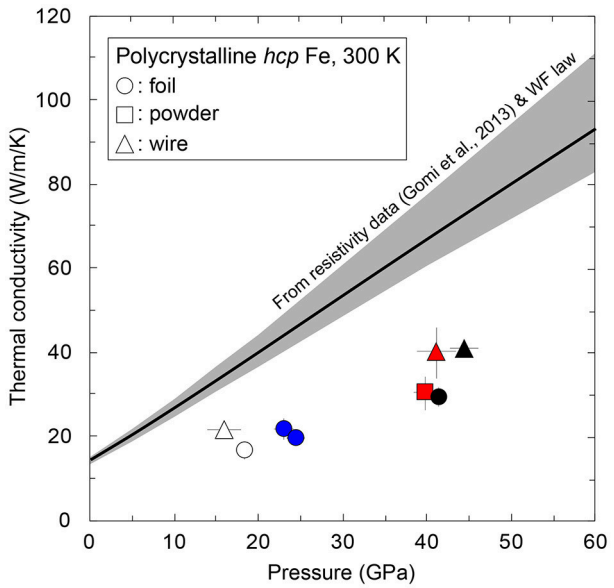

FIGURE 10 | Thermal conductivity of polycrystalline *hcp* iron as a function of *P* at 300 K. The *hcp* iron samples were synthesized from foil (circles), powder (square), and wire (triangles) starting materials. Black line with gray band shows κ_{el} of *hcp* iron calculated from the resistivity of *hcp* iron (Gomi et al., 2013) and the Wiedemann-Franz (WF) law (Equation 1). The present conductivity data were obtained along DAC compression axis, while the resistivity of *hcp* iron (Gomi et al., 2013) was measured along the direction normal to DAC compression. Pairs of symbols with same color show similar pressure and were used to calculate the anisotropy in thermal conductivity.

randomly distributed in polycrystal (Landauer, 1952):

$$\sum_{i=1}^{n} \frac{\kappa_{random} - \kappa_i}{2\kappa_{random} + \kappa_i} v_i = 0, \quad (7)$$

where κ_{random}, κ_i, and v_i are the effective thermal conductivity assuming a random texture, thermal conductivity of *i* component, and its volume fraction, respectively. As well as the parallel and series models, the effective medium approximation also shows strong anisotropy in the single crystal thermal conductivity of *hcp* iron (**Figure 11C**). In this case, the κ_c is about three times as high as κ_a, at least up to 43.1 GPa.

All the crystal mixing models indicate strong anisotropy in the thermal conductivity of *hcp* iron at high *P* and room *T* (**Table 2** and **Figure 11**). The obtained results of κ_c of *hcp* iron are comparable or higher than the κ_{el} (Gomi et al., 2013), indicating that the thermal and electrical conductivity of polycrystalline *hcp* iron would show variation up to a factor of four, depending on the CPO of the *hcp* iron sample in a DAC. Indeed, the measured electrical resistivities (or resistance) of *hcp* iron show considerable variation, especially at the onset of *bcc-hcp* transition that is about 13 GPa, but all of the experimental data obtained above 40 GPa are consistent with each other (Reichlin, 1983; Jaccard et al., 2002; Deng et al., 2013; Gomi et al., 2013; Seagle et al., 2013; Zhang et al., 2018). The discrepancy among them could be derived from difference in CPO of *hcp* iron samples just after the transition, since they have used various

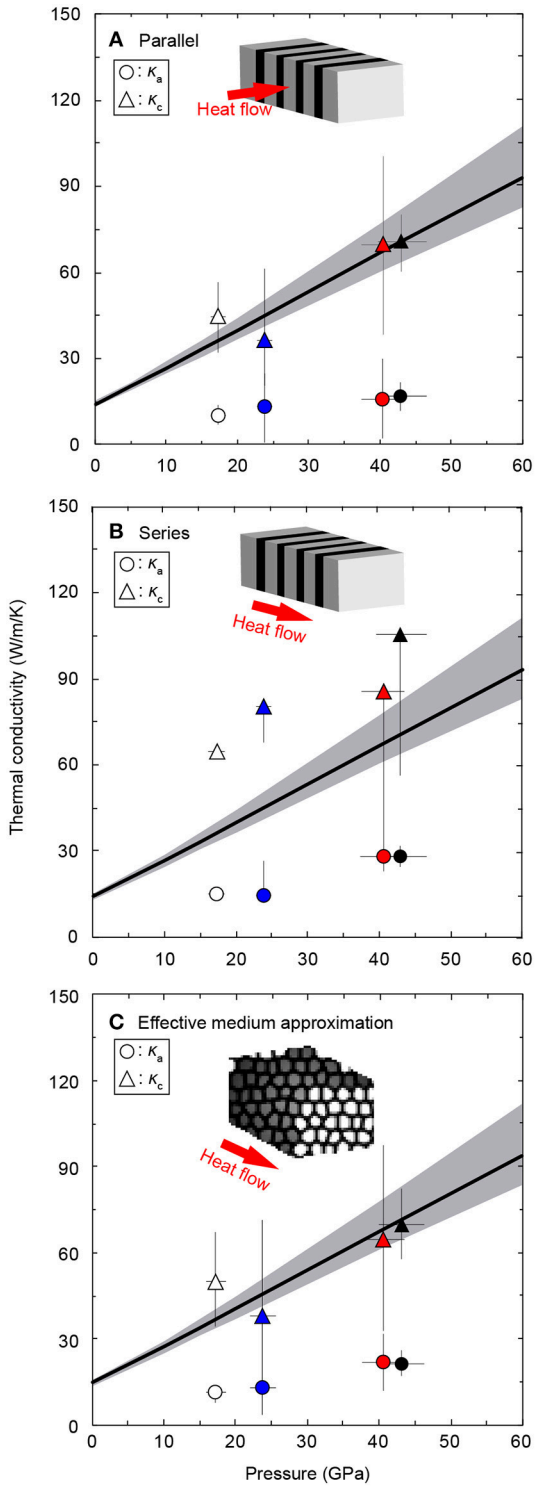

FIGURE 11 | Thermal conductivities of single crystal *hcp* iron along *a* and *c* axes (κ_a and κ_c) as a function of *P* at 300 K. **(A)** Solutions of the parallel model (Equation 5). **(B)** The series model solutions (Equation 6). **(C)** Random distribution model calculated by the effective medium approximation (Equation 7) (Landauer, 1952). Circles; κ_a, triangles; κ_c. Black line with gray band is κ_{el} of *hcp* iron as shown in **Figure 10**. Inset figures show schematic illustrations of the parallel, series, and random models, respectively.

TABLE 2 | Thermal conductivities of *hcp* iron along each axis.

Run pair	*P* (GPa)	Parallel			Series			Random		
		κ_a (W/m/K)	κ_c (W/m/K)	κ_c/κ_a	κ_a (W/m/K)	κ_c (W/m/K)	κ_c/κ_a	κ_a (W/m/K)	κ_c (W/m/K)	κ_c/κ_a
1, 2	17.3	10.4	44.5	4.3	14.9	64.5	4.3	10.7	49.8	4.7
3, 4	23.8	12.5	36.2	2.9	14.8	80.6	5.4	12.8	37.9	3.0
5, 6	40.6	15.6	69.7	4.5	27.9	85.8	3.1	21.9	64.8	3.0
7, 8	43.1	16.6	70.5	4.2	27.9	105.3	3.8	21.5	69.9	3.3

types of *bcc* iron starting materials. The CPO of such samples might become similar due to uniaxial compression of the DAC, resulting in similar resistivity values at higher *P*. Although Secco and Balog (2001) have selected Gd as the best analog material to predict the anisotropy in the conductivity of *hcp* iron, the electrical conductivity of Gd along the *c* axis is only 30% larger than that along the *a* axis at ambient conditions.

However, note that the strength of conductivity anisotropy obtained above highly depends on the strength of the CPO determined based on the XRD data. The ODF (and hence CPO) in this study was calculated using the E-WIMV algorithm, which is an improved version of WIMV. Determination of the ODF is a kind of inversion which does not have a unique solution, and WIMV algorithm (as well as E-WIMV) gives the smoothest positive solution with maximum entropy for ODF (Kocks et al., 2000; Lutterotti et al., 2007). This means that the CPO determined from XRD data with a limited pole figure coverage gives a lower bound in texture strength. Therefore, the single crystal thermal conductivity anisotropy of *hcp* iron presented in this study is considered to be the upper bound and the real anisotropy might be smaller.

Geophysical Implications

An open question raised above is whether the discrepancy in experimentally determined thermal conductivity of iron at the core conditions can be explained by anisotropy in the conductivity of single crystal *hcp* iron (Konôpková et al., 2016; Ohta et al., 2016). As a matter of fact, both studies did not determine the room-*T* conductivity of iron from their own experiments. Ohta et al. (2016) measured *T* dependence of electrical resistance of iron samples at high *P* and referred to the high-*P*/room-*T* resistivity of *hcp* iron from Gomi et al. (2013) to calculate high-*P*/high-*T* resistivity. The κ_{el} of *hcp* iron at 135 GPa and 300 K was obtained as 165(+56/−22) W/m/K. The method employed in Konôpková et al. (2016) cannot determine high-*P*/room-*T* conductivity in principle, as they acquired time-dependent thermal radiation spectra from a laser-heated iron sample. To construct a model of high-*P*/high-*T* thermal conductivity of *hcp* iron, they referred to a value of electrical resistivity of *hcp* iron at 135 GPa and 300 K inferred from the experimental results of Seagle et al. (2013) and converted it to κ_{el} of 120(+20/−30) W/m/K via the Wiedemann-Franz law with an unusual Lorenz number of 1.9×10^{-8} WΩ/K^2. In this study, we found highly anisotropic thermal conductivity of *hcp* iron at least up to 44.5 GPa and 300 K based on the present XRD and thermal conductivity measurements. Based on the pressure derivatives ($\frac{dk}{dP}$) of the obtained κ_a and κ_c of *hcp* iron

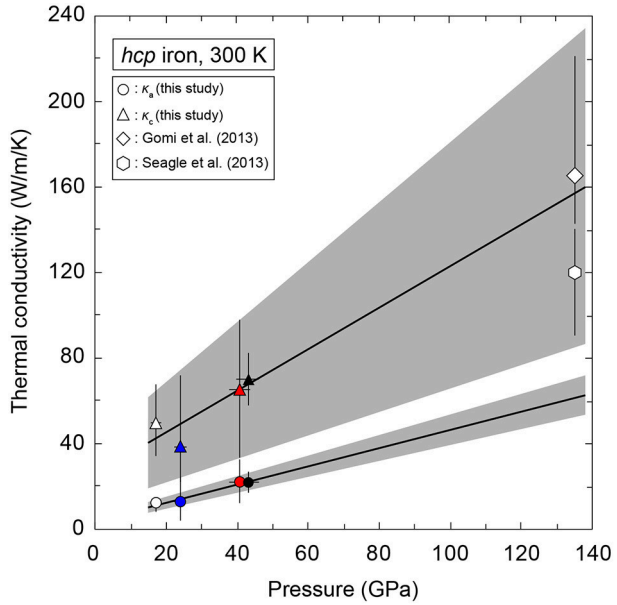

FIGURE 12 | Linear extrapolation of the obtained κ_a and κ_c at 300 K. Values of κ_{el} of *hcp* iron at 135 GPa and 300 K are also plotted that were estimated from the resistivity of *hcp* iron (Gomi et al., 2013) and the WF law with L_0 (open diamond), and from the *hcp* iron resistivity (Seagle et al., 2013) and the WF law with $L = 1.9 \times 10^{-8}$ WΩ/K^2 (open hexagon).

that are 0.43 and 0.98 W/m/K/GPa, respectively, we estimated κ_a and κ_c of *hcp* iron at higher *P*, indicating the anisotropy in the conductivity is maintained to the core pressures (**Figure 12**). At 135 GPa, the pressure of the Earth's core-mantle boundary, κ_a and κ_c of *hcp* iron are 61.4 ± 8.9 and 157.3 ± 72.6 W/m/K, respectively, and κ_c/κ_a is 2.6. Therefore, thermal conductivity anisotropy in single crystal *hcp* iron can explain the discrepancy in the reference conductivities at 135 GPa and 300 K (**Figure 12**). However, the reported values of the thermal conductivity of *hcp* iron at 135 GPa and high *T* conditions shows about a seven-fold difference (Konôpková et al., 2016; Ohta et al., 2016). It remains unclear whether the conductivity anisotropy of single crystal *hcp* iron is kept to a few thousand K. In some *hcp* analog metals, their κ_c/κ_a was getting smaller with increasing *T* (Nellis and Legvold, 1969; Alderson and Hurd, 1975; Secco and Balog, 2001). Only for magnesium, its κ_c/κ_a increases with increasing *T*, but the *T* response of κ_c/κ_a was examined only from 3 to 300 K. Unless *hcp* iron shows strongly positive *T* dependence of κ_c/κ_a, the conductivity anisotropy is unlikely to

be the main cause of the controversial reports (Konôpková et al., 2016; Ohta et al., 2016). In this context, T enhanced electron-electron scattering in compressed iron would be a key factor as shown in Pourovskii et al. (2017). Within their calculations, the thermal conductivity is depressed by 39% by electron-electron scattering. For more detailed discussion, further studies for direct determination of both electrical and thermal conductivities are required at extremely high P-T conditions.

If the thermal conductivity anisotropy in *hcp* iron single crystal is preserved to the Earth's inner core conditions, it may have important implications for evolution and dynamics there. The seismological exploration of the Earth's inner core has revealed its structural complexities (e.g., Tkalčić, 2015; Romanowicz and Wenk, 2017). One of the main features in the inner core is that a seismic wave along the polar direction propagates by about 3% faster than one along the equatorial direction (Poupinet et al., 1983; Morelli et al., 1986). The preferred alignment of *hcp* iron alloy crystals with the *c* axis parallel to the fast-seismic axis has been repeatedly suggested to explain the cause of the seismic anisotropy in the inner core (Yoshida et al., 1996; Bergman, 1997; Karato, 1999; Buffett and Wenk, 2001), although a consensus has not reached among theoretical studies to calculate sound velocity difference between *a* and *c* axes of *hcp* iron. Early theoretical calculations at 0 K showed that *c* axis was the faster direction than *a* axis in *hcp* iron (e.g., Stixrude and Cohen, 1995), but later studies at high temperatures showed that the sense of anisotropy changes, and the *a* axis becomes the fast direction (Steinle-Neumann et al., 2001), or nearly isotropic (Sha and Cohen, 2010). If the *c* axis of *hcp* iron alloy preferentially aligns along the Earth's rotational axis in the inner core, strong anisotropy of the thermal conductivity in *hcp* iron as observed in this study implies an anisotropic thermal conductivity of the inner core with higher conductivity in the polar direction and lower conductivity in equatorial radial directions. In addition, recent first-principles calculations showed that incorporation of silicon and nickel into iron enhances anisotropy in the conductivity (Gomi et al., 2016). The Taylor column type outer core convection extracts more heat away from the ICB in equatorial regions than in polar regions, even in the absence of anisotropic thermal conductivity. As a result, greater heat loss and lower thermal conductivity of the inner core along the equatorial direction than the polar direction would produce large temperature heterogeneity at the ICB, which would enhance the directionality of inner core growth and keep the crystallographic origin of the inner core anisotropy through the geological timescale via the plastic core flow mechanism (Yoshida et al., 1996). In the recent years, detailed modeling of the inner core evolution and dynamics have been reported, but no study considered the thermal conductivity anisotropy in the inner core (e.g., Alboussière and Deguen, 2012; Deguen, 2012). The magnitude of thermal conductivity anisotropy in *hcp* iron (iron alloy) at the ICB conditions needs to be confirmed for more detailed discussion about the inner core evolution and dynamics.

CONCLUSIONS

In this paper, we presented the results from the synchrotron XRD experiments and the thermal conductivity measurements on polycrystalline *hcp* iron up to 44.5 GPa and 300 K. Analyses of the XRD data yielded the CPO of *hcp* iron samples, which revealed variable CPO of *hcp* iron depending on the CPO of *bcc* iron starting materials. The obtained CPO information and thermal conductivity value of *hcp* iron samples were used to evaluate the anisotropy in the thermal conductivity of *hcp* iron single crystal. Assuming a randomly distributed aggregate texture in *hcp* iron polycrystal, we found $\kappa_c/\kappa_a \sim 3$ at 44.5 GPa and 300 K. Such strong anisotropy could be maintained to the Earth's core conditions and cause the discrepancy between recent experimental determinations of the thermal conductivity of *hcp* iron. Thermal conductivity anisotropy of *hcp* iron under Earth's actual core conditions should thus be investigated in future work to provide tighter constraints on the thermal evolution and dynamics of Earth's core and mantle.

AUTHOR CONTRIBUTIONS

KO and YN are responsible for project design and wrote the manuscript. KO, YN, and YS are responsible for sample preparation, XRD experiments, and texture analyses. KO and TY are responsible for thermal conductivity measurements. KH, SK, NH, and YO helped with XRD experiments at BL10XU, SPring-8. All authors contributed to the discussion and final manuscript.

FUNDING

This work was supported by JSPS KAKENHI (grant number 26247075, 15H03749, and 17H04861) and the Joint Usage/Research Center PRIUS, Ehime University.

ACKNOWLEDGMENTS

We thank S. Arakawa for discussion about the calculation of thermal conductivity anisotropy. Synchrotron XRD measurements were conducted at BL10XU, SPring-8 (proposal numbers 2016B0080 and 2017A0072).

REFERENCES

Alboussière, T., and Deguen, R. (2012). Asymmetric dynamics of the inner core and impact on the outer core. *J. Geodyn.* 61, 172–182. doi: 10.1016/j.jog.2012.07.006

Alderson, J. E. A., and Hurd, C. M. (1975). Anisotropic temperature-dependent resistivity of Cd, Zn, and Mg. *Phys. Rev. B* 12, 501–508. doi: 10.1103/PhysRevB.12.501

Badro, J., Siebert, J., and Nimmo, F. (2016). An early geodynamo driven by exsolution of mantle components from Earth's core. *Nature* 536, 326–328. doi: 10.1038/nature18594

Balog, P., and Secco, R. (1999). Electrical resistivity anisotropy of gd at high pressure. *Phys. Status Solid B* 214, 357–363.

Bergman, M. (1997). Measurements of electric anisotropy due to solidification texturing and the implications for the Earth's inner core. *Nature* 389, 60–63.

Biggin, A., Piispa, E., Pesonen, L., Holme, R., Paterson, G., Veikkolainen, T., et al. (2015). Palaeomagnetic field intensity variations suggest Mesoproterozoic inner-core nucleation. *Nature* 526, 245–248. doi: 10.1038/nature15523

Braginsky, S. I. (1963). Structure of the F layer and reasons for convection in the Earth's core. *Sov. Phys. Dokl.* 149, 8–10.

Buffett, B. A., and Wenk, H. R. (2001). Texturing of the Earth's inner core by Maxwell stresses. *Nature* 413, 60–63. doi: 10.1038/35092543

Deguen, R. (2012). Structure and dynamics of Earth's inner core. *Earth Planet. Sci. Lett.* 333, 211–225. doi: 10.1016/j.epsl.2012.04.038

Deng, L., Seagle, C., Fei, Y., and Shahar, A. (2013). High pressure and temperature electrical resistivity of iron and implications for planetary cores. *Geophys. Res. Lett.* 40, 33–37. doi: 10.1029/2012GL054347

Dewaele, A., Denoual, C., Anzellini, S., Occelli, F., Mezouar, M., Cordier, P., et al. (2015). Mechanism of the α-ε phase transformation in iron. *Phys. Rev. B* 91:174105. doi: 10.1103/PhysRevB.91.174105

Dobson, D. (2016). Geophysics: Earth's core problem. *Nature* 534, 45–45. doi: 10.1038/534045a

Du, Z., Jackson, C., Bennett, N., Driscoll, P., Deng, J., Lee, K., et al. (2017). Insufficient energy from MgO exsolution to power early geodynamo. *Geophys. Res. Lett.* 44, 11376–11381. doi: 10.1002/2017GL075283

Gomi, H., Hirose, K., Akai, H., and Fei, Y. (2016). Electrical resistivity of substitutionally disordered hcp Fe–Si and Fe–Ni alloys: chemically-induced resistivity saturation in the Earth's core. *Earth Planet. Sci. Lett.* 451, 51–61. doi: 10.1016/j.epsl.2016.07.011

Gomi, H., Ohta, K., Hirose, K., Labrosse, S., Caracas, R., Verstraete, M., et al. (2013). The high conductivity of iron and thermal evolution of the Earth's core. *Phys. Earth Planet. Interiors* 224, 88–103. doi: 10.1016/j.pepi.2013.07.010

Guéguen, Y., and Palciauskas, V. (1994). *Introduction to the Physics of Rocks*. Princeton, NJ: Princeton University Press.

Hall, P. M., Legvold, S., and Review, S.-F. (1959). Electrical resistivity of yttrium single crystals. *Phys. Rev.* 116, 1446–1447. doi: 10.1103/PhysRev.116.1446

Hirose, K., Morard, G., Sinmyo, R., Umemoto, K., Hernlund, J., Helffrich, G., et al. (2017). Crystallization of silicon dioxide and compositional evolution of the Earth's core. *Nature* 543, 99–102. doi: 10.1038/nature21367

Ishimatsu, N., Sata, Y., Maruyama, H., Watanuki, T., Kawamura, N., Mizumaki, M., et al. (2014). α-ε transition pathway of iron under quasihydrostatic pressure conditions. *Phys. Rev. B* 90, 014422. doi: 10.1103/PhysRevB.90.014422

Jaccard, D., Holmes, A. T., Behr, G., Inada, Y., and Onuki, Y. (2002). Superconductivity of ε-Fe: complete resistive transition. *Phys. Lett. A* 299, 282–286. doi: 10.1016/S0375-9601(02)00725-9

Karato, S. (1999). Seismic anisotropy of the Earth's inner core resulting from flow induced by Maxwell stresses. *Nature* 402, 871–873. doi: 10.1038/47235

Kocks, U. F., Tomé, C. N., and Wenk, H. R. (2000). *Texture and Anisotropy: Preferred Orientations in Polycrystals and Their Effect on Materials Properties*. Cambridge, UK: Cambridge University Press.

Konôpková, Z., McWilliams, R., Gómez-Pérez, N., and Goncharov, A. (2016). Direct measurement of thermal conductivity in solid iron at planetary core conditions. *Nature* 534, 99–101. doi: 10.1038/nature18009

Landauer, R. (1952). The electrical resistance of binary metallic mixtures. *J. Appl. Phys.* 23, 779–784. doi: 10.1063/1.1702301

Landeau, M., Aubert, J., and Olson, P. (2017). The signature of inner-core nucleation on the geodynamo. *Earth Planet. Sci. Lett.* 465, 193–204. doi: 10.1016/j.epsl.2017.02.004

Lister, J. (2003). Expressions for the dissipation driven by convection in the Earth's core. *Phys. Earth Planet. Interiors* 140, 145–158. doi: 10.1016/j.pepi.2003.07.007

Lutterotti, L., Bortolotti, M., Ischia, G., Lonardelli, I., and Wenk, H. R. (2007). Rietveld texture analysis from diffraction images. *Z. Kristallogr. Suppl.* 26, 125–130. doi: 10.1524/zksu.2007.2007.suppl_26.125

Lutterotti, L., Vasin, R., and Wenk, H.-R. (2014). Rietveld texture analysis from synchrotron diffraction images. I. Calibration and basic analysis. *Powder Diff.* 29, 76–84. doi: 10.1017/S0885715613001346

Merkel, S., Wenk, H.-R., Gillet, P., Mao, H., and Hemley, R. (2004). Deformation of polycrystalline iron up to 30 GPa and 1000 K. *Phys. Earth Planet. Interiors* 145, 239–251. doi: 10.1016/j.pepi.2004.04.001

Merkel, S., and Yagi, T. (2005). X-ray transparent gasket for diamond anvil cell high pressure experiments. *Rev. Sci. Instrum.* 76:046109. doi: 10.1063/1.1884195

Miyagi, L., Kunz, M., Knight, J., Nasiatka, J., Voltolini, M., and Wenk, H.-R. (2008). *In situ* phase transformation and deformation of iron at high pressure and temperature. *J. Appl. Phys.* 104:103510. doi: 10.1063/1.3008035

Morelli, A., Dziewonski, A., and Woodhouse, J. (1986). Anisotropy of the inner core inferred from PKIKP travel times, *Geophys. Res. Lett.* 13, 1545–1548. doi: 10.1029/GL013i013p01545

Nellis, W. J., and Legvold, S. (1969). Thermal conductivities and Lorenz functions of gadolinium, terbium, and holmium single crystals. *Phys. Rev.* 180, 581–590. doi: 10.1103/PhysRev.180.581

Nishihara, Y., Ohuchi, T., Kawazoe, T., Seto, Y., Maruyama, G., Higo, Y., et al. (2018). Deformation-induced crystallographic-preferred orientation of hcp-iron: an experimental study using a deformation-DIA apparatus. *Earth Planet. Sci. Lett.* 490, 151–160. doi: 10.1016/j.epsl.2018.03.029

Ohta, K., Kuwayama, Y., Hirose, K., Shimizu, K., and Ohishi, Y. (2016). Experimental determination of the electrical resistivity of iron at Earth's core conditions. *Nature* 534, 95–98. doi: 10.1038/nature17957

Ohta, K., Yagi, T., Hirose, K., and Ohishi, Y. (2017). Thermal conductivity of ferropericlase in the Earth's lower mantle. *Earth Planet. Sci. Lett.* 465, 29–37. doi: 10.1016/j.epsl.2017.02.030

O'Rourke, J., and Stevenson, D. (2016). Powering Earth's dynamo with magnesium precipitation from the core. *Nature* 529, 387–389. doi: 10.1038/nature16495

Poupinet, G., Pillet, R., and Souriau, A. (1983). Possible heterogeneity of the Earth's core deduced from PKIKP travel times. *Nature* 305, 204–206.

Pourovskii, L., Mravlje, J., Georges, A., Simak, S., and Abrikosov, I. (2017). Electron–electron scattering and thermal conductivity of f P travel timess core conditions. *New J. Phys.* 19:073022. doi: 10.1088/1367-2630/aa76c9

Reichlin, R. (1983). Measuring the electrical resistance of metals to 40 GPa in the diamond-anvil cell. *Rev. Sci. Instrum.* 54, 1674–1677 doi: 10.1063/1.1137308

Romanowicz, B., and Wenk, H. R. (2017). Anisotropy in the deep Earth. *Phys. Earth Planet. Interiors* 269, 58–90. doi: 10.1016/j.pepi.2017.05.005

Sanborn, B. A., Allen, P. B., and Papaconstantopoulos, D. A. (1989). Empirical electron-phonon coupling constants and anisotropic electrical resistivity in hcp metals. *Phys. Rev. B* 40, 6037–6044. doi: 10.1103/PhysRevB.40.6037

Seagle, C., Cottrell, E., Fei, Y., Hummer, D., and Prakapenka, V. (2013). Electrical and thermal transport properties of iron and iron-silicon alloy at high pressure. *Geophys. Res. Lett.* 28, 5377–5381. doi: 10.1002/2013GL057930

Secco, R. (2017). Thermal conductivity and Seebeck coefficient of Fe and Fe-Si alloys: Implications for variable Lorenz number. *Phys. Earth Planet. Interiors* 265, 23–34. doi: 10.1016/j.pepi.2017.01.005

Secco, R. A., and Balog, P. S. (2001). On the possibility of anisotropic heat flow in the inner core. *Can. J. Earth Sci.* 38, 975–982. doi: 10.1139/e00-116

Sha, X., and Cohen, R. (2010). Elastic isotropy of ε-Fe under Earth's core conditions. *Geophys. Res. Lett.* 37:L10302. doi: 10.1029/2009GL042224

Smirnov, A., Tarduno, J., Kulakov, E., McEnroe, S., and Bono, R. (2016). Palaeointensity, core thermal conductivity and the unknown age of the inner core. *Geophys. J. Int.* 205, 1190–1195. doi: 10.1093/gji/ggw080

Spedding, F., Cress, D., and Beaudry, B. (1971). The resistivity of scandium single crystals. *J. Less Common Metals* 23, 263–270. doi: 10.1016/0022-5088(71)90140-8

Steinle-Neumann, G., Stixrude, L., Cohen, R., and Gülseren, O. (2001). Elasticity of iron at the temperature of the Earth's inner core. *Nature* 413, 57–60. doi: 10.1038/35092536

Stierman, R. J., Gschneidner, K. A., Tsang, T.-W. E., Schmidt, F. A., Klavins, P., Shelton, R. N., et al. (1983). Magnetic susceptibility and electrical resistivity of electrotransport purified scandium single crystals from l resistivity *J. Magn. Magn. Mater.* 36, 249–254. doi: 10.1016/0304-8853(83)90122-1

Stixrude, L., and Cohen, R. E. (1995). High-pressure elasticity of iron and anisotropy of Earth's inner core. *Science* 267, 1972–1975.

Tkalčić, H. (2015). Complex inner core of the Earth: the last frontier of global seismology. *Rev. Geophys.* 53, 59–94. doi: 10.1002/2014RG000469

Verhoogen, J. (1961). Heat balance of the Earth's core. *Geophys. J. R. Astron. Soc.* 4, 276–281.

Williams, Q. (2018). The thermal conductivity of Earth's core: a key geophysical parameter's constrains and uncertainties. *Annu. Rev. Earth Planet. Sci.* 46, 47–66. doi: 10.1146/annurev-earth-082517-01015

Yagi, T., Ohta, K., Kobayashi, K., Taketoshi, N., Hirose, K., and Baba, T. (2011). Thermal diffusivity measurement in a diamond anvil cell using a light pulse thermoreflectance technique. *Meas. Sci. Technol.* 22:024011. doi: 10.1088/0957-0233/22/2/024011

Yamasue, E., Susa, M., Fukuyama, H., and Nagata, K. (2003). Deviation from Wiedemann–Franz law for the thermal conductivity of liquid tin and lead at elevated temperature. *Int. J. Thermophys.* 24, 713–730. doi: 10.1023/A:1024088232730

Yamazaki, D., Ito, E., Yoshino, T., Yoneda, A., Guo, X., Zhang, B., et al. (2012). *P-V-T* equation of state for ε-iron up to 80 GPa and 1900 K using the Kawai-type high pressure apparatus equipped with sintered diamond anvils. *Geophys. Res. Lett.* 39, L20308. doi: 10.1029/2012GL053540

Yoshida, S., Sumita, I., and Kumazawa, M. (1996). Growth model of the inner core coupled with the outer core dynamics and the resulting elastic anisotropy. *J. Geophys. Res.* 101, 28085–28103. doi: 10.1029/96JB02700

Zhang, C., Lin, J., Liu, Y., Feng, S., Jin, C., Hou, M., et al. (2018). Electrical resistivity of Fe-C alloy at high pressure: effects of carbon as a light element on the thermal conductivity of the Earth's core. *J. Geophys. Res.* 123, 3564–3577. doi: 10.1029/2017JB015260

Conflict of Interest Statement: The authors declare that the research was conducted in the absence of any commercial or financial relationships that could be construed as a potential conflict of interest.

APPENDIX

Derivation of the Thermal Conductivity of a *hcp* Crystal Along a Direction θ ($\kappa(\theta)$)

The Fourier's law of thermal conduction shows that the local heat flux density ($\boldsymbol{J}$), is equal to the product of the local temperature gradient (grad$T$) and thermal conductivity (κ):

$$\boldsymbol{J} = -\kappa \mathrm{grad}T. \tag{A1}$$

Let the effective thermal conductivity be the ratio of the heat flux components in the same direction caused by the temperature gradient of the direction. Here, we consider a temperature gradient having a component only in the x_3 direction:

$$\mathrm{grad}T = \begin{pmatrix} 0 \\ 0 \\ \frac{\partial T}{\partial x_3} \end{pmatrix}, \tag{A2}$$

the J_3 component can be written as follow:

$$J_3 = -\kappa_{33}\frac{\partial T}{\partial x_3}. \tag{A3}$$

Therefore, in this case, the effective thermal conductivity is κ_{33}. The thermal conductivity (κ) of a hexagonal crystal is a second-order tensor with two independent components κ_a, κ_c, and is expressed as follows:

$$\kappa = \begin{pmatrix} \kappa_a & 0 & 0 \\ 0 & \kappa_a & 0 \\ 0 & 0 & \kappa_c \end{pmatrix}, \tag{A4}$$

which indicates that the thermal conductivity of the hexagonal crystal has anisotropy axially symmetric with respect to the c axis. It thus should be able to be expressed as a function of the angle θ with the effective thermal conductivity of an arbitrary direction with the c axis. Here, we set up the thermal conductivity tensor κ' when the hexagonal crystal is rotated about the x_1 axis by the angle θ as follows:

$$\begin{aligned} \kappa' &= \begin{pmatrix} 1 & 0 & 0 \\ 0 & cos\theta & -sin\theta \\ 0 & sin\theta & cos\theta \end{pmatrix} \begin{pmatrix} \kappa_a & 0 & 0 \\ 0 & \kappa_a & 0 \\ 0 & 0 & \kappa_c \end{pmatrix} \begin{pmatrix} 1 & 0 & 0 \\ 0 & cos\theta & sin\theta \\ 0 & -sin\theta & cos\theta \end{pmatrix} \\ &= \begin{pmatrix} \kappa_a & 0 & 0 \\ 0 & \kappa_a cos^2\theta + \kappa_c sin^2\theta & (\kappa_a - \kappa_c)\, sin\theta cos\theta \\ 0 & (\kappa_a - \kappa_c)\, sin\theta cos\theta & \kappa_a sin^2\theta + \kappa_c cos^2\theta \end{pmatrix}. \end{aligned} \tag{A5}$$

Considering the relationship of Equation (A3), the effective thermal conductivity $\kappa(\theta)$ is equal to the κ'_{33} component of the thermal conductivity tensor κ' after θ rotation. Therefore, $\kappa(\theta)$ can be written as

$$\kappa(\theta) = \kappa_a sin^2\theta + \kappa_c cos^2\theta. \tag{A6}$$

frontiers in Earth Science

ORIGINAL RESEARCH
published: 02 November 2018
doi: 10.3389/feart.2018.00192

On Destruction of a Thermally Stable Layer by Compositional Convection in the Earth's Outer Core

Shin-ichi Takehiro[1]* *and Youhei Sasaki*[2]

[1] Research Institute for Mathematical Sciences, Kyoto University, Kyoto, Japan, [2] Department of Mathematics, Kyoto University, Kyoto, Japan

We discuss destruction of a thermally stable layer in the upper part of the Earth's outer core by compositional convection excited at the inner core boundary. We propose to use the radial distribution of power induced by thermal and compositional buoyancy (rate of kinetic energy production) as a measure of occurrence of thermal and compositional convection. The power consists of the terms proportional to convective entropy flux and convective compositional flux. In the region with positive power, convection is active because kinetic energy can be produced by buoyancy force, and a stably stratified layer could not be formed there. On the other hand, in the region with negative power, convection is suppressed and a stably stratified layer may be produced. Considering penetration effect of convection, we discuss possible maximum and minimum thicknesses of the stable layer based on the radial distribution of power and its radial integral, respectively. We construct a 1-dimensional thermal and compositional balance model of the Earth's core with a larger value of thermal conductivity recently suggested by high-pressure experiments and first principle calculations, and estimate radial distributions of power for various values of core mantle boundary (CMB) heat flux Q_{CMB}. When $Q_{CMB} > Q_{sCMB}$ no thermally stable layer can exist, where Q_{sCMB} is the conductive heat flux along the adiabat at the CMB. On the other hand, when $Q_{CMB} < Q_{sCMB}$, formation of an upper thermally stable layer becomes possible, depending on the extent of penetration of compositional convection excited below. When Q_{CMB} is sufficiently lower than Q_{sCMB}, a thermally stable layer survives the maximum penetration of compositional convection. The results show that a thermally stable layer becomes effectively thinner when the effect of compositional convection is considered compared with the results of previous studies where the existence of a stable layer is evaluated based on the convective flux only.

Keywords: thermal conductivity, heat flux, compositional flux, power by buoyancy forces, kinetic energy production, core dynamics, core stratification

OPEN ACCESS

Edited by:
Hagay Amit,
University of Nantes, France

Reviewed by:
Stéphane Labrosse,
École Normale Supérieure de Lyon, France
Mathieu Bouffard,
Max-Planck-Institut für Sonnensystemforschung, Germany

***Correspondence:**
Shin-ichi Takehiro
takepiro@gfd-dennou.org

Specialty section:
This article was submitted to Geomagnetism and Paleomagnetism, a section of the journal Frontiers in Earth Science

Received: *28 May 2018*
Accepted: *17 October 2018*
Published: *02 November 2018*

Citation:
Takehiro S and Sasaki Y (2018) On Destruction of a Thermally Stable Layer by Compositional Convection in the Earth's Outer Core. Front. Earth Sci. 6:192. doi: 10.3389/feart.2018.00192

1. INTRODUCTION

It is widely thought that fluid motion driven in the Earth's outer core by cooling due to mantle convection generates and maintains the geomagnetic field through dynamo action. Although thermal convection would occur as a direct effect of cooling from the core mantle boundary (CMB) and as a result of the latent heat release at the inner core boundary (ICB) associated with growth

of the inner core through solidification of Fe and Ni, the main energy source for geomagnetic field generation is considered to be supplied by compositional convection induced by the release of light elements at the ICB (e.g., Lister and Buffett, 1995). Estimation of the power available for magnetic energy as well as evolution of the structure of the Earth's core has been studied extensively using 1-dimensional thermal and compositional budget models (e.g., Loper, 1978; Gubbins et al., 1979; Stevenson, 1983).

Most of the models assumed vigorous convection mixes completely the whole fluid core, and entropy and composition are homogeneous. Alternative models considering formation of a stably stratified layer below the CMB were proposed (Labrosse et al., 1997; Lister and Buffett, 1998). They assumed that, when heat flow at the CMB Q_{CMB} determined by strength of mantle convection becomes smaller than upward conductive heat flow along the adiabatic temperature profile Q_s, heat accumulates below the CMB, and a thermally stable layer starts to develop by conduction. Labrosse et al. (1997) assumed that erosion of the stable layer by mixing due to compositional convection generated from the deeper region does not occur, whereas Lister and Buffett (1998) considered accumulation of light elements due to inner core growth explicitly. They discussed the competition between light elements accumulating in the convecting region of the core and heat accumulating in the stratified layer due to a subadiabatic heat flux at the CMB.

Recently, it was suggested from high-pressure experiments and first principle calculations that the values of thermal conductivity under conditions of planetary cores are larger than those considered so far (Gomi et al., 2013; Pozzo et al., 2014). By using 1-dimensional thermal balance models with the updated values of thermal conductivity, generation and existence of a stably stratified layer in the Earth's outer core was discussed (Gomi et al., 2013; Labrosse, 2015). Their results showed that a stable layer with a thickness of O(1,000 km) could be produced when the heat flux across the CMB is small. They assumed that the region with negative convective heat flux is stably stratified. This assumption seems to be appropriate when convection is driven only by thermal effects, however, it is not correct when compositional convection occurs simultaneously. When compositional convection is sufficiently vigorous to overcome thermally stable stratification, it would mix up the stable layer and make it neutral.

Whether the stably stratified layer is formed and maintained below the CMB or it is destroyed by compositional convection from the deeper region is a significant issue for the evolution of the Earth's core structure. Formation of the stable layer affects the thermal history of the core, such as the age of the inner core and field intensity (e.g., Labrosse et al., 1997; Lister and Buffett, 1998). It is also related to geomagnetic secular variation observed at the surface of the Earth, since it could originate from the fluid motions in the stable layer if it exists (e.g., Braginsky, 1984, 1993; Buffett, 2014).

In the present study, we propose to use radial distribution of power induced by thermal and compositional buoyancy (rate of kinetic energy production) as a measure of occurrence of thermal and compositional convection. The power consists of the terms proportional to heat flux and compositional flux. In the region with positive power convection is active because kinetic energy can be produced by buoyancy force. On the other hand, in the region with negative power, convection is suppressed and the stably stratified layer may be produced.

In the following, formulation of a 1-dimensional thermal and compositional budget model is recalled, and a criterion for formation and destruction of the stable layer is proposed in section 2. Then we apply the model and the criterion to a simple core model, and illustrate formation of a stable layer and its thickness depending on the CMB heat flux in section 3. Summary and discussion are in the final section.

2. MODEL AND METHOD

2.1. Estimation of Stratified Layer

The procedure for calculation of the power induced by thermal and compositional buoyancy (rate of kinetic energy production) in 1-dimensional thermal and compositional budget models was proposed by Lister and Buffett (1995). They did not apply it to the stable layer formation problem but estimated available energy for magnetic field generation using the integral value of the power in the whole domain. We propose to use the radial distribution of power as a criterion for the formation and destruction of the stable layer. The rationale for this criterion is as follows.

We assume that the whole outer core is well mixed by convection, so that concentrations of light elements and entropy are homogeneous in the radial direction. Temperature follows an adiabatic profile. Then the radial distribution of power by buoyancy force (kinetic energy production) $w_b(r)$ can be calculated from distributions of convective entropy flux and convective compositional flux, which are diagnostically obtained by thermal and compositional budgets as explained below.

The regions where kinetic energy production is positive ($w_b(r) > 0$) can be mixed up by convection since it can emerge there, which is consistent with the assumption. Therefore, a stable layer is not formed there. On the other hand, in the regions where kinetic energy production is negative ($w_b(r) < 0$) convection cannot be driven locally, and mixing may not occur there. However, the region would be mixed up even when $w_b(r) < 0$ if convection driven in the lower part penetrates into there. Penetration could occur when total kinetic energy production in the convecting and penetrating regions is still positive. Then, possible penetration of convection can be evaluated by the radial integral of power $W_b(r) = \int_c^r 4\pi r'^2 w_b(r')dr'$, where c is the radius of ICB. We estimate the region with $W_b(r) > 0$ which could be mixed up by penetrative convection (**Figure 1**).

Therefore, the maximum and minimum thicknesses of the stable layer are determined with $w_b(r) < 0$ and $W_b(r) < 0$, respectively.

2.2. 1-Dimensional Thermal and Compositional Balance Model

1-dimensional thermal and compositional budget model of the Earth's core used in this study basically follows that developed by Lister and Buffett (1995), Gomi et al. (2013), and Labrosse (2015).

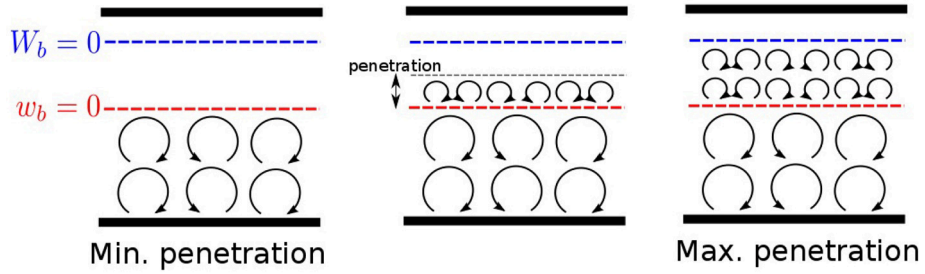

FIGURE 1 | The thickness of a stable layer depending on the extent of penetration of convection.

The equation for compositional budget is

$$X_C + F_C = S_C, \tag{1}$$

where X_C is averaged concentration increase of light elements, F_C is convective compositional flux, and S_C is light elements release at the ICB.

$$X_C(r) = \frac{d\bar{C}}{dt}\int_c^r 4\pi r^2 \rho_a dr, \tag{2}$$

$$F_C(r) = 4\pi r^2 \rho_a \overline{C'u_r}, \tag{3}$$

$$S_C = 4\pi c^2 \rho_c \bar{C}\frac{dc}{dt}, \tag{4}$$

where r is radius, b and c are radii of the CMB and ICB, respectively, $\bar{C}$ is the homogeneous concentration of light elements in the outer core, C' is the concentration fluctuation from $\bar{C}$, u_r the radial component of velocity, $\overline{C'u_r}$ the convective compositional flux, ρ_a and ρ_c are the horizontally averaged density in the outer core and at the ICB, respectively. Here, the light elements are assumed to be perfectly incompatible in the inner core for simplicity. Total compositional budget is expressed by $X_C(b) = S_C$. Using (1) and the boundary condition $F_C(b) = 0$, F_C can be described alternatively as follows:

$$F_C(r) = 4\pi c^2 \rho_c \bar{C}\frac{dc}{dt}\frac{M(b) - M(r)}{M(b) - M(c)}, \tag{5}$$

$$M(r) = \int_c^r 4\pi r^2 \rho_a dr. \tag{6}$$

The equation for the thermal budget is

$$Q_{conv}(r) = Q_{cooling} + E_{comp} + Q_{latent} - Q_s + Q_{visc} + Q_J + Q_{ICB}, \tag{7}$$

where Q_{conv}, $Q_{cooling}$, E_{comp}, Q_{latent} and Q_s are the convective heat flux, and its contributions by secular cooling, compositional energy, latent heat release, and thermal conduction, respectively, which are described as follows:

$$Q_{conv}(r) = 4\pi r^2[\mu'(r)\rho_a \overline{C'u_r} + \rho_a T_a \overline{S'u_r}], \tag{8}$$

$$Q_{cooling}(r) = -\int_0^r 4\pi r^2 \rho_a T_a \frac{\partial S_a}{\partial t} dr, \tag{9}$$

$$E_{comp}(r) = -\int_c^r 4\pi r^2 \mu'(r)\rho_a \frac{d\bar{C}}{dt} dr, \tag{10}$$

$$Q_{latent} = T_l \Delta S \rho_c 4\pi c^2 \frac{dc}{dt}, \tag{11}$$

$$Q_s(r) = -4\pi r^2 k(r)\frac{\partial T_a}{\partial r}, \tag{12}$$

where $T_a(r)$ is the adiabatic temperature profile in the outer core, S_a is entropy, which is assumed to be uniform, S' is the entropy fluctuation from S_a, $\overline{S'u_r}$ is the convective entropy flux, ΔS is the entropy jump associated with the crystallization of the inner core, T_L is liquidus temperature, $k(r)$ is thermal conductivity and $\mu'(r)$ is the chemical potential based on the value at the ICB. Following the discussion by Lister and Buffett (1995), we assume that Joule heating Q_J, viscous dissipation Q_{visc} and the heat flow coming from the inner core Q_{ICB} can be neglected in the thermal budget (7). From the total thermal budget in the whole core, we obtain

$$Q_{CMB} = Q_{cooling}(b) + E_{comp}(b) + Q_{latent}. \tag{13}$$

Previous studies showed that all the terms on the right hand side of (13) are proportional to dc/dt, and then, the radial distributions of all the terms are obtained for given CMB heat flow Q_{CMB}.

The convective entropy flux F_S is expressed as

$$F_S(r) \equiv 4\pi r^2 \rho_a \overline{S'u_r} = \frac{Q_{conv}(r) - \mu'(r)F_C(r)}{T_a(r)}. \tag{14}$$

The power by buoyancy forces $w_b(r)$ is calculated with the convective fluxes as follows:

$$w_b(r) \equiv 4\pi r^2 g\left[\frac{\alpha T_a}{C_p}\rho_a \overline{S'u_r} - \rho_a \beta \overline{C'u_r}\right] = \frac{\alpha g T_a}{C_p}F_S - \beta g F_C \tag{15}$$

where $\alpha = -\frac{1}{\rho}\left(\frac{\partial \rho}{\partial T}\right)_{P,C}$ and $\beta = \frac{1}{\rho}\left(\frac{\partial \rho}{\partial C}\right)_{P,S}$ are thermal and compositional expansion coefficients, respectively.

2.3. Analytical Expressions of the Fluxes in a Simple Model

Here, we illustrate the result of a diagnosis on the formation of a stable layer in the present Earth's core with a simple setup similar to that used in Lister and Buffett (1995).

Density in the outer core is assumed to be constant. Gravity is given in the form of $g(r) = g_o(r/b)$, where g_0 is the gravitational acceleration at the CMB. Then adiabatic temperature $T_a(r,t)$ and its radial gradient can be described as

$$T_a(r,t) = T_i(t) f_a(r), \quad \frac{dT_a}{dr} = -\frac{\alpha g(r) T_a(r)}{C_p} = -AT_a(r)r, \quad (16)$$

where $T_i(t)$ is temperature at the ICB and

$$f_a(r) = e^{-A(r^2-c^2)/2}, \quad A = \frac{\alpha g_o}{C_p b}. \quad (17)$$

Since $Ab^2 = \alpha g_o b/C_p \sim 0.44 < 1$ for the values of the Earth's core, we approximate $f_a(r)$ as $f_a(r) \sim \frac{1-(A/2)r^2}{1-(A/2)c^2}$, and get

$$\begin{aligned} T_a(r,t) &= T_i(t)\frac{1-(A/2)r^2}{1-(A/2)c^2}, \\ \frac{dT_a}{dr} &= -\frac{\alpha g(r) T_a(r)}{C_p} = -AT_a(r)r, \end{aligned} \quad (18)$$

Accordingly, $Q_s(r)$ becomes

$$Q_s(r) = -4\pi r^2 k(r)\frac{dT_a}{dr} = 4\pi r^3 k(r) A T_a(r), \quad (19)$$

The present value of T_i is determined by setting the conductive heat flow along the adiabat at the CMB $Q_{sCMB} = Q_s(b)$.

On the other hand, the time derivative of $T_i(t)$ should be evaluated to calculate $Q_{cooling}$. From entropy variation with respect to temperature, pressure and composition variations

$$\begin{aligned} T_a\frac{\partial S_a}{\partial t} &= C_p\frac{\partial T_a}{\partial t} - \frac{\alpha T}{\rho}\frac{\partial P_a}{\partial t} + Q_H\frac{\partial \bar{C}}{\partial t} \sim C_p\frac{dT_i}{dt}f_a(r) \\ &= -C_p\rho_a g\frac{dT_L}{dp}\frac{dc}{dt}f_a, \end{aligned} \quad (20)$$

where T_i is temperature at the ICB, $Q_H = T\left(\frac{\partial S}{\partial C}\right)_{T,P}$ is heat of reaction, which is neglected for simplicity as well as contribution of pressure variation. Then, we have

$$Q_{ccooling}(r) = C_p\rho_0^2 g\frac{dT_L}{dp}\frac{4\pi}{1-(A/2)c^2}\left(\frac{1}{3}r^3 - \frac{A}{10}r^5\right)\frac{dc}{dt}. \quad (21)$$

Since the chemical potential is calculated as

$$\mu'(r) = \int_c^r \beta g(r) dr = \int_c^r \frac{\beta g_o}{b} r dr = \frac{\beta g_o}{2b}(r^2 - c^2), \quad (22)$$

its radial integral becomes

$$\int_c^r 4\pi r^2 \mu'(r)\rho_a dr = \frac{2}{15}\pi\frac{\rho_0\beta g_o}{b}(r-c)^2(3r^3+6r^2c+4rc^2+2c^3). \quad (23)$$

Then we obtain, from equation (10):

$$\begin{aligned} E_{comp}(r) &= -\frac{1}{10}\frac{\beta g_o}{b(b^3-c^3)}(r-c)^2(3r^3+6r^2c+4rc^2+2c^3) \\ &\quad \times 4\pi c^2\rho_c\bar{C}\frac{dc}{dt}. \end{aligned} \quad (24)$$

Here, we used the relation

$$\frac{d\bar{C}}{dt}\frac{4\pi}{3}\rho_0(b^3-c^3) = 4\pi c^2\rho_c\bar{C}\frac{dc}{dt} \quad (25)$$

derived by the total compositional budget $X_C(b) = S_C$.

The growth rate of the inner core dc/dt is determined by the global thermal budget Equation (13). By using the value of dc/dt, the convective compositional flux is calculated by (5), while the convective thermal flux is determined by

$$Q_{conv}(r) = Q_{cooling}(r) + E_{comp}(r) + Q_{latent} - Q_s(r), \quad (26)$$

Finally, the convective entropy flux is estimated by (14), and the power by buoyancy forces is determined by (15).

The radial profile of thermal conductivity is approximated to a recent large estimated value (Gomi et al., 2013) with a quadratic function as $k(r) = (k_b - k_0)(r/b)^2 + k_0$, where k_b, k_0 are the values at the CMB and the center of the core, respectively. The adiabatic temperature at CMB is given so that $Q_s(b) = Q_{sCMB} = 9.3$TW. The parameters used in the calculation are listed in **Table 1**.

3. RESULTS

Figure 2 shows the results in the case with $Q_{CMB} = 12$TW. The radial distributions of contributions to the thermal

TABLE 1 | The parameters used in the calculation.

Radius of the outer core (CMB)[a]	b	3.5×10^6 km
Radius of the inner core (ICB)[a]	c	1.2×10^6 km
Density in the outer core[a]	ρ_a	1.2×10^4 kg m^{-3}
Density difference between inner/outer core[b]	$\Delta\rho$	580 kg m^{-3}
Density in the inner core[a,b]	ρ_i	1.258×10^4 kg m^{-3}
Specific heat capacity[c]	C_p	800 J kg^{-1} K^{-1}
Thermal expansion coefficient[c]	α	10^{-5} K^{-1}
Compositional expansion coefficient[d]	β	−0.67
Gravity at CMB[e]	g_o	10 m s^{-2}
Concentration of light elements in the outer core[d]	$\bar{C}$	0.06
Entropy jump at melting/solidification[b]	ΔS	127 J kg^{-1} K^{-1}
Pressure gradient of liquidus temperature[c]	dT_L/dP	5×10^{-9} K Pa^{-1}
Thermal conductivity at CMB[d]	k_b	90 W m^{-1} K^{-1}
Thermal conductivity at the center of the core[d]	k_0	160.0 W m^{-1} K^{-1}
Conductive heat flow along the adiabat at CMB[d]	Q_{sCMB}	9.3 TW

[a] *From PREM.* [b] *From Labrosse (2015).* [c] *From Lister and Buffett (1995).* [d] *From Gomi et al. (2013).* [e] *From Stacey and Davis (2008).*

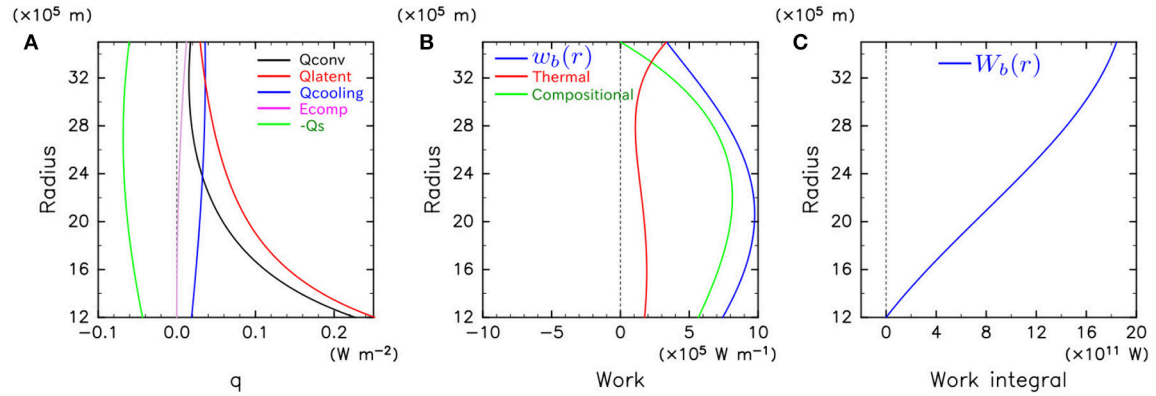

FIGURE 2 | Result of 1-dimensional thermal and compositional budget model for $Q_{CMB} = 12$TW. **(A)** Radial distributions of heat flows. Black, blue, purple, red and green lines indicate Q_{conv}, $Q_{cooling}$, E_{comp}, Q_{latent}, and Q_s, respectively. **(B)** Radial distributions of work by buoyancy forces $w_b(r)$. Green and red lines indicate contributions from compositional and thermal buoyancies. Blue line shows total work. **(C)** Radially integrated work by buoyancy forces $W_b(r)$.

budget in the left panel of **Figure 2** are qualitatively consistent with previous studies (e.g., Figure 9 in Gomi et al., 2013) although there are several differences. In this case, no stable layer is formed since Q_{conv} is positive in the whole outer core. Kinetic energy production $w_b(r)$ shown in the center panel of **Figure 2** is positive in the whole outer core. Note that both compositional and thermal contribution to $w_b(r)$ is positive in the whole outer core, indicating that thermal and compositional convection emerges there.

Figure 3 shows the results in the case with $Q_{CMB} = 8$TW. In this case, a stable layer is possible since Q_{conv} becomes negative. The region with $w_b(r) < 0$ below the CMB appears in the center panel of **Figure 3**. The middle panel of **Figure 3** shows the compositional contribution to $w_b(r)$ is positive in the whole outer core while the thermal contribution is negative at $r \gtrsim 2,200$ km, meaning that compositional convection is possible to emerge in the upper part of the outer core although thermal and compositional convection can be excited in the lower part. On the other hand, $W_b(r)$ is positive in the whole outer core as shown in the right panel of **Figure 3**. This means that formation of a stable layer depends on the extent of penetration of compositional convection from below. A stable layer survives below the CMB when penetration is weak, whereas a stable layer is completely destroyed by compositional convection when its penetration is strong. Note that the stable layer is thinner than that estimated by the criterion with thermal convective heat flux only ($Q_{conv} < 0$) used in the previous studies.

Figure 4 shows the result in the case with $Q_{CMB} = 4$TW. In the right panel of **Figure 4**, there appears the region with $W_b(r) < 0$ below CMB, meaning that a stable layer is formed even when the extent of penetration of convection is maximum in this case. Note that the thermal contribution is negative in the almost whole outer core in this case.

Figure 5 shows the summary of stable layer formation as a function of Q_{CMB}. The red and blue lines indicate the thickness of a stable layer in the case of minimum and maximum penetration, respectively. It is found that no stable layer is formed when $Q_{CMB} > Q_{sCMB} = 9.3$TW, whereas a stable layer is absolutely formed when $Q_{CMB} < 4.4$TW. We also show the bottom of a stable layer estimated by the criterion with thermal convective flux only by the black line for comparison. It is clear that destruction by compositional convection cannot be ignored in order to estimate the thickness of the stable layer.

4. CONCLUSIONS AND DISCUSSION

We proposed to use radial distribution of power by thermal and compositional buoyancy (rate of kinetic energy production) as a new criterion for estimating formation and destruction of a stably stratified layer by thermal and compositional convection. The method for calculating power by buoyancy forces in a 1-dimensional thermal and compositional budget model was presented, and was applied to a simple 1-dimensional model for the Earth's core. The thickness of the stable layer formed below the CMB is estimated for various values of the CMB heat flow considering the effect of mixing by compositional convection in the deeper region. When $Q_{CMB} > Q_{sCMB}(= 9.3$TW), no stable layer is formed due to occurrence of compositional and thermal convection in the whole outer core. When $Q_{CMB} < Q_{sCMB}(= 9.3$TW), formation of an upper thermally stable layer becomes possible, depending on the extent of penetration of compositional convection excited at ICB. When $Q_{CMB} < 4.4$TW, a stable layer can be formed even when penetration of compositional convection is maximal. Note that this critical value of Q_{CMB} varies depending on the value of Q_{sCMB} and model configuration for Earth's core. For example, constant density distribution and degree 2 polynomial isentropic temperature used in this study would not be precise enough for estimation of stable layer formation, since some discrepancies between previous studies were found to originate from different levels of approximation in the isentropic temperature profile (e.g., Labrosse, 2015). It is necessary to use more precise Earth models with more

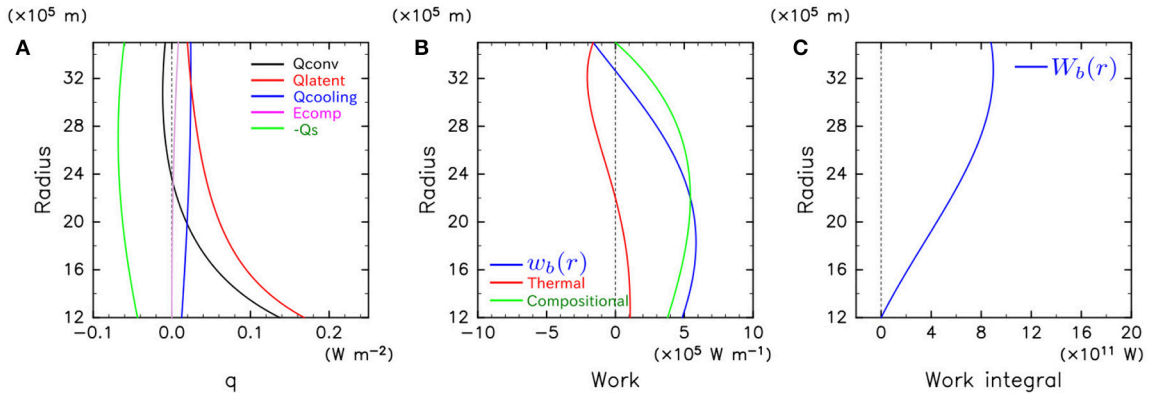

FIGURE 3 | As in **Figure 2** but for $Q_{CMB} = 8$TW.

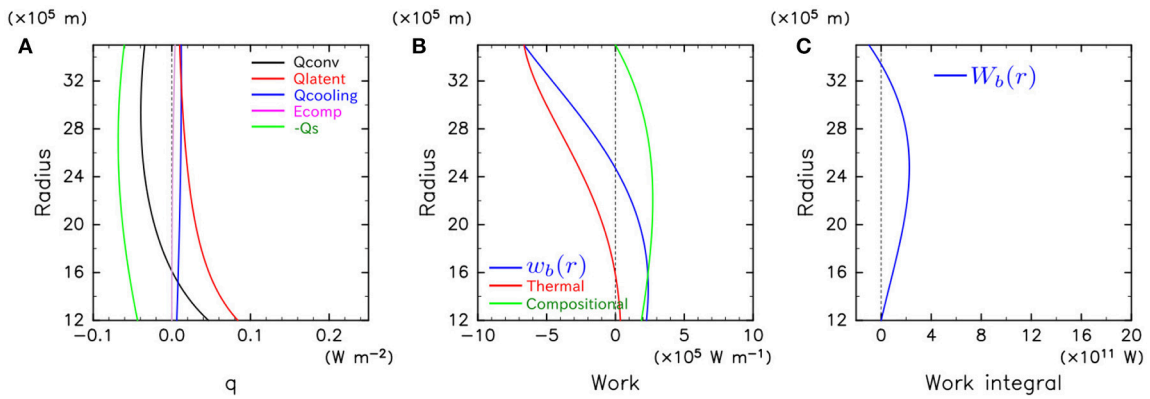

FIGURE 4 | As in **Figure 2** but for $Q_{CMB} = 4$TW.

realistic distributions of density, isentropic temperature and other physical properties for definitive conclusions about the Earth's core.

Since the present CMB heat flow is expected in the range 5–15 TW (e.g., Lay et al., 2008), our results also support possibility of a stable layer formation below the CMB as the previous studies. However our estimations show the thickness of the stable layer is significantly thinner than that estimated with the criterion only by thermal convective flux used in the previous studies due to mixing by compositional convection. For example, when $Q_{CMB} = 8$TW, the thickness of the stable layer can be 250 km at most, which is about 1,000 km thinner than the estimation by convective heat flux criterion (see **Figure 5**).

The present paper significantly contributes to thermal and compositional evolution problems in planetary cores by giving dynamically consistent estimation of stable layer formation. All the previous studies did not consider whether kinetic energy is adequately supplied to the convecting part or not, which should be checked by calculating kinetic energy production distribution.

We estimate emergence of a stable layer by assuming that the whole outer core is convecting. This procedure seems to be contradictory since existence of a stable layer breaks the assumption of the whole outer core convection. As a matter of fact, the solutions obtained by our method are first order approximations of quasi-steady states where concentrations of ight elements and temperature averaged in the whole outer core vary in time while their radial distributions are stationary. Spherically averaged conservation equation of light elements without assuming a homogeneous mixed state is described as follows:

$$\frac{\partial}{\partial t}(4\pi\rho_a C) + \frac{1}{r^2}\frac{\partial}{\partial r}(F_C + F_D) = 0, \tag{27}$$

where $C(r,t)$ is concentration of light elements, $F_C(r,t)$ and $F_D(r,t)$ are convective and non-convective fluxes such as diffusion, respectively. Assuming quasi-steady state, $C(r,t) = \bar{C}(t) + C'(r)$, and integrating from $r = c$ with the boundary condition $F_C(c) + F_D(c) = S_C$, Equation (1) is modified as

$$X_C + F_C + F_D = S_C. \tag{28}$$

This equation means that we can construct new solutions by replacing F_C obtained with the assumption of whole outer core

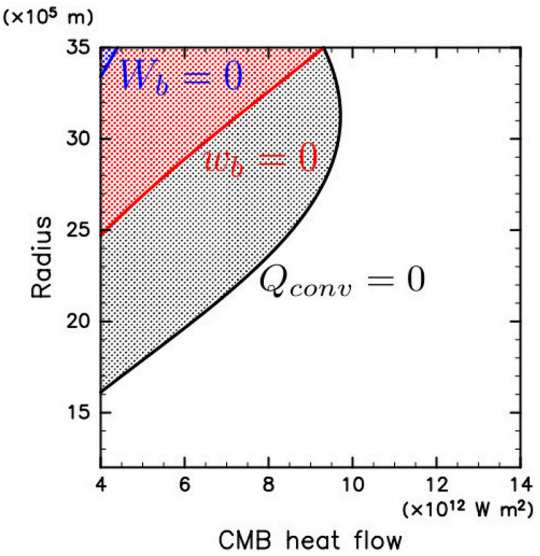

FIGURE 5 | Possible stable layer thickness as a function of CMB heat flow. The blue and red lines indicate the thickness of the minimum and maximum stable layers, respectively. The black line shows the thickness of a stable layer estimated by thermal convective flux only.

convection by $F_C + F_D$. For example, the flux distributions with $F_D = 0$ ($r < r_t$) and $F_C = 0$ ($r > r_t$) provide a quasi-steady solution for a given boundary $r = r_t$. The upper part of $C'(r)$ can be constructed from $F_D(r)$. This solution expresses the state where convection is active and mixes up the lower part $r < r_t$, while convection is suppressed and diffusion is dominant in the upper part $r > r_t$, forming stable stratification. Similar argument is possible for temperature by assuming $T(r,t) = T_i(t)f(r)$, however, the thermal fluxes would be varied due to the difference of the temperature structure between the solutions with and without a stable layer. Then, in order to estimate thickness of a stable layer more precisely, after determining its bottom boundary with the criterion of kinetic energy production, we should give a certain temperature distribution in a stable layer and calculate distribution of kinetic energy production again. By repeating this procedure we can obtain more precise estimation of a thickness of a stable layer. For example, given a thermally diffusive temperature profile stable layer, re-calculations of w_b lead to 0.07% and 1% differences of a stable layer thickness for $Q_{CMB} = 8$TW and 4TW (examples of **Figures 3**, **4**), respectively.

Quasi-steady stable layer thickness obtained in this study does not consider time scale for its formation, which would be governed by thermal diffusion. In order to discuss stable layer formation in the Earth's core more precisely, we should compare the diffusion time of possible thickness of the stable layer with a possible age of the inner core. When the diffusion time is sufficiently short, estimation with our method would be effective. In contrast, when the diffusion time is longer, we should solve thermal and chemical evolution of the core as a time-dependent problem in order to estimate formation of the stable layer, for example, as performed by Lister and Buffett (1998). For example, when the thickness of the stable layer is 100km, and thermal diffusivity is 10^{-5} m^2/s, the thermal diffusive time becomes 30Myr. This is presumably much less than the age of the inner core, since it was estimated as O(Gyr) by the previous studies without the effects of the stable layer and the stable layer would be so thin that it would not largely affect the age of the inner core. In contrast, when the thickness is 1000km, the thermal diffusive time becomes 3Gyr, which is probably larger than the age of the inner core if it is not affected by the presence of the stable layer. Note that in the case of destruction of a pre-existing stable layer due to thermal and compositional convection excited at the ICB, we should examine time scale for destruction (erosion rate), which would be determined not only by thermal diffusion but also by other physical properties, such as convective velocity, strength of stratification and rotation, and so on.

Our model assumes that thermal and/or compositional convection mixes entropy and composition uniformly because thermal and/or compositional Rayleigh numbers become so large that convective motion is turbulent due to the smallness of the molecular diffusivities of the outer core. However, there are possibilities that convection with coherent structures emerges. For example, large scale columnar convection affected by the Earth's rotation may coexist with small scale turbulent convective motion due to larger values of eddy diffusivities which may contribute to decrease the effective Rossby number for large scale fluid motions. The extent of penetration of columnar convection into the upper stable layer depends on the ratio between the Brunt-Väisälä frequency and the rotation frequency, and on the typical width scale of the convective columns in the linear theory (Takehiro and Lister, 2001). However, it is not known whether the penetration of columnar convection would be an effective mechanism to erode the stable layer. Furthermore, it has been proposed that the light elements released at the ICB may form chemical plumes and/or blobs rising through the outer core without mixing, which could create a chemically stratified layer at the top of the core (e.g., Braginsky, 1993; Shimizu and Loper, 1997). Recent numerical calculations by Manglik et al. (2010) show that chemical plumes can penetrate into the thermally stratified layer and keep rising to some extent. In order to clarify these possibilities, 3-dimensional numerical simulations are needed although it may be difficult to resolve fluid motions with wide spatial spectral ranges.

In the present paper, we illustrate formation of thermally stable layer below the CMB when the heat flow is drawn by mantle convection and its destruction by compositional convection excited at the ICB. The method presented here can also be applied to compositionally stable layer and its destruction by thermal convection. It has been proposed that a stable layer would be formed below the CMB by accumulation of light elements released at the ICB (e.g., Loper and Roberts, 1983) or by diffusion of light elements from the mantle (e.g., Buffett and Seagle, 2010, 2011). By introducing contribution terms of barodiffusion and injection of light elements from the CMB, we can model stable layer formation including the effects of mixing by convection in

a similar way with radial distribution of power by buoyancy forces.

In the layer diagnosed as thermally stable stratification, radial temperature gradient contributes to stabilize but that of concentration to destabilize. This configuration permits emergence of finger-type double diffusive convection. However, since finger-type convection mainly transports light elements (Turner, 1967) and increase stability through weakening radial concentration gradient, the stable layer would not be destroyed by this effect. In the case of a compositional stable layer, diffusive-type convection may emerge which mainly transports heat (Turner, 1965). Therefore, the stable layer would be maintained even when double diffusive convection occurs, although double diffusive convection may break up into a series of alternating convecting layers in some specific conditions.

Note that our method can apply not only to planetary cores but also to other general situations where convective and stable layers coexist. In general, the stable layer thickness, which is expected to be between the maximum and minimum estimates evaluated by $W_b(r) = 0$ and $w_b(r) = 0$, would be determined through complicated combined effects tied to the dynamics of chemical plumes and their possible interaction with the thermally stable layer, which are poorly understood. Nevertheless, in some extreme cases, the maximum or minimum estimates would give good stable layer thicknesses. For example, in planetary atmospheres where the effect of inertia is strong and advection of kinetic energy dominates local kinetic energy dissipation, the radially integrated kinetic energy production rate $W_b(r)$ presumably gives a good estimation of stable layer thickness. In contrast, in the Earth's outer core, it is expected that the inertia terms in the equation of fluid motion can be neglected since the value of compositional diffusivity is significantly smaller than that of kinetic viscosity and the work done by convection is converted into magnetic energy. This means that advection of kinetic energy can be ignored and penetration of compositional convection scarcely occurs. Therefore, we can estimate thickness of a stable layer with local kinetic energy production rate $w_b(r)$ only. For example, the red line in **Figure 5** shows that a stable layer with a thickness of 250 km is formed when $Q_{CMB} = 8$TW in the simple model presented in the previous section. We should verify our new criterion by performing numerical experiments of 2- or 3-dimensional hydrodynamic models, and check the expectation mentioned above. Effects of double diffusive convection possibly emerging in the stable layer should be examined as well. Moreover, by investigating parameter dependence of extent of penetration of convection, more precise estimation of stable layer formation will be possible.

AUTHOR CONTRIBUTIONS

ST did most of the theoretical formulation of this work. YS significantly contributed to 1D model development and figure generation.

FUNDING

This work was supported by JSPS (Japan Society for Promotion Science) KAKENHI Grant Numbers 16H01117 and 15H05834.

ACKNOWLEDGMENTS

We thank three reviewers and the editor for their valuable comments, which were very helpful for improving the manuscript. This work was supported by the Research Institute for Mathematical Sciences, a Joint Usage/Research Center located in Kyoto University.

REFERENCES

Braginsky, S. I. (1984). Short-period geomagnetic secular variation. *Geophys. Astrophys. Fluid Dyn.* 30, 1–78. doi: 10.1080/03091928408210077

Braginsky, S. I. (1993). Mac-oscillations of the hidden ocean of the core. *J. Geomag. Geoelectr.* 45, 1517–1538. doi: 10.5636/jgg.45.1517

Buffett, B. A. (2014). Geomagnetic fluctuations reveal stable stratification at the top of the earth's core. *Nature* 507, 484–487. doi: 10.1038/nature13122

Buffett, B. A., and Seagle, C. T. (2010). Stratification of the top of the core due to chemical interactions with the mantle. *J. Geophys. Res.* 115:B04407. doi: 10.1029/2009JB006751

Buffett, B. A., and Seagle, C. T. (2011). Correction to 'stratification of the top of the core due to chemical interactions with the mantle'. *J. Geophys. Res.* 116:B07405. doi: 10.1029/2011JB008376

Gomi, H., Ohta, K., Hirose, K., Labrosse, S., Caracas, R., Verstraete, M. J., et al. (2013). The high conductivity of iron and thermal evolution of the earth's core. *Phys. Earth Planet. Inter.* 224, 88–103. doi: 10.1016/j.pepi.2013.07.010

Gubbins, D., Masters, T. G., and Jacobs, A. (1979). Thermal evolution of the earth's core. *Geophys. J. Roy. astr. Soc.* 59, 57–99. doi: 10.1111/j.1365-246X.1979.tb02553.x

Labrosse, S. (2015). Thermal evolution of the core with a high thermal conductivity. *Phys. Earth Planet. Inter.* 247, 36–55. doi: 10.1016/j.pepi.2015.02.002

Labrosse, S., Poirier, J. P., and le Mouel, J. L. (1997). On cooling of the earth's core. *Phys. Earth Planet. Inter.* 99, 1–17. doi: 10.1016/S0031-9201(96)03207-4

Lay, T., Hernlund, J., and Buffett, B. A. (2008). Core-mantle boundary heat flow. *Nat. Geosci.* 1, 25–32. doi: 10.1038/ngeo.2007.44

Lister, J. R., and Buffett, B. A. (1995). The strength and efficiency of thermal and compositional convection in the geodynamo. *Phys. Earth Planet. Inter.* 91, 17–30. doi: 10.1016/0031-9201(95)03042-U

Lister, J. R., and Buffett, B. A. (1998). Stratification of the outer core at the core-mantle boundary. *Phys. Earth Planet. Inter.* 105, 5–19. doi: 10.1016/S0031-9201(97)00082-4

Loper, D. E. (1978). The gravitationally powered dynamo. *Geophys. J. Roy. Astr. Soc.* 54, 389–404. doi: 10.1111/j.1365-246X.1978.tb04265.x

Loper, D. E., and Roberts, P. H. (1983). "Compositional convection and the gravitationally powered dynamo," in *Stellar and Planetary Magnetism*, ed A. M. Soward (New York, NY: Gordon Bearch Science Publlication), 297–327.

Manglik, A., Wicht, J., and Christensen, U. R. (2010). A dynamo model with double diffusive convection for mercury's core. *Earth Planet. Sci. Lett.* 289, 619–628. doi: 10.1016/j.epsl.2009.12.007

Pozzo, M., Davies, C., Gubbins, D., and Alfe, D. (2014). Thermal and electrical conductivity of solid iron and iron-silicon mixtures at earth's core conditions. *Earth Planet. Sci. Lett.* 393, 159–164. doi: 10.1016/j.epsl.2014.02.047

Shimizu, H., and Loper, D. E. (1997). Time and length scales of buoyancy-driven flow structures in a rotating hydromagnetic fluid. *Phys. Earth Planet. Inter.* 104, 307–329. doi: 10.1016/S0031-9201(97)00035-6

Stacey, F. D., and Davis, P. M. (2008). *Physics of the Earth, 4th Edn*. New York, NY: Cambridge University Press.

Stevenson, D. J. (1983). Planetary magnetic fields. *Rep. Prog. Phys.* 46, 555–620. doi: 10.1088/0034-4885/46/5/001

Takehiro, S., and Lister, J. R. (2001). Penetration of columnar convection into an outer stably stratified layer in rapidly rotating spherical fluid shells. *Earth Planet. Sci. Lett.* 187, 357–366. doi: 10.1016/S0012-821X(01)00283-7

Turner, J. S. (1965). The coupled turbulent transports of salt and heat across a sharp density interface. *Int. J. Heat Mass Trans.* 8, 759–767. doi: 10.1016/0017-9310(65)90022-0

Turner, J. S. (1967). Salt fingers across a density interface. *Deep Sea Res.* 14, 599–611. doi: 10.1016/0011-7471(67)90066-6

Conflict of Interest Statement: The authors declare that the research was conducted in the absence of any commercial or financial relationships that could be construed as a potential conflict of interest.

frontiers in Earth Science

ORIGINAL RESEARCH
published: 30 October 2018
doi: 10.3389/feart.2018.00171

Enhanced Core-Mantle Coupling Due to Stratification at the Top of the Core

Sebastian Glane[1]* *and Bruce Buffett*[2]

[1] Institut für Mechanik, Kontinuumsmechanik und Materialtheorie, Technische Universität Berlin, Berlin, Germany,
[2] Department of Earth and Planetary Science, University of California, Berkeley, Berkeley, CA, United States

Fluctuations in the length of day (LOD) over periods of several decades are commonly attributed to exchanges of angular momentum between the mantle and the core. However, the forces that enable this exchange are less certain. Suggestions include the influence of pressure on boundary topography, electromagnetic forces associated with conducting material in the boundary region and gravitational forces due to mass anomalies in the mantle and the core. Each of these suggestions has strengths and weaknesses. Here we propose a new coupling mechanism that relies on the presence of stable stratification at the top of the core. Steady flow of the core over boundary topography promotes radial motion, but buoyancy forces due to stratification oppose this motion. Steep vertical gradients develop in the resulting fluid velocity, causing horizontal electromagnetic forces in the presence of a radial magnetic field. The associated pressure field exerts a net horizontal force on the boundary. We quantify this hybrid mechanism using a local Cartesian approximation of the core-mantle boundary and show that the resulting stresses are sufficient to account for the observed changes in LOD. A representative solution has 52 m of topography with a wavelength of 100 km. We specify the fluid stratification using a buoyancy frequency that is comparable to the rotation rate and adopt a radial magnetic field based on geodetic constraints. The average tangential stress is $0.027\,\mathrm{N\,m^{-2}}$ for a background flow of $\bar{V} = 0.5\,\mathrm{mm\,s^{-1}}$. Weak variations in the stress with velocity (i.e. $\bar{V}^{1/2}$) introduce nonlinearities into the angular momentum balance, which may generate diagnostic features in LOD observations.

Keywords: LOD variations, CMB interaction, core stratification, electro-mechanical coupling, angular momentum transfer, geomagnetic induction, rapid time variations, composition and structure of the core

OPEN ACCESS

Edited by:
Hagay Amit,
University of Nantes, France

Reviewed by:
Mathieu Dumberry,
University of Alberta, Canada
Ingo Wardinski,
UMR6112 Laboratoire de Planetologie et Geodynamique (LPG), France

***Correspondence:**
Sebastian Glane
glane@tu-berlin.de

Specialty section:
This article was submitted to Geomagnetism and Paleomagnetism, a section of the journal Frontiers in Earth Science

Received: *02 July 2018*
Accepted: *28 September 2018*
Published: *30 October 2018*

Citation:
Glane S and Buffett B (2018) Enhanced Core-Mantle Coupling Due to Stratification at the Top of the Core. Front. Earth Sci. 6:171. doi: 10.3389/feart.2018.00171

1. INTRODUCTION

Stable stratification at the top of Earth's core suppresses radial motion in the vicinity of the core-mantle boundary (CMB). Weak radial motion may still be present due to magnetic waves that propagate with periods of 100 years or less (Bloxham, 1990; Braginsky, 1993). Detection of these waves in secular variation of the geomagnetic field offers a unique probe of the core near the CMB (Buffett, 2014). Several geomagnetic field models (Jackson et al., 2000; Gillet et al., 2009; Wardinski and Lesur, 2012) support the existence of waves and yield broadly consistent estimates for the strength and thickness of stratification (Buffett et al., 2016), although other interpretations are possible (More and Dumberry, 2018). A nominal value for the layer thickness is 140 km.

Stratification also affects the morphology of the geomagnetic field. Geodynamo models predict an increase in the amplitude of the dipole field relative to the non-dipole components in the

presence of stratification (Sreenivasan and Gubbins, 2008; Olson et al., 2017). Stratification can also affect the equatorial symmetry of the geomagnetic field or the relative distribution of zonal and non-zonal field components (Christensen et al., 2010). Comparisons of model predictions with observations of the modern geomagnetic field suggest that stratification cannot exceed 400 km in thickness (Olson et al., 2017; Christensen, 2018).

A more stringent constraint on stratification comes from the time dependence of reversed flux patches at the CMB (i.e., local regions where the radial field is opposite to that expected for a dipole field). Growth of reversed flux patches has been attributed to the expulsion of magnetic field from the core by radial motion (Bloxham, 1986). The rate of growth is controlled by magnetic diffusion, and this process becomes prohibitively slow when radial motion is suppressed within 100 km of the CMB (Gubbins, 2007). While thicker layers are inferred from the detection of waves, these results are not strictly incompatible because both inferences are subject to large uncertainties. Moreover, the presence of waves can contribute to the rate of flux expulsion by allowing weak radial motion on timescales of 10^1 years to 10^2 years. The same radial motion may also contribute to other geomagnetic observations that favor limited radial motion near the CMB (Amit, 2014; Lesur et al., 2015).

Core-mantle coupling is also affected by stratification. Transfer of angular momentum across the CMB is commonly invoked to explain changes in LOD over periods of several decades (Gross, 2015). Possible mechanisms include topographic (Hide, 1969; Moffatt, 1977), electromagnetic (Bullard et al., 1950; Rochester, 1962) and gravitational (Jault et al., 1988; Buffett, 1996) torques. Topographic torques are ineffective when the flow around topography is geostrophic because the resulting fluid pressure is equal on the leading and trailing side of bumps (Jault and Finlay, 2015). As a result, the net horizontal force exerted on topography vanishes. Relaxing the condition of geostrophy, particularly by including the influences of a magnetic field, can restore the topographic torque (Anufriyev and Braginski, 1977), although plausible values for the magnetic field suggest that the resulting torques are small (Mound and Buffett, 2005).

Electromagnetic torques are a viable explanation for the LOD variations, as long as the conductance of the lower mantle exceeds 10^8 S (Holme, 1998). The origin of this conductive material on the mantle side of the boundary is not currently known. Suggestions include unusual mantle mineralogy (Ohta et al., 2010; Wicks et al., 2010), infiltration of core material (Buffett et al., 2000; Kanda and Stevenson, 2006; Otsuka and Karato, 2012) and partial melt (Lay et al., 1998; Miller et al., 2015).

Gravitational coupling between the mantle and fluid core is probably too weak to account for the LOD variations because density variations in the fluid core are expected to be very small (Stevenson, 1987). However, gravitational coupling between the mantle and the inner core can be effective (Buffett, 1996). One restriction on this particular form of gravitational coupling is that fluid motions must first transfer momentum to the inner core by electromagnetic coupling. This momentum is then transferred to the mantle by gravitational coupling to the inner core. Because fluid motion in the core tends to be nearly invariant in the direction of the rotation axis (Jault, 2008), there are large regions of the fluid core that do not directly couple to the inner core. Evidence for changes in length of day associated with torsional waves (Gillet et al., 2010) favor a more general process because waves that do not directly contact the inner core appear to transfer momentum to the mantle.

Stratification can alter core-mantle coupling by enabling a hybrid mechanism for momentum transport. Flow over topography at the CMB would normally require radial motion, but this motion is suppressed by stratification. Instead, the topography redirects or traps fluid in the vicinity of the boundary. Deeper horizontal flow in the core is unimpeded by the topography, allowing differential motion between the deeper and shallower fluid. A steep vertical gradient in the flow generates electromagnetic stresses in the presence of a radial magnetic field. These stresses alter the pressure field to produce a net horizontal force on the topography.

Such a mechanism is broadly similar to momentum transfer between the atmosphere and the solid Earth by gravity waves (Gill, 1982). However, there are several significant differences in the core. For example, fluid inertia in the core is probably too weak to generate internal gravity waves. Eliminating waves in the atmosphere would suppress any net stress on the boundary because otherwise there would be no mechanism for removing excess momentum due to a persistent boundary stress. In Earth's core the presence of a magnetic field allows low-frequency magnetic waves to transport excess momentum from the boundary region. The combination of waves and strong damping due to ohmic dissipation shift the phase of the pressure perturbation so that pressure on the leading and trailing sides of topography is different. A net horizontal force is produced on both the mantle and core. The goal of this study is to quantitatively assess the horizontal force due to a steady background flow and show that this force is capable of producing the observed changes in LOD.

A similar mechanism has previously been proposed to account for observations of coupling between the mantle and tidally driven flow in the core (Buffett, 2010). This previous application was restricted to tidal flow, where fluid inertia was expected to be important. Here the influence of fluid inertia is much smaller. A nominal flow of $0.5\,\mathrm{mm\,s^{-1}}$ over topography with wavelengths of 100 km to 1,000 km produces fluctuations with periods of roughly 10^1 years to 10^2 years. At such long periods the horizontal force balance is expected to involve a combination of buoyancy, Coriolis and magnetic forces (Jones, 2011), although we retain the effects of inertia for a more complete description of fluid motion. We begin our discussion in section 2 with the basic model setup. A simple quasi-analytical solution to the relevant governing equations shows how pressure is distributed over the topography. An estimate for the average tangential stress on the boundary is given in section 3 and we use this result to assess the consequences for changes in LOD. Broader implications are considered in section 4 before we conclude in section 5.

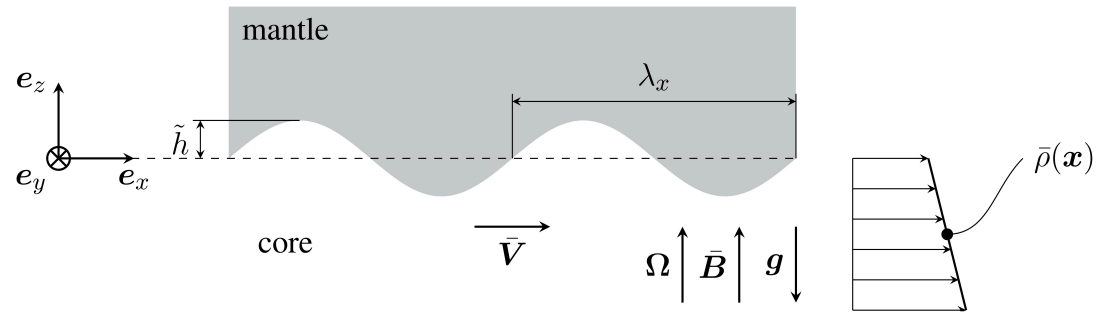

FIGURE 1 | Schematic illustration of the core-mantle boundary region. Flow $\bar{\boldsymbol{V}}$ of the core past the mantle is disturbed by topography $h(x, y)$ on the core-mantle boundary. A stable density profile $\rho(z)$ is assumed at the top of the core and a uniform vertical magnetic field $\bar{\boldsymbol{B}}$ is imposed. Fluid motion perturbs the density profile and alters the magnetic field to produce a pressure field that exerts a net horizontal force on the mantle.

2. MODEL SETUP AND RESULTS

We consider the problem of steady flow in the core past a solid mantle with undulations on the interface. We approximate the mean position of the CMB by a plane horizontal surface $z = 0$, which omits curvature terms in the governing equation. The relative errors are of order λ_x/R where λ_x is the wavelength associated to the undulations and R is the radius of the outer core. The topography is defined as positive when the boundary has a positive radial displacement from the mean position (see **Figure 1**). We allow the topography $h(x, y)$ to be two dimensional in the horizontal plane and consider a single sinusoidal component

$$h(x, y) = \tilde{h} \exp\left(\mathrm{i}k_x x + \mathrm{i}k_y y\right), \tag{1}$$

where $\tilde{h}$ is the amplitude, and k_x and k_y are the wavenumbers in the direction of the basis vectors $\boldsymbol{e}_x$ and $\boldsymbol{e}_y$. A more general description of topography can be constructed from a linear superposition of sinusoidal components (Here we follow the convention of interpreting physical quantities as the real parts of complex expressions). The surface of the CMB is described by

$$f(x, y, z) = z - h(x, y) = 0 \tag{2}$$

so the outward unit normal $\boldsymbol{n}$ to the fluid region is given by

$$\boldsymbol{n} \equiv \frac{\nabla f}{|\nabla f|} = \frac{\boldsymbol{e}_z - \mathrm{i}\boldsymbol{k}_\mathrm{T} h(x, y)}{\sqrt{1 + k_\mathrm{T}^2\,\mathrm{Re}(\mathrm{i}h)^2}} \tag{3}$$

where $\boldsymbol{k}_\mathrm{T} = k_x\boldsymbol{e}_x + k_y\boldsymbol{e}_y$, $k_\mathrm{T} = |\boldsymbol{k}_\mathrm{T}|$ and $\mathrm{Re}\,(\bullet)$ denotes the real part. When the topography is small ($k_x\tilde{h}$ and $k_y\tilde{h} \ll 1$) we can set $|\nabla f| \approx 1$ in the definition of $\boldsymbol{n}$.

A uniform background flow $\bar{\boldsymbol{V}} = \bar{V}\boldsymbol{e}_x$ is maintained in a frame that rotates with the mantle at constant angular velocity $\boldsymbol{\Omega} = \Omega\boldsymbol{e}_z$. The gravitational acceleration is $\boldsymbol{g} = -g\boldsymbol{e}_z$ and we adopt a vertical background magnetic field $\bar{\boldsymbol{B}} = \bar{B}\boldsymbol{e}_z$ because it has the largest influence on the dynamics once the flow is perturbed by boundary topography. We assume that the fluid is inviscid and the mantle is an electrical insulator, so the background magnetic field is not disturbed by $\bar{\boldsymbol{V}}$ in the absence of topography. Thus the uniform (geostrophic) background flow is sustained by a horizontal pressure gradient $\nabla\bar{P}(y)$.

Stable stratification is imposed in the core by letting the density field vary linearly with depth

$$\bar{\rho}(z) = \rho_0(1 + \alpha z), \qquad \text{where} \qquad \alpha = \frac{1}{\rho_0}\frac{\partial\bar{\rho}}{\partial z} < 0 \tag{4}$$

is required to ensure stable stratification in the region $z < 0$. We subsequently relate α to the buoyancy frequency N using $\alpha = -N^2/g$. Both α and N are treated as constants.

2.1. Linearized Governing Equations

Flow past topography alters the background flow and disturbs the magnetic field, pressure and density. We denote these perturbations using $\boldsymbol{v}$ for the velocity, $\boldsymbol{b}$ for the magnetic field, p for the pressure and ρ' for the density. All of these fields are assumed to be small when the topography is small, so we can linearize the equations for the perturbations by neglecting products of small quantities. We expect these perturbations to become time invariant in the frame of the mantle after the passage of initial transients. Further simplifications are permitted by the low viscosity of the core liquid. Neglecting the viscous term in the linearized momentum equation yields

$$\rho_0\bar{\boldsymbol{V}}\cdot\nabla\boldsymbol{v} + \rho_0\boldsymbol{\Omega}\times\boldsymbol{v} = -\nabla p + \rho'\boldsymbol{g} + \frac{1}{\mu}\bar{\boldsymbol{B}}\cdot\nabla\boldsymbol{b}, \tag{5}$$

where μ is the magnetic permeability. This particular form of the momentum equation accounts for the absence of a background electric current density, $\bar{\boldsymbol{J}} = (\nabla\times\bar{\boldsymbol{B}})/\mu = 0$. The induction equation for a steady magnetic perturbation is

$$\bar{\boldsymbol{B}}\cdot\nabla\boldsymbol{v} - \bar{\boldsymbol{V}}\cdot\nabla\boldsymbol{b} + \eta\nabla^2\boldsymbol{b} = \boldsymbol{0}, \tag{6}$$

where $\eta = 1/(\mu\sigma)$ is the magnetic diffusivity and σ is the electrical conductivity. Finally, conservation of mass requires

$$\bar{\boldsymbol{V}}\cdot\nabla\rho' + \boldsymbol{v}\cdot\nabla\bar{\rho} = 0. \tag{7}$$

These three equations are supplemented by $\nabla\cdot\boldsymbol{b} = 0$, together with $\nabla\cdot\boldsymbol{v} = 0$ in the Boussinesq approximation.

Solutions for the perturbations are sought in the form

$$\rho' = \tilde{\rho}' \exp(\mathrm{i}\boldsymbol{k}\cdot\boldsymbol{x}), \quad \boldsymbol{v} = \tilde{\boldsymbol{v}} \exp(\mathrm{i}\boldsymbol{k}\cdot\boldsymbol{x}),$$
$$p = \tilde{p} \exp(\mathrm{i}\boldsymbol{k}\cdot\boldsymbol{x}), \quad \boldsymbol{b} = \tilde{\boldsymbol{b}} \exp(\mathrm{i}\boldsymbol{k}\cdot\boldsymbol{x}), \tag{8}$$

where $\boldsymbol{k} = k_x\boldsymbol{e}_x + k_y\boldsymbol{e}_y + k_z\boldsymbol{e}_z$ is the wavenumber vector, $\boldsymbol{x} = x\boldsymbol{e}_x + y\boldsymbol{e}_y + z\boldsymbol{e}_z$ is the position vector and $\tilde{\rho}'$, $\tilde{\boldsymbol{v}}$, etc. are the amplitude of the perturbations.

2.2. Boundary Conditions

Four boundary conditions are imposed at the CMB, in addition to the requirement that the perturbations vanish as $z \to -\infty$. An inviscid fluid requires a single boundary condition on the normal component of the total velocity

$$(\bar{\boldsymbol{V}} + \boldsymbol{v}) \cdot \boldsymbol{n} = 0\,. \tag{9}$$

This condition is evaluated on the interface $z = h(x, y)$, but it is customary to transfer the boundary condition to $z = 0$ by expanding $\bar{\boldsymbol{V}}$ and $\boldsymbol{v}$ in Taylor series about the reference surface.

Three additional conditions are required to ensure that the magnetic perturbation in the core is continuous with the magnetic perturbation in the mantle, which can be represented as the gradient of a potential. A simpler treatment of the boundary condition on the magnetic field uses the so-called pseudo-vacuum condition (Jackson et al., 2014). In this case we have $b_x = b_y = 0$ at $z = 0$ to first-order in the perturbation. This approximation reduces the number of boundary conditions on the magnetic field from three to two, and eliminates the magnetic potential as an unknown in the problem. Even though both choices of magnetic boundary conditions yield quantitatively similar solutions (the relative difference in pressure is only 10^{-4}) we adopt the potential-field condition

$$\boldsymbol{b}(x, y, 0) = \boldsymbol{b}_{\mathrm{M}}(x, y, 0) \quad \text{with} \quad \boldsymbol{b}_{\mathrm{M}} = -\nabla\psi_{\mathrm{M}}(\boldsymbol{x})\,. \tag{10}$$

for all solutions in this study. Here, $\boldsymbol{b}_{\mathrm{M}}$ denotes the magnetic perturbation in the mantle and ψ_{M} is the associated scalar potential.

2.3. Solution for the Perturbation

In the Appendix, we show that Equations (5–7) can be reduced to a system of three linear equations for the amplitude of the magnetic perturbation $\tilde{\boldsymbol{b}}$. Three independent solutions are found for $\tilde{\boldsymbol{b}}$, each corresponding to a distinct value for the vertical wavenumber k_z. A linear combination of these three solutions are required to satisfy the boundary conditions at $z = 0$. For the case of a potential field in the mantle, we use four boundary conditions to determine the unknown amplitudes of the three solutions, as well as the amplitude of the magnetic potential. Once solutions are obtained for $k_z^{(i)}$ and $\tilde{\boldsymbol{b}}^{(i)}$ $(i = 1, 2, 3)$, we use the linear combination of $\tilde{\boldsymbol{v}}^{(i)}$ and $\tilde{p}^{(i)}$ to reconstruct the velocity and pressure perturbations everywhere in the fluid.

We adopt nominal values of the relevant parameters to illustrate the solution. We take the values specified in **Table 1** to define the basic state of the core. A topography with a wavelength of 100 km in the $\boldsymbol{e}_x$-direction yields the wave number stated in **Table 1**. The error due to omitted curvature terms is $\lambda_x/R \approx 0.03$, which is small enough to neglect. The radial motion over this topography has a frequency $\omega = k_x\bar{V} = 3.1 \times 10^{-8}\,\mathrm{s}^{-1}$ for the background velocity chosen in **Table 1**, which corresponds to a timescale, $2\pi/\omega$, of roughly 6 years. We explore a range of values for the fluid stratification, starting with the case of strong stratification. Chemical stratification due to barodiffusion of light elements can produce a buoyancy frequency of $N = 20\,\Omega$ to $30\,\Omega$ when the top of the core is not convectively mixed (Gubbins and Davies, 2013). Adopting $N = 20\,\Omega$ gives the following solution for the vertical wavenumbers:

TABLE 1 | Nominal values for the parameters of the model.

Quantity	Value
ρ_0	$10^4\,\mathrm{kg\,m^{-3}}$
$\bar{B}$	0.65 mT
Ω	$0.729 \times 10^{-4}\,\mathrm{s^{-1}}$
η	$0.8\,\mathrm{m^2\,s^{-1}}$
$\bar{V}$	$0.5\,\mathrm{mm\,s^{-1}}$
k_X, k_T	$6.3 \times 10^{-5}\,\mathrm{m^{-1}}$

$$k_z^{(1)} = -1.56 \times 10^{-2}(1+\mathrm{i})\ \mathrm{m}^{-1}, \quad k_z^{(2)} = 1.40 \times 10^{-4}(1\text{-i})\ \mathrm{m}^{-1},$$
$$k_z^{(3)} = 5.42 \times 10^{-6}\mathrm{m}^{-1}. \tag{11}$$

The first wave can be interpreted as a boundary-layer solution due to the short length scale in the vertical direction. The vertical length scale for this particular solution is dependent on the strength of stratification. We find that $k_z^{(1)}$ increases linearly with N, so the strongest stratification produces the thinnest boundary layer. The second wave has a larger vertical length scale, comparable to the wavelength of topography. The third wave has a much larger vertical length scale with a very small imaginary part due to the weak influence of magnetic diffusion at these larger scales. The first and third waves contribute most to the pressure field for our nominal values; the first wave sets the pressure at the boundary, and the third wave controls the broader background perturbation well below the boundary.

Figure 2 shows a vertical x-z cross-section for the pressure field using the nominal parameter values and a topography of $\tilde{h} = 30$ m. The pressure immediately adjacent to the boundary is asymmetric with respect to the topography. High pressure occurs mostly over the leading edge of the bump on the boundary, while low pressure prevails over the trailing edge. Both of these pressure perturbations exert a horizontal (tangential) stress on the boundary. A quantitative estimate for the average tangential stress is obtained by integrating the local traction over the surface of the CMB. Before turning to this question we assess the importance of stratification for producing an observable tangential stress. When the stratification is substantially reduced (say $N = 0.1\,\Omega$) the thickness of the boundary-layer solution (first wave) increases and the resulting contribution to the pressure at the CMB is small. The second and third wave

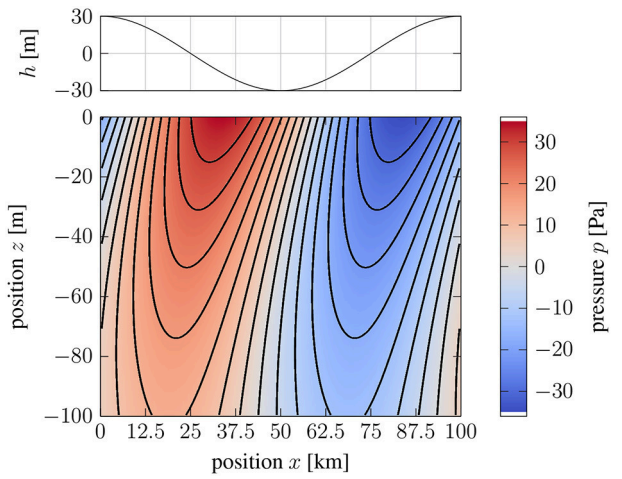

FIGURE 2 | Vertical cross-section of pressure perturbation relative to the boundary topography. A positive pressure perturbation develops over the leading edge of topography and a negative pressure perturbation occurs over the trailing edge. The disturbance in the flow is confined to the top kilometer of the core for the nominal choice of model parameters (see text).

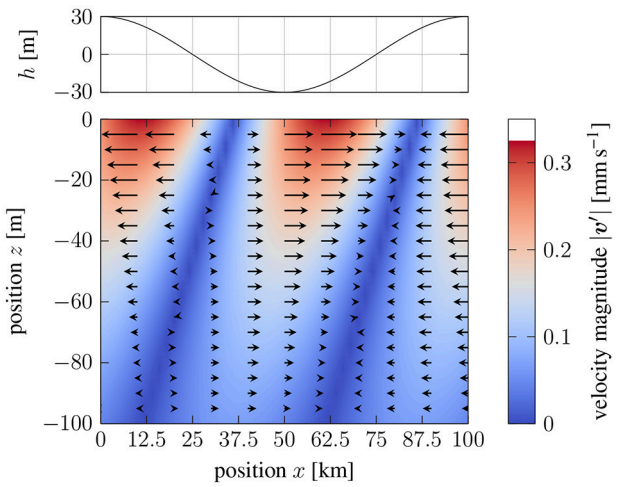

FIGURE 3 | Vertical cross-section of horizontal velocity relative to the boundary topography. Arrows show the direction of flow and background color denotes the magnitude of the flow. Negative velocity perturbations under regions of positive topography implies that the total flow is decreasing.

now contribute most to pressure perturbation. However, the distribution of pressure is symmetric relative to the topography, so the average tangential stress is vanishingly small.

The velocity perturbation on a x-z cross-section is shown in **Figure 3**. Flow over the topography causes a vertical component of flow, but the magnitude of this flow is quite small relative to the horizontal flow. The peak vertical velocity is only 0.001 mm s^{-1} because the slope of the topography is very small (e.g., $k_x\tilde{h} \ll 1$). The largest horizontal flow occurs immediately below the CMB and it decays rapidly with depth. The peak horizontal velocity is 0.3 mm s^{-1}, which is less than the background flow of 0.5 mm s^{-1}, although not substantially less. A large velocity perturbation means that the linearized equations are less accurate. We revisit this question qualitatively in the discussion, but a more quantitative assessment must retain the nonlinear terms in the governing equations. We could reduce the velocity perturbation by reducing the topography. While this change would improve the validity of the linearized equations, it would also reduce the traction on the boundary. We show in the next section that the choice of $\tilde{h} = 30$ m is sufficient to produce a torque on the mantle of roughly 10^{19} N m. Such a torque is probably more than enough to account for the LOD variations, although it does suggest that the flow is becoming nonlinear as we approach the conditions required to explain the observations.

Information about the nature of the nonlinearity can be gleaned from **Figure 3**. For example, the velocity perturbation on the leading side of the topography ($x \approx 0$ km to 20 km) is directed in the negative $\boldsymbol{e}_x$ direction. This means that the total velocity, $\bar{\boldsymbol{V}} + \boldsymbol{v}$, in this region is decreasing. In effect, the fluid is becoming stagnant below regions of positive topography. This stagnant fluid prevents flow from following the boundary, reducing the forcing of vertical motion and lowering the amplitude of the perturbation. We might view the growth of stagnant regions as a reduction in the effective topography. We speculate that increasing stratification or increasing topography would cause the flow to become increasingly stagnant below positive topography. Deeper flow would be unimpeded by the topography, so magnetic stresses on the shallower stagnant fluid would transfer momentum to the mantle by the effects of pressure on the boundary. Such a coupling mechanism is qualitatively similar to electromagnetic coupling, where the thickness of the conducting layer is set by the amplitude of the topography. A topography of $\tilde{h} = 100$ m would approximate a conducting layer with a conductance of $G = h\sigma = 10^8$ S, when the electrical conductivity is $\sigma = 10^6$ S m^{-1}. This is the conductance required to account for LOD variations (Holme, 1998). Thus, we expect nonlinearities to reduce the effectiveness of the coupling mechanism. However, we can compensated by increasing the amplitude of the topography above the nominal value of $\tilde{h} = 30$ m.

3. AVERAGE TANGENTIAL STRESS ON THE BOUNDARY

The local traction on the mantle is

$$\boldsymbol{t} = p(x, y, 0)\boldsymbol{n}\,, \tag{12}$$

where $\boldsymbol{n}$ was previously defined in Equation (3) as the outward normal to the core. In general we can expect $\boldsymbol{t}$ to have both $\boldsymbol{e}_x$ and $\boldsymbol{e}_y$ components when the wavenumbers k_x and k_y are non-zero. Setting $k_y = 0$ produces topographic ridges that are perpendicular to the background flow, so the horizontal traction is entirely in the $\boldsymbol{e}_x$ direction. A local traction in the $\boldsymbol{e}_x$ direction also occurs for a linear superposition of topography with wavenumbers $\boldsymbol{k}_\mathrm{T} = k_x\boldsymbol{e}_x \pm k_y\boldsymbol{e}_y$. This particular choice

of topography produces a checkerboard pattern of relief on the boundary, but it gives no net traction perpendicular to the direction of background flow. For the purpose of illustration, we consider the simple case where $k_x = k_T$ and $k_y = 0$, so we confine our attention to tractions in the direction of flow.

Transfer of angular momentum to the mantle depends on the average of t_x over x. We compute the average traction from the real part of t_x in Equation (12), noting that $\mathrm{Re}(p) = (p + p^*)/2$, where $(\bullet)^*$ denotes the complex conjugate. Similarly, we let $\mathrm{Re}(\boldsymbol{n}) = (\boldsymbol{n} + \boldsymbol{n}^*)/2$. Only constant terms in the product $p\boldsymbol{n}$ contribute to the average stress, so we obtain:

$$\langle t_x \rangle = \frac{1}{4}(p n_x^* + p^* n_x)\,. \tag{13}$$

For our representative parameters values we obtain an average stress of $0.027\,\mathrm{N\,m^{-2}}$, which is comparable to the estimate required to account for fluctuations in LOD at periods of several decades (Hide, 1969). A rough estimate for the axial torque due to zonal flow with constant $\bar{V}$ is $\pi^2 R^3 \langle t_x \rangle$, where $R = 3{,}480$ km is the radius of the core (details are given below). Thus the nominal value for the average stress predicts an axial torque of about $1.1 \times 10^{19}\,\mathrm{N\,m}$.

Many of the parameters in $\langle t_x \rangle$ are uncertain, so it is useful to consider a range of possible parameter values. **Figure 4** shows how $\langle t_x \rangle$ changes when a selected parameter is varied. In each case the other parameters are fixed at their nominal values. We consider variations in $\tilde{h}$, N, $\bar{V}$, Ω, and λ_x. The strongest dependence is due to topography $\tilde{h}$. Because p and n_x depend linearly on $\tilde{h}$, the product for the average stress varies as $\tilde{h}^2$. Increasing the topography to 100 m produces a tangential stress of $0.3\,\mathrm{N\,m^{-2}}$, which is much larger than the value required to account for LOD fluctuations. Independent estimates of boundary topography can exceed several kilometers (Colombi et al., 2014; Shen et al., 2016), although the corresponding wavelengths are comparable to the radius of the core. Increasing the wavelength from 100 km to 1,000 km decreases the magnitude of the stress to $0.02\,\mathrm{N\,m^{-2}}$ for $\tilde{h} = 30$ m. Restoring the stress to our nominal value of $0.027\,\mathrm{N\,m^{-2}}$ requires a modest increase in the topography to $\tilde{h} = 42$ m. Wavelengths larger than 1,000 km would likely require an explicit treatment of spherical geometry (Anufriyev and Braginski, 1977).

Stratification is essential for producing a tangential traction. We find that $\langle t_x \rangle$ varies linearly with N over a large range of stratifications (see **Figure 4B**). A resonance is evident at low N (see the inset in **Figure 4B**), possibly due to a correspondence between the frequency of the boundary forcing and the natural frequency of internal gravity waves. Further reductions in stratification causes the average stress drop to zero. A wide range of values for N can sustain a viable coupling mechanism. Decreasing stratification to $N = \Omega$ lowers the stress to roughly $\langle t_x \rangle = 0.01\,\mathrm{N\,m}$, although we can restore the stress to $0.027\,\mathrm{N\,m^{-1}}$ with a modest increase in the topography to $\tilde{h} = 52$ m (The peak amplitude of the perturbed flow is still $0.3\,\mathrm{mm\,s^{-1}}$). Thus an intermediate stratification of $N \approx \Omega$, as reported in previous studies of geomagnetic secular variation (Buffett et al., 2016), is compatible with the coupling mechanism proposed here.

A broad (140 km) layer of stratification would allow barodiffusion to drive a flux of light elements toward the CMB. As light elements accumulate at the top of the core we can expect a 1 km layer of chemical stratification to develop within a few million years, given typical estimates for the diffusivity of light elements (Pozzo et al., 2012). A buoyancy frequency of $N = 20\,\Omega$ or more is feasible due to chemical stratification, which would put the core at the high end of stratifications considered in **Figure 4**. While it is not entirely clear how a thin layer of stratification would affect the average stress, we note that the perturbed flow due to the first wave would be largely contained within the chemical stratification. Recall that the first wave was principally responsible for the average boundary stress, so it is at least possible for a thin layer of stratification to be relevant for core-mantle coupling.

The amplitude of the background flow also affects the average tangential stress. **Figure 4C** shows that $\langle t_x \rangle$ varies at $\bar{V}^{1/2}$. This implies a relatively weak dependence on the background velocity. If the amplitude of the velocity variations associated to LOD fluctuations is roughly an order of magnitude smaller than $0.5\,\mathrm{mm\,s^{-1}}$, this would lower the fluctuating stress by a factor of 3. The strong dependence on $\tilde{h}$ means that only a modest increase in topography would be required to restore our nominal estimate for the stress. A nonlinear dependence of the stress on $\bar{V}$ also has interesting consequences for the nature of the coupling mechanism, which may produce detectable signatures in the frequency spectra of LOD variations. We explore this behavior in the next section.

One other feature of the solution for $\langle t_x \rangle$ should be noted. We have assumed that the rotation vector $\boldsymbol{\Omega}$ is perpendicular to the surface. This is strictly true in polar regions. Elsewhere we might interpret $\boldsymbol{\Omega}$ as the radial component of the planetary rotation rate. This is a common assumption when the flow is confined to a thin layer (Pedlosky, 1987, p. 715). Our boundary-layer solution (first wave) is confined to a thin layer, so it might be reasonable to replace the value of planetary rotation with the radial component at mid-latitudes, which would imply a 30 % reduction in the value of $\boldsymbol{\Omega}$. A direct calculation of $\langle t_x \rangle$ with the lower rotation rate is shown in **Figure 4D**. The average stress is found to vary quadratically with $\boldsymbol{\Omega}$, although the stress does not go to zero when the rotation rate vanishes. We use this result below to estimate the torque due to the boundary stress. To simplify the calculation of the torque we adopt a linear approximation for the average stress. It gives good agreement at mid to high latitudes (e.g., $0.7\,\Omega$ to Ω), but underestimates the stress at the equator, where the usual assumption about retaining only the radial component of the rotation vector break down. It is likely that this approximation underestimates the torque on the mantle.

3.1. Torque Due to Boundary Stress

The axial torque on the mantle is evaluated using local estimates for $\langle t_x \rangle$ over the surface of the CMB. A detailed assessment should account for changes in the radial component of planetary rotation by letting $\Omega = \Omega_M \cos(\theta)$, where Ω_M is the angular velocity of the mantle and θ is the colatitude. We also require

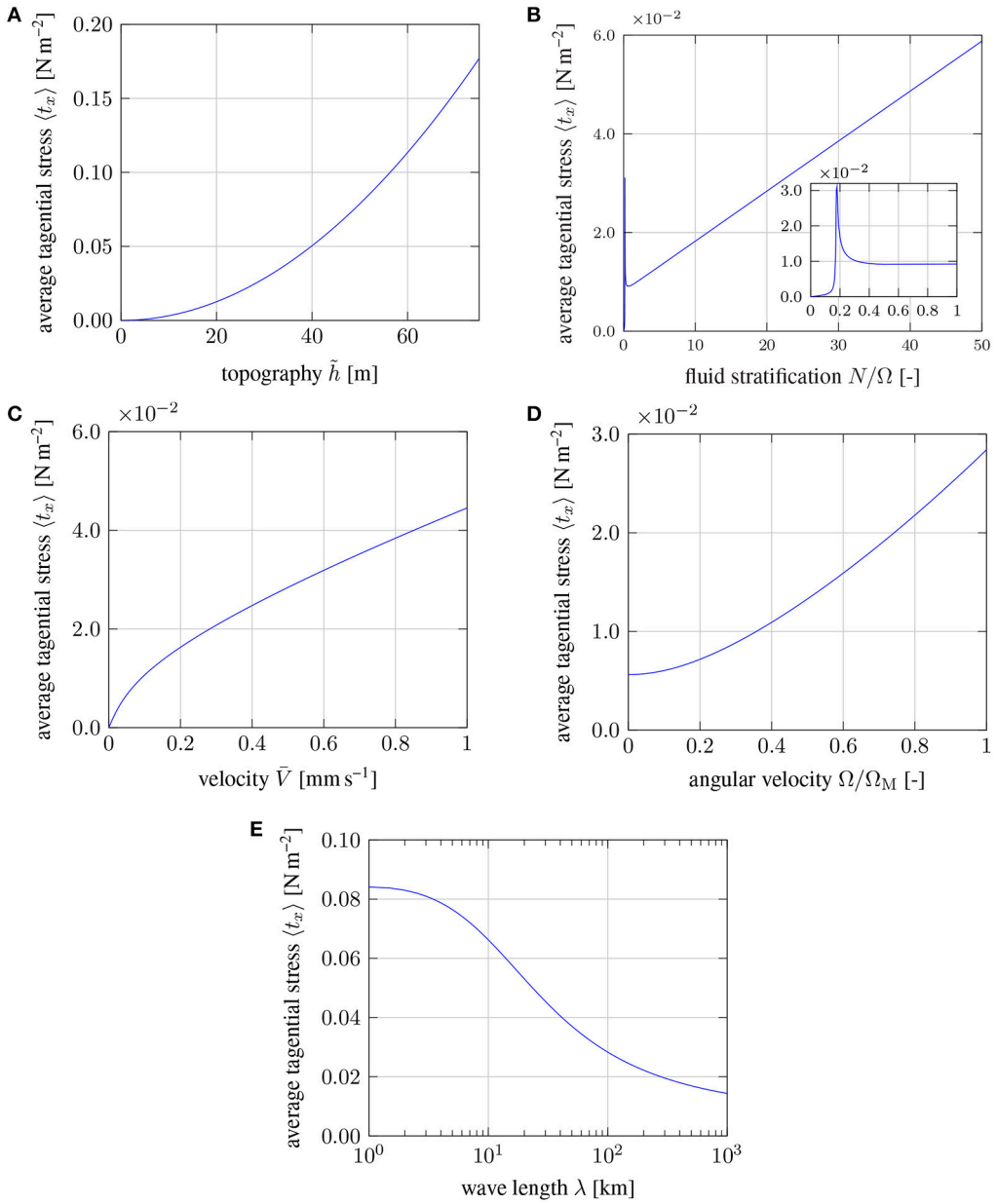

FIGURE 4 | Dependence of the tangential stress $\langle t_x \rangle$ on **(A)** the amplitude of topography $\tilde{h}$, **(B)** the strength of stratification N/Ω, **(C)** on the velocity $\bar{V}$, **(D)** on the angular velocity $\boldsymbol{\Omega}$, and **(E)** the wavelength of topography $\lambda = 2\pi/k$.

knowledge of the zonal (eastward) flow of the core $\bar{\boldsymbol{V}} = \bar{V}\boldsymbol{e}_\varphi$ relative to the mantle. Here $\boldsymbol{e}_\varphi$ denotes the unit vector in the azimuthal direction. As a first approximation, we might define the relative motion of the core in terms of an average angular velocity of the core Ω_C. Thus the relative motion can be expressed in the form

$$\bar{V} = R(\Omega_C - \Omega_M)\sin(\theta)\,. \tag{14}$$

Variations in $\bar{V}$ cause changes in $\langle t_x \rangle$, so we might define the average tangential stress (now defined in the $\boldsymbol{e}_\varphi$ direction) in the form

$$\langle t_\varphi \rangle = t_{\varphi,0}\cos(\theta)\sqrt{\frac{R(\Omega_C - \Omega_M)\sin(\theta)}{\bar{V}_0}} \tag{15}$$

where $t_{\varphi,0}$ represents the nominal value for the average stress due to the nominal background velocity $\bar{V}_0$. If we set $\bar{V} = \bar{V}_0$ at a particular co-latitude, θ, then the average stress at this location deviates from our nominal value, $t_{\varphi,0}$, only due to the change in the radial component of $\boldsymbol{\Omega}_M$. However, if $\bar{V}$ also deviates from $\bar{V}_0$ then we want to account for the $\bar{V}^{1/2}$ dependence of the stress.

For the purpose of illustration we let $\bar{V}_0 = R(\Omega_C - \Omega_M)$, so the nominal background velocity occurs at the equator. Elsewhere the background velocity from Equation (14) is lower than $\bar{V}_0$. The resulting axial component of the torque on the mantle is given by

$$\Gamma_z = \int_S \boldsymbol{e}_z \cdot (\boldsymbol{r} \times \langle t_\varphi \rangle \boldsymbol{e}_\varphi)\, \mathrm{d}S = t_{\varphi,0} \int_S R\cos(\theta)\sin^{\frac{3}{2}}(\theta)\, \mathrm{d}S = \frac{8\pi}{7} R^3 t_{\varphi,0} \tag{16}$$

where $\boldsymbol{r}$ is the position vector relative to the center of the planet and S defines the surface of the CMB. The stress is symmetric about the equator, even though the direction of the Coriolis force changes sign in the Southern Hemisphere. Consequently, we restrict the surface integral to the North Hemisphere and exploit the symmetry to evaluate Γ_z. The net torque is about a factor of 3 lower than our earlier approximation because the background flow and rotation rate are lower over most of the CMB.

3.2. Dynamics of the Core-Mantle System

The weak (square-root) dependence of the average stress on the background velocity has several consequences for the transfer of angular momentum. Consider the case where $\Omega_C > \Omega_M$. According to Equation (16) the torque on the mantle is positive, while the torque on the core is negative. The negative torque on the core causes a decrease in Ω_C, which reduces the differential rotation. The angular velocity of the mantle is also altered, but this change is smaller due to the larger moment of inertia. For the hypothetical case of a torque that depends linearly on the differential rotation, the relaxation back to solid-body rotation occurs exponentially with time. By comparison, a square-root dependence of the torque on $\Omega_C - \Omega_M$ means that the torque is smaller at large differential rotations; the initial adjustment occurs more slowly than the linear torque. However, at sufficiently small differential rotation the torque in Equation (16) must exceed the torque with a linear dependence on $\Omega_C - \Omega_M$. The larger torque drives the differential rotation to zero in finite time (unlike exponential decay).

Signatures of the coupling mechanism are potentially detectable in the dynamics of the core-mantle system. To explore this question we consider a toy problem in which the mantle is forced by an atmospheric torque $\Gamma_A(t)$ with a period of one cycle per year (cpy). The actual problem is more complicated (Gross et al., 2004), but the goal here is to assess the influence of different functional forms for the torque at the CMB. When there are no other torques on the core, we can write the coupled system of angular momentum equations in the form

$$C_M \frac{\mathrm{d}\Omega_M}{\mathrm{d}t} = \gamma\, \mathrm{sgn}(\Omega_C - \Omega_M)\sqrt{|\Omega_C - \Omega_M|} + \Gamma_A(t)\,, \tag{17}$$

$$C_C \frac{\mathrm{d}\Omega_C}{\mathrm{d}t} = -\gamma\, \mathrm{sgn}(\Omega_C - \Omega_M)\sqrt{|\Omega_C - \Omega_M|}\,, \tag{18}$$

where C_M and C_C are the polar moments of inertia of the mantle and core, γ characterizes the amplitude of core-mantle coupling and sgn(•) defines the sign of the torque according to the sign of the argument; the square-root dependence is applied to the absolute value of $\Omega_C - \Omega_M$. The moment of inertia of the mantle is about a factor of 10 larger than the moment of inertia of the core. Similarly, the atmospheric torque might be roughly 50 times larger than the torque at the CMB. We approximate these conditions by defining $\Gamma_A(t)$ with unit amplitude and take $C_M = 1\,\mathrm{kg\,m^2}$, $C_C = 0.1\,\mathrm{kg\,m^2}$, and $\gamma = 0.02\,\mathrm{N\,m\,s^{1/2}}$. We also consider a case in which core-mantle coupling is turned off ($\gamma = 0$). These results are compared with a third solution in which the torque at the CMB depends linearly on $\Omega_C - \Omega_M$. Each of these systems are integrated numerically in time using a solid-body rotation as the initial condition, i.e., $\Omega_M(0) = \Omega_C(0) = \Omega_0$, where Ω_0 is the initial rate of rotation.

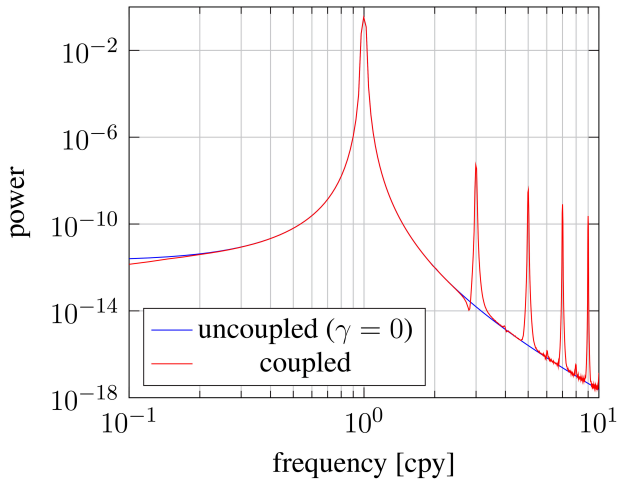

FIGURE 5 | Power spectra for the angular velocity of the mantle $\Omega_M(t)$ in response to an imposed annual torque from the atmosphere. A reference model with no coupling to the core ($\gamma = 0$) is compared to a nonlinear model, based on the horizontal boundary stress $\langle t_\varphi \rangle$. The two results are nearly identical at the forcing frequency of 1 cycle per year, whereas the nonlinear model exhibits overtones due to the nonlinearity of the coupling mechanism. Low-amplitude fluctuations near the base of the spectra are a result of discretization errors in the numerical integration of $\Omega_M(t)$.

Figure 5 shows the power spectrum computed from the numerical solution for $\Omega_M(t)$. The solution with no coupling at the core-mantle boundary produces a single spectral peak at the frequency of the atmospheric torque. The spectrum produced with the linear coupling mechanism is indistinguishable from the one with $\gamma = 0$ and therefore not shown. This result indicates that the core has a small influence on the response of the mantle to atmospheric forcing. The coupling mechanism with nonlinear (square-root) dependence also reproduces the peak at 1 cpy, but adds several other peaks at 3, 5, 7, . . . cpy. These peaks are simply a consequence of the specific form of the nonlinearity in the coupling mechanism.

4. DISCUSSION

The coupling mechanism proposed here involves a combination of pressure and electromagnetic forces. Momentum is transferred to the mantle by the influence of pressure on topography. However, the distribution of pressure over the boundary is strongly influenced by stratification and by electromagnetic forces. In fact, the coupling mechanism can be as dissipative as

electromagnetic coupling. Steep gradients in the perturbed flow distort the radial magnetic field over a length scale of roughly 10^2 m to 10^3 m, depending on the strength of the stratification. This length scale is short compared with the skin depth, based on the temporal frequency of flow over the topography. Pervasive diffusion of the magnetic perturbation occurs in a magnetic boundary-layer (i.e., the first wave).

Other components of the background magnetic field can also contribute to the coupling mechanism, although they would likely have a smaller role. Distortion of a horizontal background magnetic field is due to lateral variations in the flow, which is controlled by the wavelength of topography. This length scale is typically long compared with the vertical wavelength. The study of Moffatt (1977) dealt exclusively with the influence of a horizontal magnetic field on flow over topography (in the absence of stratification) and found that topography in excess of 4 km was required to produce a stress comparable to our nominal value of $0.027\,\mathrm{N\,m^{-2}}$. By comparison, much smaller boundary topographies are sufficient to account for the amplitude of decadal fluctuations in LOD when we allow for fluid stratification. A small topography is also consistency with our method of solution because we use a Taylor series to transfer boundary conditions to the reference surface $z = 0$. When the boundary topography is small compared with the vertical length scale of the perturbation, a first-order Taylor series suffices to relate the conditions on $z = h(x, y)$ to those on $z = 0$.

The amplitude of the topography is also important for determining the amplitude of the velocity perturbation. A nominal topography of $\tilde{h} = 30\,\mathrm{m}$ in **Figure 3** produces a maximum velocity of $0.3\,\mathrm{mm\,s^{-1}}$ at the CMB (see **Figure 3**). Thus the perturbed flow is not substantially smaller than the background flow of $0.5\,\mathrm{mm\,s^{-1}}$. We expect nonlinearities to reduce the effectiveness of the coupling mechanism, so a modest increase topography above the nominal value of $\tilde{h} = 30\,\mathrm{m}$ is probably required to compensate. Our calculations show that disturbance in the background flow is confined to the top 100 m of the core. Such a shallow disturbance may not substantially alter the influence of deeper background flow on geomagnetic secular variation (It would be analogous to diffusing the geomagnetic field through a thin conducting layer). We also expect the vertical (radial) component of the magnetic perturbation to be small, so it would be difficult to detect at the surface, particularly if the wavelength of topography was on the order of 10^2 km. Other aspects of the dynamics could more significant. Enabling an effective means of momentum transfer alters the structure of waves in the core and may also account for the damping of torsional waves in the equatorial region (Gillet et al., 2010). Electromagnetic coupling has been proposed as a damping mechanism for torsional waves (Schaeffer and Jault, 2016), but the mechanism proposed here may work similarly without requiring a large electrical conductivity on the mantle-side of the boundary. A suitably modification of the proposed mechanism is also applicable to tidally driven flow in the core (Buffett, 2010). Observations of Earth's nutation require a source of dissipation at the CMB. Electromagnetic coupling is one interpretation, but the influence of topography in the presence of stratification offers an alternative explanation.

5. CONCLUSIONS

Steady flow of Earth's core over boundary topography can produce a large tangential stress on the mantle when the top of the core is stably stratified. This stress provides an effective means of transferring angular momentum across the CMB. A linearized model is developed using a planar approximation of the CMB. Topography on the boundary disturbs the velocity and magnetic fields, causing a pressure perturbation that exerts a net horizontal force on topographic features. Reasonable choices for the amplitude of the background flow and the strength of the initial magnetic field yield dynamically significant stresses on the mantle. A viable solution has a topography of 52 m and a fluid stratification specified by $N \approx \Omega$. Stronger stratification, possibly due to a thin layer of chemical stratification, increases the stress in proportion to the value of N and lowers the required topography. We also show that the stress has a quadratic dependence on the amplitude of topography, but varies more weakly with the square root of the fluid velocity. Incorporating this coupling mechanism into a simple model for angular momentum exchange yields a nonlinear system of equations, which produces odd overtones in the response to annual forcing by an imposed torque from the atmosphere. Spectral properties of the resulting changes in LOD may offer insights into the underlying coupling mechanisms.

AUTHOR CONTRIBUTIONS

BB proposed the project and SG carried out the analysis. Both authors contributed to the writing of the paper.

FUNDING

This work is partially supported by the National Science Foundation (grant EAR-1430526).

SUPPLEMENTARY MATERIAL

The Supplementary Material for this article can be found online at: https://www.frontiersin.org/articles/10.3389/feart.2018.00171/full#supplementary-material

REFERENCES

Amit, H. (2014). Can downwelling at the top of the earth's core be detected in the geomagnetic secular variation? *Phys. Earth Planet. Inter.* 229, 110–121. doi: 10.1016/j.pepi.2014.01.012

Anufriyev, A. P., and Braginski, S. I. (1977). Effect of irregularities of the boundary of the earth's core on the speed of the fluid flow and on the magnetic field, iii. *Geomag. Aeron.* 17, 492–496.

Bloxham, J. (1986). The expulsion of magnetic flux from the earth's core. *Geophys. J. Int.* 87, 669–678. doi: 10.1111/j.1365-246X.1986.tb06643.x

Bloxham, J. (1990). On the consequences of strong stable stratification at the top of earth's outer core. *Geophys. Res. Lett.* 17, 2081–2084. doi: 10.1029/GL017i012p02081

Braginsky, S. I. (1993). MAC-oscillations of the hidden ocean of the core. *J. Geomagn. Geoelectr.* 45, 1517–1538. doi: 10.5636/jgg.45.1517

Buffett, B. A. (1996). Gravitational oscillations in the length of day. *Geophys. Res. Lett.* 23, 2279–2282. doi: 10.1029/96GL02083

Buffett, B. A. (2010). Chemical stratification at the top of earth's core: constraints from observations of nutations. *Earth Planet. Sci. Lett.* 296, 367–372. doi: 10.1016/j.epsl.2010.05.020

Buffett, B. A. (2014). Geomagnetic fluctuations reveal stable stratification at the top of the earth's core. *Nature* 507, 484–487. doi: 10.1038/nature13122

Buffett, B. A., Garnero, E. J., and Jeanloz, R. (2000). Sediments at the top of Earth's core. *Science* 290, 1338–1342. doi: 10.1126/science.290.5495.1338

Buffett, B. A., Knezek, N., and Holme, R. (2016). Evidence for MAC waves at the top of Earth's core and implications for variations in length of day. *Geophys. J. Int.* 204, 1789–1800. doi: 10.1093/gji/ggv552

Bullard, E. C., Freeman, C., Gellman, H., and Jo, N. (1950). The westward drift of the earth's magnetic field. *Philos. Trans. R. Soc.* 243, 67–92. doi: 10.1098/rsta.1950.0014

Christensen, U. R. (2018). Geodynamo models with a stable layer and heterogeneous heat flow at the top of the core. *Geophys. J. Int.* 215, 1338–1351. doi: 10.1093/gji/ggy352

Christensen, U. R., Aubert, J., and Hulot, G. (2010). Conditions for Earth-like geodynamo models. *Earth Planet. Sci. Lett.* 296, 487–496. doi: 10.1016/j.epsl.2010.06.009

Colombi, A., Nissen-Meyer, T., Boschi, L., and Giardini, D. (2014). Seismic waveform inversion for core–mantle boundary topography. *Geophys. J. Int.* 198, 55–71. doi: 10.1093/gji/ggu112

Gill, A. E. (1982). *Atmosphere-Ocean Dynamics Vol. 30 of* International Geophysics Series, 1st Edn. San Diego, CA: Academic Press.

Gillet, N., Jault, D., Canet, E., and Fournier, A. (2010). Fast torsional waves and strong magnetic field within the Earth's core. *Nature* 465, 74–77. doi: 10.1038/nature09010

Gillet, N., Pais, M. A., and Jault, D. (2009). "Ensemble inversion of time-dependent core flow models." *Geochem. Geophys. Geosys.* 10:Q06004. doi: 10.1029/2008GC002290

Gross, R. S. (2015). "Chapter 9: Earth rotation variations – long period," in *Treatise on Geophysics, Vol. 3, 2nd Edn*, ed G. Schubert (Oxford: Elsevier), 215–261.

Gross, R. S., Fukumori, I., Menemenlis, D., and Gegout, P. (2004). Atmospheric and oceanic excitation of length-of-day variations during 1980–2000. *J. Geophys. Res.* 109:B01406. doi: 10.1029/2003JB002432

Gubbins, D. (2007). Geomagnetic constraints on stratification at the top of earth's core. *Earth Planets Space* 59, 661–664. doi: 10.1186/BF03352728

Gubbins, D., and Davies, C. J. (2013). The stratified layer at the core-mantle boundary caused by barodiffusion of oxygen, sulphur and silicon. *Phys. Earth Planet. Inter.* 215, 21–28. doi: 10.1016/j.pepi.2012.11.001

Hide, R. (1969). Interaction between the Earth's Liquid Core and Solid Mantle. *Nature* 222, 1055–1056. doi: 10.1038/2221055a0

Holme, R. (1998). Electromagnetic core—mantle coupling—I. Explaining decadal changes in the length of day. *Geophys. J. Int.* 132, 167–180. doi: 10.1046/j.1365-246x.1998.00424.x

Jackson, A., Jonkers, A. R. T., and Walker, M. R. (2000). Four centuries of geomagnetic secular variation from historical records. *Philos. Trans. R. Soc. Lond. A* 358, 957–990. doi: 10.1098/rsta.2000.0569

Jackson, A., Sheyko, A., Marti, P., Tilgner, A., Cébron, D., Vantieghem, S., et al. (2014). A spherical shell numerical dynamo benchmark with pseudo-vacuum magnetic boundary conditions. *Geophys. J. Int.* 196, 712–723. doi: 10.1093/gji/ggt425

Jault, D. (2008). Axial invariance of rapidly varying diffusionless motions in the earth's core interior. *Phys. Earth Planet. Inter.* 166, 67–76. doi: 10.1016/j.pepi.2007.11.001

Jault, D., and Finlay, C. (2015). "Chapter 9: Waves in the core and mechanical core–mantle interactions," in *Treatise on Geophysics, Vol. 8, 2nd Edn.,* ed G. Schubert (Oxford: Elsevier), 225–244.

Jault, D., Gire, C., and Le Mouel, J. L. (1988). Westward drift, core motions and exchanges of angular momentum between core and mantle. *Nature* 333, 353–356. doi: 10.1038/333353a0

Jones, C. A. (2011). Planetary magnetic fields and fluid dynamos. *Annu. Rev. Fluid Mech.* 43, 583–614. doi: 10.1146/annurev-fluid-122109-160727

Kanda, R. V. S., and Stevenson, D. J. (2006). Suction mechanism for iron entrainment into the lower mantle. *Geophys. Res. Lett.* 33:L02310. doi: 10.1029/2005GL025009

Lay, T., Williams, Q., and Garnero, E. J. (1998). The core-mantle boundary layer and deep earth dynamics. *Nature* 392, 461–468. doi: 10.1038/33083

Lesur, V., Whaler, K., and Wardinski, I. (2015). Are geomagnetic data consistent with stably stratified flow at the core-mantle boundary? *Geophys. J. Int.* 201, 929–946. doi: 10.1093/gji/ggv031

Miller, K. J., Montési, L. G., and Zhu, W. -l. (2015). Estimates of olivine-basaltic melt electrical conductivity using a digital rock physics approach. *Earth Planet. Sci. Lett.* 432, 332–341. doi: 10.1016/j.epsl.2015.10.004

Moffatt, H. K. (1977). Topographic coupling at the core-mantle interface. *Geophys. Astrophys. Fluid Dyn.* 9, 279–288. doi: 10.1080/03091927708242332

More, C., and Dumberry, M. (2018). Convectively driven decadal zonal accelerations in earth's fluid core. *Geophys. J. Int.* 213, 434–446. doi: 10.1093/gji/ggx548

Mound, J. E., and Buffett, B. A. (2005). Mechanisms of core-mantle angular momentum exchange and the observed spectral properties of torsional oscillations. *J. Geophys. Res.* 110:B08103. doi: 10.1029/2004JB003555

Ohta, K., Hirose, K., Ichiki, M., Shimizu, K., Sata, N., and Ohishi, Y. (2010). Electrical conductivities of pyrolitic mantle and morb materials up to the lowermost mantle conditions. *Earth Planet. Sc. Lett.* 289, 497–502. doi: 10.1016/j.epsl.2009.11.042

Olson, P., Landeau, M., and Reynolds, E. (2017). Dynamo tests for stratification below the core-mantle boundary. *Phys. Earth Planet. Inter.* 271, 1–18. doi: 10.1016/j.pepi.2017.07.003

Otsuka, K., and Karato, S. (2012). Deep penetration of molten iron into the mantle caused by a morphological instability. *Nature* 492, 243–246. doi: 10.1038/nature11663

Pedlosky, J. (1987). *Geophysical Fluid Dynamics, 2nd Edn.* New York, NY: Springer.

Pozzo, M., Davies, C., Gubbins, D., and Alfè, D. (2012). Thermal and electrical conductivity of iron at earth's core conditions. *Nature* 485, 355–358. doi: 10.1038/nature11031

Rochester, M. G. (1962). Geomagnetic core-mantle coupling. *J. Geophys. Res.* 67, 4833–4836. doi: 10.1029/JZ067i012p04833

Schaeffer, N., and Jault, D. (2016). Electrical conductivity of the lowermost mantle explains absorption of core torsional waves at the equator. *Geophys. Res. Lett.* 43, 4922–4928. doi: 10.1002/2016GL068301

Shen, Z., Ni, S., Wu, W., and Sun, D. (2016). Short period ScP phase amplitude calculations for core-mantle boundary with intermediate scale topography. *Phys. Earth Planet. Inter.* 253, 64–73. doi: 10.1016/j.pepi.2016.02.002

Sreenivasan, B., and Gubbins, D. (2008). Dynamos with weakly convecting outer layers: implications for core-mantle boundary interaction. *Geophys. Astrophys. Fluid Dyn.* 102, 395–407. doi: 10.1080/03091920801900047

Stevenson, D. J. (1987). Limits on lateral density and velocity variations in the earth's outer core. *Geophys. J. R. Astron. Soc.* 88, 311–319. doi: 10.1111/j.1365-246X.1987.tb01383.x

Wardinski, I., and Lesur, V. (2012). An extended version of the C^3FM geomagnetic field model: application of a continuous frozen-flux constraint. *Geophys. J. Int.* 189, 1409–1429. doi: 10.1111/j.1365-246X.2012.05384.x

Wicks, J. K., Jackson, J. M., and Sturhahn, W. (2010). Very low sound velocities in iron-rich (Mg,Fe)O: implications for the core-mantle boundary region. *Geophys. Res. Lett.* 37:L15304. doi: 10.1029/2010GL043689

Conflict of Interest Statement: The authors declare that the research was conducted in the absence of any commercial or financial relationships that could be construed as a potential conflict of interest.

frontiers in Earth Science

ORIGINAL RESEARCH
published: 18 October 2018
doi: 10.3389/feart.2018.00170

Geomagnetic Dipole Changes and Upwelling/Downwelling at the Top of the Earth's Core

Ludovic Huguet[1,2]*, *Hagay Amit*[3] *and Thierry Alboussière*[4]

[1] Department of Earth, Environmental, and Planetary Sciences, Case Western Reserve University, Cleveland, OH, United States, [2] CNRS, IRPHE, Aix Marseille Université, Centrale Marseille, Marseille, France, [3] Laboratoire de Planétologie et de Géodynamique, CNRS UMR 6112, Université de Nantes, Nantes, France, [4] UCBL, ENSL, CNRS, LGL-TPE, Université de Lyon, Villeurbanne, France

The convective state of the top of Earth's outer core is still under debate. Conflicting evidence from seismology and geomagnetism provides arguments for and against a thick stably stratified layer below the core-mantle boundary. Mineral physics and cooling scenarios of the core favor a stratified layer. However, a non-zero secular variation of the total geomagnetic energy on the core-mantle boundary is evidence for the presence of radial motions extending to the top of the core. We compare the secular variation of the total geomagnetic energy with the secular variation of the geomagnetic dipole intensity and tilt. We demonstrate that both the level of cancellations of the sources and sinks of the dipole intensity secular variation, as well as the level of cancellations of the sources and sinks of the dipole tilt secular variation, are either larger than or comparable to the level of cancellations of the sources and sinks of the total geomagnetic energy secular variation on the core-mantle boundary, indicating that the latter is numerically significant hence upwelling/downwelling reach the top of the core. Radial motions below the core-mantle boundary are either evidence for no stratified layer or to its penetration by various dynamical mechanisms, most notably lateral heterogeneity of core-mantle boundary heat flux.

Keywords: geodynamo, stratification, outer core, magnetic field, core-mantle boundary, secular variation

OPEN ACCESS

Edited by:
Joshua M. Feinberg, University of Minnesota Twin Cities, United States

Reviewed by:
Peter Olson, Johns Hopkins University, United States
Maria Luisa Osete, Complutense University of Madrid, Spain

***Correspondence:**
Ludovic Huguet
huguet@irphe.univ-mrs.fr

Specialty section:
This article was submitted to Geomagnetism and Paleomagnetism, a section of the journal Frontiers in Earth Science

Received: *08 June 2018*
Accepted: *28 September 2018*
Published: *18 October 2018*

Citation:
Huguet L, Amit H and Alboussière T (2018) Geomagnetic Dipole Changes and Upwelling/Downwelling at the Top of the Earth's Core. Front. Earth Sci. 6:170. doi: 10.3389/feart.2018.00170

1. INTRODUCTION

In the outer core of the Earth, the turbulent convective flow of an electrically conducting fluid drives the geodynamo. The geomagnetic field is the measurable consequence of this geodynamo. The main feature of the geomagnetic field is the dominance of the dipole component. Based on models of the geomagnetic field and its secular variation (SV) from ground and satellite observations (Jackson et al., 2000; Finlay et al., 2015, 2016b; Gillet et al., 2015), the dipole intensity has been decreasing rapidly (e.g. Gubbins, 1987; Olson and Amit, 2006; Finlay, 2008). The dipole decrease could be related to magnetic energy cascade (Amit and Olson, 2010) or non-local transfers from the dipole to high spherical harmonic degrees (Huguet and Amit, 2012). Inferring energy transfers at the top of the Earth's core may, therefore, provide important insights into the way the fluid flow at the top of the core distributes the geomagnetic energy. Huguet et al. (2016) developed a theoretical formalism for the magnetic to magnetic and kinetic to magnetic energy transfers just below the core-mantle boundary (CMB). They showed that the existence of kinetic

to magnetic energy transfer corresponds to the presence of magnetic field stretching induced by upwelling/downwelling at the top of the core.

For decades, the existence of a stably stratified layer below the CMB has been a conundrum. Its origin (thermal or compositional), temporal evolution and the consequences for core dynamics and for the geodynamo are still puzzling. Several seismic studies suggested the presence of low P-waves velocity zone at the top of the Earth's core, which requires a lower density than the bulk of the outer core in order to remain stable (Helffrich and Kaneshima, 2010; Tang et al., 2015; Kaneshima, 2018). In contrast, Alexandrakis and Eaton (2010) did not find seismic evidence for stratification at the top of the core. Based on the observation of the SmKS waves which reflect below the CMB, Kaneshima (2018) argued that its thickness is about 450 km, larger than a previous estimate of about 300 km (Kaneshima and Helffrich, 2013). However, the new seismic model of Irving et al. (2018) explains the seismic observations without a slow and thick stable layer at the top of the outer core, that is consistent with a fully adiabatic outer core.

Several hypotheses were proposed to explain a chemical origin for a stratified region at the top of the Earth's core, but it still remains under debate. Diffusion of light elements from the mantle to the outer core could produce a thick layer (Gubbins and Davies, 2013), but it cannot explain the low seismic velocity profiles (Brodholt and Badro, 2017). During the early Earth, the release of a core impactor may explain the origin of a stably stratified layer (Landeau et al., 2016) if it has the right composition of light elements (Brodholt and Badro, 2017). Before the complete solidification of the lower mantle in the early Earth, interactions between a basal magma ocean and the top of the outer core may explain the formation of a light and seismically slow stratified layer (Brodholt and Badro, 2017).

Large outer core thermal conductivity corresponds to outer core heat flux partly conducted along the adiabat. In this case, the heat flux at the top of the core is sub-adiabatic and should lead to the formation of a thermal stably stratified layer while the deeper outer core convects (Gomi et al., 2013; Labrosse, 2015). However, the value of the thermal conductivity of iron under core pressure conditions is still under debate (Williams, 2018). Ab-initio calculations favor large core thermal conductivity (de Koker et al., 2012; Pozzo et al., 2012), whereas high pressure experiments have reported both large and low values (Gomi et al., 2013; Konôpková et al., 2016; Ohta et al., 2016). For example, the low outer core thermal conductivity proposed by Konôpková et al. (2016) would likely correspond to super-adiabatic conditions throughout the entire outer core.

Geomagnetic evidence for a stably stratified layer appears in the form of low geomagnetic SV at special points on the CMB where the field gradient is zero (Whaler, 1980). However, uncertainties on the exact locations of these points render such an analysis unreliable (Whaler and Holme, 2007). Magnetic, Archimedes and Coriolis (MAC) waves in a stratified layer are in agreement with the 60-year fluctuations of the geomagnetic dipole intensity over the historical era (Buffett, 2014; Buffett et al., 2016; Jaupart and Buffett, 2017). In contrast, intense geomagnetic flux patches at high latitudes and intensifying reversed flux patches below the South Atlantic are difficult to explain without the presence of upwelling/downwelling at the top of the core. Regional analysis of the SV at the CMB provides evidence for local magnetic flux concentrations, suggestive of the presence of fluid downwelling at the top of the core (Amit, 2014). Core flow inversions from geomagnetic SV exclude pure toroidal flow (Whaler, 1986) although the inclusion of a weak poloidal flow is sufficient to explain it (Lesur et al., 2015).

Convection in the deeper part of the outer core may penetrate a stably stratified layer (Takehiro and Lister, 2001; Takehiro, 2015; Takehiro and Sasaki, 2018). The length of penetration depends on the timescale and the length scale of the convective features of the outer core. Theoretical studies predicted a complete penetration of the stratified layer by the mean zonal flow (Takehiro and Sasaki, 2018). Outer core convection may also generate MAC waves in a stably stratified layer which include zonal radial flow (Buffett, 2014).

Recent studies attempted to reconcile evidence for a stratified layer from seismology and mineral physics with evidence for upwelling/downwelling from geomagnetism (Olson et al., 2017; Christensen, 2018). These studies relied on numerical dynamo simulations with an imposed stably stratified layer at the top of the shell and outer boundary heat flux heterogeneity. Here the main parameters controlling the competition between the stable layer and the boundary-driven convection are the layer thickness, the layer stability and the amplitude of CMB heat flux heterogeneity. The latter is estimated to be large enough (Nakagawa and Tackley, 2008) so that super-adiabatic conditions prevail where the CMB heat flux is large (Olson et al., 2017). The layer thickness and stability depend on the debated total CMB heat flux and core thermal conductivity. Olson et al. (2017) found for weak stratification that these local unstable regions stir the entire stable layer and lead to whole core convection. Their models are in agreement with the morphology of the time-average paleomagnetic field as long as the stable layer is thin. Christensen (2018) showed for strong stratification that the layer is not penetrated, and consequently, the magnetic field becomes too dipolar and too axisymmetric compared to the geomagnetic field (Christensen et al., 2010) due to a strong skin effect (Christensen, 2006; Nakagawa, 2011). In addition, such strong stratification would prevent the impact of CMB heterogeneity on the deeper core (e.g. by prescribing preferential inner core growth as proposed by Aubert et al., 2008). Mound et al. (2018) proposed that the CMB heterogeneity induces local stratification at low heat flux regions (rather than affecting a pre-existing global layer). These hot regions remain stable while in other parts convection reaches the CMB.

In this paper, we compare the temporal changes in the geomagnetic dipole with the temporal variations of the total geomagnetic energy on the CMB. In section 2 we recall the formalism of Huguet et al. (2016) for the energy transfer in 2D with radial magnetic field. Following Huguet et al. (2016),

we compare the level of cancellations in the integrands of the SV of the total magnetic energy with that of the SV of the axial dipole but in much greater details. In addition, here we also compare the level of cancellations in the integrand of the SV of the total magnetic energy with that of the SV of the equatorial dipole. These ratios are computed based on the geomagnetic field and SV from several historical (Jackson et al., 2000; Gillet et al., 2015) and satellites (Finlay et al., 2015, 2016b) models. The results are presented in section 3. In section 4 we discuss our main results and their implications for the presence or absence of stratification at the top of the Earth's outer core.

2. THEORY

2.1. Energy Transfers at the Top of the Core With Radial Magnetic Field

Here we recall the derivation of Huguet et al. (2016) for the magnetic to magnetic and kinetic to magnetic energy transfers at the top of the core. We show that non-zero SV of the total poloidal magnetic energy on the CMB requires kinetic to magnetic energy transfer. The existence of this energy transfer depends on the existence of upwelling/downwelling at the top of the core.

Our starting point is the radial magnetic induction equation in the frozen-flux limit (Roberts and Scott, 1965) just below the CMB (where, the radial velocity vanishes):

$$\dot{B}_r = -\overrightarrow{u_h} \cdot \nabla_h B_r - B_r \nabla_h \cdot \overrightarrow{u_h} \tag{1}$$

where B_r is the radial magnetic field, dot denotes time derivative, $\vec{u_h}$ is the velocity tangential to the spherical surface, and ∇_h is the horizontal part of the differentiation operator. In Equation (1) the second term is the advection of the radial field by the tangential flow, the third term is the stretching of the field by the poloidal flow, and the first term is the SV. Multiplying (1) by B_r/μ_0 (where μ_0 is the permeability of free space) gives

$$\frac{1}{2\mu_0}\dot{B_r}^2 = -\overrightarrow{u_h} \cdot \nabla_h \frac{B_r^2}{2\mu_0} - \frac{B_r^2}{\mu_0}\nabla_h \cdot \overrightarrow{u_h} \tag{2}$$

The first term in (2) is the integrand of the SV of the total (poloidal) magnetic energy:

$$\dot{E}_b = \frac{1}{4\pi r_c^2}\int_S \frac{1}{2\mu_0}\dot{B_r}^2 dS \tag{3}$$

where r_c is the radius of the core and $dS = r_c^2 \sin\theta d\phi d\theta$.

Next we split the stretching term in (2) into two halves:

$$\frac{1}{2\mu_0}\dot{B_r}^2 = -\overrightarrow{u_h} \cdot \nabla_h \frac{B_r^2}{2\mu_0} - \frac{B_r^2}{2\mu_0}\nabla_h \cdot \overrightarrow{u_h} - \frac{B_r^2}{2\mu_0}\nabla_h \cdot \overrightarrow{u_h} \tag{4}$$

The divergence theorem (or Green's theorem) for wrapped 2D surfaces like the spherical CMB gives trivially zero value for the integral of any divergence term. Therefore, integrating the sum of the second and third terms of (4) gives

$$\int_S \left(\overrightarrow{u_h} \cdot \nabla_h \frac{B_r^2}{2\mu_0} + \frac{B_r^2}{2\mu_0}\nabla_h \cdot \overrightarrow{u_h} \right) dS = \int_S \nabla_h \cdot (\overrightarrow{u_h}\frac{B_r^2}{2\mu_0}) dS = 0 \tag{5}$$

We thus obtain

$$\dot{e}_{bb} = -\overrightarrow{u_h} \cdot \nabla_h \frac{B_r^2}{2\mu_0} - \frac{B_r^2}{2\mu_0}\nabla_h \cdot \overrightarrow{u_h} \tag{6}$$

$$\dot{e}_{ub} = -\frac{B_r^2}{2\mu_0}\nabla_h \cdot \overrightarrow{u_h} \tag{7}$$

and

$$\dot{E}_b \equiv \frac{1}{4\pi r_c^2}\int_S (\dot{e}_{bb} + \dot{e}_{ub})\, dS = \frac{1}{4\pi r_c^2}\int_S \dot{e}_{ub} dS \tag{8}$$

Based on (6–7), the local magnetic to magnetic energy transfer $\dot{e}_{bb}$ is due to the advection term plus half the stretching term, and the kinetic to magnetic energy transfer $\dot{e}_{ub}$ is exclusively due to half the stretching term. Globally, the SV of the total (i.e., integrated over the CMB surface) poloidal magnetic energy is therefore due to kinetic to magnetic energy transfer only (8). This result is well-established for the 3D case, i.e., over the entire spherical shell (e.g. Alexakis et al., 2005a,b, 2007; Debliquy et al., 2005; Mininni et al., 2005; Carati et al., 2006; Mininni, 2011). Huguet et al. (2016) proved that it also holds for the 2D case.

2.2. Dipole Moment Changes

Here we recall the theory for the spatial contributions to dipole changes from Amit and Olson (2008). We describe the theory for both the axial and equatorial dipole components, which approximate the dipole intensity (Gubbins, 1987; Gubbins et al., 2006; Olson and Amit, 2006; Finlay et al., 2016a) and tilt (Amit and Olson, 2008), respectively.

The geomagnetic dipole moment vector $\vec{m}$ is generally expressed in terms of an axial component m_z and two components in the equatorial plane m_x and m_y

$$\vec{m} = m_z\hat{z} + m_x\hat{x} + m_y\hat{y} \tag{9}$$

The axial dipole moment can be written as

$$m_z = \frac{4\pi a^3}{\mu_0} g_1^0 = \int_S \rho_z dS \tag{10}$$

in terms of its integrand on the CMB ρ_z,

$$\rho_z = \frac{3r_c}{2\mu_0} B_r \cos\theta \tag{11}$$

where a is the Earth's radius, g_1^0 is the axial dipole Gauss coefficient and the spherical coordinate system (ϕ, θ, r) denotes longitude, co-latitude, and radial distance, respectively.

Integrands can also be defined for the dipole moment components along the Cartesian x and y coordinates in the equatorial plane. The dipole moment integrands along longitudes $0^\circ E$ and $90^\circ E$, respectively are

$$\rho_x = \frac{3r_c}{2\mu_0} B_r \sin\theta \cos\phi \tag{12}$$

$$\rho_y = \frac{3r_c}{2\mu_0} B_r \sin\theta \sin\phi \tag{13}$$

and the corresponding dipole moment components are

$$m_x = \frac{4\pi a^3}{\mu_0} g_1^1 = \int_S \rho_x dS \tag{14}$$

$$m_y = \frac{4\pi a^3}{\mu_0} h_1^1 = \int_S \rho_y dS \tag{15}$$

where g_1^1 and h_1^1 are the equatorial dipole Gauss coefficients.

The dipole components in the equatorial plane allow to define the equatorial component of the dipole moment as

$$m_e = \frac{4\pi a^3}{\mu_0} \sqrt{{g_1^1}^2 + {h_1^1}^2} = \int_S \rho_e dS \tag{16}$$

in terms of the equatorial dipole moment density ρ_e on the CMB,

$$\rho_e = \frac{3r_c}{2\mu_0} B_r \sin\theta \cos\phi' \tag{17}$$

where $\phi' = \phi - \phi_0$ is the longitude relative to that of the dipole axis. $\phi_0(t)$ is the time-dependent longitude of the dipole axis given by Amit and Olson (2008)

$$\phi_0 = \tan^{-1}\left(\frac{m_x}{m_y}\right) = \tan^{-1}\left(\frac{h_1^1}{g_1^1}\right) \tag{18}$$

Note that m_e is by definition positive (16). The dipole tilt angle θ_0 can be written in terms of the axial and equatorial dipole moment components,

$$\theta_0 = \tan^{-1}\left(\frac{m_e}{m_z}\right) = \tan^{-1}\left(\frac{\sqrt{{g_1^1}^2 + {h_1^1}^2}}{g_1^0}\right) \tag{19}$$

Finally, based on the above formalism, it is straightforward to write the SV of the dipole components in terms of spatial integrands. The time derivative of (11) gives

$$\dot{\rho}_z = \dot{B}_r \cos\theta \tag{20}$$

$$\dot{m}_z = \frac{3r_c}{2\mu_0} \int_S \dot{\rho}_z dS \tag{21}$$

The time derivative of (17) gives

$$\dot{\rho}_e = \dot{B}_r \sin\theta \cos\phi' + B_r \sin\theta \sin\phi' \dot{\phi}_0 \tag{22}$$

$$\dot{m}_e = \frac{3r_c}{2\mu_0} \int_S \dot{\rho}_e dS \tag{23}$$

where the azimuthal angular velocity of the dipole axis is

$$\dot{\phi}_0 = \frac{\dot{m}_y m_x - \dot{m}_x m_y}{{m_x}^2 + {m_y}^2} = \frac{\dot{h}_1^1 g_1^1 - \dot{g}_1^1 h_1^1}{{g_1^1}^2 + {h_1^1}^2} \tag{24}$$

2.3. Measures of the Level of Cancellations in the Integrands

In order to infer the significance of the values of the SV of the total geomagnetic energy, we define ratios of integrals with respect to their corresponding absolute integrals. Such integral ratios quantify the level of spatial cancellations at a given integral and may therefore assess the significance of the numerical values. Similar ratios were used to quantify the level of cancellations in the integrand of geomagnetic axial dipole change by meridional advection (Finlay et al., 2016a) and to calculate the regional level of cancellations in different SV contributions in numerical dynamos (Peña et al., 2016). Huguet et al. (2016) compared the level of cancellations of the SV of the total magnetic energy with those of the SV of the axial dipole. Here we recall these definitions and define a new quantity for the level of cancellations of the equatorial dipole.

Following (3) the ratio ε_e is defined by

$$\varepsilon_e = \frac{\int_S B_r \dot{B}_r dS}{\int_S |B_r \dot{B}_r| dS} \tag{25}$$

This ratio represents the level of cancellations in the integrand of the SV of the total magnetic energy. For comparison, the ratio ε_{mz} represents the level of cancellations in the integrand of the SV of the axial dipole and is written

$$\varepsilon_{mz} = \frac{\int_S \cos\theta \dot{B}_r dS}{\int_S |\cos\theta \dot{B}_r| dS}. \tag{26}$$

The dipole is the largest scale and the strongest component of the geomagnetic field. Its current intensity decrease is well-documented (Gubbins, 1987; Olson and Amit, 2006; Finlay, 2008; Finlay et al., 2016a; Metman et al., 2018). The ratio ε_{mz} therefore serves as a reference value to a level of cancellations that cannot be considered negligible.

In addition, following (23) we define the ratio ε_{me} which represents the level of cancellations in the integrand of the SV of the equatorial dipole

$$\varepsilon_{me} = \frac{\int_S \sin\theta \left(\dot{B}_r \cos(\phi - \phi_0) + B_r \sin(\phi - \phi_0) \dot{\phi}_0\right) dS}{\int_S |\sin\theta \left(\dot{B}_r \cos(\phi - \phi_0) + B_r \sin(\phi - \phi_0) \dot{\phi}_0\right)| dS} \tag{27}$$

This new ratio defines an additional reference value for the level of cancellations that is significant.

3. RESULTS

In this section, we plot the axial dipole SV (21), the equatorial dipole SV (23) and the total geomagnetic energy SV (3), all on the CMB, using various field models.

3.1. Changes in the Total Geomagnetic Energy

We use several geomagnetic field models. The gufm1 model in the historical era (1840–1990) (Jackson et al., 2000) was constructed from surface observatories and the MAGSAT satellite data. The COV-OBS.x1 model covers the historical era until present-day, including satellite data of the past two decades (1840–2020) (Gillet et al., 2015). COV-OBS.x1 is an ensemble of 100 models that accounts for data uncertainties. The CHAOS-5 (Finlay et al., 2015) and CHAOS-6 (Finlay et al., 2016b) models rely exclusively on recent high-quality satellite data (1997.1–2016 and 1997.1–2018, respectively). All models are expanded until spherical harmonic degree $n_{max} = 14$.

We start with an example of the radial geomagnetic field on the CMB (**Figure 1A**) and its SV (**Figure 1B**) which combine to produce the integrand of the SV of the total magnetic energy (**Figure 1C**), using the field model CHAOS-5 (Finlay et al., 2015) of the year 2015. The geomagnetic SV is dominated by small scales with numerous pairs of opposite sign structures that sum up by definition identically to zero. The integrand of the SV of the total geomagnetic energy is also dominated by pairs of opposite sign structures; However, the integrated outcome is different. At low latitudes of the Southern Hemisphere, several positive local contributions to the SV of the total geomagnetic energy appear below the Indian Ocean and West Africa, with their negative counterparts being much weaker. In addition, below Siberia a negative $B_r\dot{B}_r$ structure is sandwiched by two positive structures. Overall, there are more positive contributions than negative, i.e., the total geomagnetic energy is instantaneously increasing in this model.

Figure 2 shows $\dot{E}_b$, the integrated SV of total magnetic energy, during the historical era. Non-zero values are observed, though at this stage it still remains to be demonstrated that these values are numerically significant. In the early period, the two field models differ significantly, possibly due to some spurious edge effects in COV-OBS.x1 (Metman et al., 2018, N. Gillet, personal communication). These edge effects are well known in comprehensive field models (e.g., Wardinski and Holme, 2006; Olsen et al., 2009; Gillet et al., 2013). However, the period over which these effects may last is unknown; It may depend on the modeling strategy. Between 1910 and 1990 both models exhibit increasing total geomagnetic energy with similar trends. Interestingly, starting from 1990 the $\dot{E}_b$ value begins to decrease rapidly and around 2010 changes its sign giving decreasing total geomagnetic energy with time at present-day.

3.2. Changes in the Geomagnetic Dipole

Figure 3 shows the time-evolution of the geomagnetic dipole and its temporal rate of change. Because the dipole is the most robust feature of the field, its uncertainty is the smallest and the 100 models of COV-OBS.x1 are practically identical to its mean. In addition, all three models (gufm1, COV-OBS.x1, and CHAOS-5) are in excellent agreement for the dipole. The axial dipole (**Figure 3A**) has been decreasing since 1840 (e.g., Gubbins, 1987; Gubbins et al., 2006; Olson and Amit, 2006; Finlay, 2008; Finlay et al., 2016a) and perhaps even further back in the past (Poletti et al., 2018). However, the rate of axial dipole decrease (**Figure 3B**) has been undulating (Olson and Amit, 2006; Buffett, 2014; Finlay et al., 2016a). The equatorial dipole (**Figure 3C**) and the tilt (**Figure 3E**) are highly correlated. Until 1960 very small tilt changes are observed, but since then the dipole axis is rapidly drifting poleward. This trend, noted a decade ago by Amit and Olson (2008), persists to present-day (**Figures 3C,E**). **Figures 3D,F** are also highly correlated and show that the poleward drift of the dipole tilt is steadily accelerating.

The local contributions to the axial and equatorial dipole components are shown in **Figure 4**. The polarity of the geomagnetic field in the present chron is negative. Hence, normal flux patches, especially at high latitudes, provide dominant negative contributions to the axial dipole integrand, whereas reversed flux patches, in particular below the South Atlantic, provide positive contributions, that is, opposite to the dominant

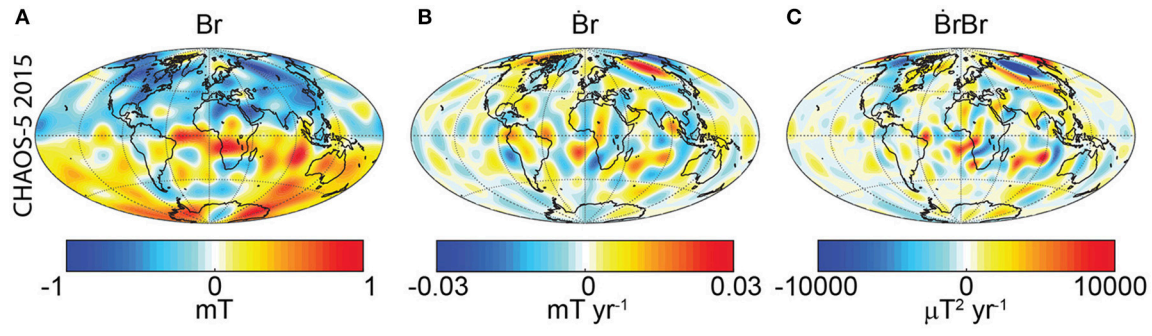

FIGURE 1 | (A) B_r, **(B)** $\dot{B}_r$, and **(C)** $B_r\dot{B}_r$, all for the geomagnetic field model CHAOS-5 in the year 2015 (Finlay et al., 2015).

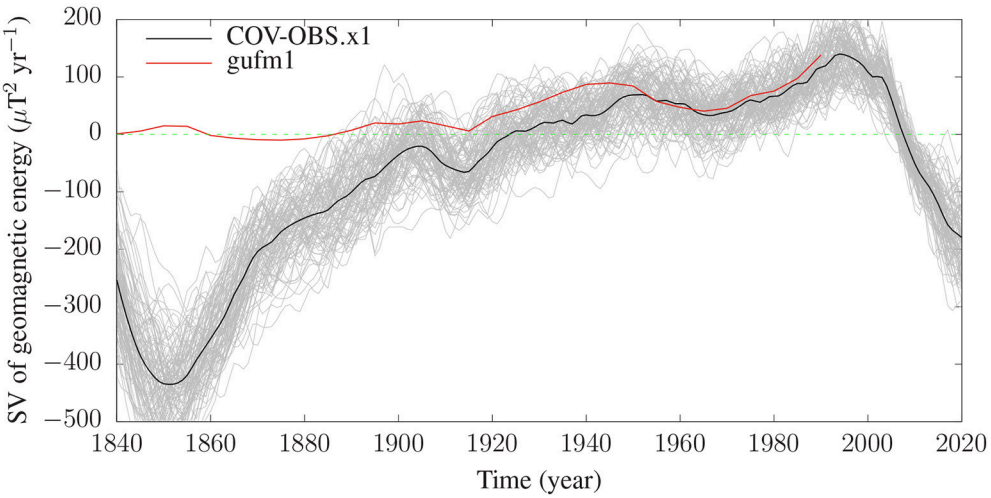

FIGURE 2 | The SV of the total geomagnetic energy on the CMB $\dot{E}_b$ as a function of time for gufm1 in the period 1840–1990 (red; Jackson et al., 2000) and COV-OBS.x1 in the period 1840–2020 (black; Gillet et al., 2015). Gray lines correspond to the ensemble of 100 models of COV-OBS.x1. Dashed horizontal green line denotes zero. Note that the SV of the total geomagnetic energy is in units of $\mu T^2 yr^{-1}$.

polarity (Gubbins, 1987; Gubbins et al., 2006; Olson and Amit, 2006; Terra-Nova et al., 2015; Metman et al., 2018). The equatorial dipole integrand is comprised of four quadrants separated by the equator and the two meridians 90 degrees east and west off the dipole longitude ϕ_0 (Amit and Olson, 2008). The Northwest and Southeast quadrants provide positive contributions to m_e, whereas the Northeast and Southwest quadrants provide negative contributions. The high level of cancellations in **Figure 4B** reflects the small magnitude of m_e relative to m_z. However, the positive contributions exceed the negative ones, yielding at present a tilt of $\sim 10^\circ$ of the dipole axis from the rotation axis (**Figure 3E**).

3.3. Comparing Total Geomagnetic Energy and Dipole Changes

The integrands of $\dot{m}_z$ (ρ_z in (20)), $\dot{m}_e$ (ρ_e in (22)), and $\dot{E}_b$ ($B_r\dot{B}_r$) are shown in **Figure 5** for four snapshots. Visually, all three of these quantities exhibit multiple sources and sinks in all four snapshots. Quantitatively, $\dot{E}_b$ is almost five times larger in 1940 than in 1900 (**Figure 2**). Indeed, fewer cancellations in $B_r\dot{B}_r$ in 1940 are seen, in particular, the positive strip along the longitude of central Asia (**Figures 5I,F**). Likewise, in 1980 when the dipole tilt was rapidly decreasing (**Figures 3C–F**), more positive ρ_e structures are observed, in particular, two long meridional strips below central Asia and Oceania (**Figure 5E**). In contrast, in 1900 and 1940 when the dipole tilt varied slowly (**Figures 3C–F**), the ρ_e distributions are much more balanced (**Figures 5H,K**). However, in order to quantitatively assess and compare the level of cancellations of the three integrands, we turn to the measures introduced in section 2.3.

Figure 6 shows the evolution of the ratios ε_e (25), ε_{mz} (26), and ε_{me} (27) for the geomagnetic field models gufm1 (Jackson et al., 2000) and COV-OBS.x1 (Gillet et al., 2015). Note that the two field models are not overlapping, a consequence of the non-linearity of the ε quantities. The 100 models of COV-OBS.x1 provide an estimate of the error.

For gufm1, until $\sim$ 1920 ε_{mz} was in general larger than ε_e, whereas after 1920 the latter was much larger. Until $\sim$ 1960 ε_{me} was nearly zero and in general smaller than ε_{mz} and ε_e. This corresponds to the constant tilt period (**Figures 3C-F**; see also Amit and Olson, 2008; Amit et al., 2018). Since 1960, ε_{me} decreases in parallel to the decrease of the dipole tilt, with maximum absolute ε_{me} value in the last decade of the model. At the end of this period $|\varepsilon_{me}|$ reaches a comparable value to $|\varepsilon_{mz}|$, both much lower than that of ε_e. At most times, however, the absolute values of ε_{me} in gufm1 are smaller than those of ε_e and ε_{mz}.

The ensemble of 100 models of COV-OBS.x1 show significant variability in ε_e, especially at earlier times, but for ε_{mz} and ε_{me} in practice the 100 models are identical to their respective mean values. This is to some extent expected because the uncertainty in COV-OBS.x1 is smallest for the dipole (Gillet et al., 2015). In COV-OBS.x1, ε_{mz} and ε_{me} exhibit similar trends as in gufm1 but with smaller amplitudes, especially for ε_{mz}. Overall ε_e exhibits large amplitude oscillations and its value is comparable to or larger than ε_{mz} and ε_{me} except for a few snapshots when ε_e changes sign (e.g., around 1940 and 2010). As in gufm1 ε_{me} is nearly zero until 1960 and decreasing thereafter, though its amplitude is smaller than in gufm1.

We proceed to further test the dependence of our results on the small scales of the geomagnetic field and its SV. In **Figure 7** we show the ratios ε_e, ε_{mz}, and ε_{me} for four snapshots as a function of the truncation degree of spherical harmonic n_{max}. For the overlapping years ε_e shows significant differences between gufm1 and the mean of COV-OBS.x1 for $n_{max} > 8$ (as in **Figure 6**), whereas, for smaller n_{max} both models are in decent agreement. For all n_{max} values, ε_{mz} and ε_{me} are very similar in

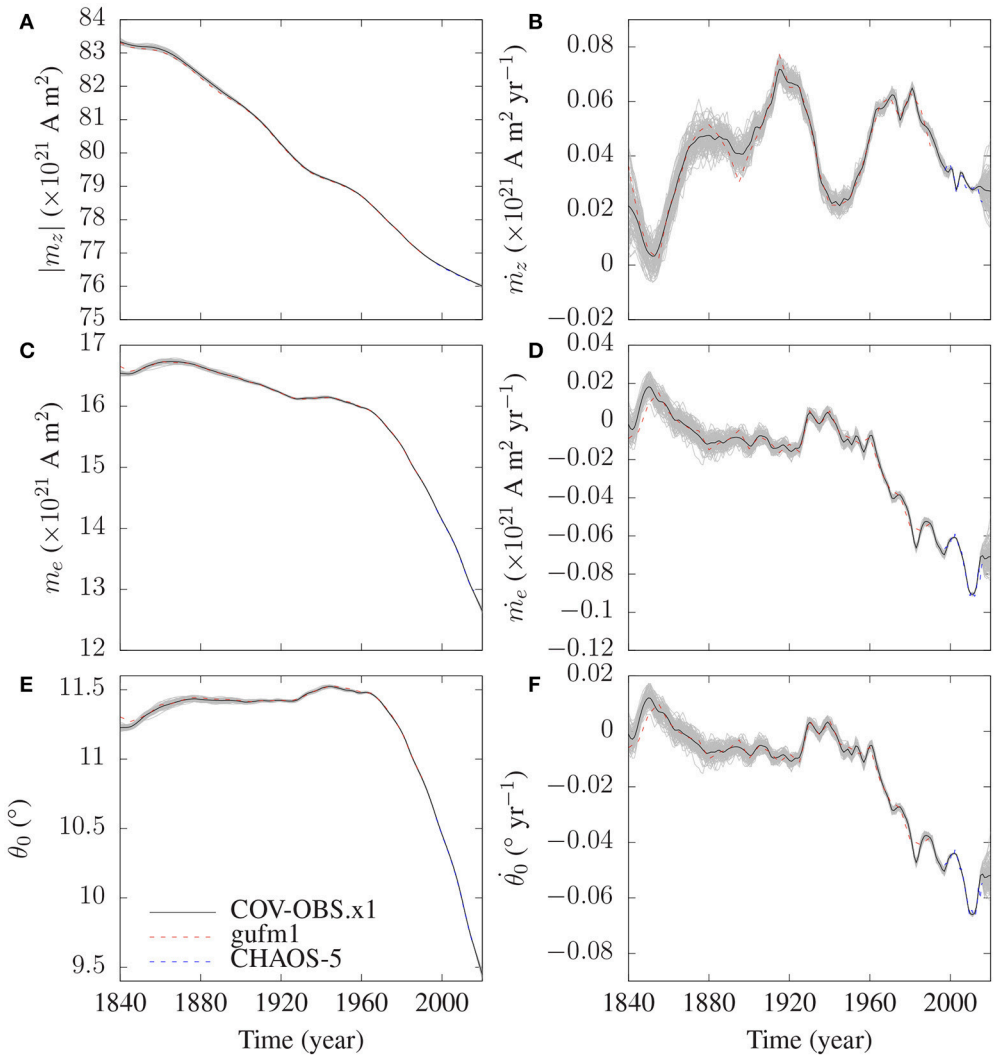

FIGURE 3 | Geomagnetic dipole as a function of time for gufm1 (red dashed line; Jackson et al., 2000), COV-OBS.x1 (black solid line; Gillet et al., 2015) and CHAOS-5 (blue dashed line; Finlay et al., 2015). Gray lines correspond to the ensemble of 100 models of COV-OBS.x1. Absolute axial component $|m_z|$ **(A)**, equatorial component m_e **(C)** and tilt θ_0 **(E)** and time derivatives of axial component $\dot{m}_z$ **(B)**, equatorial component $\dot{m}_e$ **(D)**, and tilt $\dot{\theta}_0$ **(F)**.

the two models. The three ε values approach asymptotic values with increasing resolution (**Figure 7**).

For the year 1980 in gufm1, ε_e and ε_{me} are comparable for small n_{max} but ε_{mz} is larger. For large n_{max}, the absolute values of ε_{mz} and ε_{me} are comparable while ε_e is largest. In 1940 ε_e is by far the largest and ε_{me} is very small for all n_{max} values. In 1900 ε_{mz} is the largest for most n_{max} values (**Figure 7**).

The ε_e values of the ensemble of 100 models of COV-OBS.x1 include zero values for all years. Nevertheless, all ratios show an asymptotic behavior with increasing n_{max}, which provides evidence for the significance of the ε_e and $\dot{E}_b$ values. The envelope of 100 models surrounds the mean values. For ε_e the envelope widens with increasing n_{max}, whereas for ε_{mz} and ε_{me} the corresponding envelopes are thin for all n_{max} values (**Figure 7**). In 2015 for low n_{max} the absolute ε_{me} is the largest, but at $n_{max} = 13$ the ε_e and ε_{me} of the mean of COV-OBS.x1 cross and at $n_{max} = 14$ in most of the 100 models ε_e is the largest. In 1980 for low n_{max} the absolute ε_{mz} is largest, whereas for large n_{max} the three ratios of the mean of COV-OBS.x1 are comparable with about half of the 100 models exhibiting largest ε_e values. In 1940 ε_e is by far the largest ratio, especially at low n_{max}. Finally, in 1900 for most n_{max} ε_e is the largest ratio (**Figure 7**).

Figures 8A,B show all ratios as functions of time and n_{max} respectively for the satellites era. With the full resolution during this period the absolute value of ε_{me} is the largest (**Figures 8A**). For small n_{max}, ε_e is much smaller than ε_{mz} and ε_{me}; increasing n_{max} gives ε_e comparable to ε_{mz} but still smaller than ε_{me} (**Figures 8B**). We also compared the results based on CHAOS-5 (Finlay et al., 2015) and CHAOS-6 (Finlay et al., 2016b). The results are practically identical for ε_{mz} and ε_{me}, whereas for ε_e some mild discrepancies

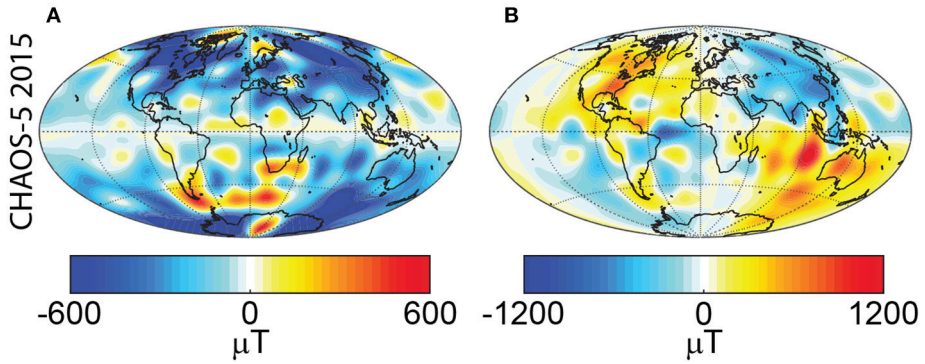

FIGURE 4 | Geomagnetic dipole integrands for the axial m_z **(A)** and equatorial m_e **(B)** components for the year 2015 of CHAOS-5 (Finlay et al., 2015).

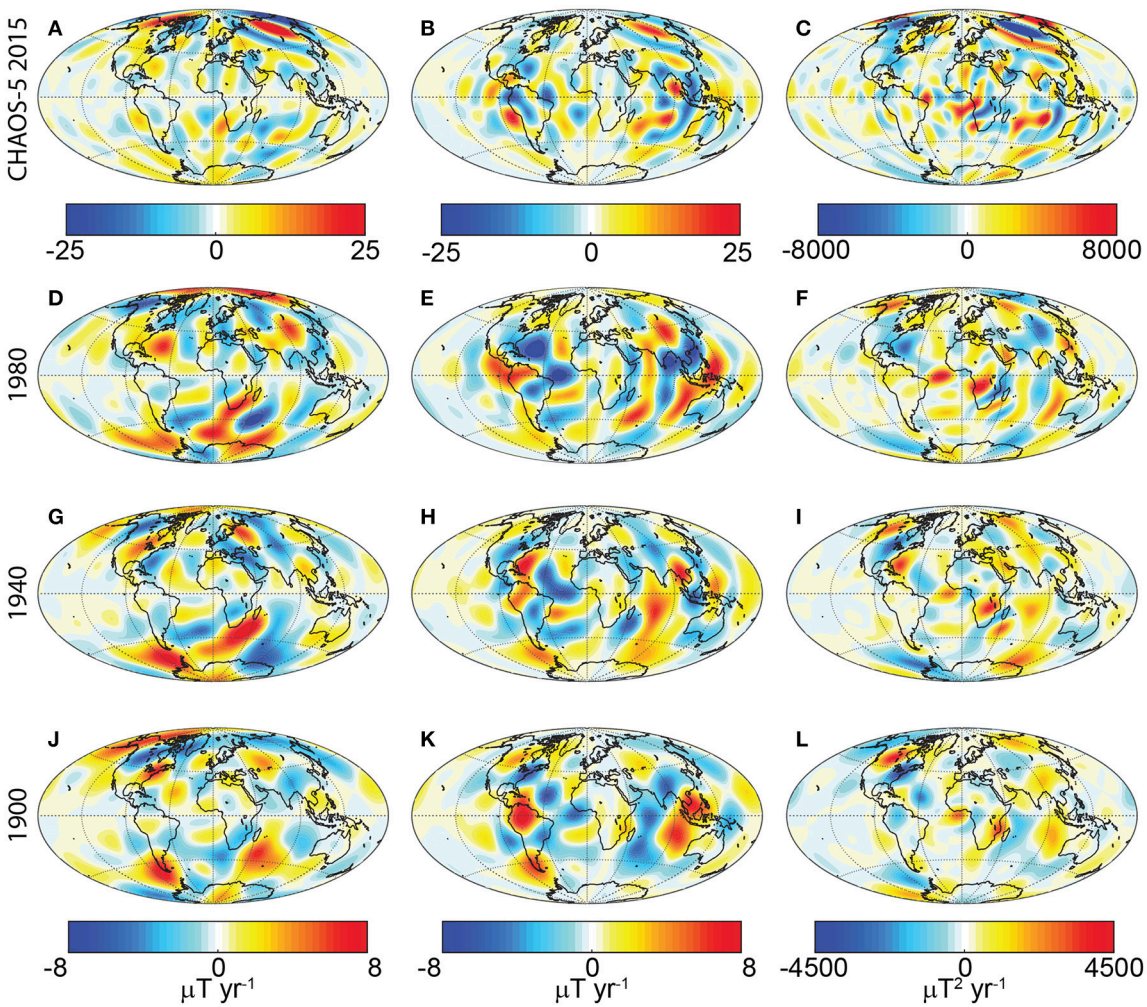

FIGURE 5 | Integrands of $\dot{m}_z$ **(A,D,G,J)**, $\dot{m}_e$ **(B,E,H,K)**, and $\dot{E}_b$ **(C,F,I,L)** for CHAOS-5 in 2015 **(A–C)** and gufm1 in 1900 **(D–F)**, 1940 **(G–I)**, and 1900 **(J–L)**.

exist. Finally, we note that the results for CHAOS-5 and CHAOS-6 (**Figure 8A**) differ from those for COV-OBS.x1 (**Figure 6**) in the overlapping period. This demonstrates the significance of the small-scale field and SV, which somewhat differ from one model to another, in the ϵ_e, ϵ_{mz}, and ϵ_{me} quantities.

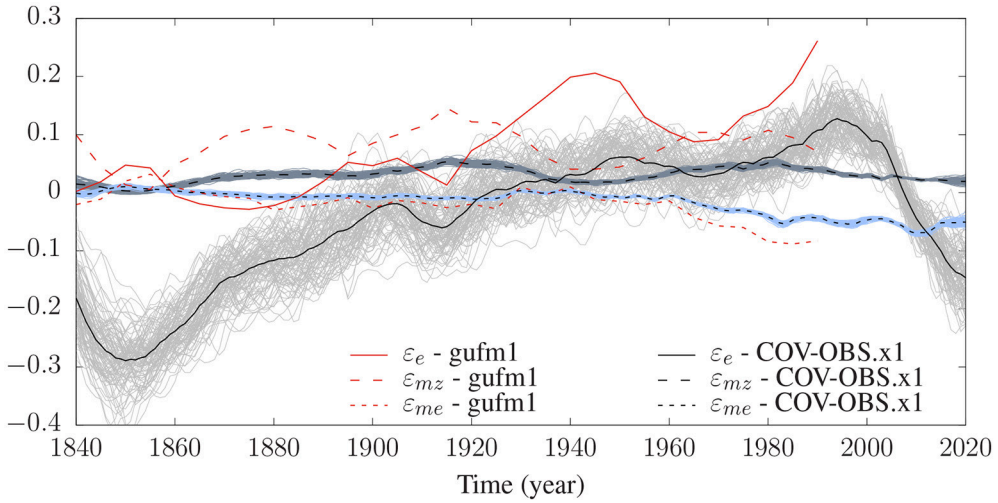

FIGURE 6 | Evolution of the ratios ε_e (solid lines), ε_{mz} (dashed lines), and ε_{me} (dotted lines) using gufm1 (red lines) and the mean of COV-OBS.x1 (dark lines). The family of 100 COV-OBS.x1 models is presented in light, dark gray, and light blue solid lines for ε_e, ε_{mz}, and ε_{me}, respectively.

3.4. Can Magnetic Diffusion Explain the Changes in the Total Geomagnetic Energy?

The analysis above relies on the frozen-flux approximation, i.e., magnetic diffusion effects are assumed negligible compared to the effects of advection and stretching (Roberts and Scott, 1965). This approximation is supported by large estimates of the magnetic Reynolds number (e.g., Holme, 2015). However, the presence of a magnetic boundary layer at the top of the core may introduce a small radial length scale and significantly larger magnetic diffusion contributions to the SV than often considered (Gubbins, 1996; Amit and Christensen, 2008; Barrois et al., 2017). In addition, for global quantities such as the dipole (or the total magnetic energy), particular field-flow interactions might yield inefficient advection and hence large relative diffusive contribution (Olson and Amit, 2006; Finlay et al., 2016a).

Modeling magnetic diffusion SV from observations is problematic because the field inside the core is in general unknown. Amit and Christensen (2008) found in numerical dynamos a significant correlation between the patterns of tangential and radial magnetic SV. They proposed that intense magnetic flux patches on the outer boundary are concentrated by fluid downwellings which are the surface expressions of columnar helical vortices. Inside a flow column the tangential divergence is weaker, therefore the magnetic flux patch diffuses both tangentially and inwards, hence the correlation between tangential and radial diffusion. This model was recently confirmed by core flow re-analysis (Barrois et al., 2017) and joint inversion of magnetic and velocity fields (Barrois et al., 2018).

The complete radial induction equation at the top of the core, including magnetic diffusion, is written

$$\dot{B}_r = -\overrightarrow{u_h}\cdot\nabla_h B_r - B_r\nabla_h\cdot\overrightarrow{u_h} + \lambda\left(\frac{1}{r_c^2}\frac{\partial^2}{\partial r^2}\left(r^2 B_r\right) + \nabla_h^2 B_r\right) \quad (28)$$

where λ is magnetic diffusivity and r is the radial coordinate. The last two terms are radial and tangential diffusion respectively. According to the model of Amit and Christensen (2008)

$$\frac{1}{r_c^2}\frac{\partial^2}{\partial r^2}\left(r^2 B_r\right) \propto \nabla_h^2 B_r \quad (29)$$

and

$$\dot{B}_r = -\overrightarrow{u_h}\cdot\nabla_h B_r - B_r\nabla_h\cdot\overrightarrow{u_h} + \lambda^*\nabla_h^2 B_r \quad (30)$$

where λ^* is the effective magnetic diffusivity which accounts for radial diffusion. Because tangential diffusion is known from geomagnetic field models, (29) allows to model the full magnetic diffusion SV. With this magnetic diffusion term, (8) becomes

$$\dot{E}_b = \frac{1}{4\pi r_c^2}\int_S (\dot{e}_{ub} + \dot{e}_d)dS \quad (31)$$

with the local diffusive contribution to $\dot{E}_b$ given by

$$\dot{e}_d = \frac{\lambda^* B_r}{\mu_0}\nabla_h^2 B_r \quad (32)$$

First we assess analytically the role of magnetic diffusion. Using the identities for tangential Laplacian and orthogonality of spherical harmonics, (32) can be rewritten as

$$\dot{e}_d = -\frac{\lambda^*}{\mu_0 r_c^2}\sum_{n=1}^{n_{max}} n(n+1)\sum_{m=0}^{n}(B_{r_n}^m)^2 \quad (33)$$

where $B_{r_n}^m$ is the radial field of degree n and order m. Equation (33) indicates that, based on the model of

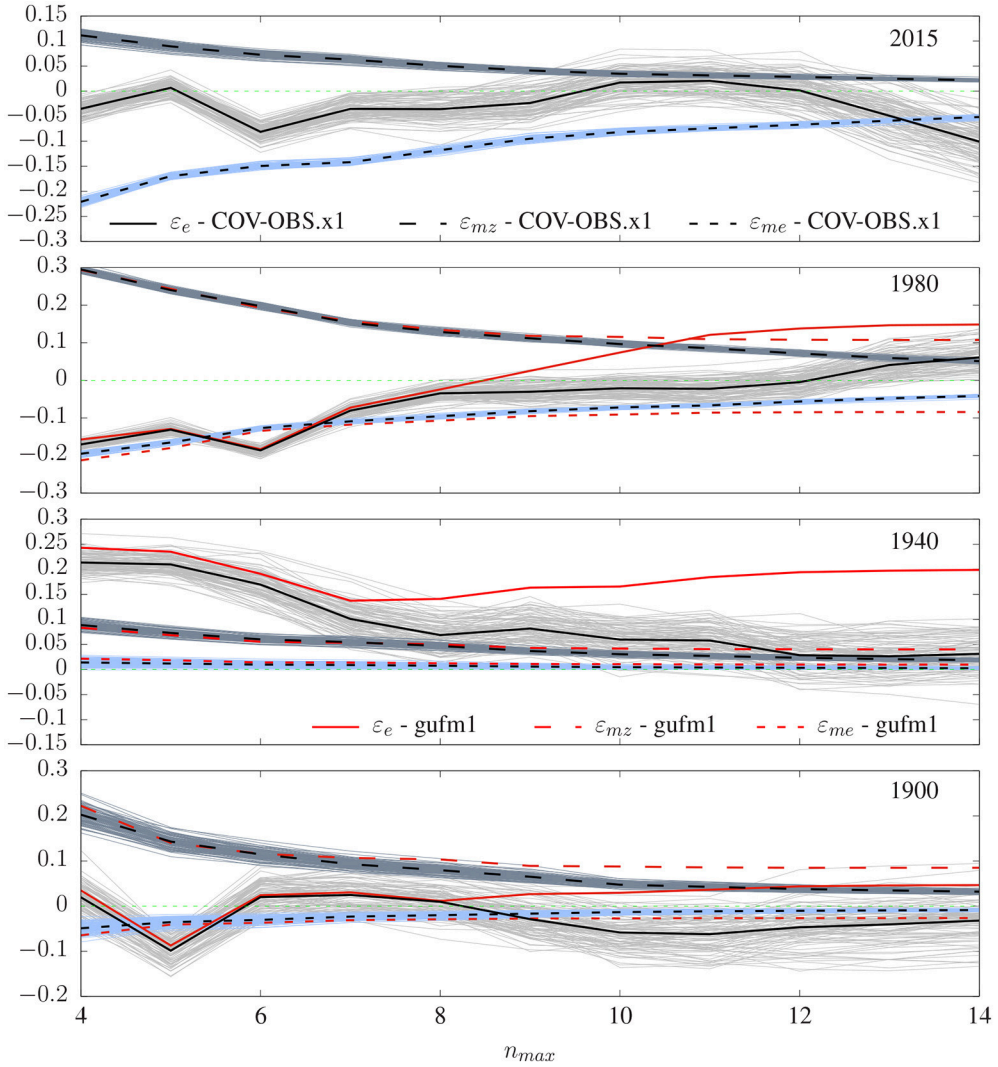

FIGURE 7 | Ratios ε_e (solid lines), ε_{mz} (dashed lines), and ε_{me} (dotted lines) as a function of n_{max} for four snapshots using gufm1 (red, Jackson et al., 2000) and the mean of COV-OBS.x1 (black, Gillet et al., 2015). The family of 100 COV-OBS.x1 models is presented in light, dark gray, and light blue lines for ε_e, ε_{mz} and ε_{me}, respectively. Green line denotes the zero value.

Amit and Christensen (2008), diffusion would always decrease the total magnetic energy. Inspection of **Figure 2** clearly shows that this is not the case. The total geomagnetic energy has increased for about a century. This proves that magnetic diffusion alone cannot explain the SV of the total geomagnetic energy.

However, can magnetic diffusion explain in part the $\dot{E}_b$ trend? Next, we assess numerically the role of magnetic diffusion. Amit and Christensen (2008) extrapolated the magnitude of the core's effective magnetic diffusivity to $\lambda^* = 100 - 1000$ m^2 s^{-1}, while the amount of diffusion in the solutions of Barrois et al. (2017) corresponds to $\lambda^* = 100 - 250$ m^2 s^{-1}. In **Figure 9** we compare the SV of the total geomagnetic energy vs. its diffusive contribution with a relatively low estimate of $\lambda^* = 100$ m^2 s^{-1}. Clearly, the trends are distinctive. In summary, based on the model of Amit and Christensen (2008), magnetic diffusion is unlikely the origin of the SV of the total geomagnetic energy.

4. DISCUSSION

In most cases ε_e is larger than ε_{mz} and ε_{me}, i.e., there are fewer cancellations in the integrand of the SV of the total geomagnetic energy. In some specific years, the ε_e curve crosses zero values in some models of the COV-OBS.x1 ensemble (Gillet et al., 2015). However, **Figure 6** clearly indicates that it is likely that there are fewer cancellations in the spatial contributions to the SV of the total geomagnetic energy than in those of the SV of the axial and equatorial dipole components.

Obviously, a geomagnetic field and SV model characterized by poor spatial resolution might bias the results. Sensitivity tests for the role of small-scale field and SV (**Figure 7**) demonstrate once again that if the geomagnetic field models over the last century are robust then the level of cancellations in the integrand of the SV of the total geomagnetic energy is in most cases comparable to

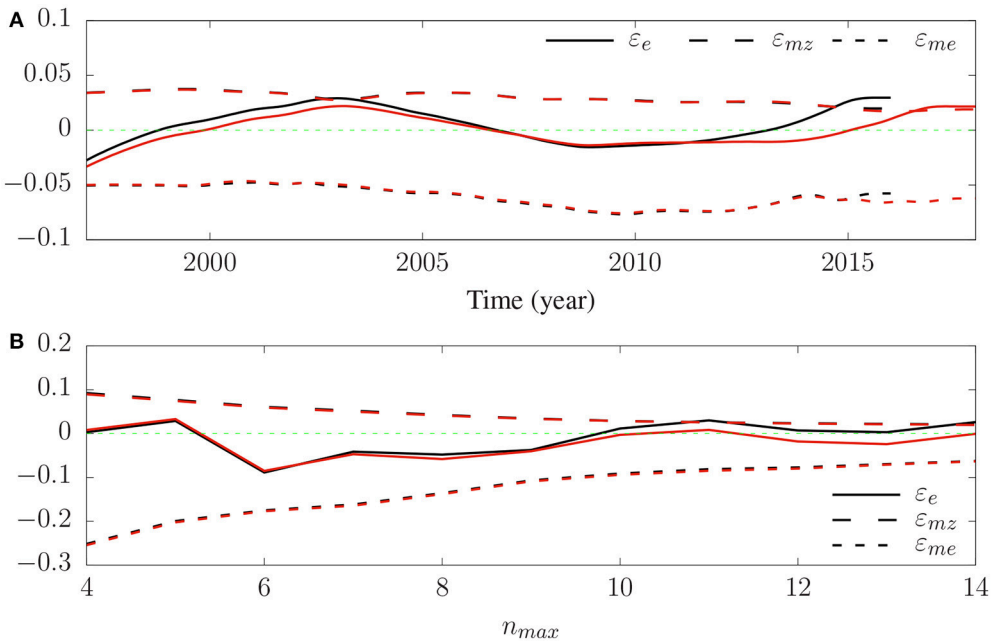

FIGURE 8 | The ratios ε_e (solid lines), ε_{mz} (dashed lines), and ε_{me} (dotted lines) for the models CHAOS-5 (black ; Finlay et al., 2015) and CHAOS-6 (red ; Finlay et al., 2016b) as a function of time for $n_{max} = 14$ **(A)** and as a function of n_{max} for the year 2015 **(B)**.

or smaller than the level of cancellations in the integrands of the SV of the axial and equatorial dipole components. An exception is the CHAOS-5 and CHAOS-6 field models which exhibit smallest cancellations in the integrand of the SV of the equatorial dipole (**Figure 8A**), but the short period covered by these models renders their interpretation statistically insignificant. The overall comparable or larger ε_e values are found in different field models, at most times and accounting for different small-scale contents. The latter test includes both the 100 models of COV-OBS.x1 (Gillet et al., 2015) as well as different truncations of field and SV models. For strongly truncated field and SV, dominance alternates in time among the three ε quantities. Asymptotic behavior with increasing n_{max} is encouraging. At present-day, according to the CHAOS-5 model (Finlay et al., 2015), the level of cancellations in the integrand of the SV of the total geomagnetic energy is comparable to that of the SV of the axial dipole, though the rapidly decelerating tilt results in the lowest level of cancellations for the SV of the equatorial dipole (**Figure 8**).

Interestingly, the evolution of m_e and ε_{me} exhibit similar trends, i.e., nearly constant until 1960 and rapidly decreasing since (see **Figures 3**, **6**; Amit and Olson, 2008; Amit et al., 2018). This transition in m_e could in principle be due to the same distribution of $\dot{\rho}_e$ but decrease in amplitude, or decrease in the level of cancellations. The first scenario involves no change in ε_{me}. We therefore conclude that the rapid tilt decrease since 1960 is related to genuine changes in the level of cancellations of $\dot{\rho}_e$.

Because the SV of the geomagnetic dipole is robust, we propose that the level of cancellations in its integrands can be considered as significant references. Our findings that the level of cancellations in the SV of the total geomagnetic energy is smaller than or comparable to those of the SV of the dipole components then indicates that the SV of the total geomagnetic energy is indeed non-zero. As we have shown, this supports the existence of upwelling/downwelling at the top of the core, in agreement with other inferences from the observed geomagnetic SV (Amit, 2014; Lesur et al., 2015).

The quantification of the effects of upwelling/downwelling at the top of the outer core is not trivial. In core flow inversions from geomagnetic SV the poloidal flow is usually coupled to the toroidal flow via some physical assumptions (e.g., Amit and Pais, 2013; Holme, 2015). Our formalism derived in section 2 may shed some light on the magnitude and size of upwelling/downwelling at the top of the core. The integrals of the SV of the total geomagnetic energy (3) and that of the kinetic to magnetic energy transfer (7) are identical. The associated integrands are not necessarily comparable. These integrals depend on the correlations between the various fields involved, which are reflected in the levels of cancellations. For example, if B_r and $\dot{B}_r$ are highly correlated or highly anti-correlated then ϵ_e will be close to unity, and conversely if B_r and $\dot{B}_r$ are nearly non-correlated then ϵ_e will approach zero. The same applies for the correlations between B_r^2 and the tangential divergence $\nabla_h \cdot \vec{u}_h$. However, because B_r^2 is positive and alternating upwelling/downwelling motions are present, it is likely that a similar high level of cancellations (or low correlations) appears in both. Assuming comparable integrands in (8) leads to the following evaluation for the magnitude of the tangential divergence

$$\delta_h \approx 2\frac{\dot{B}}{B} \tag{34}$$

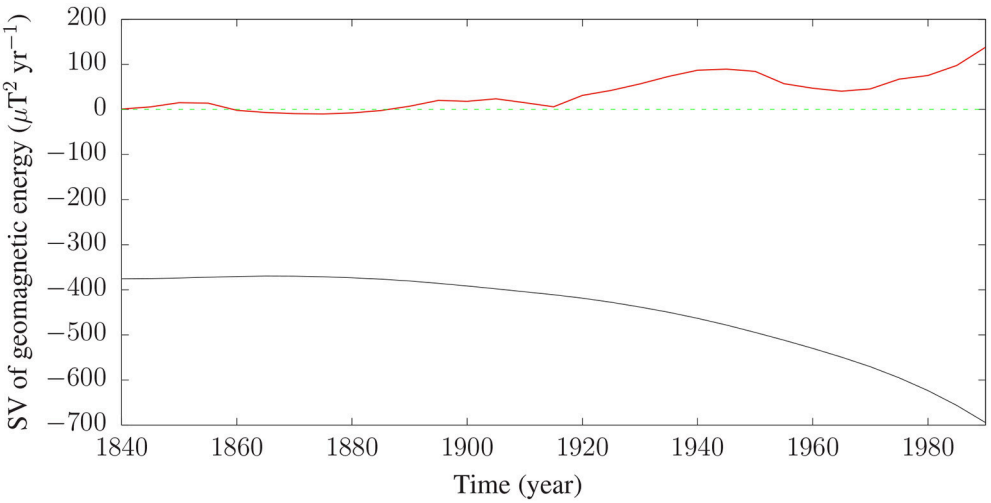

FIGURE 9 | The SV of the total geomagnetic energy on the CMB $\dot{E}_b$ as a function of time for gufm1 in the period 1840–1990 (red; Jackson et al., 2000) and its diffusive contribution with $\lambda^* = 100$ m^2 s^{-1} (black). The red line is the same as in **Figure 2**.

where B is a typical value of B_r, $\dot{B}$ is a typical value of $\dot{B}_r$ and δ_h is a typical upwelling/downwelling value. Using $\dot{B} \sim 2.5\ \mu$T yr^{-1} and $B \sim 320\ \mu$T we get an estimated tangential divergence of $\delta_h \sim 1.5$ century^{-1}, comparable to previous estimates (see Olson et al. (2018) and references therein). This estimate represents a typical value, which of course may exhibit significant spatial variability, in particular in the presence of non-uniform thermal boundary conditions. If the amplitude of the CMB heat flux heterogeneity is on the order of unity (e.g., Nakagawa and Tackley, 2008; Olson et al., 2017; Christensen, 2018), the spatial variability of the large-scale persistent upwelling pattern may then reach 3 century^{-1}. Next, the tangential divergence can be written as $\nabla_h \cdot \overrightarrow{u_h} \sim U_p/L$, where U_p is the magnitude of the poloidal flow and L is the length scale of the upwelling/downwelling. As mentioned above the poloidal flow is difficult to estimate. However, in most core flow models, the toroidal flow is dominant. Assuming that the poloidal flow is an order of magnitude smaller than the toroidal, for a typical large-scale flow of 10 km/yr^{-1} (Finlay and Amit, 2011), $U_p = 1$ km/yr^{-1} and the length scale of upwelling/downwelling is about 65 km, corresponding to spherical harmonic degree $\ell = 85$. Without a magnetic field, Takehiro and Lister (2001) showed that columnar convection larger than 100 km can penetrate a thick stratified layer, whereas the presence of a magnetic field decreases the length scale for penetration to be larger than 1 km (Takehiro, 2015). If the upwelling/downwelling motions are associated with turbulent global convection in the entire core, the timescale of mixing of a pre-existing stably stratified layer corresponds to the thickness of the stratified layer divided by the radial motion velocity, which gives at least 450 years for a 450 km thickness layer. Then, the existence of a stably stratified layer depends on the existence of regeneration mechanisms or that the upwelling/downwelling are associated with MAC waves which will not mix the stratified layer with the rest of the outer core.

What are the consequences of our study for the possibility of stratification at the top of the core? No upwelling/downwelling corresponds to stable stratification. However, the opposite is not necessarily true; The existence of upwelling/downwelling at the top of the core does not necessarily exclude a stratified layer. Radial flow may penetrate a stably stratified layer if the convection columns are large enough (Takehiro and Lister, 2001) or at quasi-geostrophic conditions (Vidal and Schaeffer, 2015). Another proposed scenario is MAC waves (Buffett, 2014; Buffett et al., 2016; Jaupart and Buffett, 2017). However, the poloidal flow associated with MAC waves is very large scale and zonal, in contrast to the small scale poloidal flow that is strongly linked to the complex toroidal flow pattern found in most core flow models inferred from the geomagnetic SV (Bloxham and Jackson, 1991; Amit and Olson, 2006; Amit and Pais, 2013; Barrois et al., 2017). Alternatively, magnetohydrodynamics simulations show that zonal flows could completely penetrate a stably stratified layer (Takehiro, 2015; Takehiro and Sasaki, 2018). Once again, a zonal flow penetrating a stably stratified layer also seems too simplistic to explain the geomagnetic SV. It therefore seems plausible that the existence of a deep stably stratified layer would correspond to no upwelling/downwelling at the top of the core, i.e., no temporal change in the total magnetic energy on the CMB (Alexakis et al., 2005a). We conclude that our results serve as geomagnetic evidence against a deep stably stratified layer at the top of the core which is consistent with the most recent seismic model arguing in favor of a fully adiabatic outer core (Irving et al., 2018).

In summary, we demonstrated that independently of the geomagnetic field model used (gufm1, CHAOS-5, CHAOS-6, COV-OBS.x1), the spatial distribution of sources and sinks of the SV of the total geomagnetic energy is either less balanced

than or as balanced as those of axial and equatorial dipole SV. The robustness of the geomagnetic dipole SV observations then indicates the existence of non-zero SV of the total geomagnetic energy. Because magnetic to magnetic energy transfer does not change the total geomagnetic SV (Huguet et al., 2016), kinetic to magnetic energy transfer should thus exist at the top of the core. Such a transfer relies on upwelling/downwelling motions at the top of the free stream. This suggests that a stratified layer at the top of the core is either shallow or destabilized by the e.g., lateral variability of CMB heat flux (Olson et al., 2017). Further exploration of the outer core using combined studies of geomagnetism, seismology, mineral physics, and numerical dynamos may shed light on the convective state of Earth's deep interior, in particular, the prospect of a stably stratified layer at the top of Earth's core.

AUTHOR CONTRIBUTIONS

LH and HA designed this study. LH ran the calculations. LH, HA, and TA discussed the results and wrote the paper.

FUNDING

LH was supported by NASA grants NNX15AH31G. HA was supported by the Centre National d'Études Spatiales (CNES) and by the program PNP of INSU.

ACKNOWLEDGMENTS

We thank Peter Olson and Maria L. Osete for their constructive reviews which helped to improve our paper.

REFERENCES

Alexakis, A., Mininni, P., and Pouquet, A. (2005a). Imprint of large-scale flows on turbulence. *Phys. Rev. Lett.* 93:264503. doi: 10.1103/PhysRevLett.95.264503

Alexakis, A., Mininni, P., and Pouquet, A. (2005b). Shell to shell energy transfer in MHD. I. Steady state turbulence. *Phys. Rev. E.* 72:046301.doi: 10.1103/PhysRevE.72.046301t

Alexakis, A., Mininni, P., and Pouquet, A. (2007). Turbulent cascades, transfer, and scale interactions in magnetohydrodynamics. *New J. Phys.* 9, 1–20. doi: 10.1088/1367-2630/9/8/298

Alexandrakis, C., and Eaton, D. W. (2010). Precise seismic-wave velocity atop Earth's core: No evidence for outer-core stratification. *Phys. Earth Planet. Inter.* 180, 59–65.doi: 10.1016/j.pepi.2010.02.011

Amit, H. (2014). Can downwelling at the top of the Earth's core be detected in the geomagnetic secular variation? *Phys. Earth Planet. Inter.* 229, 110–121. doi: 10.1016/j.pepi.2014.01.012

Amit, H., and Christensen, U. (2008). Accounting for magnetic diffusion in core flow inversions from geomagnetic secular variation. *Geophys. J. Int.* 175, 913–924. doi: 10.1111/j.1365-246X.2008.03948.x

Amit, H., Coutelier, M., and Christensen, U. R. (2018). On equatorially symmetric and antisymmetric geomagnetic secular variation timescales. *Phys. Earth Planet. Inter.* 276, 190 – 201. doi: 10.1016/j.pepi.2017.04.009

Amit, H., and Olson, P. (2006). Time-average and time-dependent parts of core flow. *Phys. Earth Planet. Inter.* 155, 120–139. doi: 10.1016/j.pepi.2005.10.006

Amit, H., and Olson, P. (2008). Geomagnetic dipole tilt changes induced by core flow. *Phys. Earth Planet. Inter.* 166, 226–238. doi: 10.1016/j.pepi.2008.01.007

Amit, H., and Olson, P. (2010). A dynamo cascade interpretation of the geomagnetic dipole decrease. *Geophys. J. Int.* 181, 1411–1427. doi: 10.1111/j.1365-246X.2010.04596.x

Amit, H., and Pais, M. A. (2013). Differences between tangential geostrophy and columnar flow. *Geophys. J. Int.* 194, 145–157.doi: 10.1093/gji/ggt077

Aubert, J., Amit, H., Hulot, G., and Olson, P. (2008). Thermo-chemical wind flows couple Earth's inner core growth to mantle heterogeneity. *Nature* 454, 758–761. doi: 10.1038/nature07109

Barrois, O., Gillet, N., and Aubert, J. (2017). Contributions to the geomagnetic secular variation from a reanalysis of core surface dynamics. *Geophys. J. Int.* 211, 50–68. doi: 10.1093/gji/ggx280

Barrois, O., Hammer, M., Finlay, C., Martin, Y., and Gillet, N. (2018). Assimilation of ground and satellite magnetic measurements: inferenceof core surface magnetic and velocity field changes. *Geophys. J. Int.* 215, 695–712. doi: 10.1093/gji/ggy297

Bloxham, J., and Jackson, A. (1991). Fluid flow near the surface of the Earth's outer core. *Rev. Geophys.* 29, 97–120. doi: 10.1029/90RG02470

Brodholt, J., and Badro, J. (2017). Composition of the low seismic velocity E' layer at the top of Earth's core. *Geophys. Res. Lett.* 44, 8303–8310. doi: 10.1002/2017GL074261

Buffett, B. (2014). Geomagnetic fluctuations reveal stable stratification at the top of the Earth's core. *Nature* 507, 484–487. doi: 10.1038/nature13122

Buffett, B., Knezek, N., and Holme, R. (2016). Evidence for MAC waves at the top of Earth's core and implications for variations in length of day. *Geophys. J. Int.* 204, 1789–1800. doi: 10.1093/gji/ggv552

Carati, D., Debliquy, O., Knaepen, B., Teaca, B., and Verma, M. (2006). Energy transfers in forced MHD turbulence. *J. Turb.* 7:51. doi: 10.1080/14685240600774017

Christensen, U. (2018). Geodynamo models with a stable layer and heterogeneous heat flow at the top of the core. *Geophys. J. Int.* 215, 1338–1351. doi: 10.1093/gji/ggy352

Christensen, U. R. (2006). A deep dynamo generating Mercury's magnetic field. *Nature* 444:1056. doi: 10.1038/nature05342

Christensen, U. R., Aubert, J., and Hulot, G. (2010). Conditions for earth-like geodynamo models. *Earth Planet. Sci. Lett.* 296, 487–496. doi: 10.1016/j.epsl.2010.06.009

de Koker, N., Steinle-Neumann, G., and Vlček, V. (2012). Electrical resistivity and thermal conductivity of liquid Fe alloys at high P and T, and heat flux in Earth's core. *Proc. Natl. Acad. Sci. U.S.A.* 109, 4070–4073. doi: 10.1073/pnas.1111841109

Debliquy, O., Verma, M. K., and Carati, D. (2005). Energy fluxes and shell-to-shell transfers in three-dimensional decaying magnetohydrodynamic turbulence. *Phys. Plas.* 12:042309. doi: 10.1063/1.1867996

Finlay, C. (2008). Historical variation of the geomagnetic axial dipole. *Phys. Earth Planet. Inter.* 170, 1–14. doi: 10.1016/j.pepi.2008.06.029

Finlay, C. and Amit, H. (2011). On flow magnitude and field-flow alignment at Earth's core surface. *Geophys. J. Int.* 186, 175–192. doi: 10.1111/j.1365-246X.2011.05032.x

Finlay, C. C., Aubert, J., and Gillet, N. (2016a). Gyre-driven decay of the Earth's magnetic dipole. *Nat. Commun.* 7:10422. doi: 10.1038/ncomms10422

Finlay, C. C., Olsen, N., Kotsiaros, S., Gillet, N., and Tøffner-Clausen, L. (2016b). Recent geomagnetic secular variation from Swarm and ground observatories as estimated in the CHAOS-6 geomagnetic field model. *Earth Plan. Space* 68:112. doi: 10.1186/s40623-016-0486-1

Finlay, C. C., Olsen, N., and Tøffner-Clausen, L. (2015). DTU candidate field models for IGRF-12 and the CHAOS-5 geomagnetic field model. *Earth Plan. Space* 67:114. doi: 10.1186/s40623-015-0274-3

Gillet, N., Barrois, O., and Finlay, C. C. (2015). Stochastic forecasting of the geomagnetic field from the COV-OBS. x1 geomagnetic field model, and candidate models for IGRF-12. *Earth Plan. Space* 67:71. doi: 10.1186/s40623-015-0225-z

Gillet, N., Jault, D., Finlay, C., and Olsen, N. (2013). Stochastic modeling of the Earth's magnetic field: Inversion for covariances over the observatory era. *Geochem. Geophys. Geosyst.* 14, 766–786. doi: 10.1002/ggge.20041

Gomi, H., Ohta, K., Hirose, K., Labrosse, S., Caracas, R., Verstraete, M. J., and Hernlund, J. W. (2013). The high conductivity of iron and thermal

evolution of the Earth's core. *Phys. Earth Plan. Inter.* 224, 88–103. doi: 10.1016/j.pepi.2013.07.010

Gubbins, D. (1987). Mechanism for geomagnetic polarity reversals. *Nature* 326, 167–169.

Gubbins, D. (1996). A formalism for the inversion of geomagnetic data for core motions with diffusion. *Phys. Earth Plan. Inter.* 98, 193–206.

Gubbins, D. and Davies, C. (2013). The stratified layer at the core-mantle boundary caused by barodiffusion of oxygen, sulphur and silicon. *Phys. Earth Plan. Inter.* 215, 21–28. doi: 10.1016/j.pepi.2012.11.001

Gubbins, D., Jones, A., and Finlay, C. (2006). Fall in Earth's magnetic field is erratic. *Science* 312, 900–902. doi: 10.1126/science.1124855

Helffrich, G., and Kaneshima, S. (2010). Outer-core compositional stratification from observed core wave speed profiles. *Nature* 468, 807–810. doi: 10.1038/nature09636

Holme, R. (2015). "8.04 - Large-Scale Flow in the Core,". in *Treatise on Geophysics (2nd Edition)*ed G. Schubert (Oxford:Elsevier), 91– 113.

Huguet, L., and Amit, H. (2012). Magnetic energy transfer at the top of the Earth's core. *Geophys. J. Int.* 190, 856–870. doi: 10.1111/j.1365-246X.2012.05542.x

Huguet, L., Amit, H., and Alboussière, T. (2016). Magnetic to magnetic and kinetic to magnetic energy transfers at the top of the Earth's core. *Geophys. J. Int.* 207, 934–948. doi: 10.1093/gji/ggw317

Irving, J. C., Cottaar, S., and Lekić V. (2018). Seismically determined elastic parameters for earths outer core. *Sci. Adv.* 4:eaar2538. doi: 10.1126/sciadv.aar2538

Jackson, A., Jonkers, A., and Walker, M. (2000). Four centuries of geomagnetic secular variation from historical records. *Phil. Trans. R. Soc. Lond.* A358, 957–990. doi: 10.1098/rsta.2000.0569

Jaupart, E., and Buffett, B. (2017). Generation of MAC waves by convection in Earth's core. *Geophys. J. Int.* 209, 1326–1336. doi: 10.1093/gji/ggx088

Kaneshima, S. (2018). Array analyses of SmKS waves and the stratification of Earth's outermost core. *Phys. Earth Plan Inter.* 276, 234–246. doi: 10.1016/j.pepi.2017.03.006

Kaneshima, S., and Helffrich, G. (2013). Vp structure of the outermost core derived from analysing large-scale array data of SmKS waves. *Geophys. J. Int.* 193, 1537–1555. doi: 10.1093/gji/ggt042

Konôpková Z., McWilliams, R. S., Gómez-Pérez, N., and Goncharov, A. F. (2016). Direct measurement of thermal conductivity in solid iron at planetary core conditions. *Nature* 534, 99–101. doi: 10.1038/nature18009

Labrosse, S. (2015). Thermal evolution of the core with a high thermal conductivity. *Phys. Earth Plan. Inter.* 247, 36–55. doi: 10.1016/j.pepi.2015.02.002

Landeau, M., Olson, P., Deguen, R., and Hirsh, B. H. (2016). Core merging and stratification following giant impact. *Nat. Geosci.* 9, 786–789. doi: 10.1038/ngeo2808

Lesur, V., Whaler, K., and Wardinski, I. (2015). Are geomagnetic data consistent with stably stratified flow at the core–mantle boundary? *Geophys. J. Int.* 201, 929–946. doi: 10.1093/gji/ggv031

Metman, M., Livermore, P., and Mound, J. (2018). The reversed and normal flux contributions to axial dipole decay for 1880"2015. *Phys. Earth Plan Inter.* 276, 106 – 117. doi: 10.1016/j.pepi.2017.06.007

Mininni, P., Alexakis, A., and Pouquet, A. (2005). Shell-to-shell energy transfer in magnetohydrodynamics. II. Kinematic dynamo. *Phys. Rev. E* 72:046302. doi: 10.1103/PhysRevE.72.046302

Mininni, P. D. (2011). Scale interactions in magnetohydrodynamic turbulence. *Ann. Rev. Fluid Mechan.* 43, 377–397. doi: 10.1146/annurev-fluid-122109-160748

Mound, J., Davies, C. J., Rost, S., and Aurnou, J. M. (2018). The apparent stratification at the top of earth's liquid core. *EarthArXiv*. doi: 10.31223/osf.io/dvfjp

Nakagawa, T. (2011). Effect of a stably stratified layer near the outer boundary in numerical simulations of a magnetohydrodynamic dynamo in a rotating spherical shell and its implications for Earth's core. *Phys. Earth Plan. Inter.*, 187, 342–352. doi: 10.1016/j.pepi.2011.06.001

Nakagawa, T., and Tackley, P. (2008). Lateral variations in CMB heat flux and deep mantle seismic velocity caused by a thermal-chemical-phase boundary layer in 3D spherical convection. *Earth Planet. Sci. Lett.* 271, 348–358. doi: 10.1016/j.epsl.2008.04.013

Ohta, K., Kuwayama, Y., Hirose, K., Shimizu, K., and Ohishi, Y. (2016). Experimental determination of the electrical resistivity of iron at Earth's core conditions. *Nature* 534, 95–98. doi: 10.1038/nature17957

Olsen, N., Mandea, M., Sabaka, T. J., and Tøffner-Clausen, L. (2009). CHAOS-2"a geomagnetic field model derived from one decade of continuous satellite data. *Geophys. J. Int.* 179, 1477–1487. doi: 10.1111/j.1365-246X.2009.04386.x

Olson, P., and Amit, H. (2006). Changes in earth's dipole. *Naturwissenschaften* 93, 519–542. doi: 10.1007/s00114-006-0138-6

Olson, P., Landeau, M., and Reynolds, E. (2017). Dynamo tests for stratification below the core-mantle boundary. *Phys. Earth Plan Inter.* 271, 1–18. doi: 10.1016/j.pepi.2017.07.003

Olson, P., Landeau, M., and Reynolds, E. (2018). Outer core stgh latitude structure of the geomagnetic field. Frontiers. *Front. Earth Sci.* 6:140. doi: 10.3389/feart.2018.00140

Peña, D., Amit, H., and Pinheiro, K. J. (2016). Magnetic field stretching at the top of the shell of numerical dynamos. *Earth Plan Space* 68:78. doi: 10.1186/s40623-016-0453-x

Poletti, W., Biggin, A. J., Trindade, R. I., Hartmann, G. A., and Terra-Nova, F. (2018). Continuous millennial decrease of the Earth's magnetic axial dipole. *Phys. Earth Plan Inter.* 274, 72–86. doi: 10.1016/j.pepi.2017.11.005

Pozzo, M., Davies, C., Gubbins, D., and Alfè D. (2012). Thermal and electrical conductivity of iron at Earth's core conditions. *Nature* 485, 355–358. doi: 10.1038/nature11031

Roberts, P., and Scott, S. (1965). On analysis of the secular variation, 1, A hydromagnetic constraint: Theory. *J. Geomagn. Geoelectr.* 17, 137–151.

Takehiro, S.-I. (2015). Penetration of alfvén waves into an upper stably-stratified layer excited by magnetoconvection in rotating spherical shells. *Phys. Earth Plan Inter.* 241, 37–43. doi: 10.1016/j.pepi.2015.02.005

Takehiro, S.-I., and Lister, J. R. (2001). Penetration of columnar convection into an outer stably stratified layer in rapidly rotating spherical fluid shells. *Earth Planet. Sci. Lett.* 187, 357–366. doi: 10.1016/S0012-821X(01)00283-7

Takehiro, S.-I., and Sasaki, Y. (2018). Penetration of steady fluid motions into an outer stable layer excited by mhd thermal convection in rotating spherical shells. *Phys. Earth Plan. Inter.* 276, 258-264. doi: 10.1016/j.pepi.2017.03.001

Tang, V., Zhao, L., and Hung, S.-H. (2015). Seismological evidence for a non-monotonic velocity gradient in the topmost outer core. *Sci. Rep.* 5:8613. doi: 10.1038/srep08613

Terra-Nova, F., Amit, H., Hartmann, G. A., and Trindade, R. I. (2015). The time dependence of reversed archeomagnetic flux patches. *J. Geophys. Res.* 120, 691–704. doi: 10.1002/2014JB011742

Vidal, J., and Schaeffer, N. (2015). Quasi-geostrophic modes in the Earth's fluid core with an outer stably stratified layer. *Geophys. J. Int.* 202(3):2182–2193. doi: 10.1093/gji/ggv282

Wardinski, I., and Holme, R. (2006). A time-dependent model of the Earth's magnetic field and its secular variation for the period 1980–2000. *J. Geophys. Res.* 111:B12101. doi: 10.1029/2006JB004401

Whaler, K. (1980). Does the whole of Earth's core convect? *Nature* 287, 528–530.

Whaler, K. (1986). Geomagnetic evidence for fluid upwelling at the core-mantle boundary. *Geophys. J. R. Astr. Soc.* 86, 563–588.

Whaler, K., and Holme, R. (2007). Consistency between the flow at the top of the core and the frozen-flux approximation. *Earth Plan. Space* 59, 1219–1229. doi: 10.1186/BF03352070

Williams, Q. (2018). The thermal conductivity of Earth's core: A key geophysical parameter's constraints and uncertainties. *Ann. Rev. Earth Plan. Sci.* 46, 47–66. doi: 10.1146/annurev-earth-082517-010154

Conflict of Interest Statement: The authors declare that the research was conducted in the absence of any commercial or financial relationships that could be construed as a potential conflict of interest.

frontiers in Earth Science

ORIGINAL RESEARCH
published: 01 October 2018
doi: 10.3389/feart.2018.00140

Outer Core Stratification From the High Latitude Structure of the Geomagnetic Field

Peter Olson[1,2]*, *Maylis Landeau*[3,4] *and Evan Reynolds*[1,5]

[1] Department of Earth and Planetary Sciences, Johns Hopkins University, Baltimore, MD, United States, [2] Department of Earth and Planetary Sciences, University of New Mexico, Albuquerque, NM, United States, [3] Department of Applied Mathematics and Theoretical Physics, Centre for Mathematical Sciences, University of Cambridge, Cambridge, United Kingdom, [4] Institut de Physique du Globe de Paris, Sorbonne Paris Cité, Université Paris-Diderot, Paris, France, [5] T-Mobile USA, Bellevue, WA, United States

The presence of stable stratification has broad implications for the thermal and compositional state of the outer core, the evolution of Earth's deep interior, and the energetics of the geodynamo. Yet the origin, strength, and depth extent of stratification in the region below the core-mantle boundary remain open questions. Here we compare magnetic fields produced by numerical dynamos that include heterogeneous stable thermal stratification below their outer boundary with models of the geomagnetic field on the core-mantle boundary, focusing on high latitude structures. We demonstrate that the combination of high magnetic field intensity regions and reversed magnetic flux spots, especially at high latitudes, constrains outer core stratification below the core-mantle boundary. In particular, we find that the negative contribution to the axial dipole from reversed flux spots is a strong inverse function of the stratification. Comparison of our numerical dynamo results to the structure of the historical geomagnetic field suggests up to 400 km of permeable, laterally heterogeneous thermal stratification below the core-mantle boundary.

Keywords: thermally stratified dynamos, outer core stratification, core-mantle boundary, core heat flux, geomagnetic field

OPEN ACCESS

Edited by:
Hagay Amit,
University of Nantes, France

Reviewed by:
Maurits Cornelis Metman,
University of Leeds, United Kingdom
Binod Sreenivasan,
Indian Institute of Science, India

***Correspondence:**
Peter Olson
olson@jhu.edu

Specialty section:
This article was submitted to Geomagnetism and Paleomagnetism, a section of the journal Frontiers in Earth Science

Received: *28 May 2018*
Accepted: *05 September 2018*
Published: *01 October 2018*

Citation:
Olson P, Landeau M and Reynolds E (2018) Outer Core Stratification From the High Latitude Structure of the Geomagnetic Field. Front. Earth Sci. 6:140. doi: 10.3389/feart.2018.00140

1. INTRODUCTION

Stable stratification at the top the outer core has been inferred using both seismic and geomagnetic data, typically with divergent results. Some investigations find that the stratification is limited to a layer extending 100–200 km below the core-mantle boundary (Whaler, 1980; Lay and Young, 1990; Garnero et al., 1993; Gubbins, 2007; Tanaka, 2007; Buffett, 2014). However, other studies indicate the stratification extends to greater depths—300 km (Helffrich and Kaneshima, 2010) and possibly deeper (Gomi et al., 2013; Tang et al., 2015; Kaneshima, 2017), while still others find little evidence for stratification (Irving et al., 2018). Interpretations of the source of the stratification include stable (subadiabatic) thermal stratification (Gomi et al., 2013; Buffett et al., 2016) as well as stable compositional stratification due to anomalous light element concentrations (Gubbins and Davies, 2013; Helffrich and Kaneshima, 2013; Brodholt and Badro, 2017).

This raises multiple questions for the dynamics of the core. First, is the outer core stratification inferred by recent seismic studies compatible with the geomagnetic field and its secular variation? Core flow inversions based on the geomagnetic secular variation are best accommodated by including upwelling and downwelling motions extending very close to the core-mantle boundary (Gubbins, 2007; Amit, 2014; Lesur et al., 2015; Huguet et al., 2016). For example, Gubbins (2007)

argued that the production of reversed flux spots on the core-mantle boundary, which are rapidly evolving in the present-day geomagnetic field (Olson and Amit, 2006; Olsen et al., 2014; Terra-Nova et al., 2015; Metman et al., 2018), limits the depth extent of the stratification to less than 150 km, assuming no radial motion in that layer and that the reversed flux spots on the core-mantle boundary result from the expulsion of magnetic flux from the outer core.

Second, can numerical dynamos provide independent constraints on the strength and depth extent of the stratification? There are relatively few systematic investigations of the geodynamo in the presence of stratification (Sreenivasan and Gubbins, 2008; Nakagawa, 2011, 2015; Olson et al., 2017; Christensen, 2018). However, stratification effects have been extensively studied in the context of the solar dynamo (e.g., Browning et al., 2006, 2007; Käpylä et al., 2008; Tobias et al., 2008; Brummell et al., 2010; Masada et al., 2013), Jupiter (Zhang and Schubert, 2000), Saturn (Christensen and Wicht, 2008; Stanley, 2010), and also Mercury (Christensen, 2006; Manglik et al., 2010). All these investigations found that the presence of a stratified layer affects the morphology of the magnetic field. In particular, a stratified layer below a convective region is key to generating a large-scale magnetic field in solar dynamo simulations (Browning et al., 2006, 2007; Käpylä et al., 2008), where strong zonal flows in the stratified layer stretch the poloidal magnetic field in the convective region into a large-scale toroidal magnetic field through an ω-effect. Other investigations have reported the generation of strong azimuthal flows within a stratified layer adjacent to a convective region (Zhang and Schubert, 2000; Takehiro and Lister, 2002; Couston et al., 2018), which attenuate high-frequency, non-axisymmetric magnetic field components in the stratified layer (Christensen, 2006; Christensen and Wicht, 2008; Stanley, 2010).

Because stratification affects the magnetic field structure, dynamo simulations are useful in constraining the stratification in Earth's core. In a previous paper (Olson et al., 2017) we conducted a systematic investigation of the flow and the time average magnetic field in the presence of thermal stratification. We showed that the high latitude structures of the time average magnetic fields in numerical dynamos are sensitive to the strength and depth extent of thermal stratification below the dynamo upper boundary. This sensitivity offers the means to infer the properties of stratification below the core-mantle boundary (CMB) in terms of the time average structure of the geomagnetic field. In this paper we quantitatively compare the high latitude CMB structure of the COV-OBS geomagnetic field model (Gillet et al., 2013) to a suite of thermally stratified numerical dynamos. Extending the analysis in Olson et al. (2017), we compute the correlation of the high latitude structures of the time average magnetic field in the COV-OBS model and in our numerical dynamos. In addition, we analyze the time varying field, focusing on the effects of reversed flux spots on the axial dipole. These comparisons favor the existence of stratification below the CMB but also indicate that substantial radial motions are present there, implying that the stratification is rather weak and permeable to outer core convection.

2. NUMERICAL DYNAMOS WITH THERMAL STRATIFICATION BELOW THE OUTER BOUNDARY

The stratification analyzed in this study is due to thermal gradients that deviate from adiabatic (i.e., uniform entropy) conditions and are maintained by the heat flux imposed at the outer boundary. We include lateral variations of the boundary heat flux, following the results of mantle global circulation models (Nakagawa and Tackley, 2013, 2015; Zhong and Rudolph, 2015) that yield vigorous deep mantle convection with locally variable heat flux on the core-mantle boundary that is large enough in some places to sustain unstable thermal stratification (Olson et al., 2015), even if the thermal conductivity of the outer core is high (Ohta et al., 2016).

We model stratified thermochemical convection in the outer core with heterogeneous heat flux at the CMB using the formulation in Olson et al. (2017). Outer core density variations are expressed in terms of the codensity, i.e., density variations due to the combination of temperature and light element concentration variations:

$$C = \rho_o \left(\alpha T + \beta \chi\right), \tag{1}$$

where ρ_o is fluid mean density, T is temperature relative to the adiabat with mean T_o, χ is the fluid light element concentration with mean χ_o, and α and β are volumetric expansion coefficients for T and χ, respectively. In terms of these, the governing equations for thermochemical convection and dynamo action in a rotating spherical shell (with the Boussinesq approximation) include the following dimensionless control parameters:

$$E = \frac{\nu}{\Omega D^2}; \quad Pr = \frac{\nu}{\kappa}; \quad Pm = \frac{\nu}{\eta}; \quad \epsilon = -\left(1 + \frac{\alpha \dot{T}_o}{\beta \dot{\chi}_o}\right). \tag{2}$$

Here E is the Ekman number, Pr is the Prandtl number, Pm is the magnetic Prandtl number, and ϵ is the volumetric codensity source. In (2), Ω denotes angular velocity of rotation, $D = r_o - r_i$ is the depth of the fluid shell, r_o and r_i, the radii of the inner and outer fluid boundaries, with ν, η, and κ denoting kinematic viscosity, magnetic diffusivity, and codensity diffusivity, respectively.

At the inner boundary r_i we assume no-slip velocity conditions and a uniform codensity C_i. At the outer boundary we also assume no-slip velocity conditions, zero light element flux, and we specify the heat flux q to be the sum of a spherical mean part (denoted by an overbar) and a deviation from the spherical mean (denoted by a prime):

$$q = \bar{q} + q'(\phi, \theta), \tag{3}$$

where ϕ and θ are longitude and colatitude, respectively, and $\bar{q}$ is measured relative to the heat flux down the adiabat, with $\bar{q} > 0$ being superadiabatic heat flux and $\bar{q} < 0$ being subadiabatic heat flux. This formulation yields three additional dimensionless

parameters that control the convection: a Rayleigh number based on the rate of increase of light element concentration in the fluid

$$Ra = \left(\frac{\beta g D^5}{\nu^2 \kappa}\right) \dot{\chi}_o, \tag{4}$$

a second Rayleigh number based on the spherical mean heat flux at the outer boundary

$$Ra_{\bar{q}} = -\left(\frac{\alpha g D^4}{k \nu \kappa}\right) \bar{q}, \tag{5}$$

and a third Rayleigh number based on the peak-to-peak variation $\Delta q'$ of the laterally varying boundary heat flux

$$Ra_{q'} = \left(\frac{\alpha g D^4}{k \nu \kappa}\right) \Delta q'. \tag{6}$$

In (4-6), g is gravity at the outer boundary and k is thermal conductivity. In the numerical dynamos, the factors $D^2 \rho_o \beta \dot{\chi}_o / \nu$ and $\sqrt{\rho_o \Omega / \sigma}$ (where σ is electrical conductivity) non-dimensionalize codensity variations and magnetic field intensity, respectively, and ν/D non-dimensionalizes the fluid velocity. In what follows, we retain these scalings for codensity and magnetic field, but we use η/D to scale the fluid velocity. With these factors, the scaling for velocity and magnetic field intensities are referred to as magnetic Reynolds number and Elsasser number units, respectively.

In Olson et al. (2017) we introduced a parameter describing the spherical mean stratification:

$$S = \frac{Ra_{\bar{q}}}{Ra} = -\left(\frac{\alpha \nu}{\beta D k \dot{\chi}_o}\right) \bar{q}, \tag{7}$$

defined to be positive when $\bar{q}$ is negative, i.e., when the spherical mean boundary heat flux is stabilizing. There is also a related stratification parameter describing the effects of the boundary heat flux heterogeneity:

$$S' = \frac{Ra_{q'}}{Ra}. \tag{8}$$

We analyze dynamos with $E = 10^{-4}$, $Pr = 1$, $Pm = 6$, and $\epsilon = -0.8$, the latter appropriate for dominantly compositional convection but with some secular cooling included. The aspect ratio of the fluid shell is fixed at $r_i/r_o = 0.351$. The solid region $r \leq r_i$ representing the inner core is assumed to have the same electrical conductivity as the fluid, and the solid region $r \geq r_o$ representing the mantle is assumed to be electrically insulating. The boundary heat flux pattern is defined by a spherical mean part plus a heterogeneous part consisting mostly of spherical harmonic degree $\ell = 2$ components at orders $m = 0$ and $m = 2$, adjusted so as to produce a pattern with nearly bilateral (i.e., 2-fold) azimuthal symmetry. The resulting boundary heat flux pattern is shown in **Figure 1A** and corresponds to the largest scale of lower mantle heterogeneity structure determined by Dziewonski et al. (2010). It is basically the same planform used by Olson and Amit (2015) in their study of the influences of lower mantle piles on magnetic polarity reversal behavior.

Dynamo calculations are made at $Ra = 6 \times 10^7$ and $Ra = 9 \times 10^7$ for stratification parameters S ranging from -0.1, corresponding to superadiabatic CMB heat flux, to +0.3, corresponding to strongly subadiabatic CMB heat flux, using the MAGIC dynamo code (Wicht, 2002). We assume a constant value of $S' = 0.58$ for all cases. We find that by preserving S', key properties of these dynamos such as the r.m.s. dipole axis tilt are nearly independent of S, while other properties such as the contribution of reversed flux to the axial dipole are relatively insensitive to Ra. We use a numerical grid with $(n_r, n_\theta, n_\phi) = (81, 128, 256)$ in the fluid shell and spherical harmonic truncation $(\ell, m)_{max} = 85$. All the calculations were run for at least one magnetic diffusion time, in order that the run averages approximate true time averages.

3. STRATIFICATION DIAGNOSTICS

For comparison with the geomagnetic field, we focus on properties of the dynamo magnetic field structures, particularly at high latitudes. Previously, Olson et al. (2017) found that the high latitude dynamo magnetic fields are especially sensitive to stratification beneath the outer boundary, and the effects of stratification produce distinct and readily identifiable structures, both inside the tangent cylinder of the inner core and beyond, down to latitudes of approximately 45^o. In contrast, some dynamo magnetic field structures at low latitudes are not so easily related to stratification. Accordingly, most of our comparisons between numerical dynamos and the geomagnetic field are based on the variable $B_r \cos(\theta)$, where θ is colatitude, which is the kernel of the axial dipole moment density on the CMB (Olson and Amit, 2006). For our applications, $B_r \cos(\theta)$ is superior to the radial component of the magnetic field B_r because the $\cos(\theta)$ factor adds weight to the high latitude field structure.

We characterize our numerical dynamos in terms of the structure of $B_r \cos(\theta)$ on the outer boundary, along with the magnitude of the stratification and the upwelling below the outer boundary. One important diagnostic is the ratio of reversed to normal polarity flux on the outer boundary. The two individual contributors to this ratio are given by

$$F^N = \int B_r^N \cos(\theta) dA; \quad F^R = \int B_r^R \cos(\theta) dA \tag{9}$$

where the superscripts N and R denote the signs of B_r (positive or negative) that define the dominant and the subordinate components, respectively, of the axial dipole moment, and A is the outer boundary surface area. The ratio of these two fluxes

$$F^* = |F^R / F^N| \tag{10}$$

is defined so that $0 \leq F^* \leq 1$, the lower limit indicating zero contribution to the axial dipole moment from reversed flux, the upper limit corresponding to a vanishingly small axial dipole. Another magnetic diagnostic we use is the distribution of high latitude, high intensity $B_r \cos(\theta)$-structures. Our previous

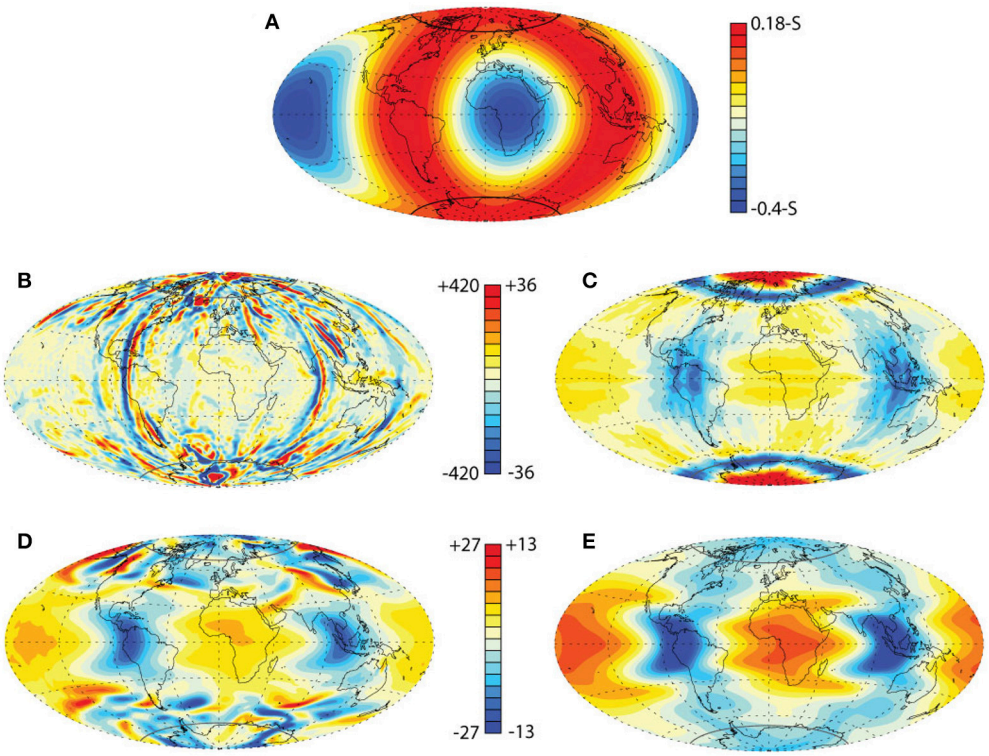

FIGURE 1 | Numerical dynamo heat flux and radial velocities near the outer boundary r_O at $Ra = 9 \times 10^7$. **(A)** is the dimensionless heat flux imposed on the outer boundary; **(B–E)** are $r = 0.95r_O$ dimensionless radial velocity patterns. **(B,C)** are a snapshot and time average radial velocity for stratification parameter $S = 0$; **(D,E)** are a snapshot and time average radial velocity for stratification parameter $S = 0.3$. Maximum and minimum dimensionless outer boundary heat fluxes are 0.18-S and –0.4-S, respectively. Velocity scales are in magnetic Reynolds number units.

study (Olson et al., 2017) documented that the morphology of high latitude, high intensity B_r-structures in time average dynamo magnetic fields can be used to constrain the stratification parameter S. In the next sections we demonstrate that $B_r \cos(\theta)$ is even more sensitive to S, both in snapshots and in time averages.

We measure the stratification in our numerical dynamos using the spherical mean thickness of the stratified region and its gravitational stability. The dimensionless spherical mean thickness of the stratified region of the dynamo is defined as

$$\delta^* = \frac{r_o - r_{min}}{r_o} \tag{11}$$

where r_{min} is the radius where the dimensionless spherical mean codensity $\bar{C}^*$ reaches its local minimum value below the outer boundary. Likewise, we define the gravitational stability of the stratified layer in terms of the dimensionless buoyancy frequency squared:

$$N^{*2} = \frac{\delta C^*}{\delta^*}, \tag{12}$$

where $\delta C^* = \bar{C}^*{}_o - \bar{C}^*{}_{min}$ is the dimensionless codensity increase across the stratified region. In Olson et al. (2017) we derived the following scaling laws for these quantities:

$$\delta^* = a_\delta S^{b_\delta} \tag{13}$$

in which $(a_\delta, b_\delta) = (1.82, 1.2)$, plus

$$N^{*2} = a_N S^{b_N} \tag{14}$$

in which $(a_N, b_N) = (0.72, 1)$. Lastly, the r.m.s. upwelling strength below the outer boundary is used to characterize the effects of stratification on the flow. We define the dimensionless outer boundary (or CMB) upwelling strength as

$$W^* = |\nabla_H \cdot \mathbf{u}| \tag{15}$$

where ∇_H and $\mathbf{u}$ are the dimensionless horizontal divergence and the fluid velocity, respectively, and || denotes r.m.s. average over the spherical shell at $0.95r_o$.

4. DYNAMOS WITH STRATIFICATION

Figure 1 shows the pattern of heat flux applied to the outer dynamo boundary and the resulting radial velocity pattern from two dynamos with $Ra = 9 \times 10^7$ but different amounts of stratification. **Figure 1A** shows the nearly bilaterally symmetric boundary heat flux in dimensionless form, with a great circle of elevated heat flux that includes both polar regions, separating two large, low latitude regions with reduced heat flux. The reduced heat flux regions correspond approximately to the Large

Low Shear Velocity Provinces (LLSVPs) imaged by seismic tomography (Garnero and McNamara, 2008) and the elevated heat flux band approximately corresponds to the high shear velocity regions at the base of the mantle. **Figures 1B,C** show a snapshot and the time average radial velocity at a depth of $0.05r_o$ below the outer boundary, for stratification parameter $S = 0$. **Figures 1D,E** are a snapshot and the time average radial velocity at the same depth for stratification parameter $S = 0.3$. The radial velocities are in dimensionless (magnetic Reynolds number) units.

In the snapshots, the effects of stratification are most evident in the difference in magnitude of the radial velocities. In the $S = 0$ dynamo, dimensionless radial velocities in **Figure 1B** exceed 400 in places, with an r.m.s. at this depth of approximately 180. In the $S = 0.3$ dynamo, in contrast, dimensionless radial velocities in **Figure 1D** nowhere exceed 30, and the r.m.s. at this depth is approximately 9. Clearly, the stabilizing effects of the boundary heat flux suppress the radial velocity below the outer boundary, reducing the r.m.s. strength of upwellings and downwellings there by a nearly a factor of 20 between the two cases.

The strong reduction in radial velocity caused by stratification that is seen in the snapshots is less extreme in the time averages in **Figures 1C,E**. Overall, the patterns of radial velocity are more similar in these time averages compared to their corresponding snapshots, because the boundary heat flux heterogeneity plays a relatively greater role in structuring the time average velocities. The greatest differences between the two dynamos in terms of their time average radial velocities are found at high latitudes. In the $S = 0$ dynamo, there are strong polar upwellings and strong downwellings along the inner core tangent cylinder in both hemispheres (**Figure 1C**), structures that are missing from the strongly stratified $S = 0.3$ dynamo (**Figure 1E**).

Figure 2 shows snapshots and time averages of the radial magnetic field intensity on the outer boundary at $Ra = 9 \times 10^7$ for stratification parameter S varying between 0 and 0.3. Unlike

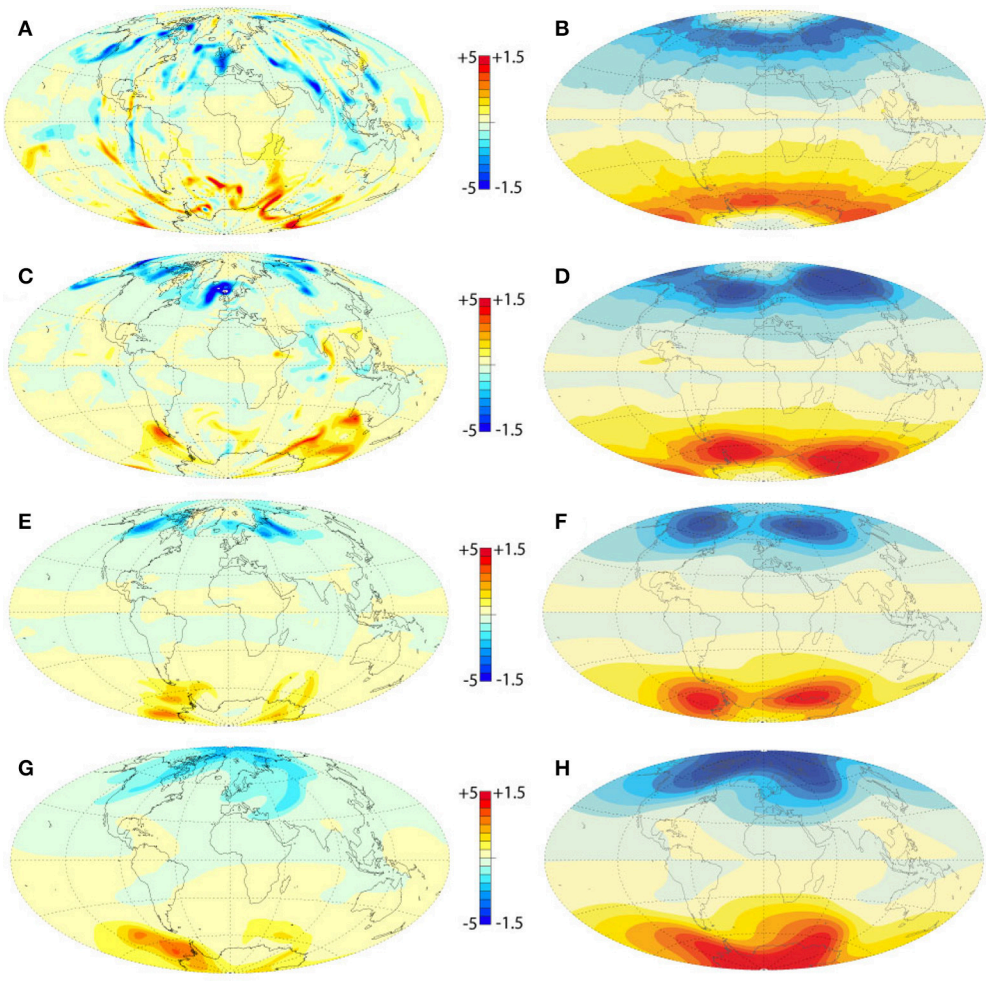

FIGURE 2 | Numerical dynamo radial magnetic field intensity B_r at the outer boundary and $Ra = 9 \times 10^7$ for different stratification parameters S. **(A,B)** Snapshot and time average fields for $S = 0$; **(C,D)** Snapshot and time average fields for $S = 0.1$; **(E,F)** Snapshot and time average fields for $S = 0.2$; **(G,H)** Snapshot and time average fields for $S = 0.3$. Magnetic field intensities are in dimensionless Elsasser number units.

the radial velocity, for which the amplitude of the upwellings and downwellings show the strongest influence of stratification, the magnetic field on the outer boundary mainly responds to the stratification through changes in its structure, rather than its amplitude. For example, in the snapshot field structures in **Figure 2** there is a progressive reduction in the number and the intensity of reversed flux spots with increasing S, such that the $S = 0.3$ dynamo snapshot (**Figure 2G**) is entirely lacking in reversed flux at high latitudes in both hemispheres, yet the overall magnetic field intensity barely changes with S.

The other expression of structural change at high latitudes is seen in the time average field structures. In the $S = 0$ and $S = 0.1$ dynamos (**Figures 2B,D**) the high latitude structure consists of rings of high intensity field located near the tangent cylinder surrounding deep intensity minima, with localized reversed flux at the poles. In the $S = 0.2$ dynamo (**Figure 2F**) the polar minima are gone and the high intensity field is localized in patches, two in each hemisphere. Lastly, in the strongly stratified $S = 0.3$ case (**Figure 2H**) the two patches in each hemisphere have merged into a single high intensity lobe, positioned such that there is a field intensity maximum located at each pole.

The trends in the time average magnetic field structure in **Figure 2** can be explained in terms of the changes in the internal dynamo structure with increasing stratification. **Figure 3** compares the azimuthally averaged structure of $Ra = 9 \times 10^7$ dynamos with $S = 0$ and $S = 0.3$, respectively. The internal structure of the $S = 0$ dynamo (**Figures 3A–C**) includes an adverse (i.e., destabilizing) codensity gradient, strong thermal wind circulations with meridional overturning inside the tangent cylinder in both hemispheres, and low magnetic field intensity near the outer boundary inside the tangent cylinder, locally reversed at each pole. The polar reversed flux, the low field intensity inside the tangent cylinder, and the high intensity field along the tangent cylinder, can be explained in this dynamo in terms of incomplete flux expulsion by the meridional circulations inside each tangent cylinder region. This circulation advects the poloidal magnetic field away from the poles and concentrates it along the tangent cylinder, producing the high latitude pattern seen in **Figure 2B**. In contrast, the azimuthally averaged internal structure of the $S = 0.3$ dynamo (**Figures 3D–F**) includes stable stratification below the outer boundary at all latitudes, a two-layer meridional circulation pattern at low and middle latitudes, and reversed circulations inside the tangent cylinder that exchange fluid with the meridional circulations outside. The meridional circulations inside the tangent cylinder region include polar downwellings that produce horizontal convergence beneath the outer boundary. These circulations concentrate poloidal magnetic flux close to the pole, producing polar intensity maxima in both hemispheres, as seen in **Figure 2H**.

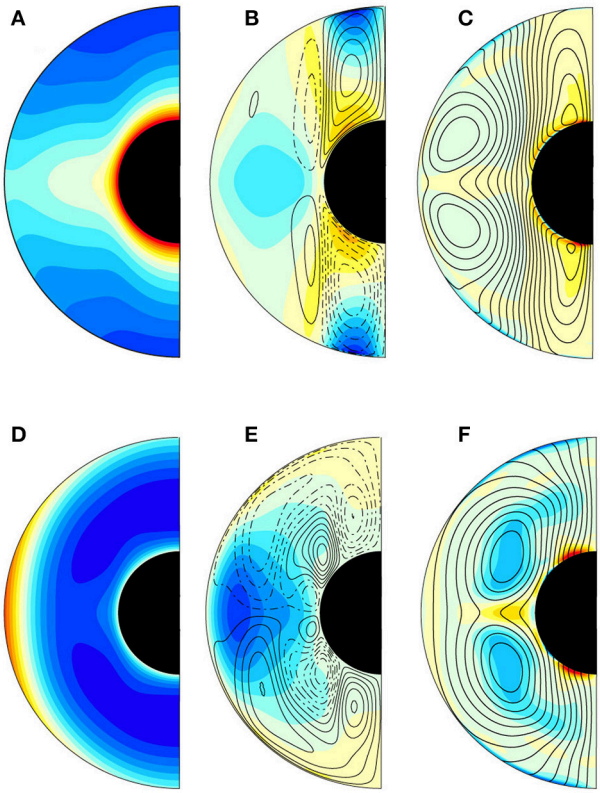

FIGURE 3 | Zonal average numerical dynamo structures at $Ra = 9 \times 10^7$ for two stratification parameters: $S = 0$ **(A–C)** and $S = 0.3$ **(D–F)**. Images **(A,D)** show codensity contours; images **(B,E)** show meridional circulation streamlines (clockwise=dashed; counterclockwise=solid) over azimuthal velocity contours; images **(C,F)** show poloidal magnetic field lines over azimuthal electric current contours, all dimensionless. Red contours=positive, blue=negative.

5. COMPARISONS WITH THE GEOMAGNETIC FIELD AT THE CMB

Figure 4 shows $B_r \cos(\theta)$ on the core-mantle boundary from the COV-OBS geomagnetic field model (Gillet et al., 2013; http://www.spacecenter.dk/files/magnetic-models/COV-OBS/COV-OBS-int.txt). **Figures 4A,B** are Northern and Southern hemisphere images at epoch 2014, whereas **Figures 4C,D** are 1840–2014 time averages for the Northern and Southern hemispheres, respectively. Data sources for this geomagnetic field model include space-borne magnetometer measurements during low altitude satellite orbits plus annual means from ground-based observatories. The COV-OBS core field is represented at epochs spaced 2 years apart, and is complete to spherical harmonic degree and order 14. We treat **Figures 4A,B** as snapshots of the present-day core field, for comparison with our dynamo snapshots. The maps of $B_r \cos(\theta)$ in **Figures 4C,D** are averages over 88 epochs, but their 174 year time span is far shorter than the averaging times in our dynamos, which are of the order of a few hundred thousand years. Nevertheless, in what follows we treat the geomagnetic field average as a true time average for purposes of comparison with the dynamo averages.

Figure 5 shows snapshots and time averages of $B_r \cos(\theta)$ from numerical dynamos at $Ra = 6 \times 10^7$ for stratification parameters ranging from $S = -0.1$, corresponding to a superadiabatic thermal gradient at the CMB, to $S = 0.3$, corresponding to a strongly subadiabatic thermal gradient at the CMB.

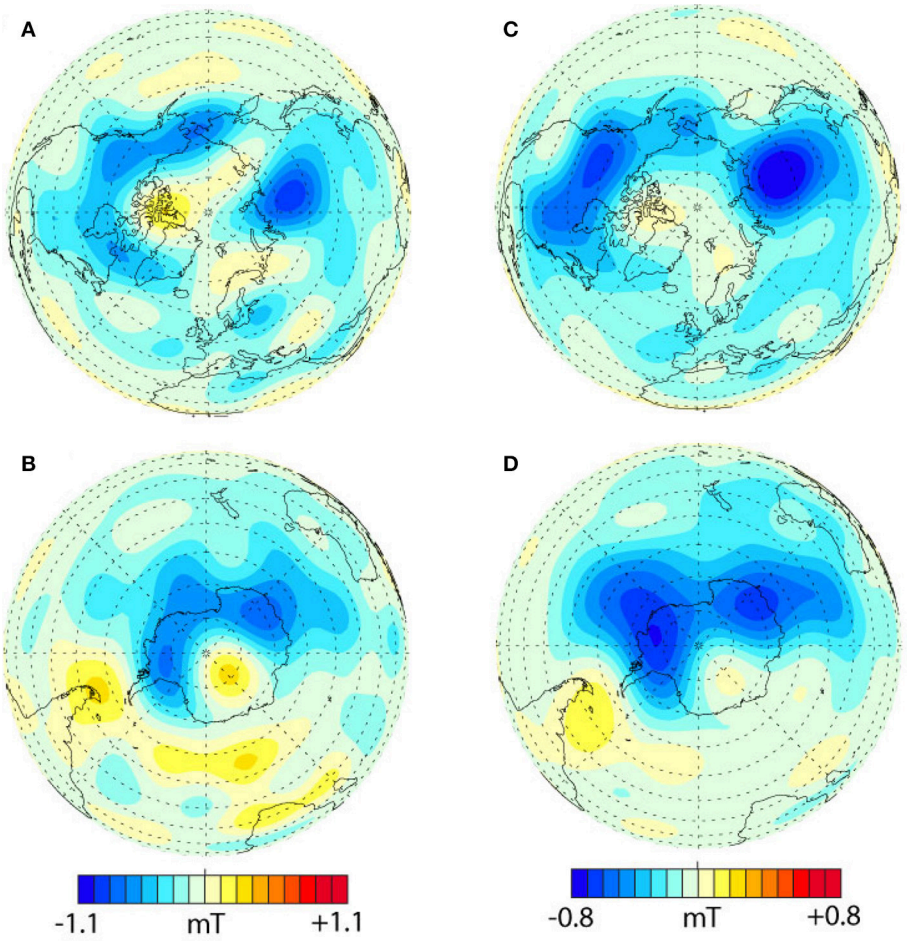

FIGURE 4 | $B_r \cos(\theta)$ on the core-mantle boundary from the COV-OBS geomagnetic field model (Gillet et al., 2013). **(A,B)** are Northern and Southern hemisphere snapshots, respectively, at epoch 2014; **(C,D)** are 1840-2014 time averages of the Northern and Southern hemispheres, respectively. Contours are in millitesla, mT.

The top row of maps in **Figure 5** are Northern hemisphere $B_r \cos(\theta)$ snapshots, the middle row are Southern hemisphere snapshots at the same times, and the bottom row are Northern hemisphere time averages. Southern hemisphere time averages differ insignificantly from their northern counterparts and are not shown.

The top and middle rows in **Figure 5** show the same qualitative trends as in **Figure 2** in terms of the disappearance of reversed flux with increasing stratification parameter. To demonstrate this quantitatively, **Figure 6** shows F^*, the ratio of reversed to normal flux defined by Equations (9) and (10) vs. stratification parameter S, for the $Ra = 6 \times 10^7$ dynamos in **Figure 5** and the $Ra = 9 \times 10^7$ dynamos in **Figure 2**. The error bars indicate the standard deviation of F^* based on six to eight snapshots from each dynamo. Although there is some dependence on the Rayleigh number at $S = 0$ and $S = -0.1$, the reversed to normal flux ratios at both Rayleigh numbers decrease strongly with increasing S, rapidly converging toward zero at larger S. Reversed flux patches are generally non-axisymmetric structures. Therefore, this decrease in F^* with increasing S agrees with previous studies that found that stratification removes not only reversed flux (Sreenivasan and Gubbins, 2008), but also other non-axisymmetric components of the magnetic field (Christensen, 2006; Christensen and Wicht, 2008; Stanley, 2010). We also show in **Figure 6** the reversed to normal flux ratio on the CMB from the Gillet et al. (2013) COV-OBS geomagnetic field model at epoch 2014. Dynamos with $S = 0.1$ best match the present-day geomagnetic field structure in terms of the relative contribution of reversed flux to the axial dipole.

There are several important differences between the numerical dynamos and the core field model that need to be factored out in order to make the comparison in **Figure 6** more direct. First, the core field model is truncated at spherical harmonic degree 14, whereas the numerical dynamos used for F^* in **Figure 6** represent the field to spherical harmonic degree 85. Second, ambiguities arise in the calculation of F^* that depend on the choice of the geographic equator vs. the magnetic equator. All of the values of F^* in **Figure 6** are based on the geographic equator, whereas the standard methods for calculating reversed flux on the CMB make use of the magnetic equator (Terra-Nova et al., 2015; Metman

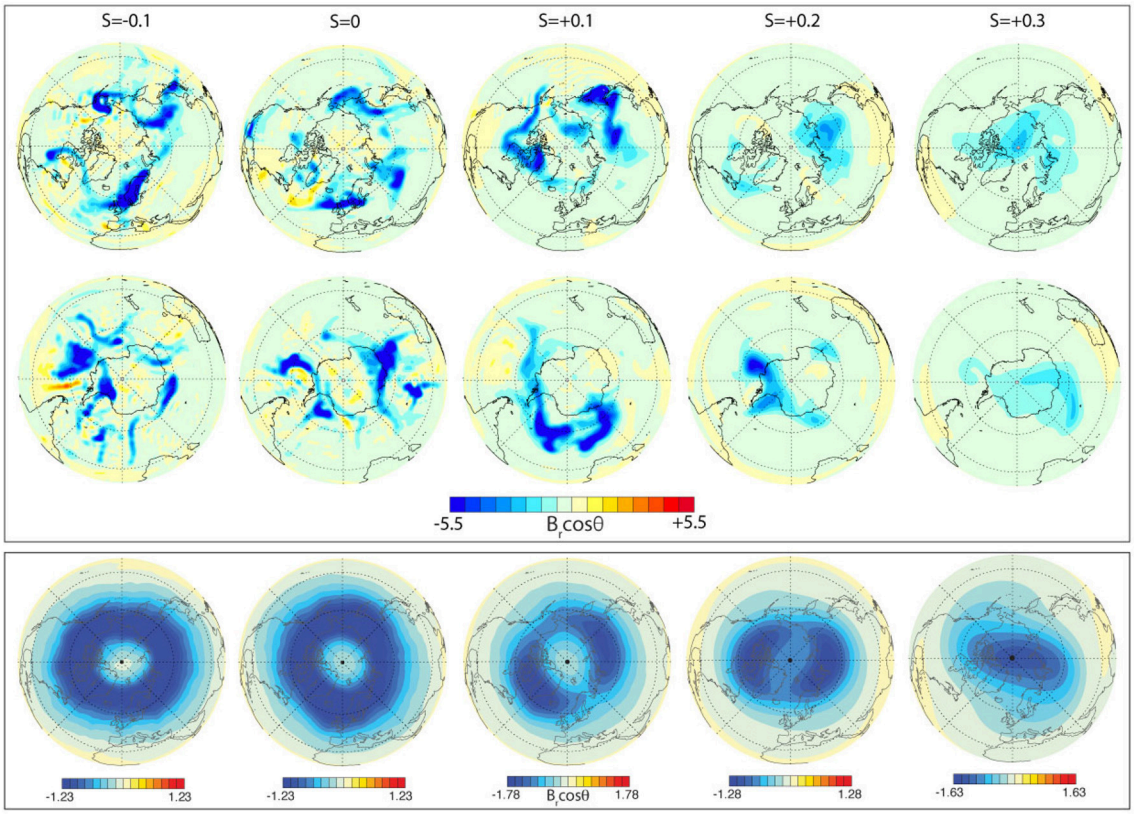

FIGURE 5 | Snapshots and time averages of $B_r \cos(\theta)$ from numerical dynamos at $Ra = 6 \times 10^7$ for different stratification parameters S. Top row: Northern hemisphere snapshots; middle row: Southern hemisphere snapshots at the same times; bottom row: Northern hemisphere time averages. Magnetic field intensities are in dimensionless Elsasser number units.

et al., 2018). The most obvious consequence of the choice of equator is the contribution to reversed flux from the tilt of the dipole axis. Dipole axis tilt contributes to the inventory of reversed flux when using the geographic equator, but it need not when using the magnetic equator. Third, the value of F^* changes with time in the core field model, being generally smaller in the past, whereas the averaging of widely spaced snapshots removes most (or all) of the secular drift in F^* from the numerical dynamos.

For these reasons, we show in **Figure 7** comparisons between numerical dynamos, the COV-OBS core field model, and two other core field models, based on a modified reversed to normal flux ratio, F_C^*. For the core field model COV-OBS, F_C^* is just F^* with the equatorial dipole terms removed. Removing the equatorial dipole represents the lowest order correction to the magnetic equator. F_C^* from COV-OBS is shown at epochs 2014 and 1964, to illustrate the magnitude of the drift in this parameter with time. MLM in **Figure 7** corresponds to the mean value of F_C^* calculated by Metman et al. (2018) for epoch 2015 using their definition of magnetic equator on core field model COV-OBS.x1 (Gillet et al., 2015). TN in **Figure 7** corresponds to the value of F_C^* calculated by Terra-Nova et al. (2015) using their definition of magnetic equator on the present-day (zero age) limit of archeomagnetic field model CALSk.4b (Korte and Constable, 2011). For the numerical dynamos, F_C^* in **Figure 7** is F^* with the equatorial dipole terms removed and with a crustal filter applied, such that the magnetic field amplitude decreases by a factor of e with each spherical harmonic degree above 14. We note that the effects of removing the equatorial dipole from the numerical dynamos and the modern core field models are comparable, because the r.m.s. dipole axis tilt of the numerical dynamos (10 degrees at $Ra = 6 \times 10^7$ and 12 degrees at $Ra = 6 \times 10^7$) are comparable to the time average dipole axis tilt in the historical geomagnetic field. Finally, we calculate F_C^* for the dynamos and for field model COV-OBS using the same 1.5 x 1.5 degree grid.

The effects of crustal filtering and correction to the magnetic equator are to reduce F_C^* relative to F^*, for the core field models as well as the numerical dynamos. Yet the same trends evident in **Figure 6** are seen in **Figure 7**, with perhaps greater clarity. The numerical dynamos with $S = 0.1$ are compatible with all three core field models, in spite of the differences in processing that went into calculating reversed and normal flux in each case. There is some suggestion in **Figure 7** that neutrally stratified dynamos with $S = 0$ may also be compatible, although this comparison is less convincing. And, just like **Figure 6**, this comparison argues against the more strongly stratified dynamos

with $S = 0.2$ and greater. In short, **Figures 6**, **7** imply that strong thermal stratification below the CMB, characterized by $S \geq 0.2$, as well as strongly superadiabatic conditions below the CMB characterized by $S \leq -0.1$, are incompatible with the present-day structure of the geomagnetic field insofar as the amount of reversed flux is concerned, whereas on this same basis, the present-day field is compatible with weak stratification characterized by $S = 0.1$ or perhaps a bit less.

Disappearance of reversed flux with increasingly strong stratification is a direct consequence of the reduction in strength of the radial velocity below the outer boundary. **Figure 8** shows F_C^* vs. the CMB upwelling strength W^* defined by (15). The CMB upwelling is given in dimensionless form, in units of η/D^2. The color and symbol schemes in **Figure 8** are the same as in **Figure 6**, and only the snapshot averaged values of W^* are plotted because the variation between snapshots is no larger than the symbols. **Figure 8** shows a strong, positive and approximately linear correlation between the dynamo reversed to normal flux ratio and CMB upwelling. CMB upwelling less than a few hundred hardly produces any reversed flux, whereas for CMB upwelling above $W^* \simeq 1700$, reversed flux reduces the axial dipole by 10% or more. **Figure 8** also shows the range in F_C^* from the core field models in **Figure 7**. The best matching $S = 0.1$ and $S = 0$ dynamos intersect the dynamo trend at dimensionless

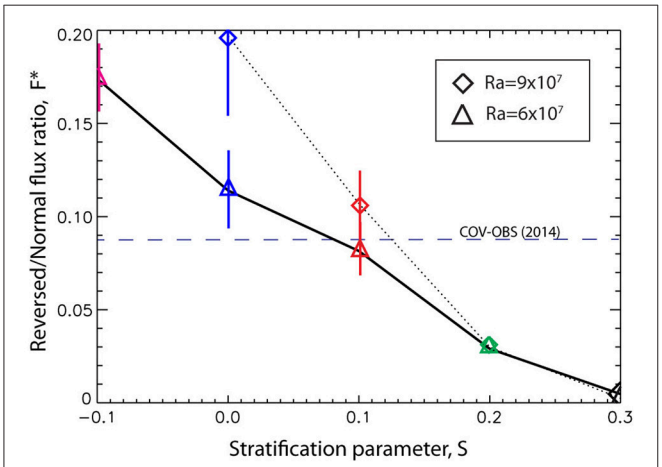

FIGURE 6 | Ratios of reversed to normal flux contributions to the axial dipole F^* vs. stratification parameter S from numerical dynamos (symbols), compared to F^* from the COV-OBS geomagnetic field model on the core-mantle boundary at epoch 2014 (dashed line). Error bars denote one standard deviation of dynamo snapshots.

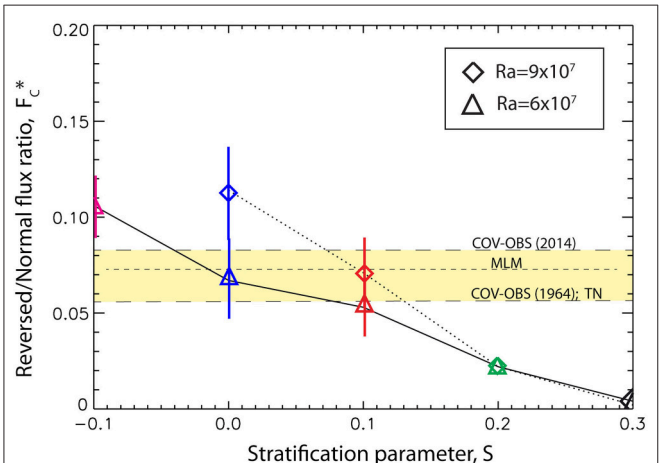

FIGURE 7 | Modified ratios F_C^* of reversed to normal flux contributions to the axial dipole vs. stratification parameter S from numerical dynamos (symbols), compared to F_C^* from geomagnetic field models on the core-mantle boundary. Geomagnetic field F_C^* values labeled COV-OBS, MLM, and TN are explained in the text. Symbol error bars denote one standard deviation of dynamo snapshots.

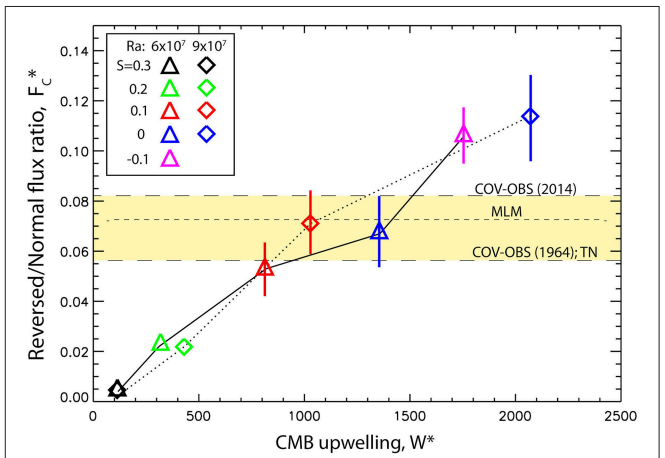

FIGURE 8 | Modified ratios F_C^* of reversed to normal flux contributions to the axial dipole vs. dimensionless r.m.s. upwelling W^* below the core-mantle boundary from numerical dynamos (symbols), compared to the geomagnetic field models on the core-mantle boundary described in the text.

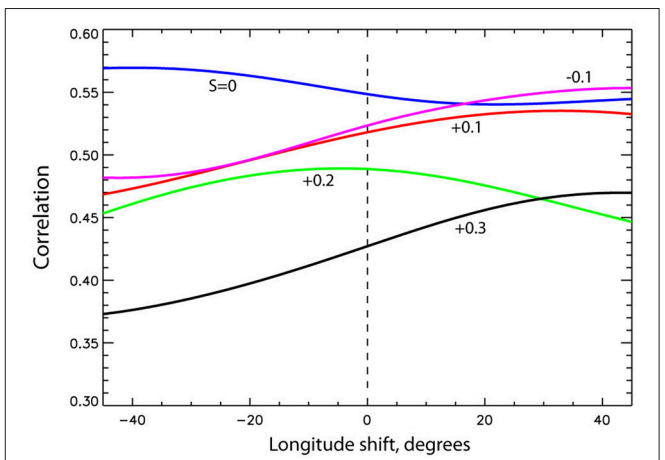

FIGURE 9 | $B_r \cos(\theta)$ cross correlations of the 1840-2014 time average COV-OBS CMB geomagnetic field model vs. numerical dynamo time averages at $Ra = 6 \times 10^7$, for various stratification parameters S.

CMB upwelling strengths of W^* = 800–1500, with $W^* \simeq 1000$ being a representative value.

In addition to reversed flux in snapshots, the polar structure of the time average geomagnetic field is also sensitive to core stratification. Based on visual comparison of the time averages in **Figures 4**, **5**, the $S = 0.1$ dynamo best replicates the polar field structure of COV-OBS geomagnetic field model. The high latitude structure of that dynamo in **Figure 5** includes two partially isolated high field intensity patches enclosing a polar intensity minimum, much like the high latitude geomagnetic field structures in **Figure 4**. In contrast, the dynamos with $S \leq 0$ in **Figure 5** have ring-shaped high intensity field regions, while the dynamos with $S \geq 0.2$ lack polar intensity minima or in the extreme case, have polar intensity maxima.

A quantitative test of this visual interpretation can be made using the cross correlation between a time average dynamo magnetic field and a 174 year geomagnetic field average. **Figure 9** shows global cross correlations of time average $B_r \cos(\theta)$ between the $Ra = 6 \times 10^7$ dynamos and the COV-OBS geomagnetic field model vs. longitude shift in degrees, with positive and negative denoting westward and eastward shifts, respectively, of the dynamo relative to the geomagnetic field model. It is helpful to include longitude pattern shifts in this analysis, since the longitudes of the high field intensity patches vary with the dynamo control parameters. Allowance for some longitude pattern shift mitigates the bias from this variation. The spectra of the time average dynamo fields on the outer boundary contain little power above spherical harmonic degree 14, so crustal filtering is not necessary here. The cross correlations were preconditioned for weak field suppression by masking boundary regions with field intensity below 20% of the maximum intensity, in order to add weight to the high field intensity regions. **Figure 9** indicates there is some dependence of the correlation on longitude shift, but for shifts of 20^o or less the effect is relatively minor. More significantly, there is a substantial difference in this correlation between unstratified and weakly stratified dynamos vs. the strongly stratified dynamos, with the former group correlating above 0.5 and the latter group below 0.5. Interestingly, the best correlation is found for the unstratified $S = 0$ dynamo and the second best is the $S = -0.1$ dynamo, although their correlations differ very little from the $S = 0.1$ dynamo overall.

6. IMPLICATIONS FOR OUTER CORE STRATIFICATION

Our comparisons between numerical dynamos and the geomagnetic field on the CMB favor the existence of outer core stratification with stratification parameter S close to 0.1. Equally significant, these same comparisons argue against stronger outer core stratification, as would be characterized by $S \geq 0.2$, say. Although our study does not consider situations in which the stabilizing effects of stratification vastly outweigh the destabilizing effects of inner core growth, as would be the case for strong compositional stratification (Landeau et al., 2016; Nakagawa, 2017; Christensen, 2018), the fact that we can exclude thermally stratified dynamos with large S suggests our results might also be applicable for constraining outer core compositional stratification.

Assuming that $S = 0.1$ in the region below the CMB, our previously-derived dynamo scaling laws yield estimates of the thickness of the stratified layer and its gravitational stability. In dimensional terms, our scaling laws for stratified layer thickness (13) and squared buoyancy frequency (14) are, for the outer core

$$\delta = 1.8 S^{1.2} r_{cmb} \tag{16}$$

plus

$$N^2 = 0.72 \frac{\alpha g}{k} (q_{ad} - \bar{q}_{cmb}), \tag{17}$$

and from the definition (7) of S, the subadiabatic heat flux on the CMB is

$$q_{ad} - \bar{q}_{cmb} = \frac{S \beta D k \dot{\chi}_o}{\alpha \nu}. \tag{18}$$

Using the core property values in **Table 1** with $S = 0.1$, (16) gives $\delta \simeq 400$ km, (18) gives $q_{ad} - \bar{q}_{cmb} \simeq 17\ mW.m^{-2}$, and (17) gives $N^2 \simeq 1.7 \times 10^{-8}$ rad^2.s^{-2}.

A 400 km layer may seem excessively thick for a thermal stratification, but it is important to note that this value refers to the full spherical mean thickness of the layer, from the CMB to the depth where the spherically averaged codensity profile has a local minimum. Furthermore, although our results favor $S = 0.1$

TABLE 1 | Core properties.

Input properties	Notation	Value
ICB radius	r_{icb}	1220 km[a]
CMB radius	r_{cmb}	3480 km[a]
Mean core density	ρ_o	1.1×10^4 kg.m^{-3} [a]
Gravity at the CMB	g	10.68 m.s^{-2} [a]
Thermal expansion coefficient	α	1.3×10^{-5} K^{-1} [b]
Compositional expansion coefficient	β	1
Thermal conductivity	k	100 W.m^{-1}.K^{-1} [c]
Electrical conductivity	σ	1×10^6 S.m^{-1} [d]
Magnetic diffusivity	η	0.8 m^2.s^{-1}
Outer core kinematic viscosity	ν	1×10^{-5} m^2.s^{-1} [e]
Adiabatic CMB heat flux	q_{ad}	$100\ mW.m^{-2}$
CMB heat flux heterogeneity	Δq_{cmb}	$100\ mW.m^{-2}$
Light element concentration change rate	$\dot{\chi}_o$	1×10^{-19} s^{-1}
Output properties	**Notation**	**Value**
Stratification parameter	S	$\simeq 0.1$
Stratified layer thickness	δ	$\leq$ 400 km
Stratified layer stability	N^2	1.7×10^{-8} rad^2.s^{-2}
CMB upwelling, r.m.s.	W	0.5 century^{-1}
Mean CMB heat flux	$\bar{q}_{cmb}$	$83\ mW.m^{-2}$

[a] *Dziewonski and Anderson (1981)*; [b] *Vocaldo et al. (2003)*; [c] *Hirose et al. (2013)*; [d] *Poirier (2000)*; [e] *Perrillat et al. (2010)*.

stratification, they are also marginally consistent with somewhat weaker stratification, $S = 0.05$ for example. In that case, the stratified layer would be substantially thinner, with $\delta \simeq 170$ km.

In dynamical terms, such a layer would not prevent upward radial motions reaching close to the CMB, as evidenced by our finding that the r.m.s. CMB upwelling strength $W^* \simeq 1000$. For the geodynamo, in dimensional units, $W \simeq 1000\eta/(r_{cmb} - r_{icb})^2$, where the subscripts cmb and icb denote outer and inner core radii, respectively. In terms of the values of core properties in **Table 1**, this corresponds to $W \simeq 0.5$/century for the r.m.s upwelling below the CMB, within the range of the estimates of the r.m.s. CMB upwelling obtained from frozen flux inversions of the geomagnetic secular variation, which vary between 0.1/century and 4/century r.m.s. (Amit and Olson, 2006; Amit and Pais, 2013). Even with S=0.1 stratification, superadiabatic thermal conditions may be present beneath approximately 5% of the CMB, according to the boundary heat flux pattern in **Figure 1**. If so, thermal instabilities originating at the CMB can penetrate the layer in these regions, making the thermal stratification somewhat permeable to outer core convection and allowing the formation of reversed flux spots as observed in the geomagnetic core field.

Permeable stratification distributed over several hundred kilometers beneath the CMB is consistent with other fluid dynamical effects, in particular, the upward penetration of convection through a weakly stratified layer (Takehiro and Lister, 2002; Rogers and Glatzmaier, 2005). Two scalings for the penetration distance have been proposed; because it is unclear which applies best to the core, we consider both. The first, by Takehiro and Lister (2002), predicts that convection penetrates a distance given by $\delta_p \sim 2\Omega\lambda/N$, where λ is the horizontal flow length scale. Using (17), we estimate $2\Omega/N \sim 1$ for thermal stratification in the Earth's core. This implies a weak stratification, where the effects of stable stratification below the CMB are only about as strong as Coriolis effects from rotation. With this stratification, the Takehiro and Lister (2002) scaling predicts that convective eddies wider than about 400 km will penetrate to the CMB. The second scaling is derived from numerical models of solar convection (Hurlburt et al., 1994; Rogers and Glatzmaier, 2005). These studies find that the penetration distance scales with the ratio of the unstable to the stable stratification, i.e., $\delta_p \sim DS^{-1}$ in our notation. This scaling also predicts that convective motions easily penetrate a 400 km layer with $S = 0.1$.

The Rayleigh number Ra, the Ekman number E and the magnetic Prandtl number Pm in our numerical dynamos are orders of magnitude away from Earth's core values. This raises a standard question for dynamo modelers: How sensitive are our conclusions to our parameter choices? Assuming reversed flux spots originate from toroidal flux expulsion (Gubbins, 2007), we expect the flux ratio at the CMB (either F^* or F_C^*) to scale as the flux ratio measured in the underlying convective region modulated by the radial velocity in the stratified region relative to that in the convective region. For dipole-dominated dynamos, the relative strength of the dipole varies only marginally with Ra, E, and Pm (Aubert et al., 2009). We hypothesize that the flux ratios in the convective region are only weakly sensitive to these parameters. In addition, the radial velocity in the stratified region relative to that in the convective region depends only on the ratio of the stratified layer thickness δ to the penetration distance of the convection δ_p. Using the scalings discussed above for δ_p and relation (16), we infer that δ/δ_p, and therefore F^* and F_C^* depend only on S and possibly Ω/N. And, in contrast to Ra, E, and Pm, the values of Ω/N and S in our dynamos are in the range expected for thermal stratification at the top of Earth's core (Takehiro and Lister, 2002; Buffett et al., 2016). Provided these expectations are met, our conclusions about stratification are applicable to the core. This can be tested by extending our analysis to stratified dynamos with more realistic values of Ra, E, and Pm.

AUTHOR CONTRIBUTIONS

PO and ML designed the study, did the analysis, and wrote the paper. ER managed the dynamo calculations and produced the dynamo data products.

ACKNOWLEDGMENTS

This research was supported in part by Frontiers in Earth System Dynamics grant EAR-1135382 from the National Science Foundation. Additional support for ML came from the European Union's Horizon 2020 Research and Innovation Programme under the Marie Sklodowska-Curie grant agreement 703767. The dynamo calculations were made at the Maryland Advanced Research Computer Center (MARCC). We thank Nicolas Gillet for directing us to the COV-OBS geomagnetic field model. This paper benefited from thoughtful reviews by M. Metman, B. Sreenivasan, and editor H. Amit.

REFERENCES

Amit, H. (2014). Can downwelling at the top of the Earth's core be detected in the geomagnetic secular variation? *Phys. Earth Planet. Int.* 229, 110–121. doi: 10.1016/j.pepi.2014.01.012

Amit, H., and Olson, P. (2006). Time-average and time-dependent parts of core flow. *Phys. Earth Planet. Int.* 155, 120–139. doi: 10.1016/j.pepi.2005.10.006

Amit, H., and Pais, M. A. (2013). Differences between tangential geostrophy and columnar flow. *Geophys. J. Int.* 194, 145–157. doi: 10.1093/gji/ggt077

Aubert, J., Labrosse, S., and Poitou, C. (2009). Modelling the palaeo-evolution of the geodynamo. *Geophys. J. Int.* 179, 1414–1428. doi: 10.1111/j.1365-246X.2009.04361.x

Brodholt, J., and Badro, J. (2017). Composition of the low seismic velocity E′ layer at the top of the core. *Gephys. Res. Lett.* 44, 8303–8310. doi: 10.1002/2017GL074261

Browning, M., Brun, A. S., Miesch, M., and Toomre, J. (2007). Dynamo action in simulations of penetrative solar convection with an imposed tachocline. *Astrophys. J.* 648, 157–160. doi: 10.1002/asna.200710849

Browning, M., Miesch, M., Brun, A. S., and Toomre, J. (2006). Dynamo action in the solar convection zone and tachocline: pumping and organization of toroidal fields. *Astron. Nachr.* 328, 1100–1103. doi: 10.1086/507869

Brummell, N., Tobias, S., and Cattaneo, F. (2010). Dynamo efficiency in compressible convective dynamos with and without penetration. *Geophys. Astrophys. Fluid Dyn.* 104, 565–576. doi: 10.1080/03091929.2010.495067

Buffett, B. (2014). Geomagnetic fluctuations reveal stable stratification at the top of the Earth's core. *Nature* 507, 484–487. doi: 10.1038/nature13122

Buffett, B., Knezek, N., and Holme, R. (2016). Evidence for MAC waves at the top of Earth's core and implications for variations in length of day. *Geophys. J. Int.* 204, 1789–1800. doi: 10.1093/gji/ggv552

Christensen, U. (2006). A deep dynamo generating mercury's magnetic field. *Nature* 444, 1056–1058. doi: 10.1038/nature05342

Christensen, U. (2018). Geodynamo models with a stable layer and heterogeneous heat flow at the top of the core. *Geophys. J. Int.* 215, 1338–1351. doi: 10.1093/gji/ggy352

Christensen, U., and Wicht, J. (2008). Models of magnetic field generation in partly stable planetary cores: applications to Mercury and Saturn. *Icarus* 196, 16–34. doi: 10.1016/j.icarus.2008.02.013

Couston, L.-A., Lecoanet, D., Favier, B., and Le Bars, M. (2018). Order out of chaos: slowly reversing mean flows emerge from turbulently generated internal waves. *Phys. Rev. Lett.* 120, 16–34. doi: 10.1103/PhysRevLett.120.244505

Dziewonski, A. M., and Anderson, D. L. (1981). Preliminary reference Earth model. *Phys. Earth Planet. Int* 25, 297–356.

Dziewonski, A. M., Lekic, V., and Romanowicz, B. A. (2010). Mantle anchor structure: an argument for bottom up tectonics. *Earth Planet. Sci. Lett.* 299, 69–79. doi: 10.1016/j.epsl.2010.08.013

Garnero, E. J., Helmberger, D. V., and Grand, S. P. (1993). Constraining outermost core velocity with SmKS waves. *Geophys. Res. Lett*. 20, 2463–2466.

Garnero, E. J., and McNamara, A. (2008). Structure and dynamics of Earth's lower mantle. *Science* 320, 626–628. doi: 10.1126/science.1148028

Gillet, N., Barrois, O., and Finlay, C.C. (2015). Stochastic forecasting of the geomagnetic field from the COV-OBS.x1 geomagnetic field model, and candidate models for IGRF-12. *Earth Planets Space* 76:71. doi: 10.1186/s40623-015-0225-z

Gillet, N., Jault, D., Finlay, C. C., and Olsen, N. (2013). Stochastic modeling of the Earth's magnetic field: inversion for covariances over the observatory era. *Geochem. Geophys. Geosyst.* 14, 766–786. doi: 10.1002/ggge.20041

Gomi, H., Ohta, K., Hirose, K., Labrosse, S., Caracas, R., Verstraete, M. J. et al. (2013). The high conductivity of iron and thermal evolution of the Earth's core. *Phys. Earth Planet. Int*. 224, 88–103. doi: 10.1016/j.pepi.2013.07.010

Gubbins, D. (2007). Geomagnetic constraints on stratification at the top of Earth's core. *Earth Planet. Space* 59, 661–664. doi: 10.1186/BF03352728

Gubbins, D., and Davies, C. (2013). The stratified layer at the core-mantle boundary caused by barodifusion of oxygen, sulfur and silicon. *Phys. Earth Planet. Int.* 215, 21–28. doi: 10.1016/j.pepi.2012.11.001

Helffrich, G., and Kaneshima, S. (2010). Outer-core compositional stratification from observed core wave speed profiles. *Nature* 468, 807–810. doi: 10.1038/nature09636

Helffrich, G., and Kaneshima, S. (2013). Causes and consequences of outer core stratification. *Phys. Earth Planet. Int*. 223, 2–7. doi: 10.1016/j.pepi.2013.07.005

Hirose, K., Labrosse, S., and Hernlund, J. (2013). Composition and state of the core. *Annu. Rev. Earth Planet. Sci*. 41, 657–691. doi: 10.1146/annurev-earth-050212-124007

Huguet, L., Amit, H., and Alboussiere, T. (2016). Magnetic to magnetic and kinetic to magnetic energy transfers at the top of the Earth's core. *Geophys. J. Int*. 207, 934–948. doi: 10.1093/gji/ggw317

Hurlburt, N., Toomre, J., Massaguer, J., and Zahn, P. (1994). Penetration below a convective zone. *Astrophys. J.* 421, 245–260. doi: 10.1086/173642

Irving, J. C. E., Cottarr, S., and Lekic, V. (2018). Seismically determined elastic parameters for Earth's outer core. *Sci. Adv.* 4:eaar2538. doi: 10.1126/sciadv.aar2538

Kaneshima, S. (2017). Array analyses of SmKS waves and the stratification of Earth's outermost core. *Phys. Earth Planet. Int*. 276, 234–246. doi: 10.1016/j.pepi.2017.03.006

Käpylä, P., Korpi, M., Brandenburg, A. (2008). Large-scale dynamos in turbulent convection with shear. *Astron. Astrophys*. 491, 353–362. doi: 10.1051/0004-6361:200810307

Korte, M., and Constable, C. (2011). Improving geomagnetic field reconstructions for 0-3 ka. *Phys. Earth Planet. Int*. 188, 247–259. doi: 10.1016/j.pepi.2011.06.017

Landeau, M., Olson, P., Deguen, R., and Hirsh, B. (2016). Core merging and stratification after giant impacts. *Nat. Geosci.* 9, 786–789. doi: 10.1038/ngeo2808

Lay, T., and Young, C. (1990). The stably-stratified outermost core revisited. *Geophys. Res. Lett.* 17, 2001–2004.

Lesur, V., Whaler, K., and Wardinski, I. (2015). Are geomagnetic data consistent with stably stratified flow at the core-mantle boundary? *Geophys. J. Int.* 201, 929–946. doi: 10.1093/gji/ggv031

Manglik., A., Wicht, J., and Christensen, U. (2010). A dynamo model with double diffusive convection for Mercury's core. *Earth Planet. Sci. Lett.* 289, 619–628. doi: 10.1016/j.epsl.2009.12.007

Masada, Y., Yamada, K., and Kageyama, A. (2013). Effects of penetrative convection on solar dynamo. *Astrophys. J.* 778:16. doi: 10.1088/0004-637X/778/1/11.

Metman, M. C., Livermore, P. W., and Mound, J. E. (2018). The reversed and normal flux contributions to axial dipole decay for 1880-2015. *Phys. Earth Planet. Int*. 276, 106–117. doi: 10.1016/j.pepi.2017.06.007

Nakagawa, T. (2011). Effect of a stably stratified layer near the outer boundary in numerical simulations of a magnetohydrodynamic dynamo in a rotating spherical shell and its implications for Earth's core. *Phys. Earth Planet. Int*. 187, 342–352. doi: 10.1016/j.pepi.2011.06.001

Nakagawa, T. (2015). An implication for the origin of stratification below the core-mantle boundary region in numerical dynamo simulations in a rotating spherical shell. *Phys. Earth Planet. Int*. 247, 94–104. doi: 10.1016/j.pepi.2015.02.007

Nakagawa, T. (2017). On the thermo-chemical origin of the stratified region at the top of the Earth's core. *Phys. Earth Planet. Int*. 276, 172–181. doi: 10.1016/j.pepi.2017.05.011

Nakagawa, T., and Tackley, P. J. (2013). Implications of high core thermal conductivity on Earth's coupled mantle and core evolution. *Geophys. Res. Lett*. 40, 2652–2656. doi: 10.1002/grl.50574

Nakagawa, T., and Tackley, P. J. (2015). Influence of combined primordial layering and recycled MORB on the coupled thermal evolution of Earth's mantle and core. *Geochem. Geophys. Geosyst*. 15, 619–633. doi: 10.1002/2013GC005128

Ohta, K., Kuwayama, Y., Hirose, K., Shimizu, K., and Ohishi, Y. (2016). Experimental determination of the electrical resistivity of iron at earth's core conditions. *Nature* 534, 95–98. doi: 10.1038/nature17957

Olsen, N., Luhr, H., Finlay, C., Sabaka, T., Michaelis, I., Rauberg, J., et al. (2014). The chaos-4 geomagnetic feld model. *Geophys. J. Int.* 197, 815–827. doi: 10.1093/gji/ggu033

Olson, P., and Amit, H. (2006). Changes in Earth's dipole. *Naturwissenschaften* 93, 519–542. doi: 10.1007/s00114-006-0138-6

Olson, P., and Amit, H. (2015). Mantle superplumes induce geomagnetic superchrons. *Front. Earth Sci.* 3:38. doi: 10.3389/feart.2015.00038

Olson, P., Deguen, R., Rudolph, M. L., and Zhong, S. (2015). Core evolution driven by mantle global circulation. *Phys. Earth Planet. Int*. 243, 44–55. doi: 10.1016/j.pepi.2015.03.002

Olson, P., Landeau, M., and Reynolds, E. (2017). Dynamo tests for stratification below the core-mantle boundary. *Phys. Earth Planet. Int.* 271, 1–18. doi: 10.1016/j.pepi.2017.07.003

Perrillat, J.-P., Mezouar, M., Garbarino, G., and Bauchau, S. (2010). *In situ* viscometry of high-pressure melts in the Paris-Edinburgh cell: application to liquid FeS. *High Pressure Res.* 30, 415–423. doi: 10.1080/08957959.2010.494844

Poirier, J.-P. (2000). *Introduction to the Physics of the Earth's Interior, 2nd Edn*. Cambridge: Cambridge University Press.

Rogers, T., and Glatzmaier, G. (2005). Penetrative convection within the anelastic approximation. *Astrophys. J.* 620, 432–441. doi: 10.1086/423415

Sreenivasan, B., and Gubbins, D. (2008). Dynamos with weakly convecting outer layers: implications for core-mantle boundary interaction. *Geophys. Astrophys. Fluid Dyn*. 102, 395–407. doi: 10.1080/03091920801900047

Stanley, S. (2010). A dynamo model for axisymmetrizing Saturn's magnetic field. *Geophys. Res. Lett.* 37:L05201. doi: 10.1029/2009GL041752

Takehiro, S., and Lister, J. (2002). Surface zonal flows induced by thermal convection trapped below a stably stratified layer in a rapidly rotating spherical shell. *Geophys. Res. Lett.* 29:50. doi: 10.1029/2002GL015450

Tanaka, S. (2007). Possibility of a low p-wave velocity layer in the outermost core from global smks waveforms. *Earth Planet. Sci. Lett*. 259, 486–499. doi: 10.1016/j.epsl.2007.05.007

Tang, V., Zhao, L., and Hung, S. (2015). Seismological evidence for a non-monotonic velocity gradient in the topmost outer core. *Sci. Rep*. 5:8613. doi: 10.1038/srep08613

Terra-Nova, F., Amit, H., Hartmann, G. A., and Trindade, R. I. F. (2015). The time dependence of reversed archeomagnetic flux patches. *J. Geophys. Res. Solid Earth* 120, 691–704. doi: 10.1002/2014JB011742

Tobias, S., Cattaneo, F., and Brummell, N. (2008). Convective dynamos with penetration, rotation, and shear. *Astrophys. J.* 685, 596–605. doi: 10.1086/590422

Vocaldo, L., Alfe, D., Gillan, M. J., and Price, G. D. (2003). The properties of iron under core conditions from first principles calculations. *Phys. Earth Planet. Int.* 140, 101–125. doi: 10.1016/j.pepi.2003.08.001

Whaler, K. (1980). Does the whole of the Earth's core convect? *Nature* 287, 528–553.

Wicht, J. (2002). Inner-core conductivity in numerical dynamo simulations. *Phys. Earth Planet. Inter.* 132, 281–302. doi: 10.1016/S0031-9201(02)00078-X

Zhang, K., and Schubert, G. (2000). Teleconvection: remotely driven thermal convection in rotating stratified spherical layers. *Science* 290, 1944–1947. doi: 10.1126/science.290.5498.1944

Zhong, S. J., and Rudolph, M. L. (2015). On the temporal evolution of long-wavelength mantle structure of the Earth's mantle since the Early Paleozoic. *Geochem. Geophys. Geosyst.* 16, 1599–1615. doi: 10.1002/2015GC005782

Conflict of Interest Statement: ER, is currently employed by T-Mobile USA. At the time this research was done, ER was employed by the Johns Hopkins University, under the grant listed in the acknowledgments of our paper.

The remaining authors declare that the research was conducted in the absence of any commercial or financial relationships that could be construed as a potential conflict of interest.

Advantages of publishing in Frontiers

OPEN ACCESS
Articles are free to read for greatest visibility and readership

FAST PUBLICATION
Around 90 days from submission to decision

HIGH QUALITY PEER-REVIEW
Rigorous, collaborative, and constructive peer-review

TRANSPARENT PEER-REVIEW
Editors and reviewers acknowledged by name on published articles

Frontiers
Avenue du Tribunal-Fédéral 34
1005 Lausanne | Switzerland

Visit us: www.frontiersin.org
Contact us: info@frontiersin.org | +41 21 510 17 00

REPRODUCIBILITY OF RESEARCH
Support open data and methods to enhance research reproducibility

DIGITAL PUBLISHING
Articles designed for optimal readership across devices

FOLLOW US
@frontiersin

IMPACT METRICS
Advanced article metrics track visibility across digital media

EXTENSIVE PROMOTION
Marketing and promotion of impactful research

LOOP RESEARCH NETWORK
Our network increases your article's readership